Synthesis of Photoluminescent Tin (II) Sulphide Colloidal Quantum Dots for Bioimaging Applications

Zhanet Zaharieva Zaharieva
St Cross College
University of Oxford

A thesis submitted in fulfillment of the requirement for the degree of

Doctor of Philosophy in Materials Science

Trinity 2018

Abstract

The primary focus of this thesis is to achieve control over the chemistry by developing new synthetic methods for the fabrication of tin (II) sulphide (SnS) colloidal quantum dots (CQDs) with optimised optoelectronic and physicochemical properties revealing novel photoluminescent (PL) characteristics and investigate their potential for biological applications.

The reactivity of different sulfur (S) precursors and their effect on the reaction thermodynamics and kinetics were examined. The final composition of the QDs was investigated using scanning transmission electron microscopy (STEM) and energy-dispersive X-ray spectroscopy (EDS). It was observed that depending on reaction conditions such as reaction temperature, reaction times and reactivity of precursors resulted in CQDs with tunable sizes and optoelectronic properties. The faster reacting S precursor resulted in stoichiometrically balanced CQDs (Sn:S = 1:1) compared to the slower reacting S precursor, which produced CQDs with a range of aspect ratios with close molar ratios (xSn:1S) giving rise to novel multi-colour PL emission properties due to quantum confinement. The data obtained from 3D PL, time-resolved μPL (TRPL), UV-Vis and STEM/EDX analysis revealed that both size- and composition-changes are in the origin of the excitation-dependent PL emission features of SnS CQDs.

An alternative synthetic procedure for passivating the surface of SnS CQDs was developed with the aim to study the effect of different surface chemistries on the PL properties of the QDs. UV-Vis data revealed that the incorporation of organic molecules as surface stabilisers could induce strong quantum confinement effect evident from the absorption excitonic peak at ~ 440 nm.

SnS CQDs were investigated as a potential material in biofilm and bioimaging applications due to their multi-colour PL emission properties. The growing curves of *P. fluorescence* bacterial

strain showed that the initiation of the biofilm formation was not toxicity but rather surface chemistry phenomenon not affect the reproduction of the bacterial community. The imaging studies demonstrated the high photostability of SnS CQDs by acquiring bright, high-quality fluorescence images with no photobleaching features.

The following literature review summarised the key challenges that have been observed in the field of SnS CQDs such as synthesising high-quality CQDs with optimised physical, chemical and optoelectronic properties. It covered solution processing techniques including different surface passivation strategies resulting in QDs with excellent stability and durability for bioimaging applications as a future low-cost and non-toxic bioimaging gents.

Dedicaiton

In honour of my father, Zahari Zhekov Zahariev in appreciation of his inspiration, continuous support and unconditional love.

В чест на моя баща, Захари Жеков Захариев, оценявайки неговото вдъхновение, нестихваща подкрепа и безусловна любов.

Acknowledgments

I would like to express my sincere gratitude to my supervisor Prof. Andrew. A. R. Watt for his guidance and support. I would like to thank about the resources and opportunities for visiting conferences and making collaborations he has provided. His suggestions have always inspired me to be creative and search for answers. Furthermore, I would like to thank Prof. Hazel E. Assender for proving beneficial discussions and support during our group meetings.

I would like to thank my amazing colleagues, Nanlin Zhang, Yujiro Tazawa, Wing Chong Liu, Thomas Cosnahan for their encouragement and great memories. I would like to thank Isabel Al-Dhahir, Daniel Gregory, Brett Castle, Suer Zhou, Yu Li and Zhang Zhang. I would also like to thank my college advisor Prof. Kevin Marsh.

I would like to thank Dr Judy Kim for her advice and support in TEM analysis. I would like to thank Prof. Robert Taylor from the Department of Physics, University of Oxford for providing me with the opportunity for collaboration and discussions. I would like to thank Dr Tim Puchtler for his support in TRPL measurements. I would like to thank Philip Holdway for the support in XPS and XRD analysis. I would like to acknowledge and thank all department staff.

Statement of originality

This thesis is an account of work carried out by the author in the Department of Materials, the University of Oxford under the supervision of Professor Andrew Watt and Professor Jamie Warner. Any work of others that have been utilised, directly or indirectly, is duly acknowledged in the text, and a list of references is presented at the end of each chapter. No part of this thesis has been submitted towards the completion of another degree at the University of Oxford or elsewhere. Parts of the thesis have been described in a manuscript for submission:

First author articles:

Zaharieva, Zhanet *et al.* **Multi-colour Photoluminescence emission of SnS CQDs for Bioimaging Applications.** (Manuscript under review)

Zaharieva, Zhanet *et al.* **Strong quantum confinement effect in PVP-encapsulated SnS CQDs.** (Manuscript under review)

Co-author articles:

Gabriel Nagamine, Jaqueline O. Rocha, Luiz G. Bonato, Ana F. Nogueira, Zhanet Zaharieva, Andrew A. R. Watt, Carlos H. de Brito Cruz, Lazaro A. Padilha. **Two-photon Absorption and Two-Photon Induced Gain in Perovskites Quantum dots.** Journal of Physical Chemical Letters 9, 12 (2018). doi: 10.1021

Nanlin Zhang, Daniel Gregore, Yujiro Tazawa, Zhanet Zaharieva, Darren C. J. Neo, Hazel E. Assender, Andrew A. R. Watt. **CsI Passovated Quantum Dot Solar Cells—Eliminating Surface Oxides without Dimethylformamide.** (Manuscript under review)

Signed…… Date…….

Contents

List of Abbreviations

E_g	Band gap
α_b	Bohr exciton radius
CQDs	Colloidal quantum dots
EDS	Energy dispersive X-Ray spectroscopy
FFT	Fast Fourier transform
FTIR	Fourier transform infra-red spectroscopy
HRTEM	High-resolution transmission electron microscopy
NCs	Nanocrystals
NPs	Nanoparticles
OA	Oleic acid
OLA	Oleylamine
ODE	1-Octadecene
PCE	Power conversion efficiency
PL	Photoluminescence
PLE	Photoluminescence excitation
PV	Photovoltaic
PVP	Polyvinylpyrrolidone
Sn	Tin
SnS	Tin (II) sulphide
S	Sulfur
STEM	Scanning transmission electron microscopy
SSP	Size-selective precipitation
TAA	Thiourea
TEM	Transmission electron microscopy
TRPL	Time-resolved photoluminescence
$(TMS)_2S$	Bis(trimethylsilyl) sulphide
UV-VIS	Ultraviolet-visible absorption spectroscopy
XRD	X-Ray diffraction
XPS	X-Ray photoelectron spectroscopy

List of Figures

List of Tables

Chapter 1 Introduction

1.1 Nanocrystals

Semiconductor nanocrystals (NCs) have attracted considerable attention since their first discovery in the 1980s.(1) They can be thought as small crystalline spheres having dimensions falling in the nanoscale range of 1-100 nm.(2) The most characteristic properties of semiconductor materials are attributed to their size-tunable band structures and band-gap energies (E_g in eV) as illustrated in *Figure 1-1* below.

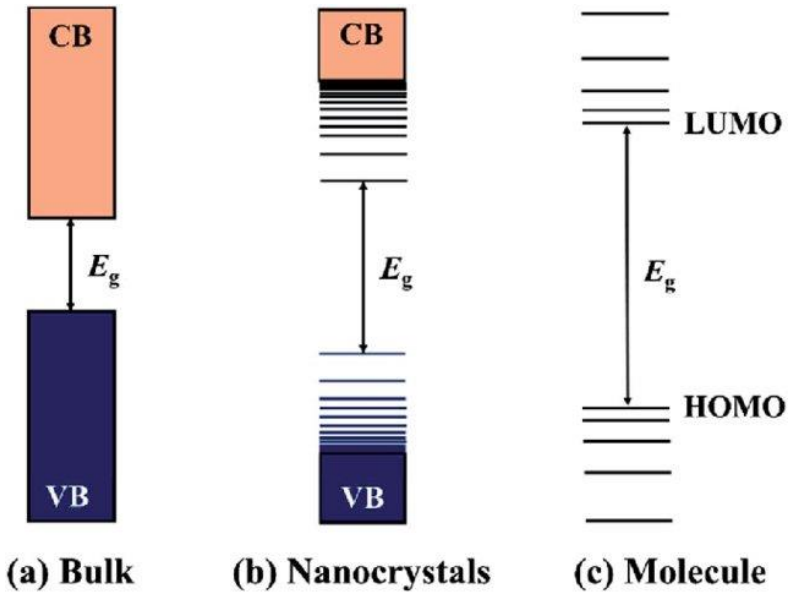

Figure 1- 1. A schematic illustration comparing different band structures and their corresponding electronic states of (a) bulk inorganic semiconductors, (b) inorganic semiconductor nanocrystals and (c) molecular semiconductors. (3)

The band-gap energy of a semiconductor is the minimum absorption energy required from the collector of solar radiation to excite an electron (e^-) from the ground state known as valence band (VB) to an excited state in the conduction band (CB). Apart from these properties, semiconductor nanomaterials are well known for their size-dependent optical and electronic properties. Tuning the size of the NPs close to the Bohr excitation radius results in a three-

dimensional quantum confinement effect of electrons and holes due to significant modifications of their optoelectronic properties.(4) When the size of a semiconductor nanocrystal is tuned below the size of its corresponding exciton Bohr radius (1-10 nm according to the material), it enters a quantum regime in which the optical band-gap shifts to higher energy resulting in an overall modification of the band structure of the semiconductor material.(5) The exciton Bohr radius could be described as the energy difference between the electron-hole pairs formed when the light is absorbed by the material. The modified nanoparticles will change to semiconductor quantum dots (QDs) revealing new optoelectronic properties unknown to their bulk semiconductor properties.(6)(7) By entering the quantum confinement regime, the electronic structure of the QDs changes by spatially separating the edge of the VB and CB to discrete electronic energy levels (quantized levels) where electron-hole pairs get spatially confined.(8) Tuning the size of the NPs in the nm scale will increase the spacing of both the band-gap and electronic levels. This phenomenon is due to an increase in the overall kinetic energy of the system because of stronger Coulombic attractions between the electron-hole pair attracting the carriers closer and stronger to one another.(9) However, tuning the size of the QDs below 10 nm will not necessarily result in a quantum confinement effect since different semiconductor materials have different certain size limits (Bohr exciton radiuses). The quantum confinement is not only a size-dependent but material dependent effect as well. For example, lead sulphide (PbS) and cadmium sulphide (CdS) NCs can enter the quantum regime at sizes smaller than 10 nm (Bohr exciton radius of bulk PbS NCs)(10) and 4 nm (Bohr exciton radius of bulk CdS NCs)(11) compared to tin sulphide (SnS) NC sizes, which must be below 7 nm.(12) The estimation of the Bohr exciton diameter, α_b, of quantum dot semiconductor nanocrystals can be calculated using the Brus equation, given by,

$$E_{g(qd)} = E_{\text{bulk}+} \frac{h^2}{8R^2}\left(\frac{1}{m_e^*} + \frac{1}{m_h^*}\right) \quad (1)$$

where E_{gap} is the energy band-gap, h is the Plank's constant, r is the radius of the quantum dot, m_e^* is the effective mass of the excited electron and m_h^* is the effective mass of the excited hole. (13)

In addition to the size tuning effect, the physicochemical properties of semiconductor NCs could be tailored depending on the crystal structures, shapes, surface chemistry (passivation) and composition (stoichiometry). The possibility of changing the optoelectronic properties of semiconductor NCs enables their application as photoactive materials in various scientific fields.(14)

1.2 Aims of the thesis/ new science

Despite the numerous synthetic strategies developed for the fabrication of semiconductor quantum dots (QDs) with good optoelectronic and physicochemical properties in the last decades, the best-reported results for the syntheses of monodisperse and highly stable QDs have been mainly achieved for Cd-based and Pb-based systems.(15)(16) The pursuit of low-cost, earth-abundant and non-toxic alternatives to those materials has raised the attention of the scientific community for a search of new candidates. Although, SnS NPs have shown great potential as a next generation material in the battery(17) and photovoltaic(18) applications due to their excellent optoelectronic properties as well as a low-cost and non-toxic nature, this material is still a challenge to many research groups to explore its full potential.

Therefore, the novelty and goal of this thesis are to develop new synthetic strategies for the fabrication of binary SnS colloidal quantum dots (CQDs) by tuning their optoelectronic properties via altering the chemistry of the QDs. This thesis introduces the synthesis of highly

stable photoluminescent SnS CQDs with enhanced optoelectronic properties as excellent multi-colour fluorescence agents in bioimaging applications. The following studies will be performed in the thesis:

1) First, to achieve my objective to synthesise high-quality QDs with uniform size, shape, and a single crystal structure, I will study and improve the synthetic procedure for SnS QDs through initial attempts using different reaction precursors with the aim to understand the effect of precursor type on the optoelectronic properties of SnS. A desired range of temperatures will be used to synthesise SnS CQDs with tunable band-gaps and study the effect of temperature on SnS absorption and emission properties.

2) When homogeneous inks of QDs with uniform size and a single crystal structure are achieved, I will evaluate the surface chemistry of the QDs using different types of organic stabilisers. Ligands play an active role in controlling the growth rate and morphology by binding to specific crystallographic facets on the surface of the QDs and thereby determining their growth rate. Manipulating ligand to precursor ratios will potentially lead to the achievement of enhancing the stability of SnS CQDs in ambient conditions.

3) However, over time exposure to water together with the dynamic binding and unbinding between the inorganic NC surface and the stabilising ligands can lead to aggregations of the particles. An attempt to further improve the stability of the QDs, the long-chained capping ligands can be synthetically replaced with new organic molecules that can provide alternative properties or functionality to the nanoparticles, resulting in highly stable CQDs with bright emission features.

Additionally, the following questions will be addressed and explained in the thesis:

- Can the overall QD size be tuned by altering the molar ratio of passivating ligands and reaction temperature revealing hidden or unknown optoelectronic properties?
- Can the QD composition be tuned by varying the precursor molar ratios in the synthesis?
- Can modification to the surface chemistry of the QDs using different stabilising agents alter their optoelectronic properties and improve their long-lasting stability?
- Whether the novel wavelength-dependent PL emission properties of SnS CQDs are size, composition or surface chemistry dependent?
- Whether biofilm formation of SnS CQDs and bacterial cells is initiated by the surface chemistry of the QDs
- Whether optimised SnS CQDs posses toxicity to living organisms such as bacterial cells and can be applied in bioimaging applications?

1.3 Structure of the thesis

Chapter 2 provides the reader with an introduction about semiconductor nanocrystals and their related optoelectronic properties. This chapter also covers a literature review on the synthetic and physicochemical properties of QDs as well as the current advances in the fabrication and application of SnS CQDs. Chapter 3 details the synthetic procedures of materials, characterisation and related biological applications. Chapter 4 describes the experimental results of synthesising and characterising SnS QDs with unique optoelectronic properties. It focuses on determining the photoluminescence origin in SnS QDs in means of relative size, surface passivation, and stoichiometry. Chapter 5 explores an alternative surface passivation

technique for synthesising non-degradable and air-stable SnS CQDs and study the effect of a new surfactant agent on their absorption and emission properties. Chapter 6 emphasises on the utilisation of SnS CQDs from chapters 4 and 5 for biological applications. Toxicity, brightness, and stability of the QDs are all studied as well as their effect of the bacterial cells. Chapter 7 concludes the most significant findings in the thesis and provides with future work suggestions to be carried out.

Chapter 2 Literature Review

2.1 Direct band-gap semiconductor materials

The concept of direct band-gap semiconductor materials can be presented and better understood by a so-called E-K diagram as seen in *Figure 2-1*. In the E-K diagram, E stands for electron energy in the y-direction, and K is a wave-vector or propagation constant in the x-direction and is related to crystal momentum.(19) The energy band-gap (E_g) of a semiconductor material is represented as the difference between the highest energy level of the valence band (VB) to the lowest energy level of the conduction band (CB). When a direct band-gap semiconductor material is excited with energy equal or higher than the energy of its corresponding band-gap, the absorbed photon energy promotes an electron from the lowest energy level the electron can occupy in the VB (ground state) to a higher energy level in the CB (excited state). This process results in the formation of an electron-hole pair (e^-/h^+) called an exciton.(20) Depending on the number of energy levels an atom can have an electron can travel and jump between those energy levels (an e^- cannot exist between energy levels) as a result of the number of photons absorbed by the electron. As the electron gets excited to a higher energy level, it tends to lose its energy and come down to a lower energy level in the CB until it reaches the band-edge of the lowest occupied energy level in the CB, which is the most favourable energy level for the e^- and h^+ to recombine. The loss of energy by the electron when returning to the ground state energy level results in the release or emission of light in the form of photons. This is one of the most common radiative relaxation processes resulting in spontaneous luminescence from the QDs in which both the electron energy and momentum are conserved. If the electron in the ground state gets excited with higher photon energy (above the energy level of the first excited state), the electron can jump all the way up to a second excited state, for example, and will fall back down to the ground state. However, in this case, the electron can have a couple of ways of falling back down. One possibility is that the electron

can fall all the way down to the ground state emitting the absorbed high energy of photons in the process. Alternatively, the electron can first fall and relax to the first excited energy level within the atom emitting some of the photons (in eV) and continue falling to the ground state emitting the rest of the absorbed photons. Sometimes electrons will drop multiple energy levels at a time and sometimes they will choose to take individual steps, but the energy of the photons is always equal to the difference in electron energy levels (E of photon = higher E level – lower E level).(21)

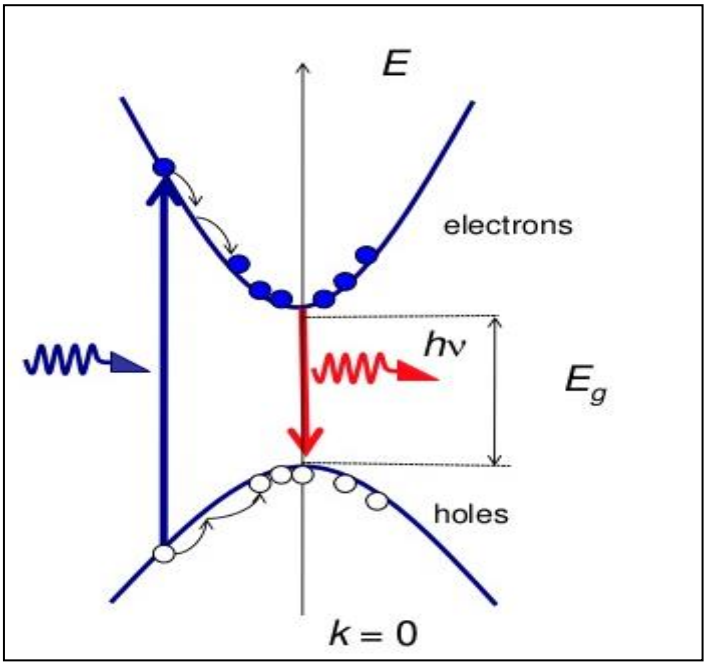

Figure 2- 1. E-K diagram of direct band-gap semiconductor materials showing a direct transition of an electron from the CB to VB. (https://goo.gl/images/wSQhfV)

2.2 Carrier generation and recombination processes

In semiconductor materials, generation and recombination are processes that involve the formation and elimination of charge carriers (electron-hole pairs). Generation and recombination of carriers occur when an electron gains enough thermal or optical energy due to interactions or collisions with phonons (crystal lattice vibrations), photons, other electrons

or holes.(22) Charge generation is a result of an electron transition from a ground energy level in VB to an excited energy level in CB of a semiconductor compared to charge recombination, which involves the reverse process. In semiconductor materials, the rates of carrier generation and recombination are well-balanced at thermal equilibrium, in which there is no net flow of matter or energy within the system. This means that the product of charge carrier densities (electron and hole densities) is a constant, maintained by the equal generation-recombination rates. When the rates of carrier generation and recombination are imbalanced disturbing the overall equilibrium of the system, then one of the processes prevails over the other to maintain equal carrier rates.(23) In the case of excess carrier generation, the rate of charge recombination becomes higher than the rate of generation driving the system towards equilibrium. Similarly, when the carriers are less in the system, then the generation rate dominates over the recombination rate resulting in an overall equilibrium of the system. The different mechanisms behind the electron transition in direct band-gap semiconductor materials are illustrated in *Figure 2-2*.

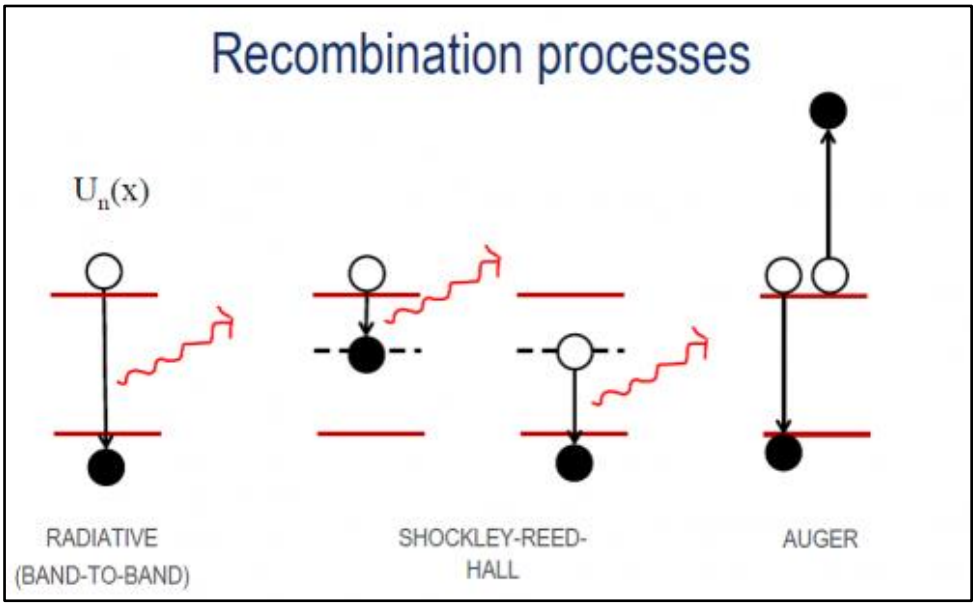

Figure 2- 2. Charge carrier recombination mechanisms in direct band-gap semiconductor materials. (The Quartz Corporation 2016).

2.2.1 Radiative recombination

Radiative charge recombination, also called band-to-band recombination, dominates in direct band-gap semiconductors and occurs when an electron gets excited to an empty state in the CB with energy equal or higher than the energy of the band-gap generating an exciton. Once the electron loses some of the absorbed energy, it will fall down recombining with the hole in the VB releasing energy in the form of photons or light. In radiative recombination, the emission of light is a spontaneous process, in which most of the absorbed light is emitted as photons with a small percentage being lost in the form of heat or vibrations with lattice atoms.(24) In band-to-band recombination, both electrons and holes are required to be available determining the rate of the charge recombination process, which is expected to be equal (proportional) to the product of electron (*n)* and hole (*p)* densities. However, the recombination process changes when the system is in thermal equilibrium requiring the rate of carrier recombination to be equal to the rate of carrier generation due to the lack of net recombination and generation. The process of the net recombination in thermal equilibrium conditions ($n_0 p_0 = n_i^2$) can be expressed with the following formula,

$$U_{b-b} = b\,(np - n_i^2) \quad (2)$$

where *b* is the biomolecular constant, *n* is the electron density, *p* is the of hole density, and n_i^2 is the product of electron and hole densities at equilibrium.

2.2.2 Shockley-Reed-Hall (SRH) recombination

Shockley-Reed-Hall (SRH) or trap-assisted recombination is a two-step recombination process (from CB to VB) involving the formation of a new localised energy state (forbidden region)

created within the middle of the band-gap of the semiconductor material caused by the presence of crystalline defects or lattice impurities (deep charge trap states, E_t).(25)(26) The rate of net recombination for trap-assisted recombination is given by:

$$U_{SHR} = \frac{pn - n_i^2}{p + n + 2n_i \cosh(\frac{E_i - E_t}{kT})} N_t v_{th} \sigma \quad (3)$$

where E_t is an intermediate trap energy level, N_t is the density of trap states and E_i is the product of trap level densities.

The defects in the crystal lattice of the material can be either intentionally added by doping or introduced to the system during synthesis.(27) In the first step of the trap-assisted recombination, the transition electron falls into the 'trap' energy state releasing some of its energy as a photon. In the second step of the charge recombination process, the electron occupying the deep, intermediate band-gap level can further fall all the way down recombining with the empty hole in the VB releasing an extra photon with a blue-shifted emission wavelength compared to the emission wavelength of the photon released in the first recombination step. Alternatively, SRH charge recombination can occur directly in the forbidden gap if the hole in the VB moves up to the same trap energy state occupied by the electron before it gets thermally re-emitted. The rate of recombination of charge carriers in the energy level near the mid-gap is highly dependent on the position and distance of the trap energy level relative to VB and CB band edges. If the defect level is introduced close to either of the band edges, then the excited electron is more likely to be re-emitted close to the band edge of the CB rather than recombining with the hole in the VB. For this reason, it is of a great importance to decide on the most suitable reaction conditions or doping elements for synthesising a material with good optoelectronic properties for effective charge recombination.

2.2.3 Auger recombination

Auger recombination involves three charge carriers compared to the other carrier recombination processes discussed above. The charge recombination mechanism is characterised by an energy transfer from an exciton to a third charge carrier (either an electron or hole) in the CB rather than emission of energy as a photon or heat release. By absorbing the energy given by the exciton, the third charge carrier gets excited to a higher energy level within the CB but does not move to another energy band (band level). After the interaction, the third carrier falls to the edge of the CB releasing its excess energy as heat due to lattice vibrations (thermal vibrations).(28)(29)(30) The rate of net recombination in Auger recombination is similar to the band-to-band recombination since the process involves a charge recombination of excitons in a band-to-band transition giving off the resulting energy to a third carrier but including the density of electrons (holes) from the third carrier as a result of the electron-hole annihilation given by the formula:

$$U_{Auger} = \Gamma_n n(np - n_i^2) + \Gamma_p p(np - n_i^2) \quad (4).$$

However, Auger recombination is highly uncommon charge recombination process found in direct band-gap semiconductors because the third charge carrier is required to start recombination in a highly unstable high energy state.

2.2.4 Surface recombination

Surface recombination is one of the most common charge carrier recombination processes observed in semiconductor materials. It is highly favourable due to the large surface-to-volume ratio of nanomaterials (*i.e.*, quantum dots). A large number of surface and interface trap states

in semiconductors act as charge recombination centres due to poor crystal passivation of electrically active dangling bonds and surface atoms.(31)(32) Also, the partial surface termination of the semiconductor crystal can be easily oxidised and degraded when exposed to air. Surface recombination is a trap-assisted process almost identical to SRH recombination. The only difference between the two mechanisms is that in the surface recombination the charge carriers recombine two-dimensionally (N_{st}) at the surface and interfaces of the crystal compared to the SRH recombination, in which the recombination is a trap-assisted three-dimensional mechanism within the band-gap of the material. The rate of surface net recombination is given by:

$$U_{s,SHR} = \frac{pn - n_i^2}{p + n + 2n_i \cosh(\frac{E_i - E_{st}}{kT})} N_{st} v_{th} \sigma \quad (5).$$

2.3 Photoluminescence

Photoluminescence (PL) is a luminescence process characteristic for semiconductor materials, which involves absorption of energy in the form of photons (coming from light or other electromagnetic radiation) and excitation of electrons to a higher energy level in an atom, storage of absorbed energy (decay time of absorbed photons) and final emission of photons.(33) Depending on the decay time between the absorption and emission of photons, the PL lifetime of a system may vary from picoseconds (ps) in organic materials, nanoseconds (ns) in inorganic semiconductors and milliseconds (μs), seconds (s) or even minutes (min) and hours (hrs) in molecular systems.(34) Photoluminescence is an essential process for determining the quality of semiconductor materials such as their good crystallinity, high purity, and a number of defect states present in the crystal structure (crystal distortions).

2.3.1 Factors affecting photoluminescence (PL) in direct band-gap semiconductor materials

2.3.1.1 Relative size/ size tuning

Semiconductor nanocrystals are small crystalline particles in the range of 10-100 nm that exhibit size-dependent optical and emission properties.(35)(36) However, when the size of semiconductors falls below the Bohr exciton radius of the bulk material as mentioned before, then semiconductors transform to quantum dots with sizes between 1-10 nm. When entering the quantum confinement regime, the size, energy levels and emission colours of quantum dots could be precisely tuned depending on the desired application.

A unique property of quantum dots is their size-dependent band-gaps and emission colours, which are material dependent. There are several known ways of tuning the sizes of QDs such as reaction temperature, reaction time and amount of surface passivation groups (e.g., organic ligands).(37)(38) A simple schematic illustration of QD size-tuning as a temperature-dependent phenomenon is depicted in *Figure 2-3*. By a modification of the reaction temperature conditions, the size of the QDs will increase at higher temperatures red-shifting the absorption and emission properties of the material to longer wavelengths. This suggests that bigger QDs will emit in red colours and small ones will emit in blue colours with all other QD sizes emitting in intermediate colours covering the entire wavelength region of the electromagnetic spectrum.

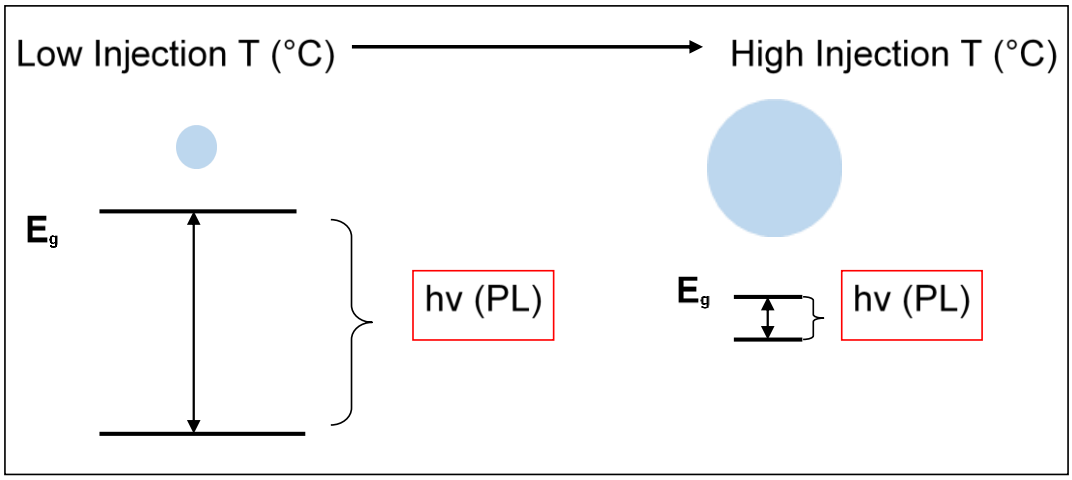

Figure 2- 3. A schematic illustration of size-dependent photoluminescence (PL) emission of spherical nanoparticles (NPs).

The size-dependent emission phenomenon is related to a difference in the energy band-gaps of the QDs due to size differences. Small QDs have large band-gaps requiring high energy of excitation to promote an electron from the ground energy level (VB) to an excited energy level (CB) resulting in the emission of higher energy at shorter wavelengths. Small QDs emit light in the blue region of the electromagnetic spectrum. Bigger size QDs require lower excitation energy to promote an exciton (e-/h+ pair) due to their narrower band-gaps compared to smaller QDs.

Figure 2-4 shows the effect of size-tuning on PL emission properties of CdSe QDs. As the size of CdSe QDs increases the emission is red-shifted to longer wavelengths changing the emission colour from blue to red. The observed tuning of the emission colour is due to changes in the surface-to-volume ratio with size and quantum confinement effect.(39)

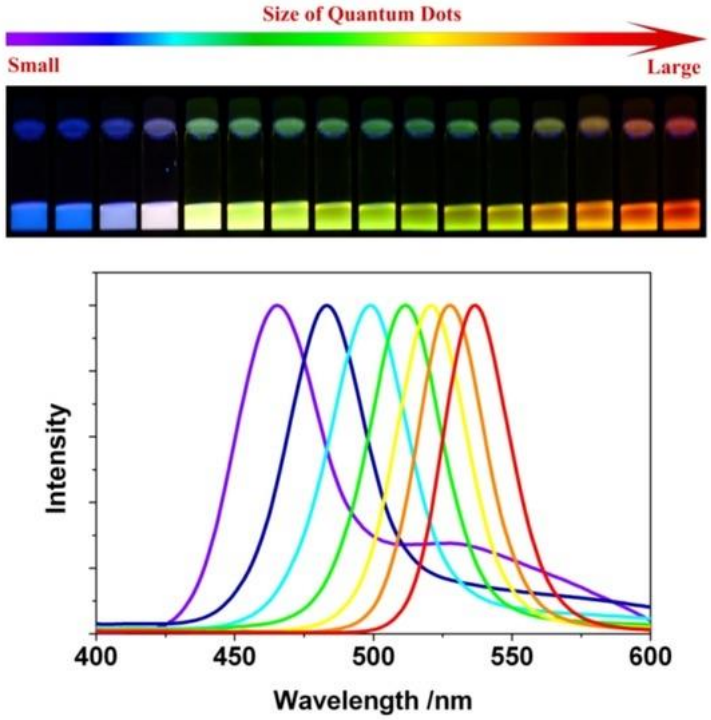

Figure 2- 4. Tuning (a) the optical absorption of CdSe QDs covering the whole visible spectrum by synthetically changing the size of the CdSe QDs from small (blue) to large (red). (mage reprinted from Reference 35).

2.3.1.2 Surface Passivation/ surface tuning

Surface passivation or surface tuning is another powerful strategy for protection and surface optimisation of organically-capped QDs against degradation from oxidation and photo-oxidation processes.(40) Dangling bonds or stoichiometry changes in the crystal structure of the material due to atomic differences can create new surface energy states known as surface defects increasing the number of non-radiative charge recombination pathways in the QDs and quenching their emission features. The use of a coating shell could result in the successful elimination of charge recombination centres by passivating surface trap states with shell atoms and improving the overall stability, optical and emission properties of the initially synthesised core material.

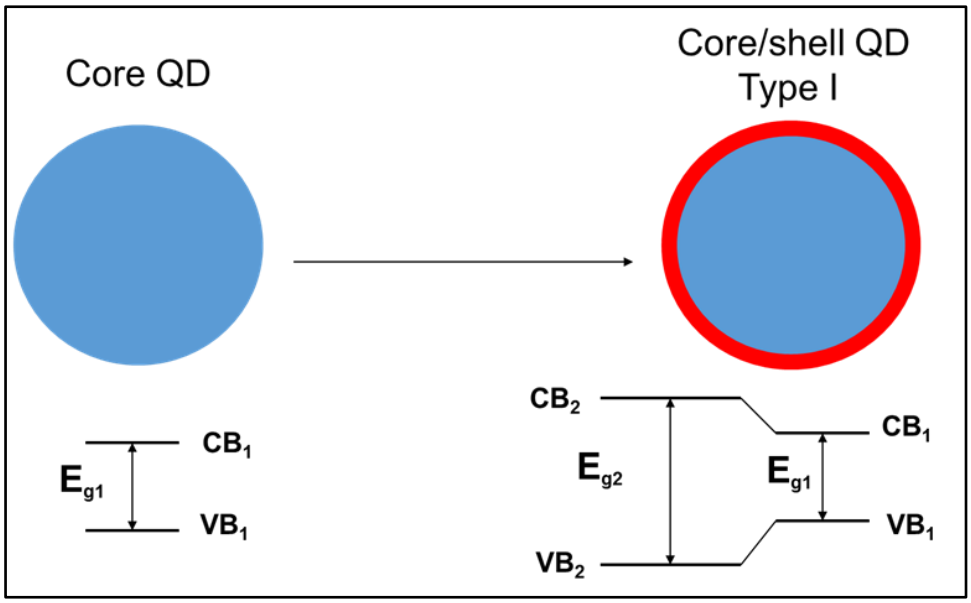

Figure 2- 5. Schematic illustration of organically capped (Left) core and (Right) type I core/shell QDs with their corresponding energy band diagrams showing the band-gap difference between the two types of structures.

Figure 2-6 presents two of the main core/shell methods used for quantum dots surface passivation. In type I core/shell (refer to *Figure 2-6 (b)*), the shell material is a semiconductor in nature having a wider band-gap than the core material. This type of core/shell heterostructure confines the charges (both electrons and holes) within the core material because both VB and CB of the core lie within the energy band-gap of the shell material. As a result, the overall PL emission is quantised within the core obtaining a high quality photoluminescent composite material. The most common way of synthesising a highly protective and crystalline shell coating is through epitaxial shell growth. The semiconductor shell material is chosen such that it crystalizes in the same crystal structure as the naked core material resulting in negligible lattice mismatch and consequently low distortion or strain-related defects between the two semiconductors.(41) This will lower the possibility of forming non-radiative charge recombination sites. Furthermore, the process of shell growing involves the slow addition of the shell precursors to the core solution to prevent secondary nucleation events or the formation of separate nanoparticles from the precursor's ions. Also, the required core/shell reaction

temperature should usually be lower than the original temperature used for the core synthesis avoiding homogeneous side-nucleation.(42)(43) Dabbousi *et al.* demonstrated in their work a successful passivation procedure for the synthesis of CdSe/ZnS core/shell quantum dots with improved optical and emission properties by ZnS epitaxial shell growth.(44) The authors observed that the addition of only ~1.3 monolayers of a ZnS shell was enough for improving the PL quantum yields of the composite material reaching a maximum value due to optimum surface functionalization.

In type II core/shell as seen in *Figure 2-6 (c)*, the band alignment of the semiconductor shell material to the core material results in the formation of a new smaller energy band-gap compared to the band-gaps of the individual core and shell materials. This phenomenon occurs when the band edges of the VB and CB of the core material are either lower or higher than the band edges of the shell material. In the type II case, the charge separation of the electron and hole is confined in the energy levels of both the core and shell semiconductors as the hole being confined in the VB of the shell and the electron in the CB of the core. In this case, the emission of the exciton is determined by the energy difference between the two occupied energy levels. The type II core/shell method is of great interest in materials, which emission properties do not cover certain regions of the electromagnetic spectrum regardless of size-tuning.(45) For example, the emission wavelength of CdTe or CdSe core materials could be tuned in the NIR region if only coated with shell materials forming type II core/shell heterostructures. However, type II core/shell QDs suffer from low photostability and low PLQY due to localised charges in the shell material (either electron or hole). These charge separation events in type II core/shell heterostructures reveal the shell charge to the surrounding environment of the material increasing the chances of surface charge recombination events observed in non-passivated core materials.(46) Reiss *et al.* demonstrated in their work that the addition of a

secondary shell coating improved the PLQY and photochemical stability in type II core/shell semiconductors forming a core/shell/shell heterostructure.(47)

Cationic exchange reactions are well-known as an alternative to epitaxial growth in the core/shell synthesis. In a typical cationic exchange reaction, the cation ions in the shell precursor solution are introduced to the crude core solution by replacing the cation ions near the surface of the core material. As a result, the originally synthesised core QDs transform to core/shell QDs, which have a smaller-sized core (consequently wider band-gap energy) and show blue-shifted absorption and emission properties due to surface modification.(48) Kim *et al.* reported the synthesis of highly luminescent $CuInS_2$/ZnS (CIS/ZnS) core/shell quantum dots with quantum yields as high as 65% by a simple cationic exchange reaction. In comparison to cation exchange reactions, the implementation of anion exchange alternatives has also been applied with the aim of improving the chemical stability of the materials.(49) However, the large size of the anion species and their lower diffusion into the crystal lattice can deteriorate the reaction kinetics altering the morphology of the quantum dots.(50)(51)(52)(53) Additionally, both cationic exchange and epitaxial growth core/shell are promising passivation strategies in eliminating surface defect states in the quantum dots.

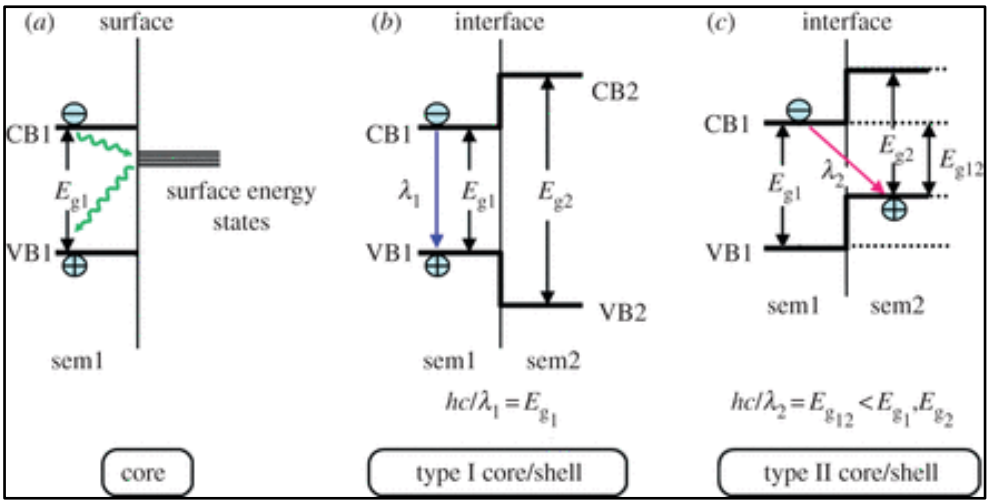

Figure 2- 6. (a) Core, (b) type I core/shell, and (c) type II core/shell structures of semiconductor materials illustrating the band edge alignment and the exciton localisation at the surface and the heterointerface.(54)

2.3.1.3 Stoichiometry changes/ composition tuning

Improvements of the photoluminescence properties of direct band-gap semiconductors can also be achieved by tuning the composition of the materials. Changes in the composition of the QDs could affect their optoelectronic and emission properties.(55) For example, small changes to the regular crystal structure of the QDs could be achieved by the addition of impurity atoms known as doping. Doping of intrinsic semiconductors is used either to increase the electron or hole concentration resulting in the creation of new energy levels within the band structure of the materials. According to the Octet rule, atoms achieve the highest stability when they are surrounded by eight valence electrons (valence shell) in a covalent bond. Any changes to this rule will result in electron rearrangements between atoms either sharing or donating electrons to meet the required number of electrons in their outer valence shells.

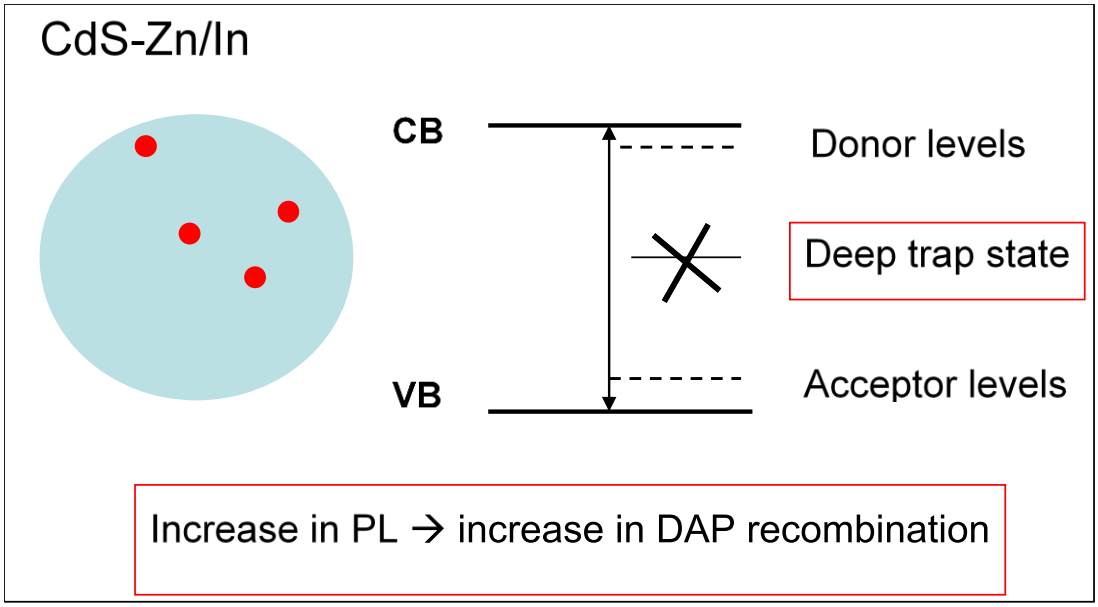

Figure 2- 7. Change of the composition of QDs by doping creating donor-acceptor pairs (DAP) resulting in PL emission and PL quantum yield (PLQY) tuning.

Depending on the choice of dopants and their corresponding valence electrons the conductivity properties of the materials could be tuned producing either n-type or p-type semiconductors (56) as illustrated in *Figure 2-8*.

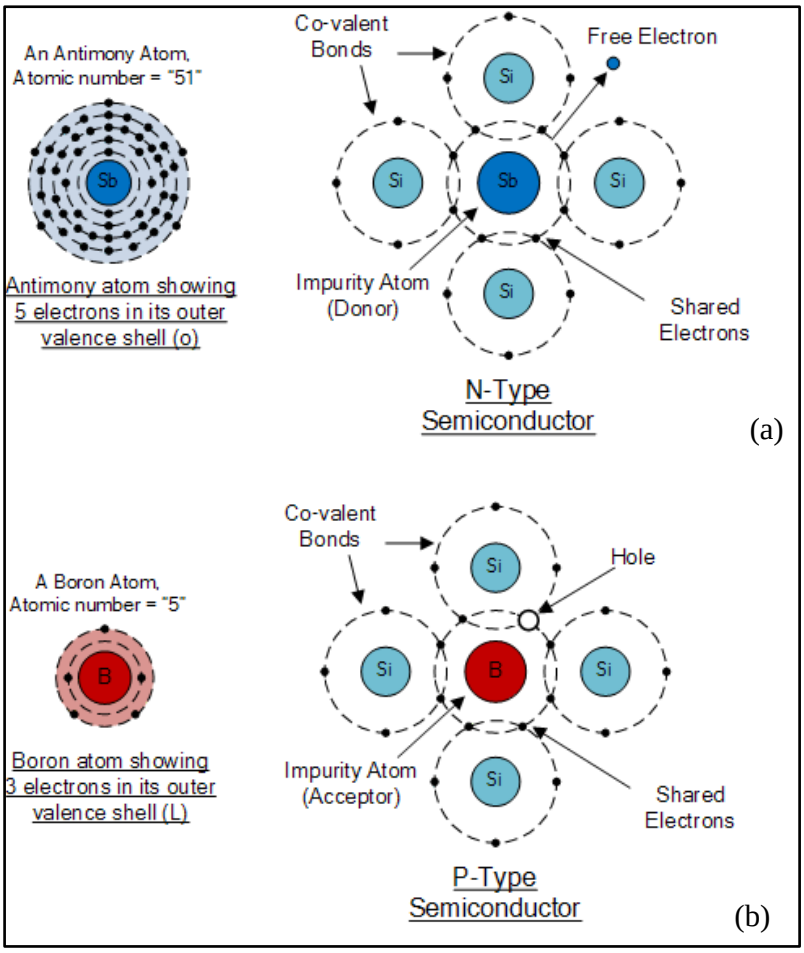

Figure 2- 8. Schematic diagrams of (a) N-type and (b) P-type doping of Silicon (Si) using donor impurity Antimony (Sb) and acceptor impurity Boron (B) atoms, respectively. (AspenCore 2018).

In n-type semiconductors, the dopant atoms known as donor impurities have a higher number of valence electrons contributing free electrons. Some of the most popular examples of pentavalent impurity donors (having five valence electrons) include arsenic (As), antimony (Sb) and phosphorous (P).(57) As an example, doping of Silicon with pentavalent elements, such as Sb results in extra free electrons, which are weakly bonded to the impurity atom and thus making them highly mobile when gaining enough thermal energy. In donor doping, the concentration of electrons is significantly increased which represents the majority of charge

carriers. *Figure 2-7 (a)* shows that in n-type semiconductors the donor energy levels lie close to the top of the band-gap, which allows for easy excitation of electrons into the CB.

Furthermore, in p-type semiconductors, trivalent atoms (having three atoms) are used as dopant materials such as boron (B), aluminum (Al), gallium (Ga) and indium (In) known as electron acceptors.(57) The addition of electron deficient impurities within the crystal lattice creates voids (missing covalent bonds) or valence holes in the crystal resulting in the formation of acceptor energy levels near the VB. The nearby electrons can be attracted to the missing bond (hole) creating another empty hole moving freely in the crystal lattice. In the acceptor doping process, the concentration of holes is increased without affecting the concentration of electrons within the materials.

Generally, surface trap states are related to un-passivated atoms or dangling bonds forming mid-band-gap energy levels in the electronic structure of the material increasing the probability of non-radiative charge recombination events. The trap sites could substantially alter the emission properties of the material. However, in order to assist and improve the charge recombination in direct band-gap semiconductors, the introduction of intermediate energy states within the band-gap by doping could be considered. It is common for semiconductors to be doped either by donor (e^- donating) or acceptor (e^- accepting) impurities that lie close to CB and VB edges, respectively as seen in *Figure 2.7*. This allows for easy excitation of the charge carriers to the new energy levels and therefore resulting in a radiative charge recombination within the core material rather than dissociating the exciton to surface defects. This approach could significantly improve the overall PL emission properties of the material.

Therefore, doping of intrinsic semiconductors could not only be used as a promising method of changing the conductivity properties of the materials but could also be adopted for improving their emission properties.(58) In the case of CuS NCs, it has been found that increasing the concentration of In dopant atoms within the crystal lattice resulted in a prominent

increase of the PL emission intensity and PLQYs of the resulting $CuInS_2$ (CIS) NPs.(59) The authors suggested that the observed improvement of the emission properties was due to an increase of the donor-acceptor pair (DAP) recombination as an impurity concentration effect. However, a precise dopant concentration must be considered in an attempt of improving the absorption and emission properties of semiconductors preserving the overall stability of the materials.

.

2.4 Nanocrystal synthesis

2.4.1 Introduction

Nanocrystals use colloidal chemistry to make inks with a variety of optoelectronic properties which can be used in photovoltaic (PV), optoelectronic (OLED) and biological devices.(60)(61) NCs have been demonstrated to work with reasonable efficiencies using a range of low-cost processing methods such as colloidal,(62)(63) sol-gel,(64) water-oil microemulsion,(61) hydrothermal and polyol (65)(66) synthesis at low temperatures. This project aims to develop colloids with the appropriate physicochemical properties. The challenge is to synthesise non-toxic, cost-effective materials with good photoluminescent properties.

2.4.2 Colloidal synthesis

2.4.2.1 Nucleation and growth kinetics

Monodisperse CQDs can be formed by precise manipulation of reaction conditions and by balancing nucleation and growth kinetics. In the monodisperse colloidal growth of QDs, the nucleation event must happen for a short reaction time followed by a slow-growing phase. To achieve equilibrium in nucleation and growth kinetics, optimising reaction conditions such as reaction temperature and time should be maintained.(67) An alternative method for the synthesis of monodisperse QDs first described by La Mer *et al.* involves the rapid addition of

all reaction reagents to the reaction system, which will increase the precursor concentration above the nucleation threshold increasing the reaction rate.(68) *Figure 2-9 (b)* shows a schematic depicting the stages of nucleation and growth of monodispersed NPs. A short nucleation phase will relieve the supersaturation followed by a temperature drop allowing the growth of the NPs. This synthetic route is favourable for obtaining colloidal NPs with uniform size-distribution since it involves a single nucleation event in which all NPs will continue to grow together until the monomer concentration drops down to below a critical level.

Furthermore, if the growth of the NCs continues, then Ostwald ripening may occur. During this second growth event, smaller particles with larger surface-to-volume ratios decompose and incorporate to bigger particles with smaller surface-to-volume ratios. This is a result of the higher number of un-passivated surface atoms in the smaller QDs having a lower coordination number leading to the formation of unsaturated dangling bonds, which result in substantial reconstructions of atomic positions.(69) The average size and size-distribution of the resulting NCs is highly dependent on reaction parameters such as reaction temperature and precursors concentration since they can directly influence nucleation kinetics and lead to Oswald ripening.(70)

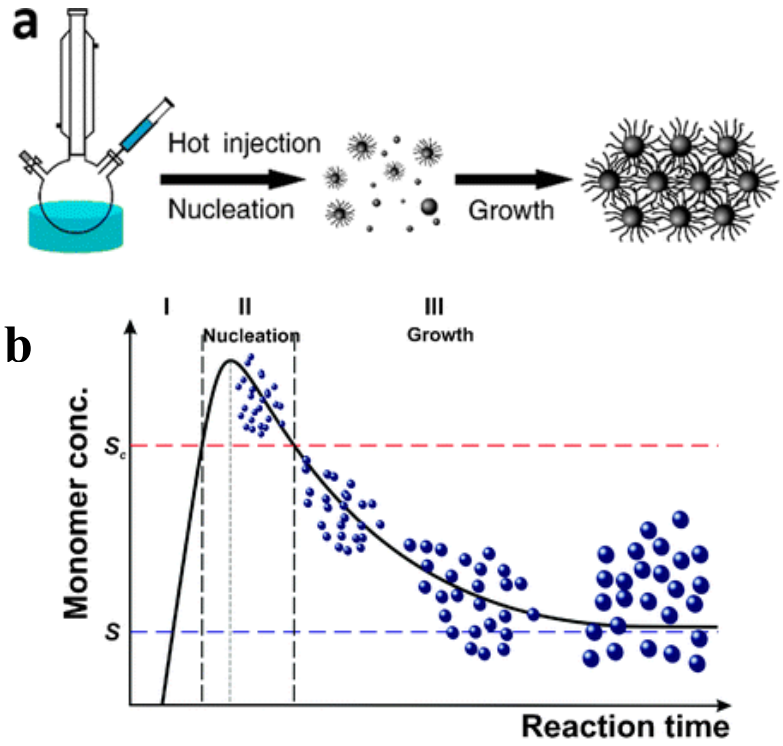

Figure 2- 9. (a) Schematic illustration detailing the hot-injection CQD synthesis, in which a room-temperature precursor is injected into a high-temperature surfactant, followed by a temperature drop allowing the growth of the NCs and b) Plot showing the stages of nucleation and growth for the preparation of monodisperse NCs using La Mer model.(71)

2.4.3 Control of colloidal NC physical properties

2.4.3.1 Crystal structure, size, shape, and distribution

In the hot injection synthesis, there are several parameters to be controlled and employed to optimise reaction thermodynamics and kinetics. Precursors play an essential role in determining the nucleation and growth rate, which is directly related to the number of monomer species. The concentration of the formed monomers depends on the reactivity of the precursors and can be tailored by their correct choice. The higher the reactivity of precursors, the higher the monomer concentration leading to faster nucleation rate resulting in the formation of a larger concentration of small nuclei. Kergommeaux *et al.* demonstrated the use of various tin precursors with different reactivities resulting in the formation of NCs with different sizes and shapes based on the monomer concentration during nucleation.(72) *Figure 2-10* summarises a growth mechanism of SnS NCs showing the different reaction stages depending on precursor

concentrations and reaction times. It is evident that the monomer concentration may also influence the growth kinetics during synthesis. A high monomer concentration could accelerate the growth rate forming NCs with bigger sizes compared to a low monomer concentration, which was observed to result in small NCs.(73)

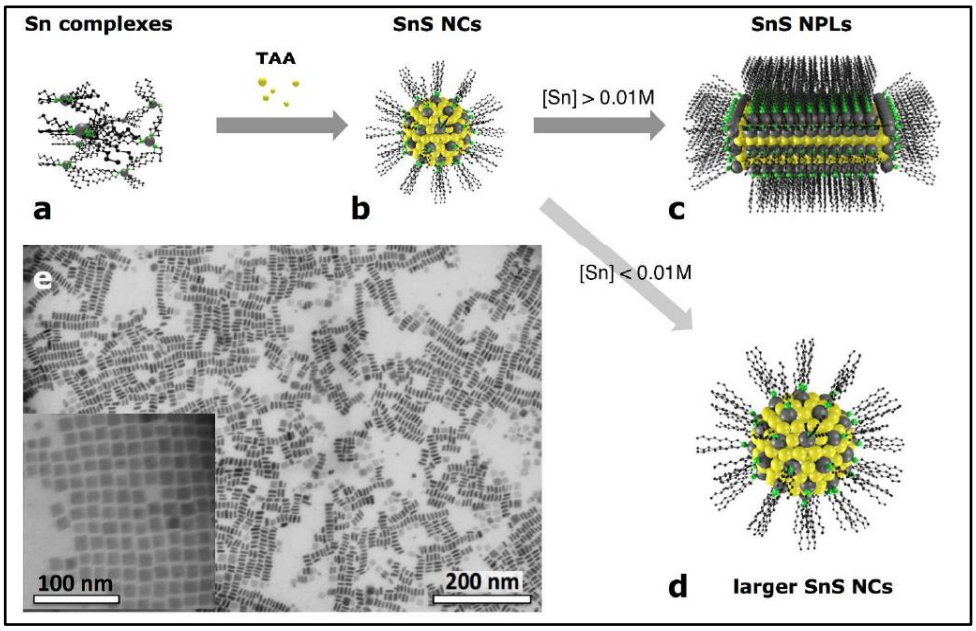

Figure 2- 10. Illustration of the growth mechanism of SnS nanoplatelets (NPLs) using the hot-injection synthesis. (Adapted from reference 66).

The second important parameter in the colloidal synthesis of semiconductor NCs is the choice of organic ligands that interact and adhere to the NC surface. Like precursors, ligands directly affect both the reaction thermodynamics and kinetics. Due to their interactions with precursors, ligands can influence or even reduce the overall nuclei concentration when present in higher molar ratios. Hickey and co-workers reported the synthesis of monodisperse SnS NCs demonstrating control over sizes by tuning the ratio of ligands in the reaction synthesis.(74) They found that when the OA/OLA ligand ratio was 1:2 the shape of the NPs was more spherical-like. Non-spherical NC geometries with triangular shapes, distinct facet terminations and bigger sizes were achieved by increasing the concentration of the carboxylic acid in the

synthesis (OA/OLA= 1:1). The change of the NC sizes and shapes could be attributed to a substantial alteration of precursor's reactivities in the means of organic surfactants. On the one hand, increasing the concentration of OA (a strongly binding ligand) with respect to the concentration of OLA in the reaction would decrease the reactivity of the metal precursor. This will result in monomer species with insufficient energies to reach the supersaturation level resulting in a low nuclei concentration but a high monomer concentration accelerating the growth rate forming larger NCs. On the other hand, when the concentration of OLA is decreased by two times (OA/OLA= 1:1), this would result in partial surface passivation of the NCs. The un-passivated crystallographic facets will continue to grow until the monomer concentration drops down to below a critical level. This will alter the final shape of the NCs.(75) The authors concluded that not only a high monomer concentration would alter the relative growth rate of the facets, but the precise manipulation of the molar ratios of the stabilising surfactants leading to anisotropic shapes.

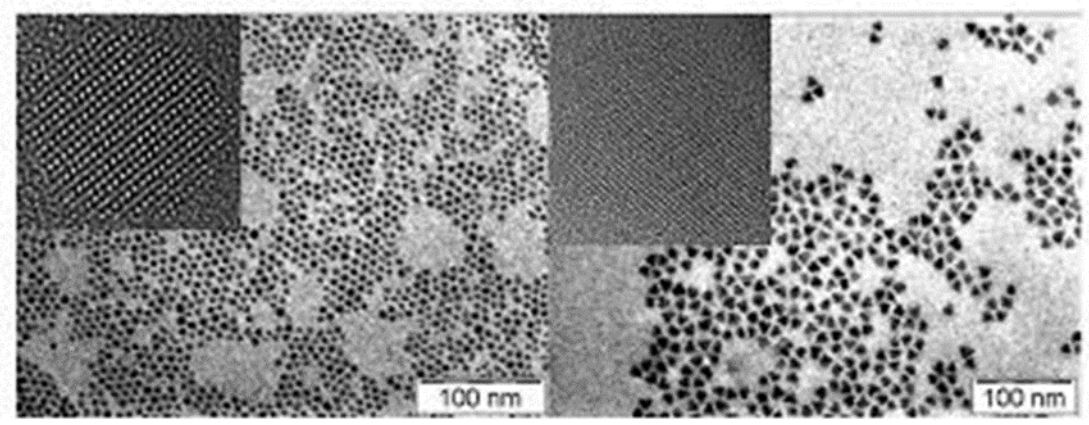

Figure 2- 11. Low and high-resolution TEM micrographs of SnS NCs with spherical and triangular shapes achieved by varying the concentration of capping ligands. (Reprinted from reference 68)

The third important factor in the hot injection method is the reaction temperature, which has a direct effect on reaction kinetics, morphology and size-distribution. The temperature

controlling nucleation kinetics is usually higher than the growth temperature resulting in fast precursor decomposition and generation of monomers from the chemical reaction between precursors. The high concentration of monomer species with energy greater than the activation energy of the reaction will quickly reach the supersaturation level. This will result in fast or discrete nucleation events forming a large concentration of small critical nuclei that will all hypothetically grow with the same rate and thus narrowing the final size-distribution of the NCs. Also, the NP size-distribution and morphology may also be affected by the growth temperature. The growth temperature is usually lower than the nucleation temperature to prevent secondary or continuous nucleation events by decreasing the thermal energy of the reactant species below the transition state threshold of the reaction. This will result in the continuous aggregation of monomers on the pre-existing small nuclei growing the final NCs rather than being involved in the formation of new supersaturated monomers.(76) The ability to optimise the chemistry behind the synthesis resulting in monodisperse NCs with tunable sizes and band gaps could be a promising approach for the successful fabrication of various devices.

2.4.4 Control of colloidal NC chemical properties

2.4.4.1 Ligand exchange reaction

Ligands not only interact with the NC surface resulting in monodispersed NCs with narrow size distribution, but they also prevent from the aggregation of the NPs. Although, their stabilizing potential, organic surfactants may lose their strong binding ability to the inorganic NC surface over time exposure to air and moisture. For example, long-chained carbon surfactants like oleylamine (OLA) and oleic acid (OA) play the role of “insulators” of the charge transport creating longer inter-particle distances by influencing reaction kinetics. The exchange of the long-chained capping ligands with alternative short chain capping agents can

reduce the inter-particle distances and improve charge transport in the NCs. A suitable ligand choice will be the one that binds stronger to the NC surface acting as a better protector from environmental conditions.(77)

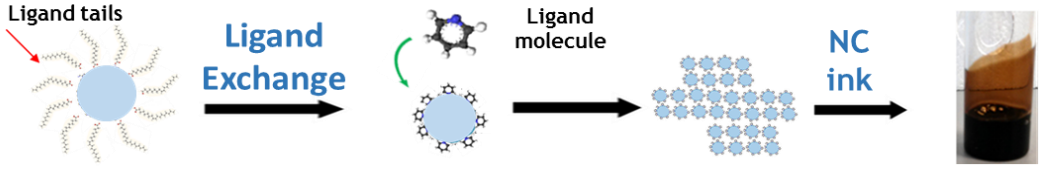

Figure 2- 12. Schematic illustration of a ligand exchange reaction, in which the long-chained OLA ligand is replaced with a smaller pyridine ligand molecule resulting in the formation of monodispersed NCs forming a NC ink.

2.4.5 Core/shell synthesis

Poor ligand passivation of the NC surface may lead to trapping states or defects acting as non-radiative charge recombination centres in the band gap (somewhere between the valence and conduction bands) of the semiconductor material.(78) The insulating inorganic shell can potentially stabilise and maximise fluorescence. The process of coating an organic NCs (core) with inorganic material (shell) results in better surface passivation and improved optoelectronic properties of NPs. The shell layer will concentrate the charge carriers in the NC core rather than been lost at the surface. It has been shown that core/shell structures exhibit good stability and fewer photodegradation.(47) Moreover when the core is coated by a shell, the number of dangling bonds at the surface is reduced. Prastani *et al.* demonstrated in their work the synthesis of SnS NCs capped with an In_2S_3 shell using a CVD method resulting in better passivation of the SnS surface as evident from the HRTEM results in *Figure 2-13 (a)*. Surface passivation of the core SnS NPs could be clearly distinguished forming an amorphous outer shell from the

HRTEM images below. The core SnS material appears darker in colour with well-defined characteristic fringes compared to the amorphous In_2S_3 shell material. In addition to the TEM results, the blue-shifted absorption spectra (*Figure 2-13 (b)*) of the SnS/In_2S_3 core/shell NPs compared to bare SnS core NPs could suggest of a significant surface modification of the core NPs due to shell growing by narrowing the overall size of the originally synthesised core SnS NPs by ripening off surface atoms during shell growth. The authors proposed that the SnS/In_2S_3 core/shell material results in an overall improvement of the electrical properties by tuning the surface of the NPs.(79)

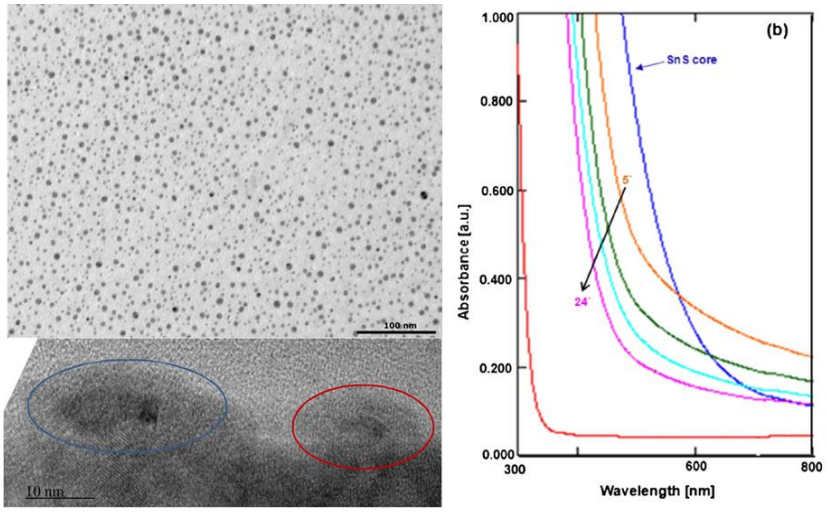

Figure 2- 13. (a) TEM image of SnS/In_2S_3 core–shell NPs and HRTEM image of SnS/In_2S_3 core–shell nanoparticles and b) absorption spectra of SnS/In_2S_3 core–shell NPs with a range of deposition times (reference red spectrum corresponds to the absorption of ethanol used as a dispersant solvent for the core and core/shell NPs). (Reprinted from reference 71).

2.5 Materials selection

2.5.1 Background

2.5.1.1 Structure of SnS

Tin sulphide (SnS) is one of the four semiconductors which form the IV-VI materials (SnSe, GeS, and GeSe).(80)(81)(82)(83) SnS possess an orthorhombic crystal structure (84) in which every Sn atom is bonded to three S atoms. The SnS crystal structure can be best described as a distorted rock salt (NaCl) structure with lattice parameters of a = 4.334 Å, b = 11.200 Å, c = 3.987 Å illustrated in *Figure 2-16 (c)*. Each double zig-zag layer of atoms (Sn and S) in α-SnS is separated only by van der Waals forces (*ca.* 1Å). The arrangements of the cations and anions within the crystal lattice are highly ordered resulting in a symmetric crystal structure.(85) The strong anisotropic properties of this material are directly related to this double layered crystal structure resulting in high electrical conductivity and hall mobility when measured along the layers.(86) Depending on the crystal structure, different SnS materials give different band-gaps (E_g), as shown in *Table 2-1*.

The properties of SnS depend on the different crystal structures and geometries of these materials illustrated in *Figure 2-14*. The crystal structure is an essential factor that influences the electronic properties of SnS materials depending on the different bonding arrangements between the component elements of the material. The two most common allotropes of SnS are α-SnS (orthorhombic) and β-SnS (orthorhombic).(87)(88) The most common phase at room temperature is that of the orthorhombic Pbnm α-SnS structure (a = 11.14 Å, b = 3.97 Å, c = 4.34 Å) because it is thermodynamically more stable than the metastable cubic F-43m SnS structure (a= 6.00 Å).(89) Upon heating at temperatures above 600 ^{0}C, the Pbnm structure of α-SnS undergoes a phase transition to the orthorhombic Cmcm β-SnS structure.(90) Greyson *et al.* studied the thermal stability of as-synthesised SnS by heating the NCs under an inert atmosphere at 300 ^{0}C for 3h resulting in no change in the SnS crystal structure and morphology

which is by the theoretical predictions. This fact leads to the conclusion that these materials could possess high chemical and environmental stability.

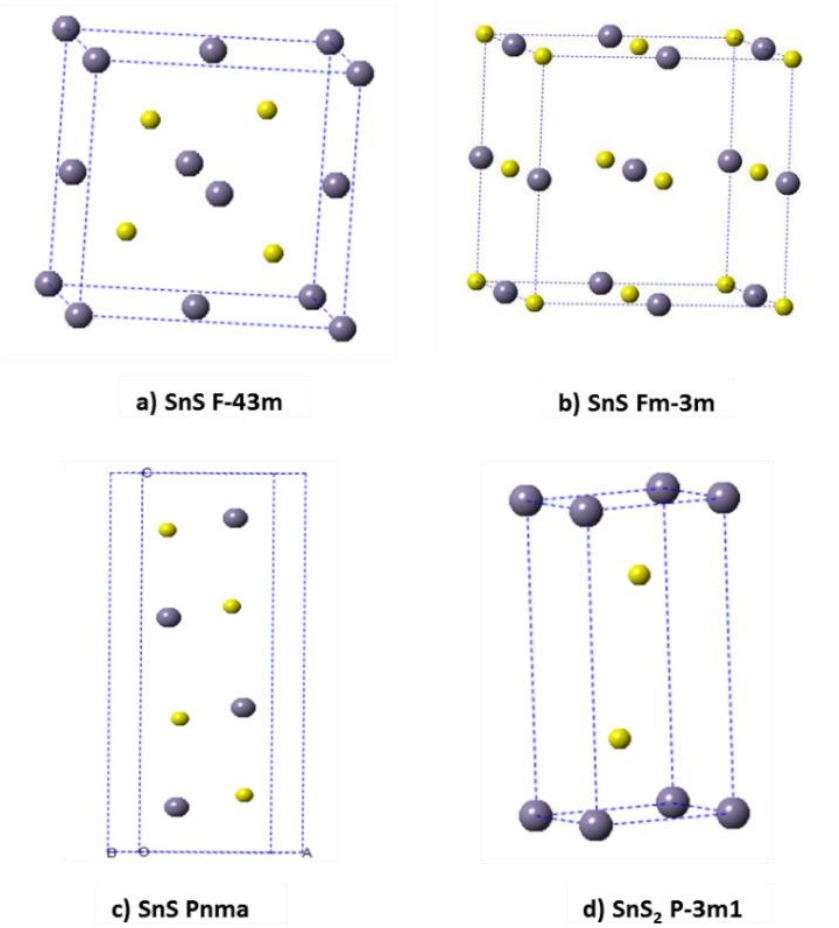

Figure 2- 14. Illustrations of the different SnS_x structures and geometries. (Gray colour corresponds to Sn atoms and yellow colour—to S atoms).

Table 2- 1. Summary of phases, crystal structures, space groups and band-gaps (E_g) for SnS_x compounds.

Experimental Parameters			
Phase	***Crystal Structure***	***Space group***	***E_g (eV)***
SnS	Cubic	F-43m	1.1-1.8
SnS	Cubic	Fm-3m	-
α-SnS	Orthorhombic	Pbnm	1.0-1.4
β-SnS	Orthorhombic	Cmcm	-
SnS_2	Hexagonal	P63/mmc	1.6-2.9
SnS_2	Trigonal	P-3m1	-
Sn_2S_3	Orthorhombic	Pnma	0.85-1.16

Liu *et al.* have reported the synthesis of SnS NCs with tunable sizes. In this work, they state that both the change in SnS size and crystal structure are due to increases in temperature from 150 ^{0}C to 280 ^{0}C resulting in the transformation from cubic (d ~ 8 nm) to truncated polyhedral crystal structure with sixteen-facet SnS polyhedral crystals (d ~ 100 nm).(91) This fact leads to the conclusion that the size and crystal structure of these materials can be easily manipulated depending on the careful choice of chemical precursors and reaction conditions.

2.5.1.2 Properties of SnS

SnS is of a great interest to many research groups because this material has both direct (1.3 eV) and indirect (1.1 eV) band-gap values(92) with a direct band-gap close to the optimum value (1.5 eV) (93) required for the ideal collector of solar radiation forming more than one electron-hole pairs when absorbing energy. The high absorption coefficient of SnS ($\alpha > 10^4$ cm^{-1}) in the solar spectrum allows the absorption of light at narrow thicknesses.(94) SnS constituent

elements Sn and S are abundant, non-toxic and relatively cheap, thus making SnS a promising alternative in thin-film device fabrication.

The unique optoelectronic properties of SnS make it a suitable *p*-type semiconductor material (95) in a thin-film form with an electrical resistively of 32.9 Ω.cm, carrier density of 2 x 10^{15} cm^{-3} (96)(97) and hall mobility of 90 cm^2 V^{-1} s^{-1}.(86) SnS may also be applied as an n-type material in PV applications or change its conductivity properties upon various heat treatments. Ristov *et al.* described the preparation of *p*-type SnS thin films using a simple chemical bath deposition (CBD) technique at room temperature ($SnCl_2$ and Na_2S precursors). In this experiment, they observed a change in the conductivity of the SnS absorber layer conductivity from *p*- to *n*-type upon annealing the thin-film at T > 280 ^{0}C for a short period of time with no noticeable change in composition.(98)

The electrical properties of SnS absorber layers can be modified by doping using elements like Sb, Se, Te, In, Al, N, etc. Guo *et al.* studied the effect of various dopants on the electrical properties of SnS thin-films by vacuum evaporation. The best dopant source was found to be Sb resulting in doubled photosensitivity and reduced resistivity (from 99 Ω.cm to 24 Ω.cm) by annealing the SnS thin-film in a hydrogen atmosphere at 400 °C for 3h.(99) All these characteristics make SnS a suitable semiconductor material for incorporation into various applications.

2.6 Applications

Colloidal quantum dots (CQDs) have been extensively studied and applied in a wide range of solution-processed devices including photovoltaic (PV) cells,(100) photodetectors, (101)(102)(103) light-emission devices (LEDs), (104)(105)(106) and medical devices.(107) Recent improvements in QDs research have led to significant progress in achieving control over the chemistry by mastering the synthetic methods, optimising materials system and

optoelectronic properties, and in processing techniques and characterisation. Current applications of SnS QDs include their incorporation into batteries (108)(109) and photovoltaics (110) due to a limited application due to synthetic difficulties.

2.6.1 SnS-based batteries

SnS QDs are a promising candidate for applications in both lithium- (LIBs) (111) and sodium-ion batteries (SIBs). (112)(113) However, batteries based on sodium-ion chemistry are gaining significant research interest due to the abundant sodium nature as alternatives to the established lithium-ion ones. SnS-based SIBs can offer low-cost and large-scale battery energy storage and conversion due to their size-dependent optoelectronic properties and high abundance. However, SnS-based batteries have so far resulted in low conductivity and phase aggregations preventing their practical applications in batteries. To address these issues and mitigate the aggregations of active materials, embedding SnS QDs in a conductive matrix has been mainly researched.(114) Ying *et al.* demonstrated in their work a promising encapsulation method, in which they embedded ultra-small SnS QDs in sulphur and nitrogen co-doped porous carbon fibres (SnS@SNCF-55) synthesised by a facile electrospinning process for sodium-ion batteries (NIBs).(112) The results of the electrochemical performance of the hybrid SnS composite material are compared to previously reported SnS systems and summarised in *Table 2-2*. The authors explained the superior properties of SnS@SNCF-55 composite material as a result of optimised structural stability upon cycling due to the carbon-like matrix, fast capacitive sodium storage induced by doping (creating active sites) and enhanced conductivity of carbon fibres, factors that all demonstrate the promising potential of SnS QDs as a future anode material for sodium-ion batteries.(115)

Table 2- 2. Achievements in SnS-based sodium ion battery research. (Table reprinted from reference 107).

Author	***Current density (mA g⁻¹)***	***Capacity retention (mAh g⁻¹)***	***Sample electrode***
Ying *et al.*	200/ 500	493/ 447	Ultra-small SnS NPs embedded in carbon sphere
Wu *et al.*	100/ 800	485/ 348	Sn-SnS-C
Wu *et al.*	100/ 400	405/ 351	SnS@rGO
Choi *et al.*	100	540	SnS-C microspheres
Cho *et al.*	30/ 200	450/ 400	SnS 3D flowers
Dutta *et al.*	100/ 500	550/ 390	SnS nanorods
Zhou *et al.*	810	492	SnS@Graphene
Wu *et al.*	100/ 400	544/ 493	SnS-C
Lu *et al.*	50/ 500	590/ 458	SnS/GO+C
Wang *et al.*	50/ 100/ 800	796/ 630/ 400	SnS@SNCF

2.6.2 Thin film photovoltaics (PV)

Interest in tin sulphide (SnS) as an alternative PV material has increased significantly. The component elements of SnS—tin, and sulphur are abundant, environmentally benign and inexpensive, making it an alternative candidate for various applications such as incorporation into thin film solar cells and optoelectronic devices,(116)(117) particularly in the development of heterojunction PV solar cells.(118) However, SnS devices have so far produced PCE of fewer than 5 % (119) due to inhomogeneities in the physicochemical properties, while theoretically such cells are expected to reach 24 % efficiency.(120) SnS thin-film PV materials show high absorption coefficients,(121)(94) electrical conductivity,(86) hall mobility,(86) large dipole moments for enhanced charge separation, tunable band-gaps via controlling the size and shape of the NCs and multiple excitation generations (MEG),(122) factors that should be considered

when developing alternative semiconductor materials. *Table 2-3* summarises key advances in SnS-based solar cell devices from the literature. The highest device efficiencies achieved to date include fabrication methods using high vacuum deposition techniques resulting in greater grain growth compared to the solution-processed SnS device reported by Rath *et al*.(123)

Table 2- 3. Summary of reported SnS nanocrystal solar cells is utilising novel device architectures and hybrid passivation techniques.

Author	***J_{sc} (mAcm^{-2})***	***V_{oc} (V)***	***FF (%)***	***η (%)***	***Comments***
Rath *et al.*(123)	11.6	0.28	38	1.30	ITO/planar-TiO_2/SnS/P3HT/MoO_3/Ag solution-processed and open-air fabrication
Reddy *et al.*(100)	9.6	0.26	53	1.30	p-SnS/n-CdS polycrystalline thin film solar cells using spray pyrolysis
Schneikart *et al.*(97)	19.0	0.22	-	1.60	ITO/Al:ZnO/CdS/SnS/Au using RF sputter deposition
Ikuno *et al.*(124)	12.1	0.27	64	2.10	ITO/Zn0/Zn (O,S)/SnS/Mo by RF magnetron sputtering
Sinsermsuksakul *et al.*(125)	19.4	0.24	43	2.04	glass/Mo/SnS/Zn(O,S)/ZnO/ITO using pulsed-CVD + treatment with ($Sn(MeC(N\text{-}iPr)_2)_2$) and hydrogen sulfide ($H_2S$)
Steinmann *et al.*(126)	20.7	0.33	56	3.88	Si/SiO_2/Mo/SnS/Zn(O,S)/ZnO/ITO/ Ag thermal evaporation
Sinsermsuksakul *et al.*(119)	20.2	0.37	58	4.36	Mo/SnS/SnO_2/Zn(O,S):N/ZnO/ITO using ALD with highly doped ZnO n-type layer

2.7 Conclusions

Despite improvements in achieving control over the chemistry, morphology, assembly and related applications, controlling the crystal structure, size, shape and stability of SnS QDs is still a compelling objective for many research groups. These materials are difficult to synthesise as a single crystal type with controlled size and shape due to their ability to access

high oxidation states and consequently, form various crystal structures. The principle control in these systems is through the precise manipulation of reaction variables such as fine control of the ratio of capping ligands to precursor types, reaction times and temperature. However, SnS QDs have a great potential not only in their current fields of research owing to their excellent optoelectronic properties and abundance but also in biological applications due to their non-toxic nature.

Therefore, this thesis will focus on the development of fabrication methods for synthesising high-quality SnS CQD with optimised optoelectronic and physicochemical properties and investigate their potential in biological applications.

Chapter 3 Materials and Methods

3.1 Materials and reagents

Tin (II) chloride anhydrous (> 99.99 %), elemental sulphur, S (99.98 %), thiourea, TAA (99 %), bis(trimethylsilyl)sulphide, $(TMS)_2S$, oleic acid (90 %), 1-octadecene, ODE (90 %) were all purchased from Sigma-Aldrich, UK. Ethylene glycol, EG and Oleylamine, OLA (80-90 %) were purchased from Fischer Scientific, UK. All chemicals were used as received without purification.

3.2 Synthesis

3.2.1 Colloidal synthesis of SnS QDs

A novel synthetic procedure for the synthesis of SnS CQDs using a low reactivity precursors and low reaction temperatures has been developed and described in this section. In a typical hot injection synthesis $SnCl_2$, ODE, OA and OLA (molar ratios listed in *Table 3-1*) were loaded into a 50 mL three-neck flask and connected to a Schlenk line. The system was evacuated using a rotary pump and left on continuous stirring at 105^0 C for at least 1 h to maintain moisture free conditions. Then, the Schlenk line was purged with Argon flow and these reaction conditions were maintained for another 1 h to aid the complete dissolution of the Sn-based precursor yielding a clear yellowish transparent organotin solution. In a desired range of reaction temperatures between 40 and 60ºC depending on the required band-gap value 1 mmol of elemental sulphur (S) precursor was injected into the three-neck flask followed by an immediate colour change from clear yellowish to dark within 15 s, indicating a nucleation. After the S injection, the solution was left on the heating mantle for another 5-10 min for growing of the quantum dots. The reaction vessel was cooled down to room temperature in a

cold-water bath for 30 s. The modification required for the reaction synthesis of other SnS CQDs described in chapter 4 of the thesis involved the replacement of the low reactivity elemental S precursor with a highly reactive bis(trimethylsilyl)sulphide $(TMS)_2S$ acting as a sulphur precursor with the rest of the conditions kept constant.

Table 3- 1. Reagent quantities for the synthesis of SnS CQDs using different S precursors

Reagents	**Moles (mmol)**
Tin (II) chloride	2.00
Oleic acid	5.00
Oleylamine	12.00
1-Octadecene	10.00-30.00
Bis(trimethylsilyl) sulphide $(TMS)_2S$ or elemental sulphur (S)	1.00

The next step after the synthesis of the CQDs involved a solvent/antisolvent cleaning procedure for removing any unreacted precursors, impurities and excess surfactants. First, the CQDs solution was divided into two 50 mL centrifuge tubes and 20 mL of ethanol (antisolvent) was added to each batch to precipitate out the quantum dots. The suspension was centrifuged at a speed of 6000 revolutions/min (rpm) for 5 minutes and the flocculate was discarded after the precipitation. The supernatant (QDs) was re-dispersed in 5 mL of hexane (solvent). The ethanol/hexane cleaning procedure was repeated once more. The final precipitate of QDs was re-dispersed in 5 mL of hexane with a concentration of 20 mg/mL and the colloidal solution of SnS QDs was instantly used for further analysis. All samples in the thesis prepared by this synthetic method were washed using the same cleaning procedure.

3.2.2 PVP-encapsulated SnS QDs

In the synthesis of PVP-capped SnS CQDs, 0.001-0.1 mmol of PVP (M_W= 10.000, 40.000, 55.000 and 360.000 g/mol) was added to a 50 mL three-neck flask that contained 10 mL EG and connected to a Schlenk line. The solution was heated to 105^0 C under vacuum to maintain a moisture free atmosphere and left on stirring for 1h. Then, the Schlenk line was purged with argon flow and the solution temperature was increased to 140^0 C. Sn and S precursor solutions were prepared by dissolving 0.38-2.00 mmol of $SnCl_2xH_2O$ in 0.75 mL EG (% w/v) and 0.5-1.00 mmol of TAA in 0.75 mL EG (% w/v). The precursor solutions were loaded into a syringe and quickly injected into the PVP solution once the reaction temperature got stabilised at 140^0 C followed by a progressive change of the solution colour from clear yellowish to dark greyish as the reaction went to completion. Solution aliquots were collected every 30 min of reaction time using a syringe and a needle and cooled down to room temperature in a cold-water bath for 30 s.

Table 3- 2. Reagent quantities for PVP-encapsulated SnS CQDs.

Reagents	**Moles (mmol)**
Sn (II) chloride	0.38-2.00
PVP	0.001-0.1
Ethylene glycol	18.00
Thiourea	0.5-1.00

After cooling down to room temperature, the aliquots were washes with 10 mL of methanol and centrifuged at 6000 rpm for 5 min to remove unreacted precursors, solvents and surfactant agents. The cleaning procedure was repeated once more, and the final precipitate was re-dispersed in 5 mL of methanol and stored for future analysis. All SnS/PVP CQDs samples prepared by this synthetic procedure were washed using the same cleaning method.

3.3 Bacterial strains

Pseudomonas fluorescence (P. fluorescence) ATCC 13525 bacterial strain was used in all biofilm and bioimaging experiments. The bacterial cells were provided by Miss Marimar Bravo Cadena from the Department of Engineering Science.

3.3.1 Liquid medium preparation

For liquid medium preparation, 10 g of Luria-Bertani (LB) broth powder was mixed with 500 mL DI water and swirled until reaching homogeneous solution. The LB medium was autoclaved at 121^0 C for 15-20 min. The LB medium was ready for use after cooling down to room temperature.

3.3.2 Bacterial culture and preparation

Bacterial cultures of *P. fluorescence* were prepared in 50 mL centrifuge tubes by transferring one colony grown overnight on LB plate into a 25 mL solution of fresh LB broth and incubated at 30^0 C and agitated at 250 rpm overnight (> 20 h). Aliquots of bacteria were removed from the culture solution with a sterile pipette to monitor growth by measuring optical density (OD). Once the OD (600 nm) was reached, aliquots (~ 1 mL) of bacterial culture were added to fresh LB medium (~ 24 mL) forming a total volume of 25 mL and incubated for another 5 h at 30^0 C reaching a mid-exponential (log) growing phase.

3.3.3 Toxicity assay

100 µL of bacteria culture was added to 96-well plate containing different concentrations of SnS/L CQDs ranging from 0.31 to 20 % (v/v). The plate was covered with a lid and incubated in a plate reader (Tecan instrument) at 30^0 C overnight. After the overnight incubation, the lid was removed, and the dose-response growth curves of bacteria were recorded using Spark control software.

3.4 Characterization techniques

This section gives a summary of the analytical and characterisation techniques used in the thesis.

3.4.1 X-ray diffraction (XRD)

X-ray diffraction spectroscopy is a characterization technique that determines the interference pattern and rearrangements of atoms within a crystal. XRD patterns are observed in crystals with atomic planes through which an incident beam of X-rays interferes with the crystal structure and leaves the sample as a diffracted beam. This analysis provides a good understanding of the orientation of a single crystal or grain and measures the size, composition and internal stress within the sample based on the intensity of the diffraction patterns vs angle (2θ). The instrument used in this study was equipped with a fully automated Bruker D8 ADVANCE eco powder diffractometer employing copper Kα1 electromagnetic radiation with a wavelength of 1.5406 Å (with a mode of two theta (2θ)) and a LYNXEYE XE detector. Samples were continuously spun during data collection and scanned using a step size of 0.02^0 2θ between the range of 10^0 to 90^0 2θ. Thin-film samples were prepared by drop casting SnS CQDs solution onto a silicon wafer.

3.4.2 Ultraviolet-visible near infra-red (UV-Vis-NIR) spectroscopy

The optical absorption properties of all CQDs samples were measured on a Cary Varian 4000 UV-Vis-NIR spectrophotometer. A typical arrangement of the instrument includes a light source, diffraction grating, aperture through which light travels to the sample cuvette and is captured by a detector (photomultiplier tube). The detector measures the resulting light intensity of a sample irradiated with a monochromatic beam of light. Liquid samples of diluted CQDs solutions and pure organic ligands were loaded in quartz cuvettes. A baseline measurement was performed at 100 % transmission (with no sample) and 0 % transmission (blocking the light) before the analysis of the samples. Measurements were taken with respect to a reference sample containing the dispersant solvent. This type of analysis is appropriate not only for solutions but also for solid samples and gases. The energy band-gap, E_g, was calculated using the so called Tauc plot equation,

$$(\alpha h\nu)^{1/r} = A\,(h\nu - E_g) \quad (6)$$

where $h\nu$ is the energy of light, A is a constant, α is the absorption coefficient of the material and r corresponds to the transition process (e.g. r= 1/2 and 1/3 for direct and forbidden transitions, respectively). (127)

3.4.3 Fourier transform infrared spectroscopy (FT-IR)

Infrared spectroscopy is a non-destructive technique capable of identifying particular functional groups that are present mostly in organic compounds according to their specific vibrational characteristics. In FTIR analysis, a beam of infrared light is passed through the sample and radiation of molecular absorption is measured as a function of frequency. A spectrum is produced which shows wavelengths at which the sample absorbs IR and this allows

identification of functional groups, compounds, chemical bonding and molecular structures. The obtained FTIR results in this work were performed using a Varian Excalibur FTS 3500 spectrometer. All samples were prepared on glass substrates by drop casting SnS CQDs solution and waiting for the evaporation of the solvent before taking the measurement. The obtained FTIR spectra in each sample is an average of 64 scans. The achieved FTIR spectra were analysed using an Origin software.

3.4.4 X-ray photoelectron spectroscopy (XPS)

X-ray photoelectron spectroscopy is a powerful chemical technique used for surface analyses allowing determination of the elemental composition, chemical and electronic states within a material and empirical formula. Samples were analysed using a Thermo Scientific Instrument K-Alpha XPS spectrometer equipped with microfocussed monochromated aluminium X-ray source operating at 12 keV and a 400-micron spot size was used measuring the irradiated light in the form of X-ray photoemitted electrons from the top surface of the sample and the resulting kinetic energy. Survey scans and detailed scans were performed at a constant analyser energy (CAE) of 200 eV and 50 eV, respectively. Charge neutralisation was applied using a combined low energy/ ion flood source. Thin-film samples of SnS CQDs were prepared by drop casting and placed on a steel bar sample holder using double-sided carbon tapes. Thermo Scientifics Advantage software was used to aquire and analyse XPS spectra. XPS measurements were carried out by Philip Holdway in Begbroke Science Park, University of Oxford.

3.4.5 Transmission electron microscopy (TEM)

Transmission electron microscopy is a powerful imaging technique that provides information about sample's morphology enabling the precise measurement of the quantum dot sizes, shapes, compositions, size-distribution and crystallinity. Most of the TEM analyses of CQDs in the thesis were performed on a JEOL 2100 TEM operating at 200 kV along with an EDS detector connected to an INCA software. Dilute dispersions of CQDs were prepared, in which TEM grids were briefly dipped in and left to dry at ambient conditions. The obtained mean-particle sizes were calculated using an experimental size histogram with a Gaussian distribution curve generated from the counts of multiple quantum dots present in the TEM sample.

In addition, the FFT images were obtained by selecting an area of interest (e.g., the area of a single quantum dot) and performing an FFT analysis using an ImageJ software. The resulting FFT images were composed of an array of dots, which correspond to the d-spacing values of specific lattice planes in the crystal structure, which were later compared to theoretical values to assign the correct crystal phase of the material.

TEM reconstruction images were obtained by selecting the diffraction dots from the FFT images and performing an inverted FFT analysis. This allowed precise confirmation of the d-spacing values to the values of the original HRTEM images as well as determine crystal faults or imperfections. The observed extended stripes beyond the region of the QDs could be related to a thin organic layer covering the surface of the QDs due to the presence of organic ligands, which was also observed from the TEM/STEM analysis of CdSe/ZnS core/shell quantum dots.(128)

3.4.6 Energy dispersive X-ray (EDS) spectroscopy

EDS analysis provides a reliable chemical characterisation quantifying the constituent elements of the quantum dots. Elements have an electronic structure with specific energy. When a beam of high energy electrons excites the sample, the electrons in the atoms of the constituent elements are excited to a higher energy level in the conduction band and released to a lower energy level in the valence band once they lose some of the absorbed energy. The release of specific energy during exciton recombination provides information about the elemental composition of the sample. The EDS measurements were performed at low magnifications acquiring statistical average data of multiple quantum dots. INCA analytical software was used to process the EDS spectra for chemical identification and quantification.

3.4.7 Scanning transmission electron microscopy (STEM)

Scanning transmission electron microscopy (STEM) is a unique characterisation technique with advanced analytical capabilities compared to a conventional TEM analysis. STEM enables high atomic resolution imaging and elemental composition mapping even on light elements. High-resolution STEM/EDS imaging and line scan measurements of the chemical composition and distribution of elements within the quantum dots were performed using a JEOL JEM-ARM200CF aberration-corrected microscope operated at 200 kV, with STEM/EDS capabilities and JEOL JEM-3000F TEM Aberration Corrected, Monochromated EG-TEM operating at 80 kV. TEM specimens were prepared by dip-coating a TEM grid into a dilute solution of QDs followed by drying under ambient conditions. Samples were further backed under vacuum at 120^0 C for 12 h to clean excess solvent or hydrocarbon contamination. The STEM analysis was carried out with the help of Dr Judy Kim.

3.4.8 Photoluminescence (PL) analysis

Photoluminescence spectroscopy is a non-destructive characterisation tool that provides information about the electronic structure of a material. It allows the determination of band-to-band electronic transitions and the rate of charge recombination processes providing information about the presence of defect energy levels within the electronic structure of the crystal. Additionally, time-resolved μPL (TRPL) measurements monitor directly the dynamics of the charge carrier recombination processes based on the emissive PL lifetime decay of the material. The PL lifetime is inversely proportional to the sum of both radiative and non-radiative charge recombination rates. The 3D wavelength-dependent PL emission measurements were taken using an automated Agilent Cary Eclipse Fluorescence Spectrophotometer equipped with an Agilent xenon flash lamp allowing for fast acquisitions times (capturing data every 12.5 ms), highly sensitive optics and photomultiplier tube detectors connected to an Agilent Cary WinFLR software. Dilute dispersions of CQDs were loaded in quartz cuvettes and excited with an excitation wavelength in the range of 350 nm to 500 nm (with 10 nm increments). The steady-state PL spectra was collected and processed using an Origin software.

Steady-state photoluminescent optical measurements were performed using a mode-locked Ti:Sapphore laser (Coherent Mira, operating at 76MHz with a pulse width of 150ps), with frequency doubled to 395nm. The excitation was directed onto the sample through a 100x objective (0.7NA) giving an excitation spot of approximately 800nm. Emission was collected through the same objective and directed to a 0.3 m spectrometer (with available gratings of 300, 600 and 1200 lines/mm). Time-resolved PL measurements were carried by directing the emission to an output slit on the spectrometer (to act as a monochromator) and passed to a photomultiplier tube (PMT) (Becker and Hickl PMH-100) with an instrument response function width of 150 ps. A fast-photodiode detector was used at the excitation laser to act as

a start timer for time-correlated single-photon counting (TCSPC) measurements. Fitting of lifetime data was performed (mono-or dual-exponential fits where appropriate) using an Origin software. Samples were prepared by drop casting diluted solutions of quantum dots onto silica substrates. For the temperature-dependent TRPL measurement, thin-film samples prepared by drop-casting of SnS CQDs were loaded onto liquid nitrogen/argon cryostat and left under vacuum for 10 h to remove excess solvents before performing the analysis. All steady-state and time-resolved PL measurements were performed at the Department of Physics with the kind help of Dr Tim Puchtler.

3.4.9 DeltaVision widefield fluorescence system

Widefield fluorescence images were collected on a DeltaVision Core epifluorescence imaging system (Imsol, Preston, UK) using an Olympus (Olympus Keymed, Southend-on-Sea, UK) IX-71 microscope fitted with a 60x/1.4NA oil immersion objective. Green fluorescence was generated by illuminating the sample at 488nm using a Lumencor SpectraX light source (Lumencor, Beaverton, Oregon, USA) and bright-field transmission illumination was generated using a broad-spectrum white LED (Imsol). A Photometrics CoolSNAP HQ2 cooled Charge Coupled Device (CCD) camera (Photometrics, Tuscon, Arizona, USA) was used to sequentially capture fluorescence and bright-field images using the software package softWoRx (Imsol). Post-acquisition processing, including generating merged images was performed using ImageJ/FIJI (NIH, Bethesda, Maryland, USA). All samples were prepared by adding a small amount of the biofilm to a glass substrate and covered by microscope slide glass.

3.4.10 Perkin Elmer UltraView spinning disc confocal

A Perkin Elmer UltraView VoX (Perkin Elmer, Beaconsfield, UK) spinning disc confocal mounted to an Olympus IX-81 microscope fitted with a 60x/1.4NA oil immersion objective (Olympus Keymed) was used to capture single plane fluorescence and bright-field images. A laser at 488nm was used to excite green fluorescence and bright-field illumination was used for transmission imaging, with images collected sequentially on a Hamamatsu C9100-13 Electron Multiplying-CCD (EM-CCD) camera (Hamamatsu Photonics UK, Welwyn Garden City, UK) using the software package Volocity (Perkin Elmer). Post-acquisition processing, including generating merged images was performed using ImageJ/FIJI. All samples were prepared by adding a small amount of the biofilm to a glass substrate covered by a microscope slide glass.

3.4.11 Olympus FluoView 3000 laser scanning confocal

An Olympus FluoView 3000 laser scanning confocal incorporating an Olympus IX-83 microscope stand fitted with a 60x/1.4NA oil immersion objective (Olympus Keymed) was used to collect lambda scans in order to characterise the fluorescence emission characteristics of nanoparticles when excited at different wavelengths. Quantum dots were excited at either 405 nm, 488 nm or 561 nm and lambda scans performed by collecting light in 10nm bands from 420 nm-600 nm, 490 nm-690 nm and 570 nm-760 nm for each excitation wavelength respectively using the native FluoView confocal software. Data analysis was performed by measuring fluorescence intensity at each 10 nm collection band using ImageJ/FIJI with the Olympus file format plug-in installed (Olympus Keymed). All samples were prepared by adding a small amount of the biofilm to a glass substrate covered by a microscope slide glass.

Lambda scan measurements were performed with the kind help of Dr Andrew Jefferson from the Department of Biochemistry at the University of Oxford.

Chapter 4 Excitation-dependent photoluminescent (PL) emission properties of SnS CQDs

This chapter presents the synthesis and optimisation of SnS CQDs with novel photoluminescent (PL) properties for the first time. Dr Tim Puchtler from the Department of Physics, University of Oxford, assisted with Temperature-dependent PL and time-resolved PL (TRPL) measurements. Dr Judy Kim performed high-resolution STEM/EDS analysis used to obtain elemental composition through line scans analysis of SnS QDs.

4.1 Introduction

The different strategies of tuning and optimising the optoelectronic properties of colloidal quantum dots (CQDs) developed in the literature were discussed in chapter 2 of the thesis. Chapter 4 will provide the reader with a synthetic procedure for fabricating high-quality SnS CQDs with novel multi-colour photoluminescent (PL) properties and a systematic explanation of the factors affecting their optical and emission features and link those theoretical hypotheses to experimental results. The implementation of a low reactivity S precursor in the synthetic procedure was examined.

Table 4- 1. Summary of SnS QDs synthesised by various reaction procedures and conditions reported in the literature.(129)(130)(131)(132)(133)(91)(134)(135)(136)

Author	Types of nanomaterials	Preparation Method	Band-gap (eV)	Size (nm)	Shape	Sn:S	Crystal Structure	Comments	Applications
Odom *et al.(129)*	Size-tunable SnS nano- and microcrystals	Colloidal synthesis using $SnCl_2$ and elemental S	1.3-1.8	20-200	Zinc blend tetrahedral and 2D orthorhombic plates	--	Orthorhombic and Zinc blend	Size-tuning effect on SnS crystal structure	--
Eychmuller *et al.(130)*	Size and shape-tunable SnS NPs	Colloidal synthesis using $Sn[N(SiMe_3)_2]_2$ and TAA and different ligands ratios of OA/OLA	1.5	7-20	Spherical- and triangular-shaped NPs	1:1	Orthorhombic (space group Pbnm)	Monodispersed NPs with spherical (1:1 OA/OLA) and triangular (1:2 OA/OLA) shapes	--
Tilley *et al.(131)*	Size-tunable SnS NPs	Colloidal synthesis using $SnBr_2$ and Na_2S and ligands w/ different number of hydroxyl groups	1.1	3-5	Spherical-shaped NPs	1:1	Orthorhombic (space group Pbnm)	Small, monodispersed NPs with uniform size and shpe	--
Davar *et al.(132)*	Shape selecrtive SnS NPs	Hydrothermal synthesis using $SnCl_2xH_2O$ and TGA at low T	--	20-200	Nanoparticles, Nanoflowers and Nanosheets	1:1	Orthorhombic (space group Pbnm)	Various SnS morphologies and shapes such as NPs, NFs and nanosheets formed when TGA/Sn, rxn T an rxn time varied	--
Liu *et al.(133)*	Size-tunable SnS NPs	Colloidal synthesis using $SnCl_2$ and TMS	1.3	6-20	Uniform cubes	1:1	Orthorhombic β-SnS (space group Cmcm (63))	Monodisperse, size-tunable SnS NPs	Solar cells
Ning *et al.(91)*	Size and shape-tunable SnS NPs	Colloidal synthesis by varying rxn T and Sn/S molar ratios	3.6	5-15	Nanoparticles, Nanoflowers and Nanosheets	1:1 1:2/ 2:1 1:2	Orthorhombic	Various SnS shapes such as NPs, NFs and nanosheets formed when rxn T and Sn/S varied	--
Liu *et al.(134)*	Size-tunable SnS NPs	Colloidal synthesis using SnI_4 and S and various rxn T	1.6	8-200	Various shapes	1:1	Metastable zinc-blend	--	Solar cells
Reiss *et al.(135)*	Size-tunable SnS NPs	Colloidal synthesis using slow and high reactive Sn and S precursors	1.3	7-14	Various shapes	1:1	Orthorhombic (space group Pnma)	Instantaneous surface oxidation after air exposure	--
Prastani *et al.(136)*	SnS NPs	Colloidal synthesis using $SnCl_2$ and TAA	1.6	4	Spherical NPs	1:1	--	Good electrical conductivity	Solar cells

Several research groups reported the synthesis of monodisperse, size-tunable SnS QDs with control over the size, shape, stoichiometry, (single) crystal structure and surface passivation of the final material and the achievements are summarised in *Table 4-1*. Various synthetic methods and reaction conditions such as precursors types with different reactivities, stabilising agents (organic ligands with different alkyl chain lengths), reaction temperature and reaction time all have been explored with the aim of synthesising chemically-optimised SnS CQDs with improved stability. Hickey *et al.* are one of the very few groups who described the fabrication of SnS NPs with sizes below 10 nm. They found that the high reactive Sn precursor they used

in the synthesis of SnS resulted in fast nucleation events forming uniform NPs with a narrow size-distribution.(74) Tilley and co-workers reported the first facile fabrication of ultra-small SnS QDs by varying the length of the organic ligands (number of hydroxyl groups) in the synthesis resulting in sizes between 3-5 nm with stoichiometrically balanced NPs (Sn:S molar ratios of 1:1).(131) Reiss et al. demonstrated in their work an adapted procedure for the surface passivation of SnS NPs using a Cd-phosphonate complex under inert conditions resulting in the appearance of a broad PL emission peak at around 600 nm (FWHM= 180 nm). Although the promising achievements of inducing PL emission properties in SnS/CdS core/shell NPs, the authors revealed that the Cd-passivated NCs showed same stability behaviour as the core SnS NCs completely losing their PL emission due to surface degradation when exposed to air.(135)

Despite the promising synthetic achievements of SnS QDs described in the literature, none of the SnS-based reports presented significant improvements in the control of the optoelectronic and emission properties of SnS QDs. Here comes the question then what could be the potential reasons for producing size- and composition-tunable SnS NCs with a narrow size-distribution, single crystal structure and good surface passivation as described in the literature, which does not possess photoluminescent properties characteristic to direct band-gap semiconductor materials?

In the first part of this chapter, preliminary synthetic results of SnS QDs will be discussed. I will investigate the effect of changing the reaction conditions in the synthesis such as precursor reactivity, reaction T and reaction time on the photoluminescent properties of SnS QDs. The chapter will start with a characterisation assigning the optical and photoluminescent properties to the size, and elemental composition of SnS QDs synthesised at different reaction temperatures. The crystal structure and elemental composition of the SnS samples will be studied as a function of reaction T.

In the second part, I will investigate three main hypotheses regarding the observed excitation-dependent emission properties of SnS CQDs and understand the origin of their PL emission:

1) Relative size—different populations of QD sizes with close absorption and emission profiles giving rise to excitation-dependent PL emission properties
2) Composition tuning—QDs with various elemental compositions (Sn:S stoichiometric ratio difference) resulting in different sizes of QDs with close PL emission profiles
3) Effect of organic ligands and organometallic compounds on PL emission features

4.2 Synthesis and characterization of SnS CQDs

4.2.1 Precursor reactivity

There are several key reaction parameters in the colloidal synthesis of QDs to be controlled and maintained such as precursor types, passivating ligands and reaction temperature producing QDs with narrow size-distributions. In chapter 4 of the thesis, the effect of precursor reactivity on the reaction synthesis of SnS QDs was carefully examined. It was observed that the precursor type has a direct influence on the nucleation and growth rates as well as the final size-distribution of the resulting QDs. The samples will be abbreviated as SnS-S (referred to elemental sulphur) and SnS-TMS (referred to bis(trimethylsilyl)sulphide).

4.2.1.1 Effect on nucleation and growth kinetics

Figure 4-1 represents two synthetic routes for the fabrication of SnS CQDs and the observed differences in the nucleation rates when using a low (*Figure 4-1(a)*) and high (*Figure 4-1(b)*) reactive Sulphur (S) precursors in the reaction synthesis. It was observed that the higher the

precursor reactivity, the faster the nucleation rate (instant nucleation) resulting in the formation of a larger number of small nuclei.(137)(138) Additionally, the use of the low reactive S precursor (elemental S) decreased the overall rate of nucleation resulting in multi-step nucleation events (gradual nucleation) with apparent solution colour changes from clear yellow to dark red as seen in *Figure 4-1 (a)*. This observation could be explained by the slow rise of reactant species due to delayed nucleation.(139) Although the use of elemental S caused slow nucleation events and thus increased the possibility of producing polydisperse samples of quantum dots with a broad size-distribution, it improved my understanding of the different reaction stages in the synthesis and helped me observe unseen properties of SnS QDs as before.

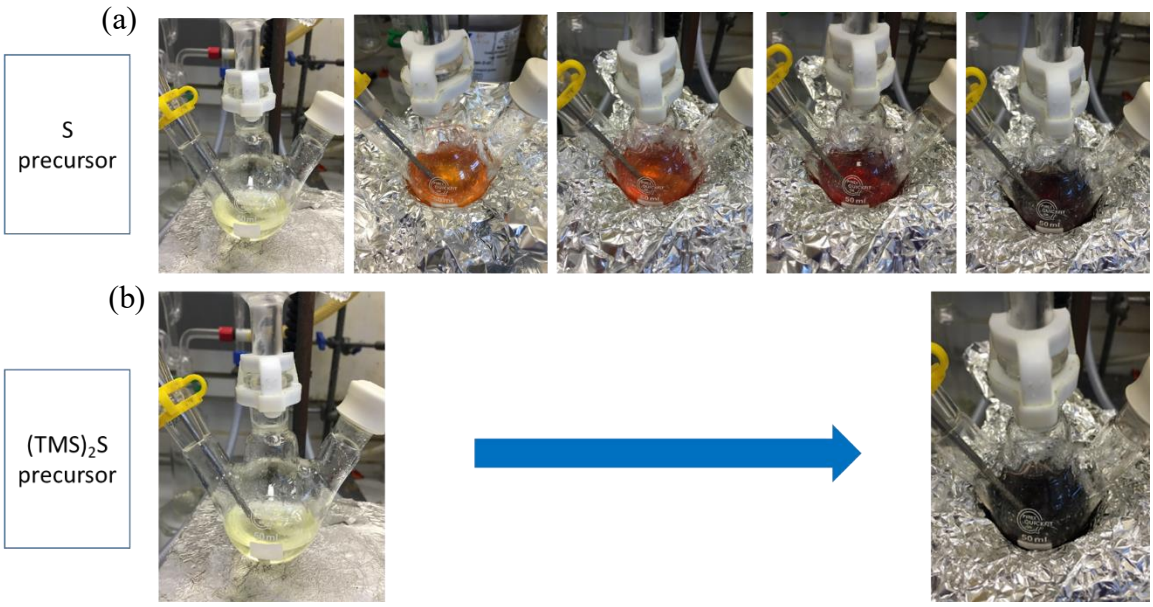

Figure 4- 1. Images of the changes in the nucleation rates in the synthesis of SnS CQDs when as a function of slow (top) and fast (bottom) reactive Sulphur precursors (elemental S and $(TMS)_2S$), respectively).

4.2.1.2 Effect on absorption properties

Figure 4-2 shows a significant change in the optical properties between the two SnS samples synthesised by varying the reactivity of the S precursors. The optical band-gap of SnS-TMS appears to be narrower (2.55 eV) as seen in *Figure 4-2.2(b)* compared to the band-gap of SnS-

S, which appears to be wider (2.95 eV). It is expected that the reason of the band-gap difference between the two SnS samples to be a size-related phenomenon.(140)(35) The narrower the band-gap of SnS CQDs (2.55 eV) the larger the average size of the quantum dots compared to the size of the wider band-gap SnS CQDs (2.95 eV). This hypothesis will be further explored using TEM analysis in the next section (refer to 4.2.1.3).

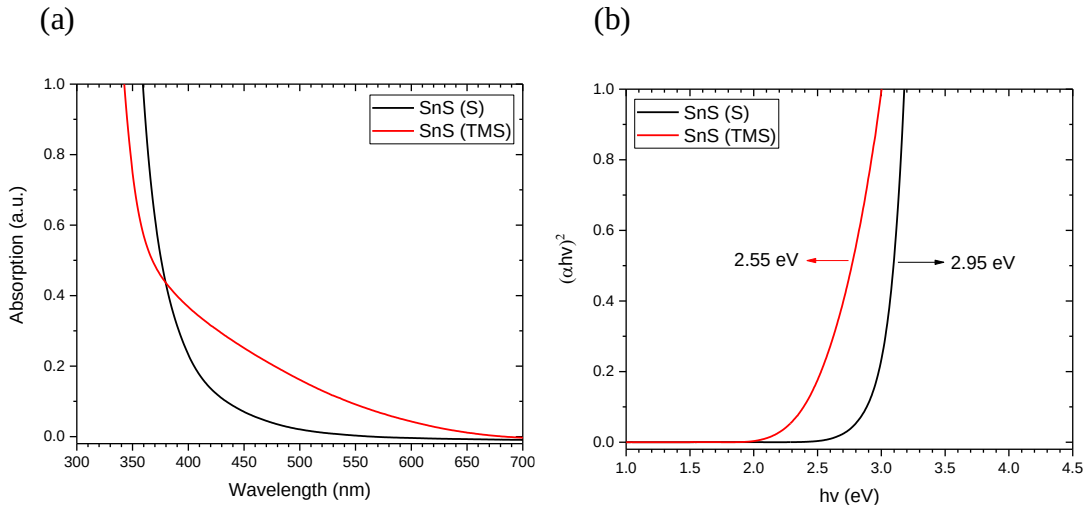

Figure 4- 2. (a) UV-Vis absorption spectra and (b) calculated band-gap energy values of SnS CQDs synthesised with elemental S (black spectrum) and $(TMS)_2S$ (red spectrum) precursors showing the change in absorption with the degree of precursors' reactivities.

4.2.1.3 TEM analysis

The mean-particle sizes of SnS-S and SnS-TMS CQDs were obtained using TEM analysis. The results were measured and fitted with a Gaussian distribution curve. Both SnS-S (*Figure 4-3(a)*) and SnS-TMS (*Figure 4-3(e)*) samples appear to be polydisperse having a range of sizes between 2-5 nm with semi-spherical shapes. The mean-quantum dot diameter of SnS-TMS is bigger (1.76 nm) as seen in *Figure 4-3 (j)* compared to the mean-quantum dot diameter of SnS-S (1.14 nm) (refer to *Figure 4-3 (i)*). The size measurements obtained from the TEM analysis are in a good agreement with the corresponding band-gap values of the two samples as seen from the UV-Vis spectra in *Figure 4-2 (b)*.

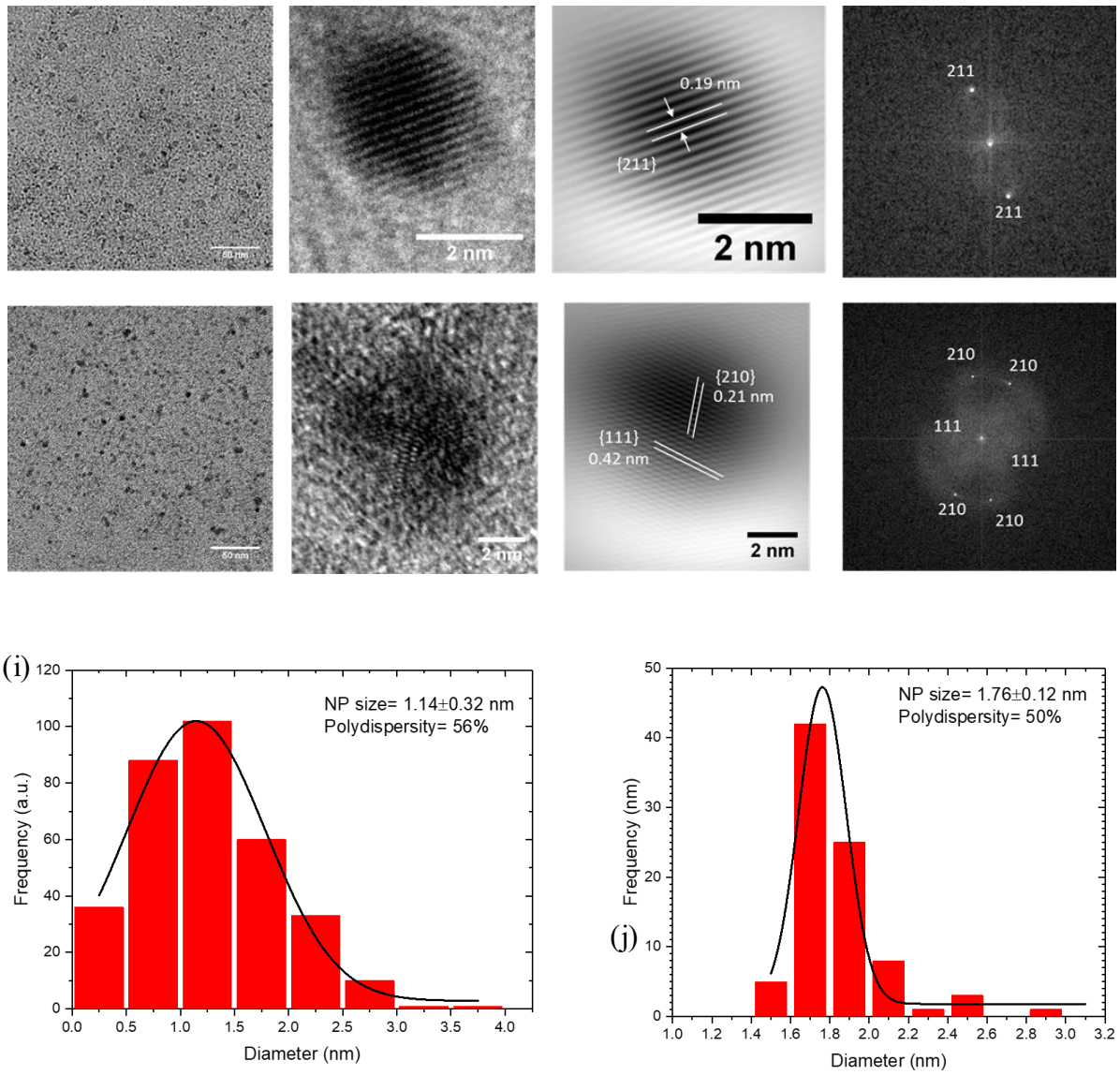

Figure 4- 3. TEM micrographs of (a-d) SnS-S and (e-h) SnS-TMS CQDs. (a, e) Low magnification images are showing the high polydispersity nature of SnS-S and SnS-TMS samples, respectively. (b, f) HRTEM micrographs and corresponding (d, h) FFT patterns of single SnS-S and SnS-TMS, respectively, confirming the crystallinity of the QDs. (c, g) Reconstruction HRTEM images obtained from the FFT patterns. (i, j) Histograms of the size-distribution, with a Gaussian curve fit, of SnS-S and SnS-TMS CQDs, respectively.

Although the minor size differences between the two batches of quantum dots, noticeable chemical composition variations are observed from the EDS summary data in *Table 4-2*. The EDS data represents the at % composition of Sn and S elements in SnS CQDs excluding the rest of the elements present in the sample, which could be a result of sample contamination and thus avoiding misinterpretation of the results. It appears that the elemental composition changes

in the quantum dots are highly dependent on the reactivity of the precursors used in the synthesis. In the case of SnS-S CQDs, the Sn:S ratio is significantly higher compared to SnS-TMS CQDs. This could be a result of both SnS QDs and Sn atoms present in the sample due to the slow nucleation rate as a result of precursor reactivity.

Table 4- 2. Average elemental composition of (a) SnS-S and SnS-TMS CQDs obtained from EDS analysis.

(a)

Element	Weight %	Atomic %
S K	12.55	31.31
Sn L	87.45	68.69
		Atomic Ratio
Totals	100.00	Sn : S= 2.2 : 1

(b)

Element	Weight %	Atomic %
S K	21.77	48.34
Sn L	78.23	51.66
		Atomic Ratio
Totals	100.00	Sn : S= 1 : 1

4.2.1.4 Photoluminescence (PL) studies

The PL emission properties of the final precipitates of SnS CQDs were measured and presented in *Figure 4-4*. Interestingly, when the high reactivity TMS precursor was employed in the fabrication method, quantum dots with excitation-independent emission properties are achieved (refer to *Figure 4-4 (a)*) regardless of the sample's polydispersity (see *Figure 4-3 (e)*). The PL emission spectrum of SnS-TMS CQDs showed no other significant emission features at longer excitation wavelengths (> 300 nm) except a single PL emission peak at 370 nm.

Additionally, *Figure 4-4 (b)* reveals that the use of elemental S results in the formation of quantum dots with multi-colour PL emission characteristics covering the entire visible region of the electromagnetic spectrum (λ_{em}= *390-580 nm*). This is a commonly observed phenomenon in semiconductor materials due to the high size-distribution of quantum dots with close absorption and emission profiles within the sample.(141) Despite the similarities in

absorption, quantum dot sizes and size-distribution observed in SnS-S and SnS-TMS CQDs, their PL emission features differ significantly. This result could be related to the observed differences in the stoichiometric balance of the quantum dots (Sn:S) as observed from the elemental composition analysis (refer to *Table 4-2 (a, b)*). Such changes in the composition of SnS could be in the origin of the wavelength-dependent PL emission.(142) Alternatively, the observed PL emission of SnS-TMS CQDs at 370 nm could be ligand-induced since this is the region of the electromagnetic spectrum at which organic ligands are expected to emit light, and this hypothesis will be further discussed in section 4.3.5.2. The effect of the low reactivity S precursor on the optical and PL emission properties of SnS-S CQDs will be further explored in the following section.

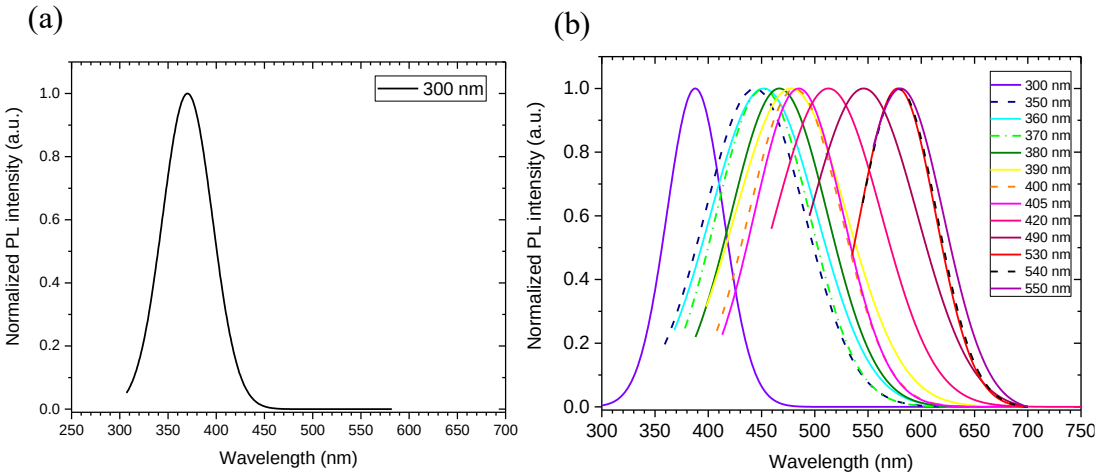

Figure 4- 4. Photoluminescence spectra of (a) SnS-TMS and (b) SnS-S CQDs showing noticeable differences in the PL emission features. The samples were illuminated with excitation wavelengths from 300 nm to 550 nm.

4.2.2 Reaction temperature studies

In this section, SnS CQDs synthesised with elemental S at 40^0 C, 50^0 C, and 60^0 C will be studied. The samples are abbreviated as SnS-1, SnS-2 and SnS-3 corresponding to increasing reaction temperature.

4.2.2.1 TEM analysis

Figure 4-5 shows low and high-resolution TEM (HRTEM) micrographs of SnS-1, SnS-2, and SnS-3 samples. The low magnification images in Figure 4-5 (a, e, i) and the histogram plots as seen in *Figure 4-5 (m, n, o)* reveal the broad distribution of quantum dot sizes in all three samples regardless of reaction temperature. The resulting quantum dots show a semi-spherical morphology with well-defined lattice fringes corresponding to their high crystallinity. The d-spacing values of 0.22 nm and 0.34 nm correspond to lattice planes of {041} and {120} of the orthorhombic (Pbnm) crystal structure of SnS. Interestingly, the crystal facets in sample SnS-2 (refer to *Figure 4-5 (f)*) are formed from the lower index planes with a higher density of surface atoms.(143) This observation could suggest the formation of fewer dangling bonds due to higher coordination of surface atoms.

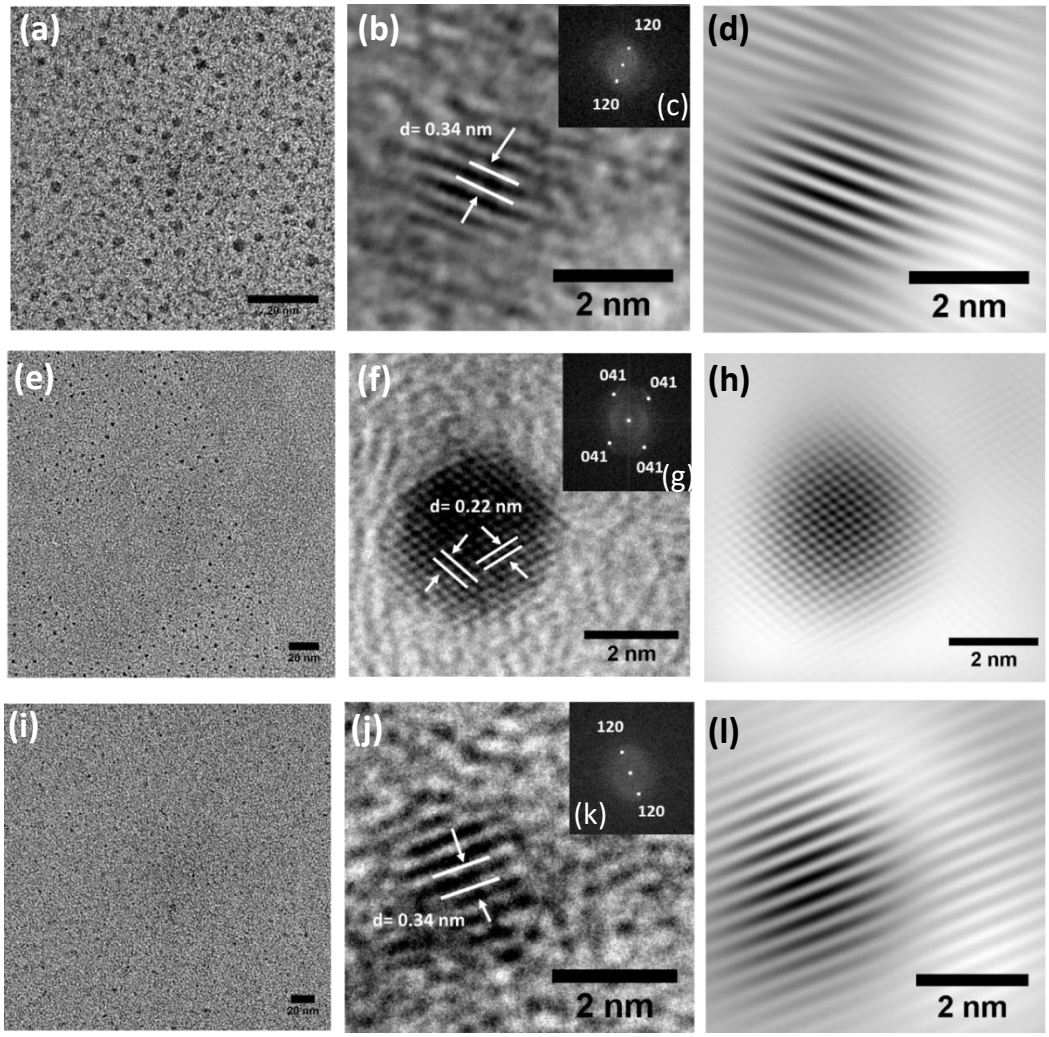

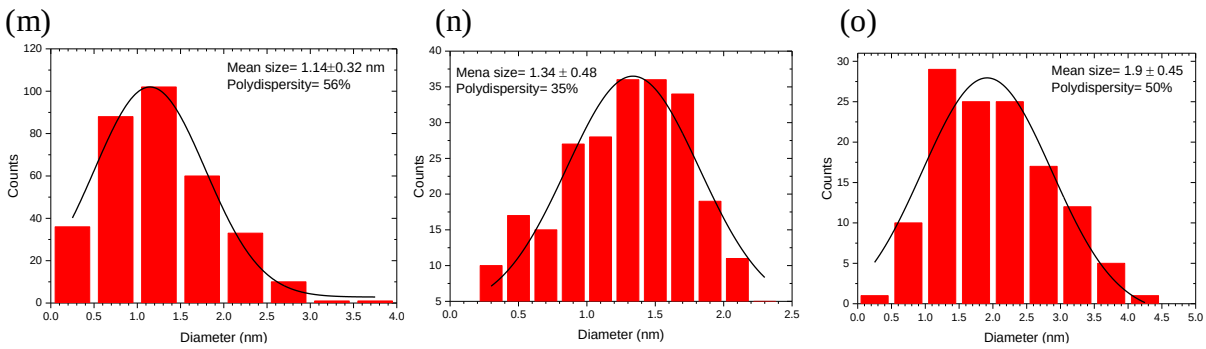

Figure 4- 5. Low, HRTEM and FFT micrographs of SnS-S CQDs synthesised at (a-d) 40⁰ C, (e-h) 50⁰ C and (i-l) 60⁰ C. (m, n, o) Corresponding histograms presenting the degree of size distribution within the three temperature samples, respectively.

Table 4- 3. Optical, emission and elemental composition change of SnS CQDs as a function of reaction temperature.

SnS QDs	λ_{max} (nm)	E_g (eV)	NP size distribution (nm)	Sn:S (atomic %)	Polydispersity (%)	FWHM (nm)
SnS-1	**486**	**2.55**	**1.14±0.32**	**2.2:1**	**56**	**~80**
SnS-2	**528**	**2.35**	**1.34±0.24**	**2.2:1**	**35**	**~60**
SnS-3	**443**	**2.80**	**1.90±0.45**	**1.5:1**	**50**	**~80-100**

4.2.2.2 Effect on optical and emission properties

The graphs in *Figure 4-6* illustrates the 3D PL emission spectra and calculated optical band-gap energy values of SnS-1, SnS-2, and SnS-3. Excitation-dependent emission characteristics are observed in all three samples regardless of reaction temperature differences, which could be related to a wavelength-dependent excitation of a subpopulation of quantum dots due to the samples' polydispersity as observed from the TEM analysis in *Figure 4-5*. Alternatively, a composition tuning of the quantum dots could be in the origin of their emission-dependent characteristics. This hypothesis could be supported by differences in the average atomic ratios

of Sn:S in each sample as seen from the summary results in *Table 4-3* or a combination between changes in both size and composition. Furthermore, the measured band-gap values of samples SnS-1 and SnS-2 are in a good agreement with the measured mean-quantum dot sizes (refer to *Figure 4-5 (m), (n)*), showing size-dependent absorption properties. However, an unexpected trend in sample SnS-3 is observed, which shows widening of the band-gap with increasing the mean-quantum dot sizes as seen in *Figure 4-6 (f)*. The discrepancy in the result could be related to changes in the nucleation kinetics at higher reaction temperatures compared to the other two samples. For example, an increase in the reaction temperature will increase the total thermal energy of the reactant species increasing their reactivity. This will result in faster nucleation of monomers forming a larger concentration of small nuclei that will all hypothetically grow with the same rate into the final QDs compared to the other two samples. However, there is still a continuous formation of new nuclei even at elevated temperatures. This is a result of the multi-step nucleation events due to the lower S reactivity, but the nuclei concentration is significantly higher in sample SnS-3 because of a faster nucleation rate. An attempt to further narrow the size-distribution and study the origin of the excitation-dependent PL emission phenomenon in each sample has been made by a size-selective precipitation (SSP) procedure (144) using a solvent/antisolvent method as described in section 4.3.

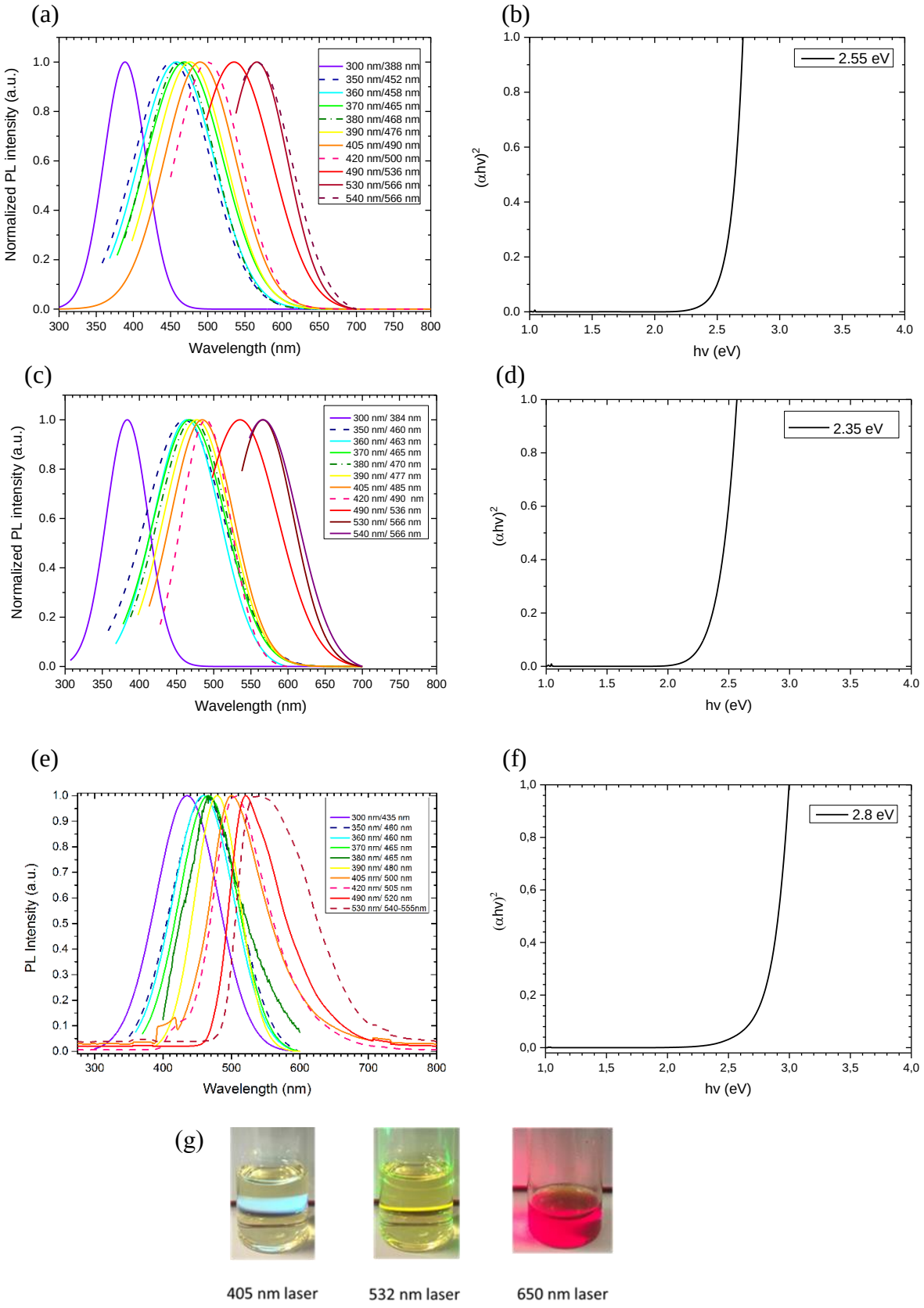

Figure 4- 6. Room temperature 3D PL and band-gap spectra of (a, b) SnS-1, (c, d) SnS-2 and (e, f) SnS-3 CQDs. Wavelength-dependent emission characteristics were observed in all samples regardless of reaction temperature. Samples were excited from 300 nm to 540 nm. (g) An image of SnS-3 CQDs excited at 405 nm, 532 nm, and 650 nm laser wavelength.

4.3 Origin of the excitation-dependent PL emission properties of SnS CQDs

4.3.1 Hypothesis I: Polydispersity of SnS CQDs

Polydisperse samples of QDs with non-uniform size and shape-distribution is a common phenomenon observed in the synthesis of CQDs. However, size-selective strategies have been developed to obtain monodisperse QD samples with the desired size-dependent properties. The first method involves a direct synthesis-based approach, which aims to control the size of the QDs by optimisation of reaction conditions.(145) The second strategy comprises of an alternative post-synthesis precipitation of the QDs by size or shape.(146) The size-separation methods include filtration,(147) gel electrophoresis,(148) chromatography (149) and solvent/antisolvent procedures for achieving size-uniform NCs.

4.3.1.1 Size-selective precipitation (SSP) procedure

4.3.1.1.1 Effect on absorption properties

In this section, a size-separation strategy using a solvent/antisolvent precipitation was performed on samples SnS-1, SnS-2, and SnS-3. Polar acetone solvent (antisolvent) was used for the precipitation of the quantum dots while non-polar hexane solvent (solvent) was used to re-disperse the final colloid of quantum dots. The observations from the UV-Vis spectra after the size-selective precipitation (SSP) step show the existence of two phases of QDs in the original samples as seen in *Figure 4-7.* The measured band-gaps of the three bottom phase samples narrow from 2.55, 2.35 to 2.40 eV for samples SnS-1, SnS-2, and SnS-3, respectively as reaction temperature increases, suggesting an increase in the mean-particle sizes (as shown in *Figure 4-7 (b), (e), (h), respectively*). In contrast to the band-gaps of the bottom phase samples, the calculated band-gaps of the top phase samples widen from 2.95, 2.98 to 2.75 eV for SnS-1, SnS-2 and SnS-3, respectively suggesting that those samples are composed of

smaller-sized QDs compared to the bottom phase samples in each batch. However, from the UV-Vis results and measured optical band-gaps of the three samples, one can notice separate growing events in each phase of the quantum dots. While the band-gaps of the top SnS-1 and SnS-2 samples remain constant regardless of the increase in reaction temperature, the band-gaps of their corresponding bottom phases narrow by 0.20 eV with an increase of the reaction temperature suggesting further size growth. This observation could be attributed to size and composition focusing event in the growing mechanism of the QDs. This hypothesis will be further studied and discussed in section 4.3.1.2.

A second size-focusing or size-growing event was evident in all top phase samples (refer to *Figure 4-7 (b, e, h)*). In top phase SnS-1 and SnS-2 the band-gaps of the two samples are relatively close (constant) and equal to 2.95 eV (see *Figure 4-7 (b)*) and 2.98 eV (see *Figure (e)*), respectively. Top phase SnS-3 undergoes a red-shift in the absorption spectrum and consequently resulting in a narrower band-gap value of 2.75 eV as seen in *Figure 4-7 (h)*. This suggests a further size growth with increasing reaction temperature. However, top phase SnS-1, SnS-2, and SnS-3 samples appear to be composed of multiple populations of quantum dots with close absorption profiles depicted from the PLE spectra in *Figure 4-7 (c), (f), (i),* respectively regardless of the SSP step. Furthermore, the band-gap values of all top phase samples have an average absorption spectrum corresponding to the sum of the two main absorption peaks (~ 400 nm and ~ 450 nm) revealed from the 3D PLE plots. It is important to notice that the 3D PLE spectra of top phase SnS-1 (refer to *Figure 4-7 (c)*) and SnS-2 (see *Figure 4-7 (f)*) samples overlap at λ_{em}= 450-540 nm except their absorption intensities, which increase with increasing reaction temperature. The increase in the absorption intensity in both top phase SnS-2 and SnS-3 could be referred to the higher concentration of QDs formed in the samples with increasing reaction temperature due to faster nucleation events compared to top phase SnS-1.

Furthermore, the 3D PLE spectra of top phase SnS-3 QDs as shown in *Figure 4-7 (i)* illustrates a narrowing of the PLE peaks (λ_{em}= 370-460 nm) compared to the broader range of absorption peaks (λ_{em}= 350-470 nm) depicted in the 3D PLE spectra of SnS-1 (refer to *Figure 4-7 (c)*) and SnS-2 (refer to *Figure 4-7 (f)*). This result could be related to the regular size and composition tuning of the quantum dots with increasing reaction temperature having a higher number of quantum dots with closer absorption profiles. The changes in absorption as a function of size and composition will be further studied and discussed in section 4.3.2.

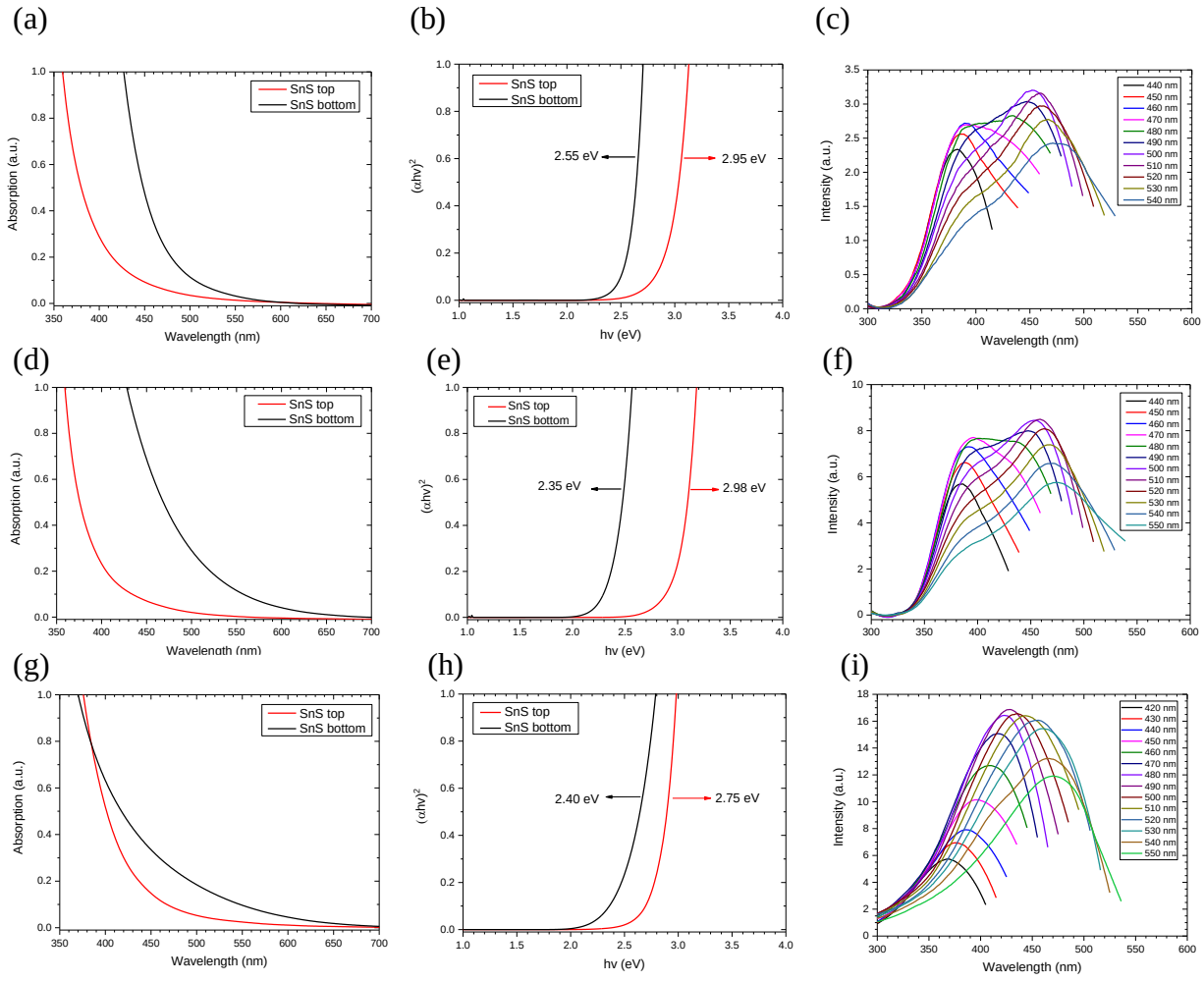

Figure 4- 7. (a, d, g) Optical absorption and (b, e, h) energy band-gap spectra after the size-selective precipitation (SSP) step of SnS-1, SnS-2 and SnS-3 CQDs, respectively composed of bottom (black spectra) and top (red spectra) phase CQDs. (c, f, i) 3D PLE spectra after SSP of top phase SnS-1, SnS-2 and SnS-2 CQDs, respectively.

4.3.1.1.2 Effect on PL emission properties

The 3D PL data in *Figure 4-8* present the achieved size-focusing of the top phase quantum dots after the SSP step. A gradual narrowing of the FWHM of the PL emission peaks at λ_{ex}= 400-460 nm is observed in all three samples (see *Figure 4-8 (b, e, h)*). In sample SnS-1 the narrowing of the PL emission peaks is less significant with a decreasing line width of 2-3 nm with every 10 nm shifts of the excitation wavelength resulting in a total decrease of the FWHM of the PL peaks of 10 nm as seen from the summary graph in *Figure 4-8 (c)*. In SnS-2 (see *Figure 4-8 (f)*) and SnS-3 (refer to *Figure 4-8 (i)*) samples further narrowing of the PL emission peaks of 14 nm and 17 nm, respectively is observed. The size-distribution narrowing with increasing reaction temperature could be related to faster size-focusing events during the growth of the QDs at elevated temperatures. In the colloidal synthesis of QDs the growth process can be divided into two stages—an initial, faster diffusion-controlled growth followed by a slower growth of the QDs through aggregations of the initially formed small NCs .(150) During the diffusion-controlled growth the monomer concentration is high resulting in fast size-focusing events narrowing the overall size-distribution. Therefore, increasing the reaction temperature could result in faster size-focusing events. This trend of size-distribution narrowing is observed from the FWHM of the PL emission peaks in the three samples.

However, the overall FWHM of the highest PL emission peak (λ_{ex}= 460 nm, λ_{em}= 510 nm) in SnS-1 (λ_{ex}= 450 nm, λ_{em}= 500 nm), SnS-2 (λ_{ex}= 420 nm, λ_{em}= 480 nm) and SnS-3 (λ_{ex}= 460 nm, λ_{em}= 520 nm) appears to be broad and equal to 105 nm, 95 nm and 99 nm for SnS-1, SnS-2 and SnS-3, respectively. This phenomenon could be related to achieved optimum surface structure due to small reconstruction changes to the surface of the quantum dots and size-focusing processes during the growing step. Therefore, forming quantum dots with close stoichiometries (Sn:S) or sizes with similar emission properties. Further narrowing of the PL emission peaks at longer excitation wavelengths (λ_{ex}= 460-500 nm) is evident in all three

samples. This result could be due to minor changes to the polydispersity of the QDs in all samples.

The PL emission spectra in *Figure 4-8 (b, e)* supports the data from the 3D PLE measurements (refer to *Figure 4-7 (c, f)*) of top phase SnS-1 and SnS-2 samples showing an overlap in their emission (λ_{ex}= *400-500 nm*) and absorption profiles (λ_{em}= *450-540 nm)* except emission and absorption intensities, which increase with temperatures. These results further support the findings of the performed UV-Vis analysis of samples SnS-1 and SnS-2 as shown in Figure 4-7 (a, b) and (d, e), respectively. However, as seen in *Figure 4-8 (g)* of SnS-3, a 5 nm red-shift (λ_{ex}= 400-450 nm) and a further 10 nm red-shift (λ_{ex}= 460-500 nm) in the PL emission wavelength is observed compared to the lower temperature samples. This result further supports the observed red-shift change in the optical band-gap energy of SnS-3 (2.75 eV) compared to SnS-2 (2.98 eV) and SnS-1 (2.95 eV) (refer to *Figure 4-7 (h), (e), (f),* respectively). These findings could further support my hypothesis of growing bigger quantum dots with narrower band-gaps at higher reaction temperatures.

Furthermore, a PL bright point is reached in all three samples, which is a general phenomenon found in semiconductor quantum dots during the growing step. This is a result of an optimal surface rearrangement of the nanocrystals under given reaction conditions.(151) However, a significant increase of the PL emission intensity in samples SnS-2 and SnS-3 compared to SnS-1 is observed. This could be related to an increase of the optimal surface structure of the quantum dots due to composition changes at higher reaction temperatures. *Figure 4-8 (g)* illustrates that SnS-3 exhibits the highest intensity PL emission compared to SnS-1 and SnS-2 as seen in *Figure 4-8 (a) and (d), respectively*. In particular, the rise in the PL emission intensity of SnS-3 could be due to higher chemical stability as a result of size or chemical composition effects as seen in *Figure 4-8 (g)*. A slightly lower atomic ratio of Sn to S ions could passivate

the surface of the quantum dots better forming an atomic shell around them. The higher number of S ions could eliminate mid-gap states acting as non-radiative charge recombination centres. In conclusion, the obtained results from the 3D PL measurements after the SSP procedure as shown in *Figure 4-8* support the data from UV-Vis absorption (refer to *Figure 4-7 (a, d, g)*) and 3D PLE spectra (see *Figure 4-7 (c, f, i)*), which indicate an increase in the size of SnS CQDs and therefore red-shifting the absorption and emission wavelengths with increasing reaction temperature. These observations support my initial hypothesis of growing bigger QDs with optimised surface chemistries resulting in less surface charge recombination centres at higher reaction temperatures.

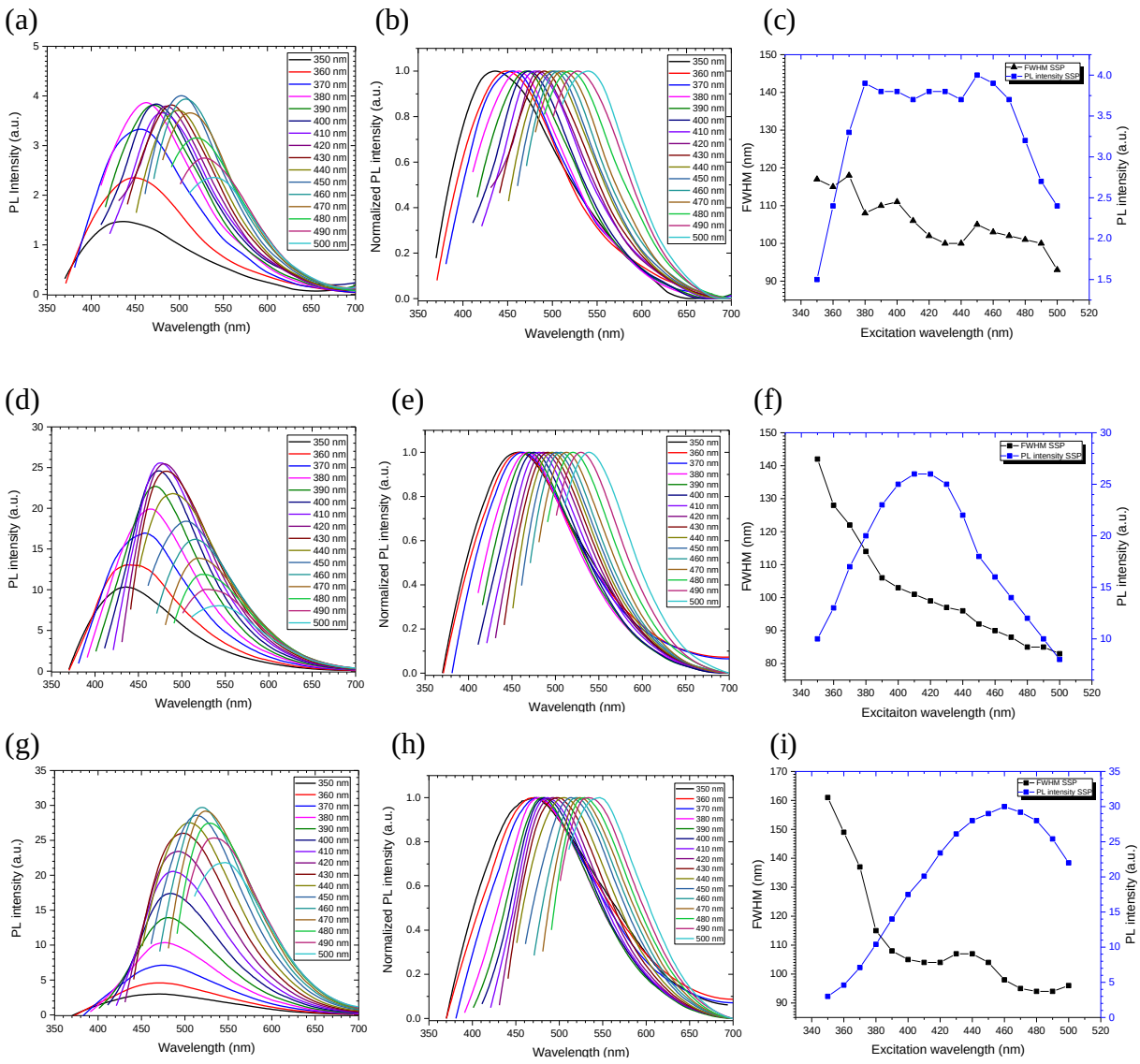

Figure 4- 8. Room temperature (a, d, g) 3D PL and (b, e, h) normalised 3D PL spectra after the size-selective precipitation (SSP) step of top phase SnS-1, SnS-2 and SnS-3 CQDs, respectively, showing multiple populations of QDs as a function of excitation wavelength. (c, f, i) Summary plots of the size-distribution changes after SSP in SnS-1, SnS-2, and SnS-3 CQDs, respectively.

4.3.2 Size-selective precipitation (SSP) of sample SnS-3

4.3.2.1 Effect of SSP on size uniformity (dispersity)

The size-selective precipitation (SSP) procedure resulted in the separation of two phases assigned as a top phase comprised of QDs with a wider band-gap energy and a bottom phase comprised of QDs with a narrower band-gap energy as seen in *Figure 4-9*. The obtained TEM results confirm the polydispersity nature of the two sample phases having a wide range of size-distributions even after the size-narrowing precipitation.

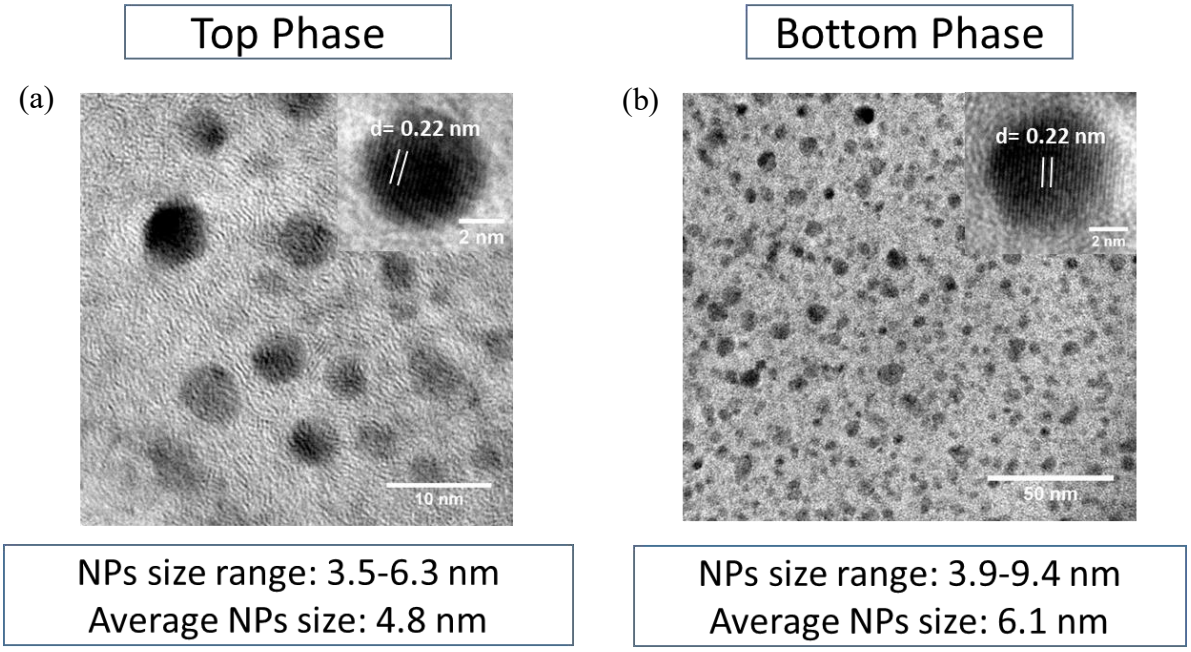

Figure 4- 9. Low and high-resolution TEM (HRTEM) images of SnS-3 CQDs after the size-selective precipitation (SSP) procedure are resulting in the separation of (a) top phase CQDs with a mean QD size of 4.8 nm and (b) bottom phase CQDs with a mean QD size of 6.1 nm.

Table 4- 4. Summary tables of the chemical composition in (a) SnS-top and (b) SnS- bottom phase samples acquired from an EDS analysis.

(a)

Element	Weight %	Atomic %
S K	14.59	38.73
Sn L	85.41	61.27
		Atomic Ratio
Totals	100.00	Sn : S= 1.6 : 1

(b)

Element	Weight %	Atomic %
S K	18.77	46.11
Sn L	81.23	53.89
		Atomic Ratio
Totals	100.00	Sn : S= 1.1 : 1

The summary data from EDX analysis (refer to *Table 4-4)* performed on both samples reveal considerable differences in their elemental compositions. A close examination of the EDS results shows the existence of two main types of SnS QDs—a bottom phase composed of SnS QDs with molar ratios of Sn:S= 1.1:1 (refer to *Table 4-4 (b)*) and a top phase consistent of QDs with Sn:S= 1.6:1 as shown in *Table 4-4 (a)*. The discrepancy in the initial UV-Vis of SnS-3 (2.8 eV) taken before the SSP step (see *Figure 4-6 (f)*) compared to samples SnS-1 (2.55 eV) and SnS-2 (2.35 eV) could be due to an increase in the number of Sn-rich QDs (Sn: S= 1.6:1) compared to the number of stoichiometric QDs (Sn: S= 1.1:1).

The obtained UV-Vis results (see *Figure 4-7 (g)*) indicate that tuning of the molar ratios of Sn and S can result in shifting of the band-gap to shorter wavelengths. Additionally, the observed blue-shift in the absorption of the top phase sample could be due to sulphur vacancies (V_s) within the crystal structure of SnS compared to the bottom phase one. The lower S content could form mid-band gap energy states acting as non-radiative charge recombination centres (or where charge carriers can relax losing some of their absorbed energy before recombining and emitting light) and thus blue-shifting the optical band gap of the material.(152) Alternatively, the blue-shifted absorption could merely be due to the smaller-sized QDs found in the top phase sample compared to the bottom phase one as confirmed by TEM analysis (see *Figure 4-9 (a)*). Continuously increasing the S content during the crystal formation could

increase the mean-particle sizes and narrow the absorption band-gap of the QDs. This hypothesis was further studied, and the results will be discussed in section 4.3.4.

4.3.2.2 Effect of SSP on emission properties

To further explore the effect of the size-selective precipitation (SSP) procedure on the absorption and PL emission properties of SnS QDs, PL studies were carried on the two phase-separated samples. *Figure 4-10 (c)* illustrates that the excitation-dependent emission properties of SnS are characteristic to the QDs of the top phase sample, which show a red-shifted emission with longer excitation wavelengths. In contrast, the PL emission properties of the bottom phase QDs show excitation-independent features with a representative PL emission peak at 378 nm as depicted in *Figure 4-10 (d)*. However, there is a small emission peak in the range of 450-500 nm observed on the 3D PL spectra of the bottom phase QDs. Further analysis using μPL measurements with a high energy pulsed laser source (λ_{ex}= 400 nm) confirms that the low-intensity PL emission is coming from the QDs. This observation could be related to a small concentration of top phase QDs still present in the bottom phase sample after the SSP procedure. However, this separation technique does not allow for a precise precipitation control over sizes. The 3D PLE spectra in *Figure 4-10 (f)* support the 3D PL data (refer to *Figure 4-10 (d))*, which indicate the content of the bottom phase sample being mainly composed of QDs with identical absorption (λ_{ex}= 370-380 nm) and emission (λ_{em}= 378 nm) properties except of a small population of top phase QDs (λ_{ex}= 400 nm, λ_{em}= 475 nm).

Furthermore, the 3D PL spectra support the data from TEM analysis (refer to *Figure 4-9)*, which reveal the separation of two main phases of QDs with different compositions depicted in SnS-3 before SSP. Based on the performed PL analyses before and after SSP, it appears that the Sn-rich nature of the QDs (Sn: S= 1.6:1) in the top phase sample having a greater variety of sizes and stoichiometries compared to the bottom phase QDs having a close stoichiometric

ratio difference (Sn: S= 1.1:1) is in the origin of the excitation-dependent PL emission properties of SnS. However, this hypothesis will be further examined and discussed based on HRTEM studies of multiple single QDs in section 4.3.4.

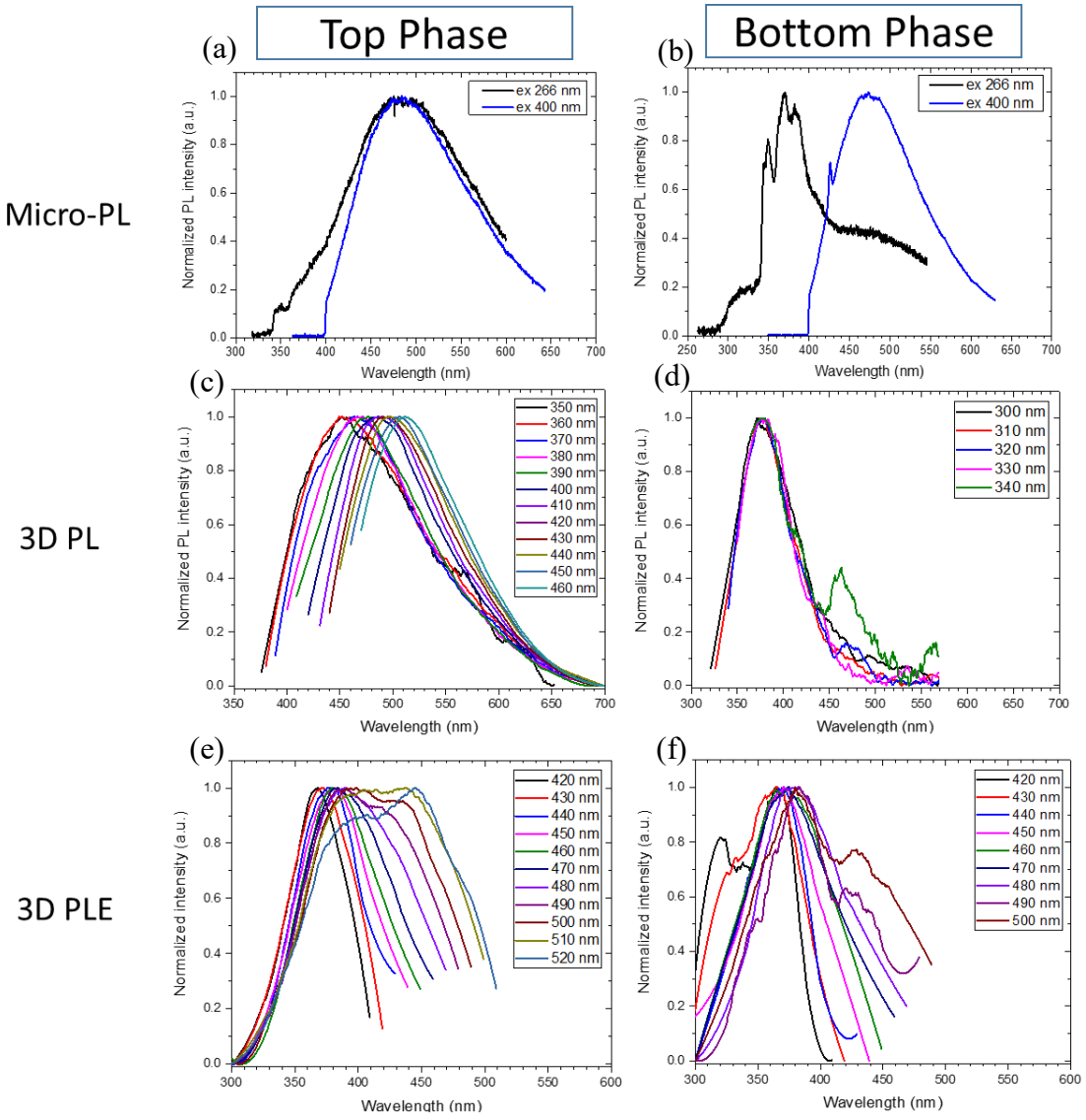

Figure 4- 10. Normalised (a, b) micro photoluminescence (μPL), (c, d) 3D PL and (e, f) 3D PLE analysis of top and bottom phase SnS-3 CQDs.

4.3.2.3 Effect of SSP on chemical properties

To further study the degree of surface passivation on the PL emission properties of the quantum dots, the chemical environment of SnS QDs was verified using FT-IR spectroscopy analysis.

The 600-2000 cm^{-1} region of the IR spectra is shown in *Figure 4-11* where the most emblematic absorption bands are present. The absence of the most characteristic C=O stretching band at 1705 cm^{-1} in the IR spectrum corresponding to the carboxylic acid of the reference pure oleic acid sample indicates the formation of a monolayer surfactant-capped structure of SnS QDs. Also, the absence of the out-of-plane O-H stretching mode at 937 cm^{-1} is noticed. Furthermore, the appearance of a new broad absorption band $(COO)^-$ at 1553 cm^{-1} indicates the formation of a new covalent bond to the Sn atom in SnS QDs observed in other semiconductor systems.(153) The lack of the strong C=O and O-H stretching bands together with the appearance of the new $(COO)^-$ mode all suggest of a dynamic system, in which there is a preferential formation of an Sn-oleate complex.

On the other hand, the appearance of a stronger NH_2 bending mode at 909 cm^{-1} and a weaker NH_2 bending mode at 992 cm^{-1} confirm the oleylamine passivation on the surface of the QDs, which is by literature values. However, the absence of the N-H broad wagging mode at 792 cm^{-1}, which is present in the reference oleylamine sample could indicate a preferential attachment of OLA to the surface of the QDs inhibiting the region of the N-H wagging band (700-900 cm^{-1}).(154) Finally, the observed similarities in the 1465 cm^{-1} absorption mode in both OLA and SnS further confirm the partial surface capping of SnS QDs by OLA. In conclusion, there is a competing reaction between OA, OLA and Sn^{+2} ions resulting in a mixed ligand surface passivation of the QDs. In addition, there are no observable differences between the IR spectra of the top and bottom SnS QDs. This observation indicates that the excitation-dependent emission features of SnS QDs are not ligand induced.

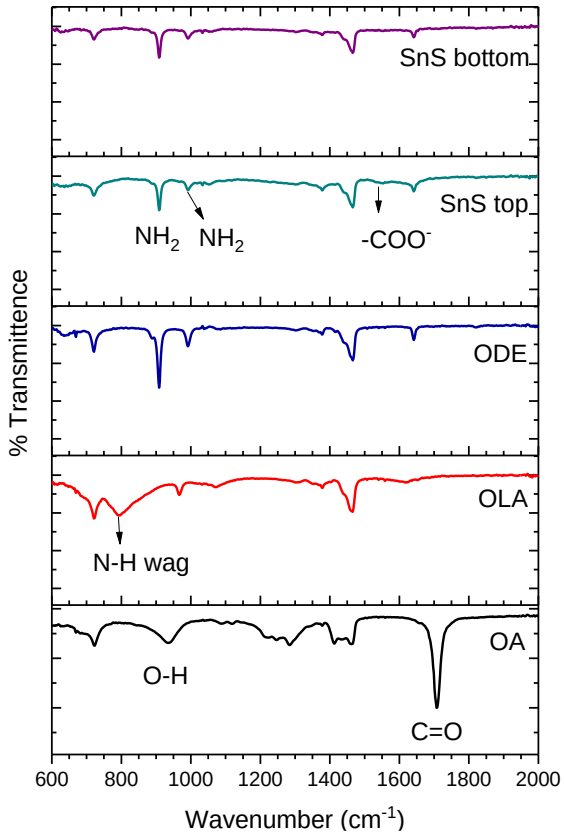

Figure 4- 11. FT-IR spectra of SnS-top and SnS-bottom CQDs compared to the spectra of pure OA, OLA and ODE in the 600 cm^{-1}-2000 cm^{-1} region.

4.3.3 Additional characterization of top phase SnS QDs

4.3.3.1 Temperature-dependent emission characteristics of SnS QDs

4.3.3.1.1 Micro-photoluminescence (μPL) measurements

The dynamics of the charge carrier recombinaition processes of semiconductor CQDs are strongly influenced by the presence of defect energy levels due to surface degradations as a result of their small sizes and high surface-to-volume ratios.(155) The presence of surface disorders forming non-radiative charge recombination channels could decrease the PL emission intensity and overall chemical stability of the QDs. SnS CQDs were measured using μPL spectroscopy on a representative PL emission peak of 430 nm from 5 K to 300 K in order to investigate carriers transport and effect of non-radiative surface traps (localized states) on their electronic properties and structural quality.

Figure 4-12 illustrates the temperature-dependent μPL emission spectra of top phase SnS-3 CQDs. The PL intensity of the emission wavelength significantly increases with decreasing reaction temperature. The intensity of the PL emission smoothly increases up to 90 K. Further decrease in the temperature below 60 K is followed by a drastic increase in the PL emission intensity. The overall PL emission intensity of the quantum dots is increased by twenty times due to elimination or deactivation of non-radiative surface charge pathways.(156)(157) The obtained results indicate that the thermal quenching effects in SnS QDs are significantly high at room temperature.

Additionally, the μPL spectra consist of a single broad PL emission peak (FWHM= 185 nm) regardless of reaction temperature. The broad emission peak could be related to the high polydispersity nature of the sample consisting of various (mixed) subpopulations of QDs with close emission profiles (close sizes or stoichiometries) and thus resulting in a single broad emission peak. However, a pronounced line narrowing (FWHM= 150 nm) and a significant increase in the PL emission intensity are observed when the temperature is decreased in the range of 150-5 K (refer to *Figure 4-13*) On the other hand, the excitonic emission shows a small, monotonic blue-shift and line narrowing as temperature decreases (~ 2.48 eV at 300 K and 2.58 eV at 5 K). The observed 20 nm energy shift in the PL emission wavelength could be related to a temperature-dependent band-gap broadening due to a bond length shrinkage between adjacent atoms decreasing the mean inter-particle distances in SnS QDs.(158) In semiconductor materials, such a phenomenon is commonly observed due to bond length contractions as a function of temperature.(159) The higher the reaction temperature, the higher the chance of expanding the bond length between adjacent atoms within the crystal structure of the material depending on the bonding strength due to higher thermal energy. The obtained results from the temperature-dependent μPL measurements confirm no changes in the PL emission spectra related to defects or organic ligands at shorter wavelengths even at low

reaction temperatures. The observations from the μPL spectra as seen in *Figure 4-12 (a)* and the summary graph in *Figure 4-14* together with the TEM micrographs (refer to *Figure 4-9 (a, b)*) prove the high crystal quality of SnS CQDs with PL emission features corresponding to lattice-related exciton emissions.

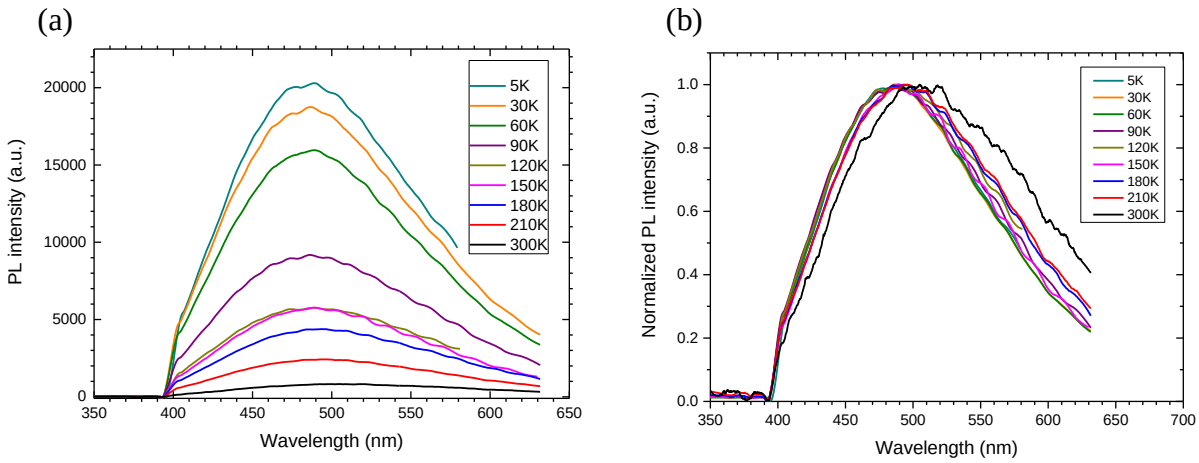

Figure 4- 12. (a) Temperature-dependent and (b) normalized temperature-dependent PL emission properties of top phase SnS-3 CQDs showing variations in QD emission with temperature (up to 300 K).

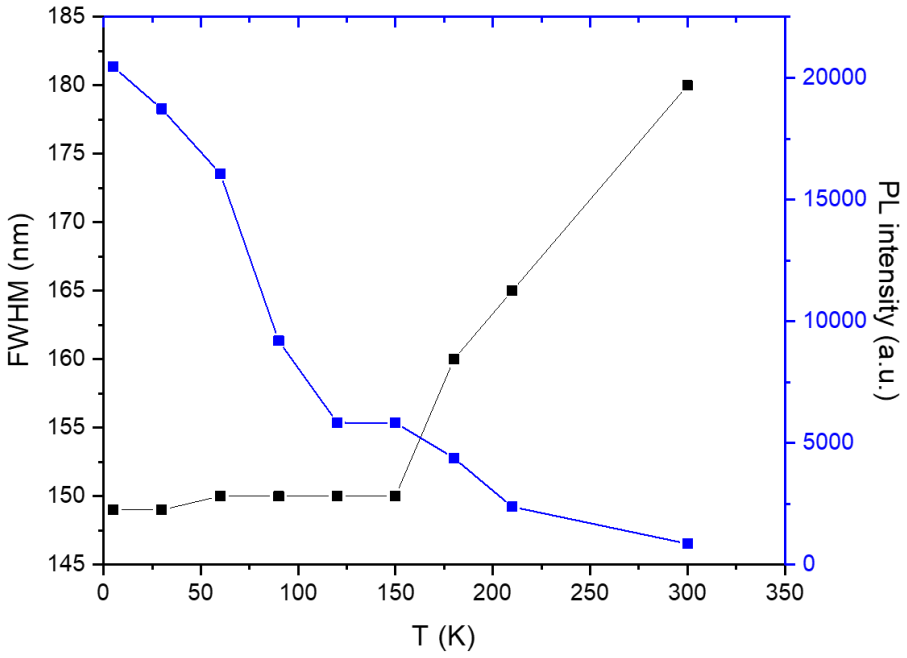

Figure 4- 13. A summary graph is showing the PL emission intensity vs. size-distribution of the CQDs showing a blue-shift, increase in PL emission intensity and decrease in line width of the PL peaks with decreasing temperature from 300 K to 5 K as expected for QD emission.

4.3.3.2 Temperature-dependent emission characteristics

4.3.3.2.1 Time-resolved micro-photoluminescence (TRPL) measurement

Figure 4-14 presents the temperature-dependent time-resolved μPL (TRPL) decay spectra of SnS QDs acquired at illumination wavelengths of λ_{em}= 430 nm and λ_{em}= 480 nm based on the PL emission peak gathered from the temperature-dependent μPL measurements in *Figure 4-12 (a)*. A biexponential decay of excitons is observed in the TRPL decay spectra at both emission wavelengths and all reaction temperatures. The PL decay dynamics consist of two components—a fast and slow component due to non-radiative and radiative charge transfer pathways, respectively. Those components are reversely proportional to one another. When the sample is cooled down below 300K, the PL lifetime of the fast component remains almost unchanged compared to the PL lifetime of the slow component, which becomes even slower with a temperature decrease.

The PL lifetimes gradually increase with decreasing reaction temperature for both PL emission wavelengths. The longest recorded PL lifetimes at λ_{em}= 430 nm and λ_{em}= 480 nm emission wavelengths are 2.7 ns (refer to *Figure 4-14 (c)*) and 3.4 ns (see *Figure 4-14 (d)*), respectively. The difference in PL lifetimes found between the two PL emission wavelengths could be due to the different emission properties of a subpopulation of QDs in the sample. Smaller-sized QDs (λ_{em}= 430 nm) tend to have shorter exciton lifetimes compared to bigger-sized QDs (λ_{em}= 480 nm) because the time required for an e^- and h^+ to recombine after excitation tends to be shorter.(160)(161) For example, the smaller the size of the QDs, the stronger the special overlap of the e^- and h^+ wavefunctions in the confined structure. The decrease of the special distance or diameter of the exciton would result in stronger Coulombic attractions and therefore in a faster recombination rate between the charge carriers.(162) This observation will be further studied and explored in section 4.3.3.3. The obtained results from the temperature-dependent μPL measurements in *Figure 4-12* and the summary graphs in *Figure 4-14* reveal that the non-

radiative charge transfer pathways in SnS QDs are thermally activated processes, which perplex carrier transport by trapping of excitons and thus quenching the PL emission intensity of the quantum dots.

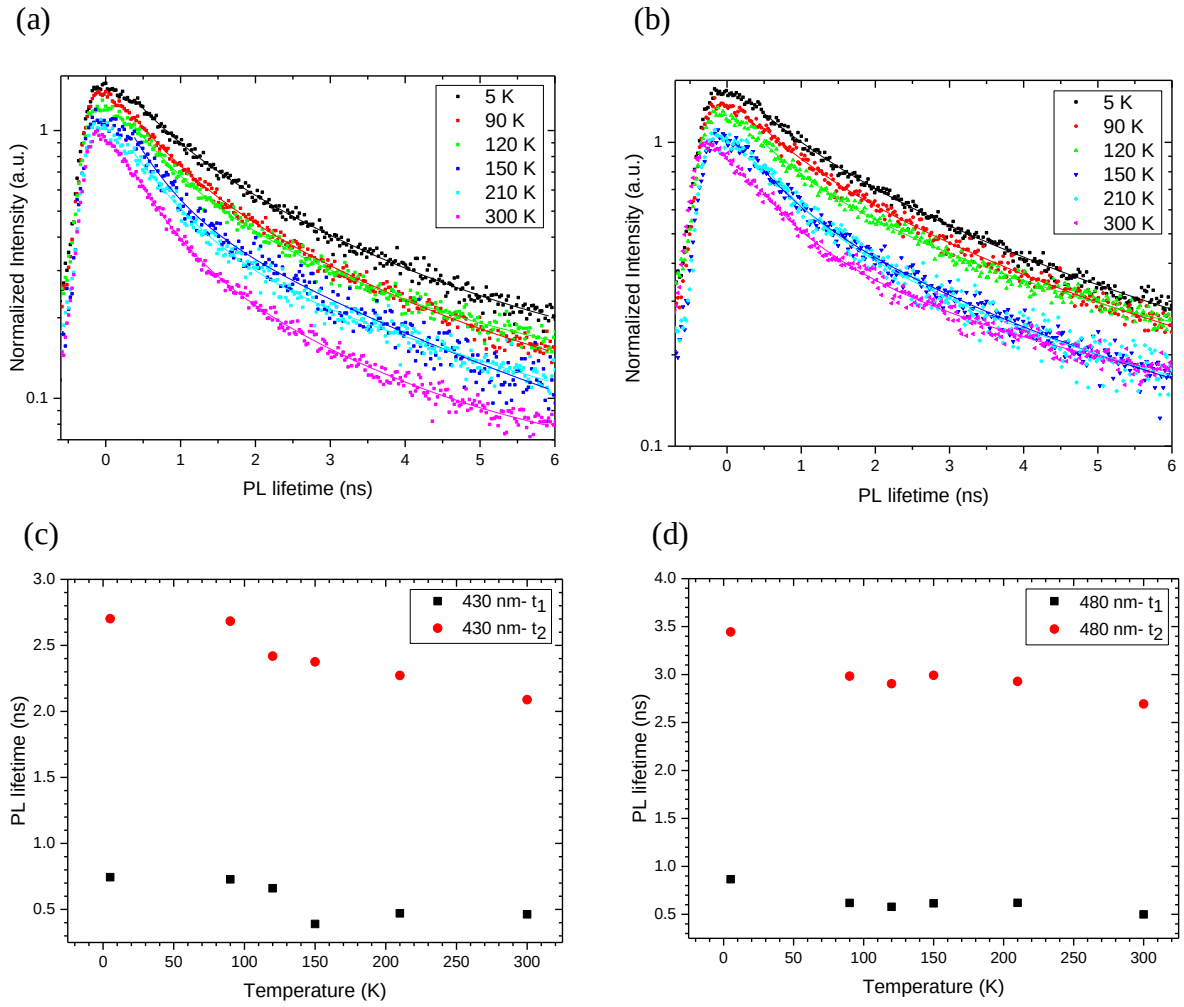

Figure 4- 14. Temperature-dependent time-resolved PL decay spectra of SnS-top CQDs collected from various temperature runs from 5 K to 300 K using (a) 430 nm and (b) 490 nm illumination wavelengths based on the PL emission peaks from the TRPL spectra in Figure 4-12. (c, d) PL lifetime changes as a function of reaction temperature obtained from the fitted PL decay curves in (a) and (b), respectively.

Table 4- 5. Fitted PL lifetimes for the PL decay curves displayed in Figure 4-15.

		SnS 430 nm		SnS 480 nm	
Temperature (K)	Two exp fit	Lifetime t_1 (ns)	Lifetime t_2 (ns)	Lifetime t_1 (ns)	Lifetime t_2 (ns)
5		0.74	2.70	0.86	3.44
90		0.73	2.68	0.62	3.00
120		0.66	2.42	0.58	2.90
150		0.39	2.37	0.61	3.00
210		0.47	2.27	0.62	2.92
300		0.46	2.01	0.50	2.70

4.3.3.3 Wavelength-dependent emission characteristics of SnS QDs

4.3.3.3.1 Time-resolved micro-photoluminescence (TRPL) measurements

The size dependence of the PL lifetimes indicates that the amount of non-radiative surface trap states is related to the size of the quantum dots.(159)(161) The smaller the quantum dot size, the higher its surface-to-volume ratio resulting in a higher number of surface trap states quenching the PL lifetimes. The TRPL measurements in *Figure 4-14* together with the summarised results from the fitted PL decay curves in *Table 4-5* show a progressive increase in the PL decay lifetime as the PL emission wavelength is red-shifted to longer wavelengths. This result could suggest that the increase in the PL lifetimes might be attributed to the reduction of non-radiative surface pathways due to the lower surface-to-volume ratio of SnS QDs as they grow bigger compared to the smaller ones or due to weaker Coloumbic attractions between the charge carriers as a function of increasing exciton's distance.

Furthermore, the polydisperse nature of SnS QDs consistent of a variety of different sizes revealed from the TEM analysis in *Figure 4-10* might contribute to the quenching of the PL excitonic lifetime of the smaller QDs accompanied by an enhancement of the PL decay lifetime of the larger QDs. The proposed electronic energy transfer from small to large SnS QDs is in

a good agreement with the observations that have been made in other works of mixed semiconductor quantum dot materials. (163)(164) In conclusion, the performed 3D PL, 3D PLE and TRPL lifetime measurements (refer to *Figure 4-10 (b)*, *Figure 4-10 (c)* and *4-15*, respectively) all support my initial hypothesis of the origin of the excitation-dependent emission properties of SnS QDs due to sample polydispersity composed of different populations of quantum dot sizes with close absorption and emission profiles.

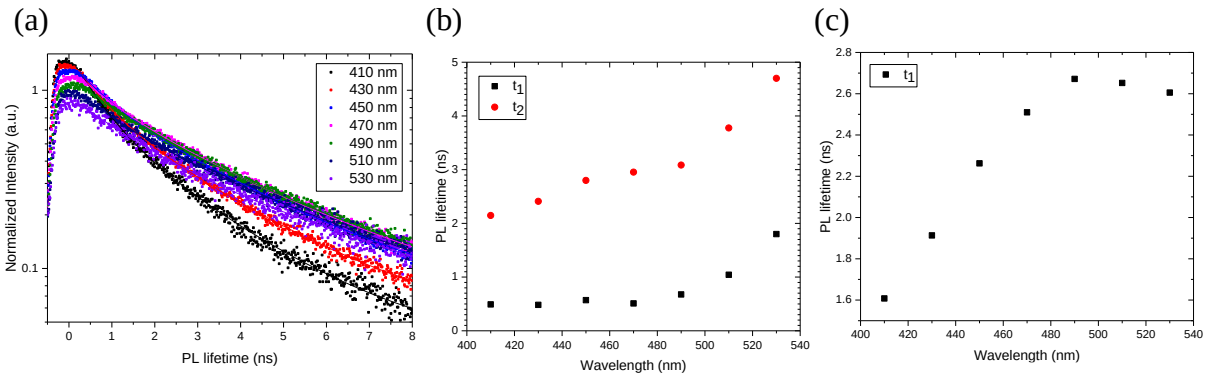

Figure 4- 15. (a) Time-resolved PL (TRPL) decay spectra of SnS-top CQDs. (b) Bi- and (c) mono-exponential fittings of the PL decay curves in (a). Data collected at 300 K.

4.3.4 Hypothesis II: Chemical composition on PL emission properties

4.3.4.1 Stoichiometric control of SnS QDs

In the previous section of this chapter (refer to section 4.3.3), I have shown that the relative size of the quantum dots has a direct effect on their absorption and emission properties. High-resolution STEM/EDS studies on single quantum dots were performed with the aim to reveal any composition changes to the size of the quantum dots. The top phase quantum dots of SnS-3 were studied.

4.3.4.1.1 STEM analysis

Figure 4-16 (a) shows representative low-magnification bright-field (BF) (*Figure 4-16 (a)*) and high-angle annular dark-field (HAADF) STEM images of SnS quantum dots as seen in *Figure 4-16 (b)*. The quantum dots are highly crystalline with clear lattice fringes regardless of their small average sizes of < 5 nm. The resulting quantum dots show a semi-spherical morphology with small shape irregularities. Although the relatively high polydispersity of the sample, the inter-particle distances between the individual quantum dots are well-separated showing minor aggregations, which could be related to the damaging nature of the electron beam at high magnifications.

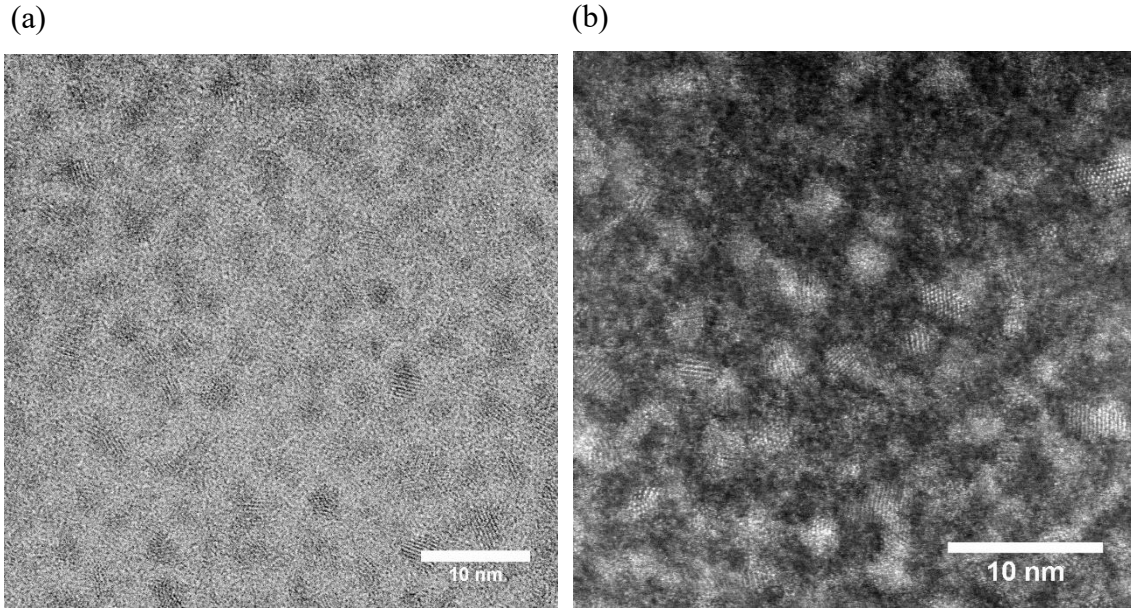

Figure 4- 16. High-resolution (a) BF-STEM and (b) HAADF-STEM micrographs of SnS CQDs. Images obtained with JEOL ARM200 with the help of Dr Judy Kim.

4.3.4.1.2 High-resolution STEM and EDS analyses

An aberration-corrected scanning TEM (STEM) analysis was performed on specially separated single quantum dots. *Figure 4-17* presents BF (*Figure 4-18 (a), (d), (g)*), HAADF (*Figure 4-17 (b), (e), (h)*) and reconstruction (*Figure 4-17 (c), (f), (i)*) HRTEM images of three individual

SnS quantum dots. The quantum dots are crystalline with well-defined lattice distances and highly ordered arrangements of lattice atoms, which provide substantial information for determining the correct crystal phase. The d-spacing values of 0.28 nm, 0.29 nm and 0.34 nm correspond to lattice planes of {111}, {101} and {120} of the orthorhombic (Pbnm) crystal structure of SnS. Furthermore, the HAADF image in *Figure 4-17 (k)* presents that the facets of the quantum dot are formed from the lower index planes composed of higher density of atoms closely packed with respect to one another. (143)(165)(166) The surface atoms in the low-index planes are coordinated to more neighboring atoms and thus result in a lower density of dangling bonds reducing the number of non-radiative charge sites on the surface of the quantum dots. Also, close examination of the crystal lattices reveals no dislocations of atoms or twinning effects resulting in an ordered crystal structure.

STEM-EDS mapping was performed to study chemical changes in the composition relative to the size of the quantum dots. The obtained results from the elemental mapping are summarised in *Table 4-6* revealing the Sn-rich composition of the quantum dots. Although the small composition and size differences observed between the three quantum dots, a trend of increasing size with respect to S content is depicted in all samples. The increase of the S content could be related to an increase of the smallest dimension (shortest width) of the quantum dots. Thus decreasing the overall atomic ratio of Sn to S. Additionally, this finding could suggest that the richness of S atoms plays an essential role in passivating surface atoms and defect states confining the electrons within the QDs.(167) However, to be able to confirm the observed regularity in the results, STEM/EDS analysis will be performed on multiple single quantum dots with the aim of achieving more detailed statistical results.

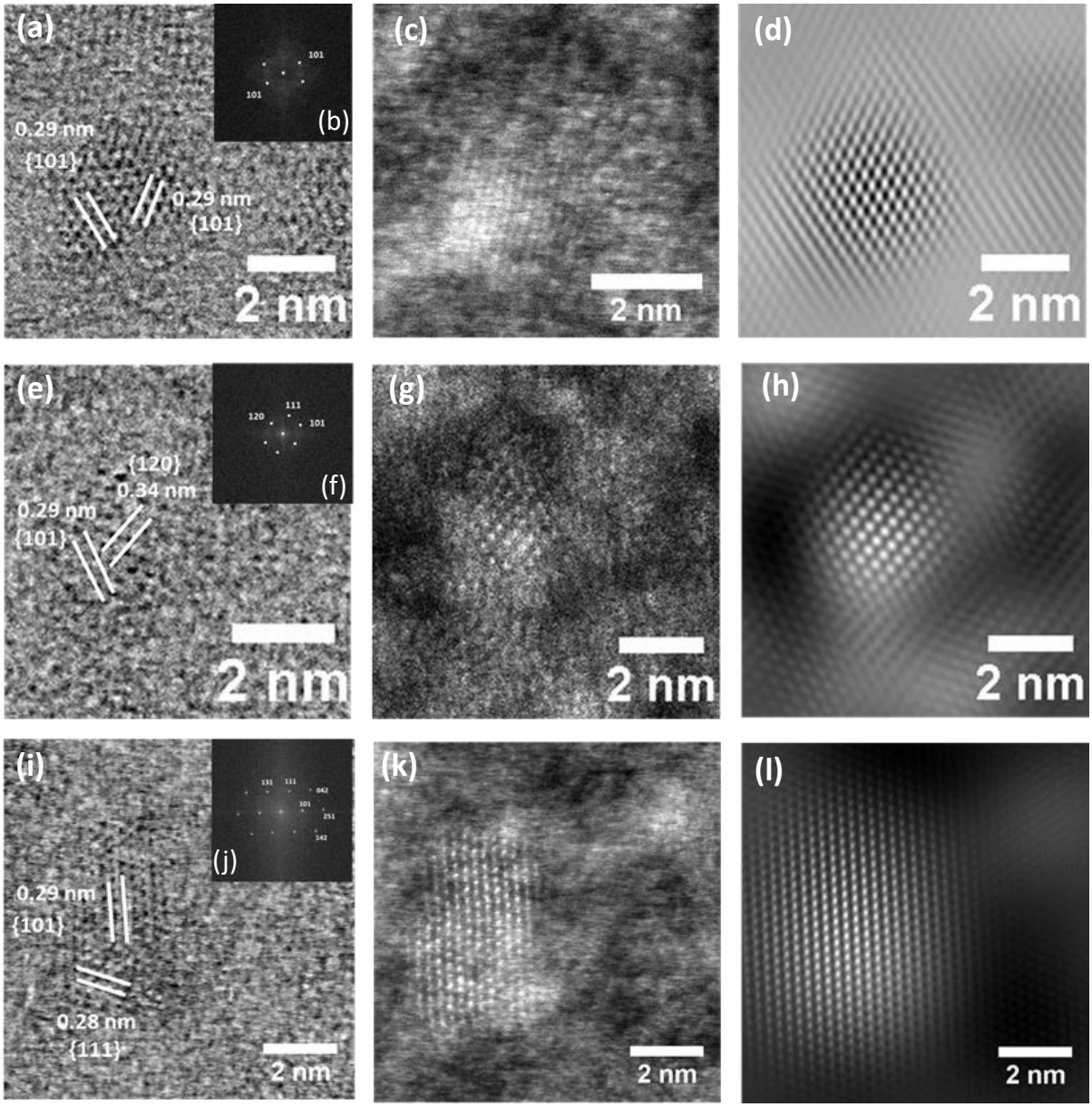

Figure 4- 17. Representative high-resolution (a, e, i) BF/STEM, (c, g, k) HAADF/STEM, (b, f, j) FFT and (d, h, l) reconstruction images of three individual SnS quantum dots. All three QDs appeared highly crystalline nature with clear lattice fringes, which provide enough information for assigning their corresponding crystal phases. The STEM/EDS analysis was carried with JEOL ARM200 with the help of Dr Judy Kim.

Table 4- 6. Summary of the mean quantum dot sizes revealing variations in the atomic ratio of SnS.

SnS QDs	Sn:S (atomic ratio)	Size (nm) Shortest width	Size (nm) Longest width	Aspect ratio (nm)
QD-1	2.5:1	2.0	2.8	2.4
QD-2	2.4:1	2.1	2.8	2.5
QD-3	2.3:1	2.8	3.6	3.2

4.3.4.1.3 STEM/EDS line scan analysis

In this section, high-resolution STEM-EDS line scan analysis was performed on multiple single quantum dots with the aim of acquiring more reliable and accurate information on the elemental distribution over a selected line due to the light nature of S and the much smaller degree of damage caused to the sample.

Figure 4-18 presents a HAADF/STEM image containing multiple quantum dots used for the line scan measurements determining the chemical composition of SnS. An even distribution of Sn and S constituent elements within the crystal structure of the quantum dots is observed from the line measurements of QD 4-12. An example of the even elemental distribution within the quantum dots is presented by the line scan data of QD 9 in *Figure 4-19 (b)*. In contrast, the line scan of QD 3 shows a migration of S atoms towards the edge of the quantum dot (refer to *Figure 4-19 (a)*). This phenomenon could be related to the release of S atoms at early stages from the initial STEM scan before spectra collection due to the higher surface to volume ratio of the quantum dot. However, the obtained results from the line scan spectra reveal a uniform elemental distribution of Sn and S atoms within the majority of the quantum dots.

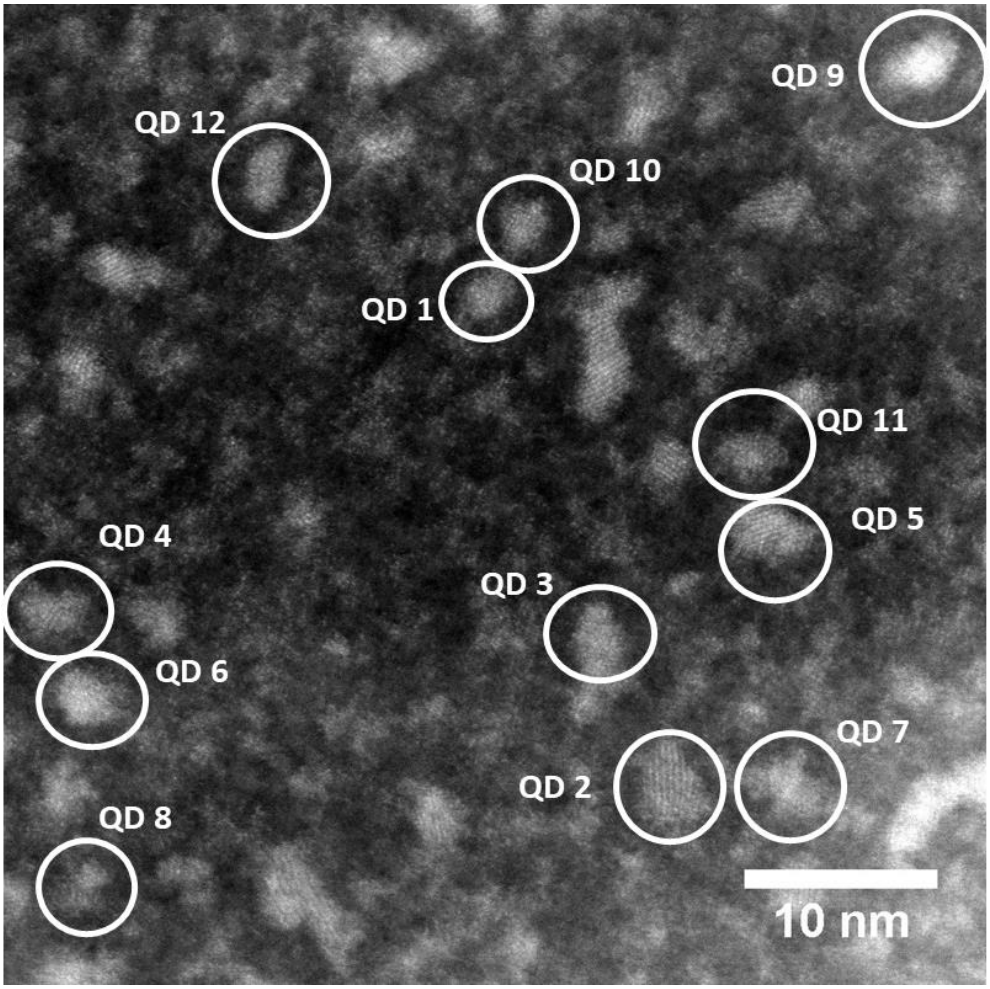

Figure 4- 18. A representative high-resolution HAADF/STEM image is showing the size-distribution of quantum dots within the sample. STEM/EDS line scan measurements were performed on multiple single QDs with the aim to study the changes in their relative size to elemental composition.

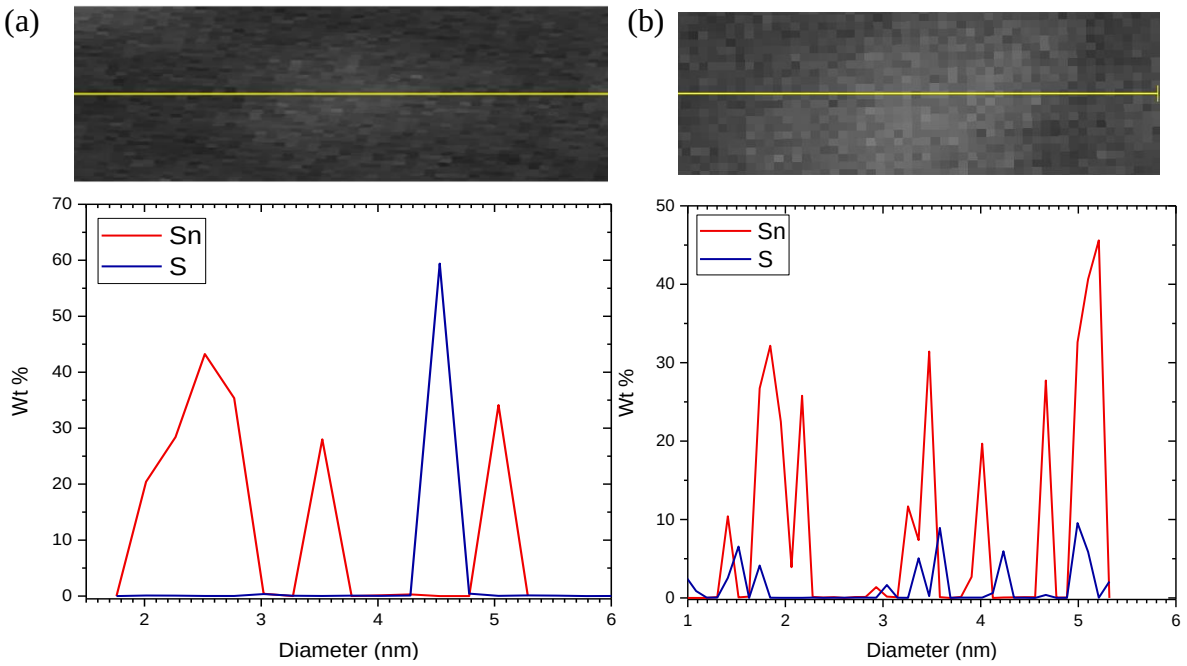

Figure 4- 19. Line scan data of QDs (a) 3 and (b) 9 were compared and discussed as showing essential observations from their chemical composition and elemental distribution within SnS quantum dots.

Table 4- 7. Summary data obtained from the statistical STEM/EDS line scan measurements on multiple individual SnS CQDs.

SnS QDs	Sn:S (atomic ratio)	Size (nm) Smallest dimension	Size (nm) Largest dimension	Aspect ratio (nm)
QD 1	9.0:1	1.7	2.3	2.0
QD 2	6.0:1	2.2	3.5	2.8
QD 3	4.5:1	1.4	2.8	2.1
QD 4	4.0:1	1.6	2.7	2.2
QD 5	3.5:1	2.3	2.4	2.3
QD 6	3.0:1	2.0	2.8	2.4
QD 7	1.8:1	1.7	3.2	2.5
QD 8	1.7:1	2.3	2.8	2.6
QD 9	1.5:1	2.3	3.6	2.9
QD 10	1.2:1	2.3	2.8	2.6
QD 11	1.0:1	2.4	3.6	3.0
QD 12	0.7:1	1.8	3.7	2.8

4.3.4.1.4 Discussion

Interestingly, regardless of the damaging nature of the STEM analysis due to the high voltage of the electron beam, one can notice a clear trend of an increasing quantum dot size with an increasing S content. *Figure 4-20 (a)* illustrates that the small dimensions of the quantum dots are showing less S at low aspect ratios and a progressive increase with increasing the S content increasing the overall size of the quantum dots. However, line scan 2 (QD 2, circled in red) appears to be an outlier, which does not follow the trend line through the rest of the data points in *Figure 4-20 (b)*. This observation could be explained by the higher degree of quantum dot orientation and exposure to the electron beam compared to the other quantum dots in the sample together with the high imaging resolution, which might have contributed to the sputtering of S

atoms out of the quantum dot during the scanning. QD 9 and 12 show minor deviations from the trend line, but their values are within a reasonable error.

In conclusion, the results from the HRTEM-EDS line scans in *Table 4-7* together with the size measurements of the quantum dots from the HRTEM images as seen in *Figure 4-18* confirm my initial hypotheses that the excitation-dependent PL emission properties of SnS CQDs are both size and composition dependent. The elemental composition of the smaller-sized quantum dots has a higher Sn to S atomic ratio giving rise to a PL emission at shorter wavelengths, which is red-shifted to longer wavelengths with an increase of the S content and overall aspect ratio of the quantum dots.

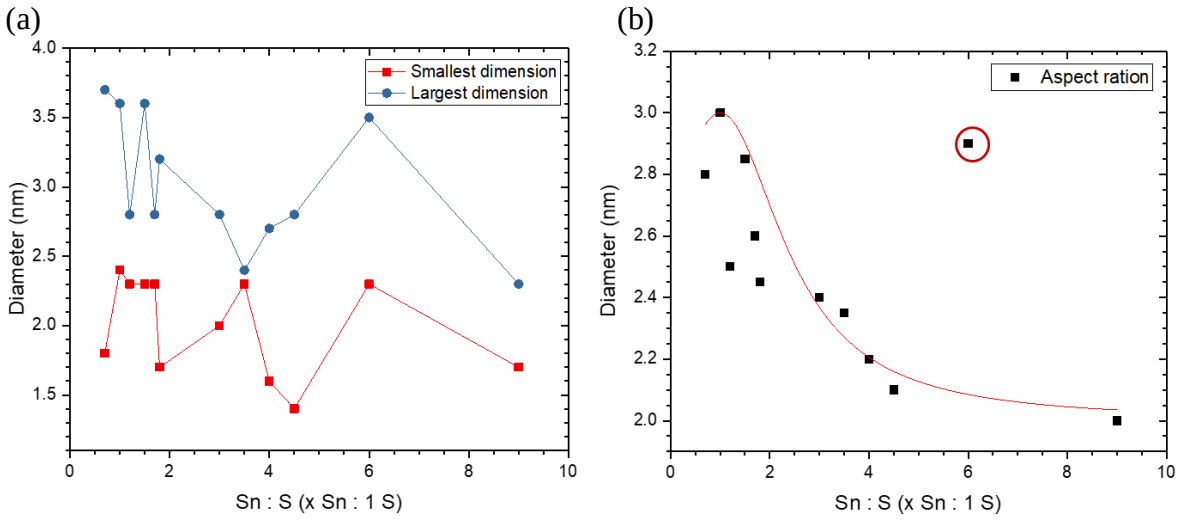

Figure 4- 20. Summary plots showing changes in the (a) smallest dimension and (b) a gradual increase of the aspect ratios of SnS quantum dots with increasing S content generated from the line scan data in Table 4-7.

4.3.5 Hypothesis III: Effects of organic ligands and organometallic compounds

4.3.5.1 Effect on optical properties

In this section, I will examine the effect of organic ligands and organometallic complexes on the optical and emission properties of SnS QDs. *Figure 4-21 (a)* shows the absorption spectra of organic ligands (OA and OLA) and Sn-oleate complexes compared to SnS QDs. According to the UV-Vis graph, there is a significant difference in the absorption profiles of the organic compounds and organotin complexes to SnS QDs. The absorption of OA and OLA organic ligands are relatively close to the organotin complex, which was formed by a chemical reduction of a Sn-based precursor in the presence of both aforementioned organic ligands using same reaction conditions used for the synthesis of SnS QDs except the injection of the S precursor. On the other hand, the prominent red-shift in the absorption of SnS QDs compared to the organotin complex, for example, implies composition and size-related changes during the growth of the QDs.

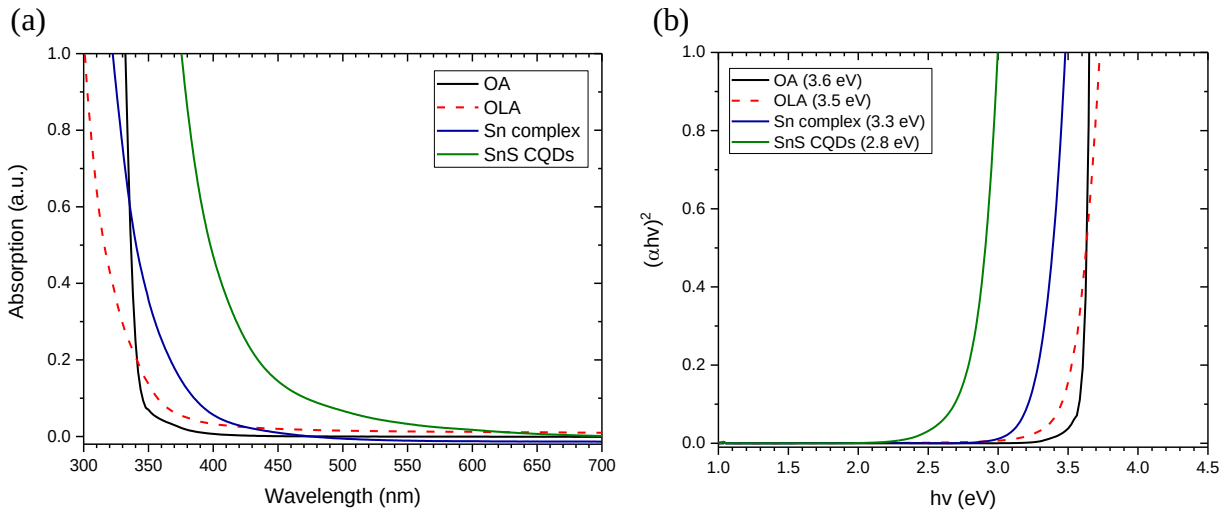

Figure 4- 21. (a) UV-Vis absorption spectra and (b) band-gap energy values of SnS CQDs compared to organic ligands and organotin complexes revealing changes in their absorption profiles.

4.3.5.2 Effect on emission properties

The 3D PL and 3D PLE spectra as seen in *Figure 4-11* support the results obtained from the UV-Vis analysis (refer to *Figure 4-21)* which show red-shifting of the emission and absorption of SnS with size compared to organotin complexes and organic ligands. Furthermore, the PL spectra of SnS CQDs and Sn-oleate complexes as seen in *Figure 4-22 (a)* and *(c)*, respectively appear to be composed of a variety of PL emission peaks with a range of different wavelengths. However, there is a significant difference in their absorption and emission wavelengths as well as PL emission intensity, which is seen from the PL excitation contour maps in *Figure 4-23.* Additionally, the 3D PLE spectra of SnS CQDs in *Figure 4-22 (b*) present three main PLE peaks at 370 nm, 430 nm, and 490 nm, which suggest that different species in SnS CQDs give rise to PL properties with close emission wavelengths. In contrast, the 3D PL spectra of organotin complexes in *Figure 4-22 (c)* follow the PL emission profile of OLA (refer to *Figure 4-22 (g))* resulting in a monotonous PL red-shift followed by a drastic decrease of the PL intensity at longer excitation wavelengths compared to SnS. This observation could suggest that both organic ligands and organotin complexes are not in the origin of the excitation-dependent emission properties of SnS CQDs. It could be suggested that this phenomenon is induced by different subpopulations of QDs with close size-dependent emission characteristics.

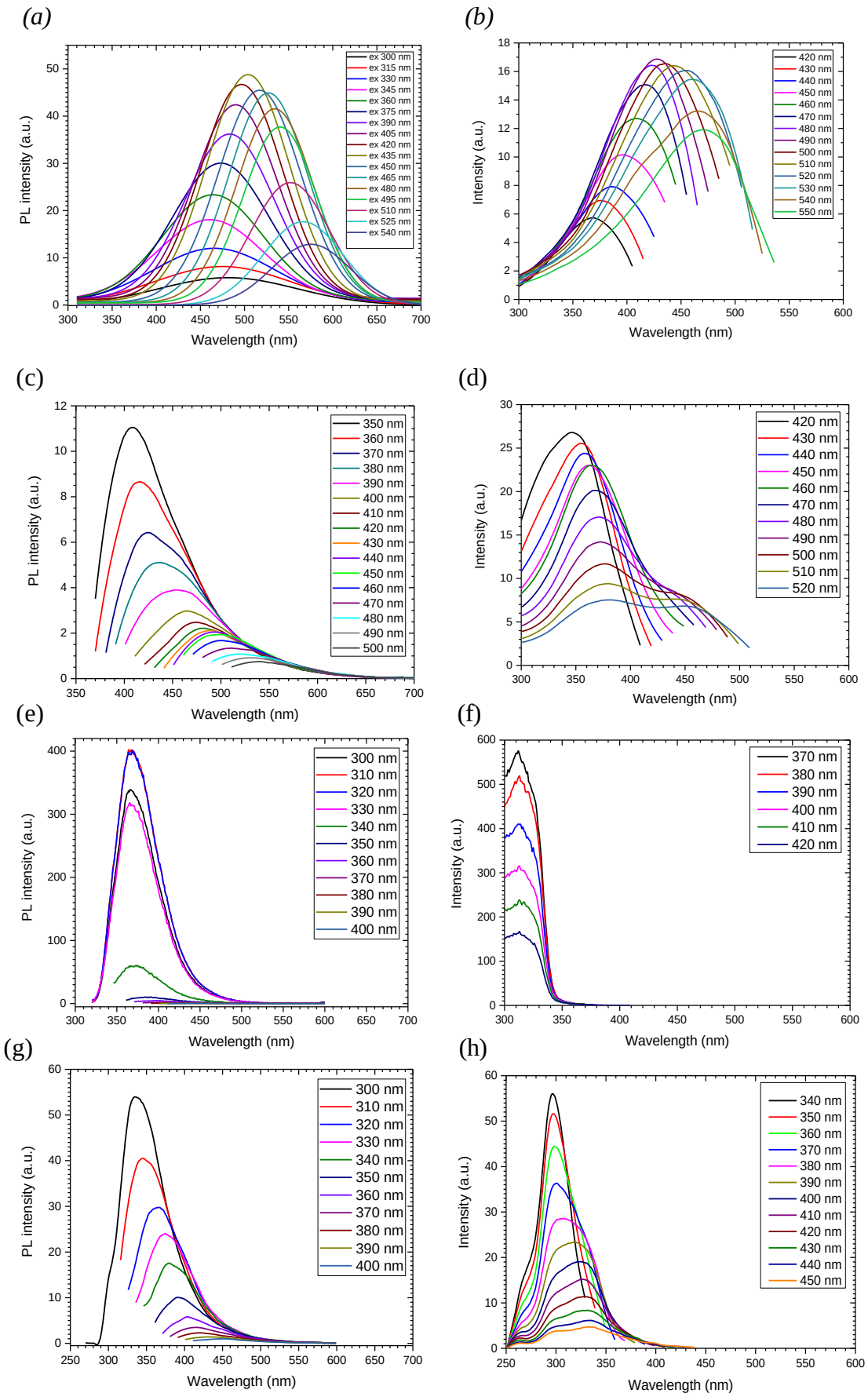

Figure 4- 22. (a, c, e, g) 3D PL emission and (b, d, f, h) 3D PLE spectra of SnS CQDs, organotin complexes, OA and OLA ligands, respectively.

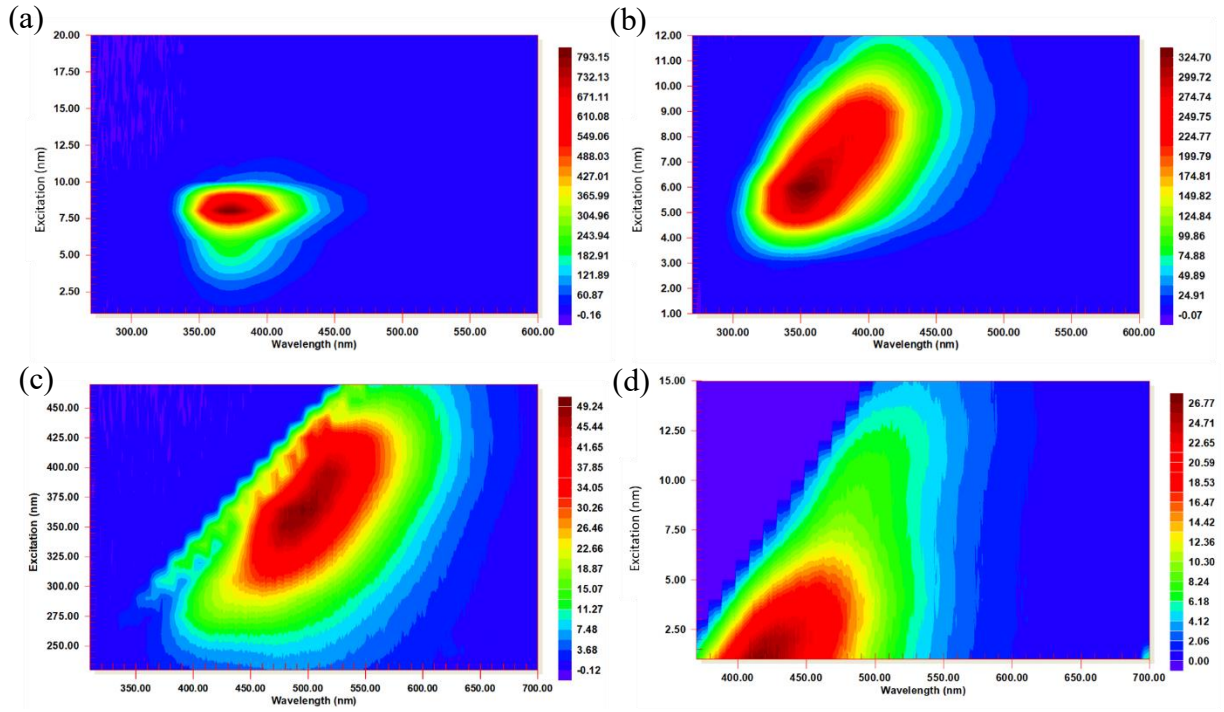

Figure 4- 23. PL excitation contour plots of (a) OA, (b) OLA, (c) SnS CQDs and (d) Sn-oleate complexes. PL emission intensity increases from blue to green to red depending on the PL emission characteristics of the sample.

4.3.5.3 Temperature-dependent PL emission properties of organic ligands compared to SnS QDs

4.3.5.3.1 Time-resolved micro-photoluminescence (TRPL) measurements

Temperature-dependent TRPL measurements were also carried on organic ligands to study their electronic energy transfer in comparison to SnS QDs. *Figure 4-24* shows an evident difference in the PL emission spectra of the three samples with decreasing reaction temperature (from 300 K to 5 K). The increase in the PL emission intensity implies an effective reduction of non-radiative charge recombination pathways as a function of decreasing temperature. However, in the case of SnS QDs, the PL emission spectra (refer to *Figure 4-24 (a)*) do not show significant changes rather than a small, monotonic blue-shift in the PL emission wavelength with decreasing reaction temperature. In comparison, the PL emission spectra of both OA and OLA (see *Figure 4-24 (b)* and *(c)*, respectively) undergo a noticeable modification

by blue-shifting the PL emission to shorter wavelengths at lower temperatures. The PL peak of OA becomes considerably narrower resulting in an overall line width decrease of 90 nm (FWMH= 35 nm) at 5 K.

Interestingly, the PL spectra of OLA undergoes an inverse transformation compared to the PL spectra revealed for OA. The PL spectra of OLA appear to be composed of three separate PL peaks with close emission wavelengths at $\lambda_{em=}$ 420, 460 and 510 nm (λ_{ex}= 400 nm). These results could suggest multiple optical transitions revealed by the introduction of new energy states in OLA, which appeared to be hidden due to non-radiative recombination centres at room temperature. However, a closer investigation of the phenomenon is required to understand and confirm the optical processes happening in OLA at lower temperatures.

Furthermore, the TRPL measurements in *Figure 4-25* reveal much longer PL lifetimes for both SnS QDs and OA at lower reaction temperatures compared to OLA. This discrepancy in the PL decay lifetimes of OLA could originate from the multiple PL peaks present in the sample at low temperatures. The PL decay lifetimes become slightly faster as temperature goes down probably due to the introduction of new energy states (extra PL peaks) at longer PL emission wavelengths. They could provide alternative charge recombination pathways by increasing the rate of charge recombination resulting in faster PL decay lifetimes.

In the case of OA, the PL decay lifetimes become slightly slower as temperature goes down. This observation could be due to the elimination of defect energy levels in the electronic structure of OA, which are thermally activated and therefore significantly altering the charge recombination pathways at higher reaction temperatures.

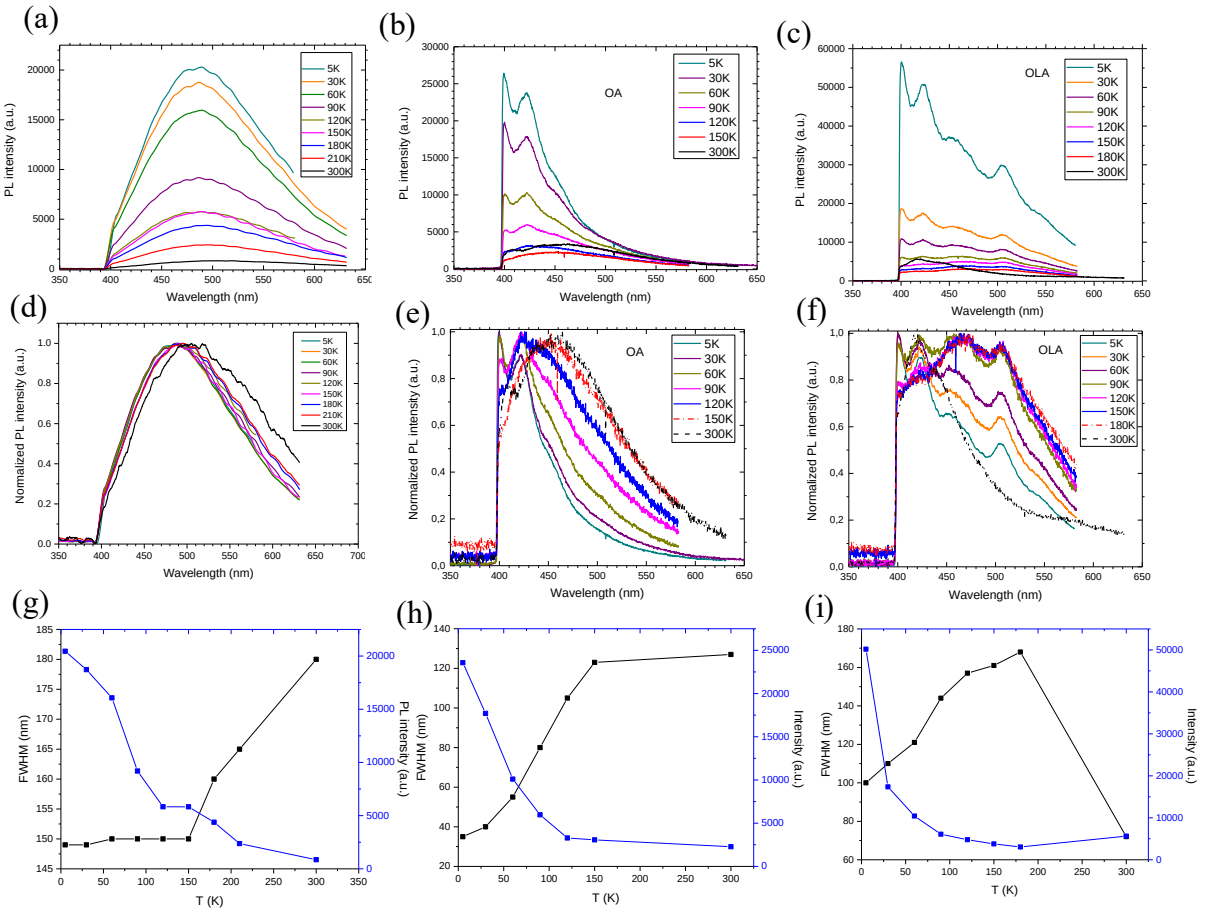

Figure 4- 24. (a, b, c) Steady-state PL spectra, (d, e, f) normalized steady-state PL spectra and (g, h, i) summary plots of SnS CQDs, OA, and OLA, respectively showing a blue-shift and increase in PL emission intensity and narrowing of the size-distribution as a function of decreasing temperature. Data was collected at reaction temperatures between 5 K and 300 K.

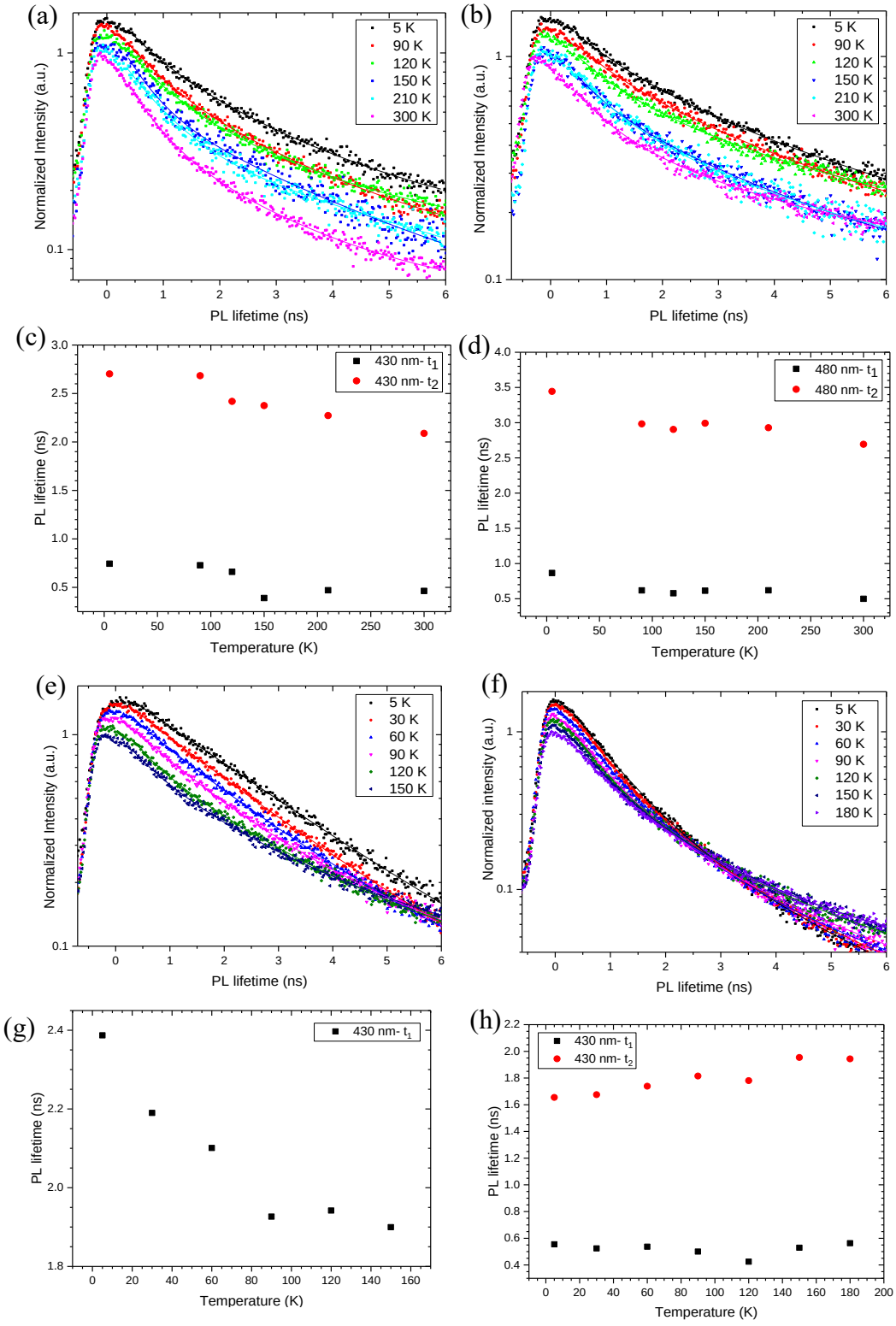

Figure 4- 25. Time-resolved PL decay spectra of (a, b) SnS QDs collected at an illumination wavelength of 430 nm and 480 nm; (e) OA illuminated at 430 nm and (f) OLA illuminated at 430 nm and 480 nm. The curve fittings are based on bi-exponential decay for (c, d) SnS CQDs and (h) OLA and mono-exponential PL decay for (g) OA. Data was collected from 5 K to 300 K (with 30 K increments).

Table 4- 8. Summary results of the fitted PL decay curves in Figure 4-24 showing comparing the obtained PL lifetimes of SnS CQDs to OA and OLA organic ligands.

		SnS 430 nm		SnS 480 nm		OLA 430 nm		OA 430 nm	
Temperature (K)	Two exp fit	Lifetime t_1 (ns)	Lifetime t_2 (ns)	Lifetime t_1 (ns)	Lifetime t_2 (ns)	Lifetime t_1 (ns)	Lifetime t_2 (ns)	Single exp fit	Lifetime t_1 (ns)
5		0.74	2.70	0.86	3.44	0.55	1.65		2.39
30		--	--	--	--	0.52	1.68		2.20
60		--	--	--	--	0.54	1.73		2.10
90		0.73	2.68	0.62	3.00	0.50	1.81		1.93
120		0.66	2.42	0.58	2.90	0.42	1.78		1.94
150		0.39	2.37	0.61	3.00	0.53	1.95		1.90
180		--	--	--	--	0.56	1.94		--
210		0.47	2.27	0.62	2.93	--	--		--
300		0.46	2.01	0.50	2.70	0.61	--		--

4.3.5.4 Wavelength-dependent PL emission properties of organic ligands and organotin complexes compared to SnS QDs

4.3.5.4.1 Time-resolved micro-photoluminescence (TRPL) measurements

The small change of ~ 0.2 ns in the PL lifetime of OA and OLA ligands as seen in *Figure 4-26* and *Figure 4-27*, respectively might be a result of a small distribution of organic molecules with close PL lifetimes present in the samples. The effect seems a lot more significant in the SnS sample due to the size-distribution changes compared to the Sn-oleate and organic ligand samples, which consist of only organic molecules. However, the organic molecules might exist in a variety of conditions as a function of temperature. Their interactions with solvents could result in different bond-lengths and bond angles adjusting the overall energy levels of the ligands altering their PL decay times at different emission wavelengths. Additionally, the ligands might have a similar band structure to QDs with discrete energy levels, which could be giving rise to different emission wavelengths and consequently different PL lifetimes. However, this hypothesis requires further investigation and analysis.

In addition, a small increase in the PL lifetimes up to 470 nm emission wavelengths is observed. This is followed by a decrease of the PL lifetimes at 490 nm and 510 nm in both OA and OLA. However, in SnS a continuous increase of the PL lifetime reaching a maximum value of 4.7 ns at λ_{em}= 530 nm is evident. This result further supports our hypothesis of the size-dependent PL emission of SnS QDs compared to passivation ligands and organometallic complex, which are consistent of organic molecules and organometallic complexes only and do not possess such size-dependent features.

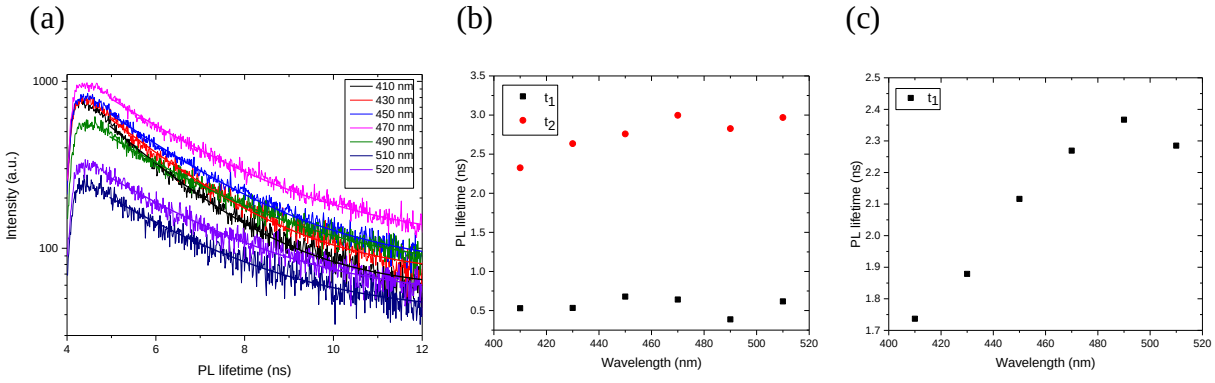

Figure 4- 26. Wavelength-dependent (a) TRPL decay curves of OA. PL lifetime plots of (b) bi-exponential and (c) mono-exponential curve fittings. Data collected at 300K and PL emission wavelengths ranging from 410 nm to 510 nm.

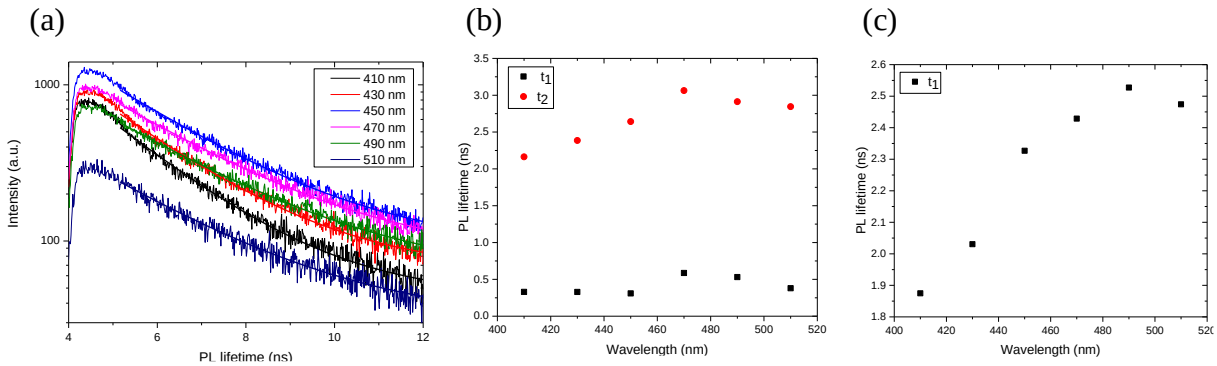

Figure 4- 27. Wavelength-dependent (a) TRPL decay curves of OLA. PL lifetime plots of (b) bi-exponential and (c) mono-exponential curve fittings. Data collected at 300K and PL emission wavelengths ranging from 410 nm to 510 nm.

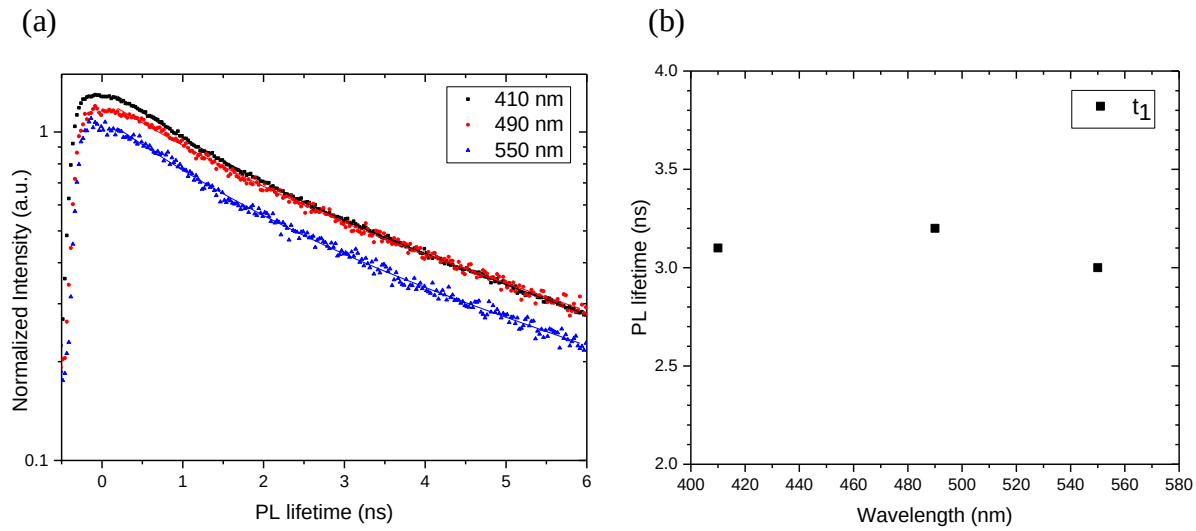

Figure 4- 28. Wavelength-dependent (a) TRPL decay curves of organotin complexes measured at PL emission wavelengths of 410 nm, 490 nm, and 550 nm.

Table 4- 9. Wavelength-dependent TRPL lifetimes of SnS CQDs with respect to OA, OLA and organotin complexes.

		SnS		OA		OLA		Sn-complex	
Wavelength (nm)	Two exp fit	Lifetime t_1 (ns)	Lifetime t_2 (ns)	Lifetime t_1 (ns)	Lifetime t_2 (ns)	Lifetime t_1 (ns)	Lifetime t_2 (ns)	Single exp fit	Lifetime t_1 (ns)
410		0.49	2.15	0.52	2.32	0.33	2.16		3.1
430		0.48	2.41	0.53	2.63	0.32	2.38		
450		0.57	2.80	0.67	2.65	0.30	2.64		3.1
470		0.50	3.00	0.64	2.99	0.58	3.06		
490		0.67	3.08	0.38	2.82	0.53	2.91		3.2
510		1.04	3.80	0.61	2.96	0.37	2.84		
530		1.85	4.70	--	--	--	--		3.0

4.3.6 Conclusions

In conclusion, this chapter presents a new synthetic method for producing high-quality SnS CQDs using a low reactivity S precursor and low injection temperatures. By controlling the

precursor molar ratios and reaction temperature, SnS CQDs with novel excitation-dependent PL emission properties covering the whole visible electromagnetic spectrum have been synthesised. A systematic study of the origin of their PL emission features has been precisely examined. STEM/EDS reveals the high polydispersity nature of SnS CQDs composed of a variety of quantum dot sizes with different stoichiometries (Sn:S) suggesting their size and composition-dependent emission properties. Furthermore, TRPL measurements reveal size-dependent PL lifetime characteristics of SnS CQDs with a gradual increase from 2.2 ns to 4.7 ns with increasing PL emission wavelength. Finally, the obtained results all agree to one another revealing that the multi-colour emission properties of SnS CQDs are both size and composition-related phenomena, which can be influenced by the degree of surface coverage.

Chapter 5 Strong quantum confinement effect in PVP-encapsulated SnS CQDs

This chapter presents an alternative surface passivation procedure for the fabrication of high-quality SnS CQDs with novel optical and emission properties demonstrating size-dependent absorption and emission spectra. Dr Tim Puchtler from the Department of Physics, University of Oxford, assisted with the temperature-dependent μPL and time-resolved μPL (TRPL) measurements. XRD and XPS analyses were performed with the help of Philip Holdway.

5.1 Introduction

In the previous chapter, I presented an optimised synthetic procedure for the fabrication of high-quality SnS CQDs with novel multi-colour emission properties. I proved that by tuning reaction conditions such as precursor types and reaction temperature all influenced the observed PL emission features of SnS due to both quantum dot size and stoichiometry differences between Sn and S atoms within the crystal structure of SnS. In chapter 5, I will apply an alternative surface passivation strategy for the synthesis of chemically stable and highly luminescent SnS CQDs. To do so, I will replace the organic ligands in the synthesis with a polymer alternative as a new capping agent. This study aims to show that surface passivation is another critical factor in achieving good chemical stability by reducing non-radiative charge recombination pathways obtaining improved optical and emission features of SnS CQDs.

5.2 Surface tuning/passivation

5.2.1 Principle

As discussed in chapter 2, there are various surface passivation strategies employed in the synthesis of metal sulphide quantum dots maintaining their optimum brightness and improved photostability. Among the majority of reports describing these synthetic methods, organic polymer shell passivation has been shown to produce highly stable, monodisperse quantum dots with efficient luminescent properties.(168) Saravanan *et al.* demonstrated in their work the synthesis of highly monodisperse surface-modified PVP-capped CdS QDs with enhanced blue PL emission.(169) Such coating shell reduced the number of surface trap states related to the green PL emission of bare CdS NPs (non PVP-capped) increasing the probability of exciton recombination within the core material.

5.2.2 Role of PVP in the synthesis of SnS CQDs

Polyvinylpyrrolidone (PVP) is one of the most commonly used organic polymers for the (colloidal) synthesis of nanomaterials providing high photochemical stability. PVP was found to be as a good alternative to the variety of organic surfactants used in the colloidal synthesis of nanomaterials. PVP is not only used as a suitable colloidal surfactant, but it is often used as a dispersant, reducing agent, surface coating and shape-control agent depending on the specific type of material used in the reaction synthesis, type of PVP (and corresponding reaction conditions, factors which are equally important when considering optimum morphological, optoelectronic and chemical properties.(170)(171)(172) The unique chemical features of PVP belong to its mixed component system comprised of a hydrophilic pyrrolidone moiety and a hydrophobic alkyl group that is in the origin of its excellent solubility in both water and many other polar solvents. Moreover, the long organic hydrophobic chains prevent aggregations of

NPs due to steric hindrance effects (repulsive forces) improving interparticle distances and thus making PVP a good dispersant.(173) Also, the biocompatibility of PVP together with its high passivation ability make it a suitable organic stabilizer to a variety of metal chalcogenide quantum dots with improved photoluminescent properties and reduced toxicity features.

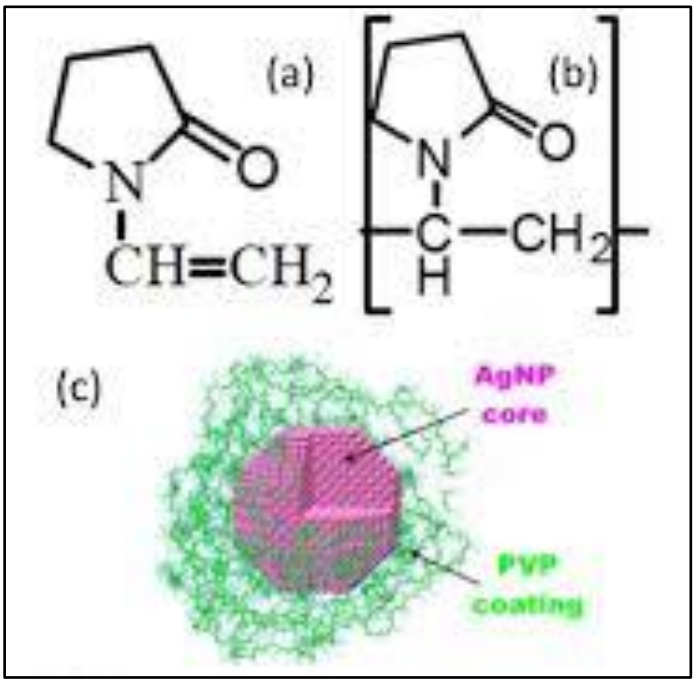

Figure 5- 1. (a) The molecular structure of N-vinylpyrrolidone monomer and (b) the repeating unit of PVP. (c) Image of an Ag NP interacting passivated with PVP oligomers. (Reprinted with permission from reference 157).

5.3 Synthesis and characterization of SnS/PVP CQDs

I will investigate the reaction mechanism behind a modified polyol synthesis of SnS CQDs using a polyvinylpyrrolidone (PVP) polymer as an alternative capping surfactant at elevated temperatures. I propose that the use of the organic PVP polymer will be highly effective in passivating more un-protected surface atoms and dangling bonds due to the large surface-to-volume ratio of SnS QDs resulting in optimum optoelectronic and physicochemical features. I will present that the optical and emission properties of PVP-coated SnS QDs can be tuned by

a systematic modification and control of the reaction conditions covering in the following studies:

1) Effect of PVP molecular weight (M_W)
2) Effect of PVP concentration and reaction time
3) Effect of reaction temperature
4) Effect of precursors' concentration

5.3.1 Polymer molecular weight study

Polymers with different molecular weights usually find use in various applications depending on their corresponding chain lengths, which have a direct effect on their physical properties.(174) In this section, I will examine the degree of surface passivation on absorption and PL emission properties as well as determine the final morphology of PVP-capped SnS CQDs by making a direct comparison between four types of PVP polymers with different chain lengths as a function of molecular weight using the reaction conditions described in chapter 3 (see section 2.2.2). To achieve the above, I will make a comparison between PVP 10 (M_w ~ 10,000 g/mol), PVP 40 (M_w ~ 40,000 g/mol), PVP 55 (M_w ~ 55,000 g/mol) and PVP 360 (M_w ~ 360,000 g/mol), which chain lengths increase with increasing molecular weight (the higher the MW the longer the PVP chain length). The four SnS/PVP samples in this study are abbreviated as SnS/PVP 10, SnS/PVP 40, SnS/PVP 55 and SnS/PVP 360 corresponding to PVP 10, PVP 40, PVP 55 and PVP 360, respectively.

5.3.1.1 TEM analysis

TEM analysis was performed in order to determine the effect of PVP molecular weight on the morphology and size-distribution of the resulting SnS colloidal quantum dots. *Figure 5-2*

represents high-resolution TEM (HRTEM) micrographs of PVP-encapsulated SnS CQDs at various molecular weights. The quantum dots in all four samples appear semi-spherical in shape, similar in size with an average diameter of less than 5 nm regardless of the length of the surface passivator as described for other materials in the literature.(175)(176) However, the mean inter-particle distances in SnS/PVP 55 (refer to *Figure 5-2 (c*)) appear well separated compared to the size-distribution of the quantum dots synthesised either with the lower (refer to *Figures 5-2 (a, b)*) or higher molecular weight PVP polymer (see *Figure 5-2 (d)*), in which separation is compromised forming aggregations of quantum dots. As a result, the use of PVP 55 can be considered as having an optimum chain length forming a uniform and ordered polymer matrix for the passivation of the quantum dots compared to the other molecular weight PVP polymers used in the synthesis. In addition, the compromised size-distribution of the quantum dots as seen in *Figure* 5-2 *(a), (b)* and *(d)* might further affect the optical and emission properties of the resulting CQDs by quenching their quantum confinement and PL emission. This hypothesis will be examined by UV-Vis and PL analyses in the following section.

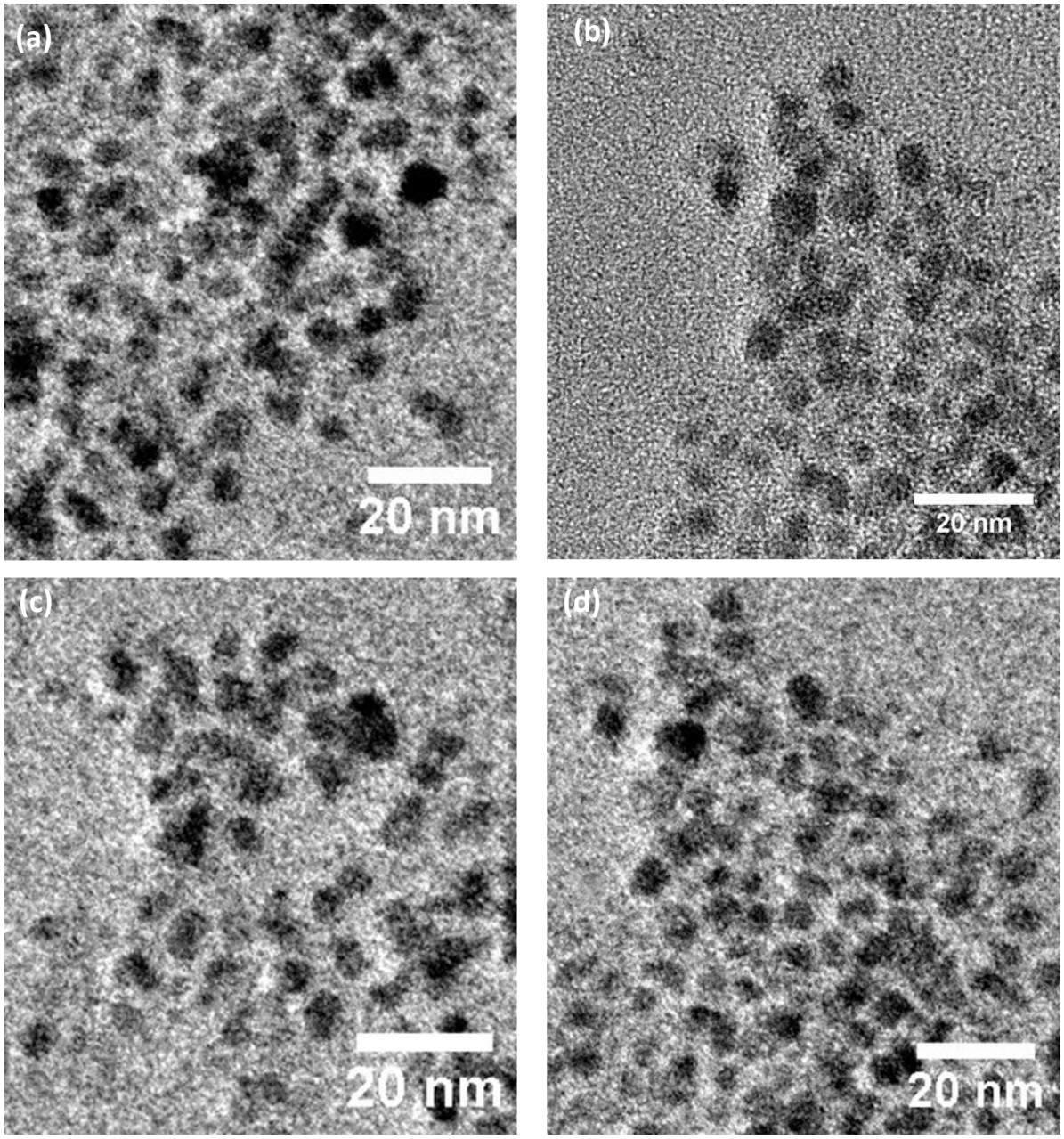

Figure 5- 2. High-resolution TEM (HRTEM) micrographs of SnS CQDs stabilized with (a) PVP 10, (b) PVP 40, (c) PVP 55 and (d) PVP 360 at 140^{0}C and a fixed reaction time of 40 min. The samples were dip-coated onto thin graphene oxide (GO) grids and dried under ambient conditions before analysis.

5.3.1.2 EDX analysis

The elemental composition of SnS/PVP 55 CQDs was further examined due to their homogeneous size-distribution compared to the QDs in the other three samples as seen in

Figure 5-2. The summarised EDX results in *Table 5-1* show stoichiometrically balanced SnS CQDs with approximately 1:1 molar ratio.

Table 5- 1. A summary table of the average elemental composition observed in SnS/PVP 55 CQDs.

Element	Weight %	Atomic %
S K	18.55	49.80
Sn L	81.45	51.20
		Atomic Ratio
Totals	100.00	Sn : S= 1 : 1

5.3.1.3 Effect on optical properties

The prominent blue-shift in the excitonic peak position (2.8 eV) with respect to the bulk band-gap of SnS NCs (1.3 eV) (177) is a clear indication of strong quantum confinement in all four PVP-encapsulated SnS CQDs. *Figure 5-3* shows a significant change in the absorption profiles between PVP-capped CQDs compared to non-luminescent SnS NCs synthesised using similar reactions conditions such as reaction temperature and time except the type of organic stabiliser used in the fabrication method. The large blue-shift in the absorption spectrum of PVP-capped SnS QDs compared to ligand-passivated SnS NCs together with the appearance of an excitonic peak at ~ 440 nm signifies a notable surface modification due to reduced trap states and aggregation of quantum dots. Furthermore, the partial loss of the exciton peak as observed in the absorption spectra of SnS/PVP 40 and SnS/PVP 360 signifies that the quantum dots have lost some of their quantum confinement due to quantum dot aggregation. Furthermore, the complete loss of the excitonic peak in SnS/PVP 10 demonstrates the much higher degree of

quantum dot aggregation formed in the sample compared the higher MW samples. These observations are in a good agreement with the TEM results (see *Figure 5-2*).

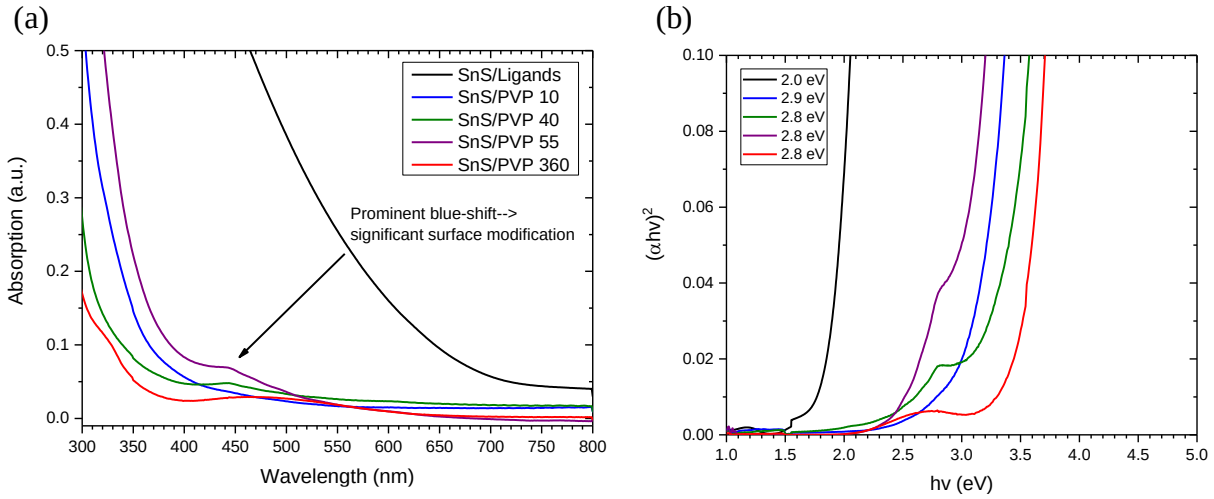

Figure 5- 3. (a) UV-Vis absorption spectra and (b) corresponding band-gap values of four SnS CQDs encapsulated with different PVP MWs compared to the spectrum of SnS CQDs passivated with organic ligands. All samples were syntheses at synthesised at 140^{0}C.

5.3.1.4 Effect on emission properties

It might be expected that the longer the chain, the better the surface passivation providing long-lasting surface protection compared to the use of a PVP polymer with a slightly shorter chain length.(178) However, the absorption spectra in *Figure 5-3* together with the results from the 3D PL and PLE measurements in *Figure 5-4* all reveal that the longer chain length of the polymer does not necessarily provide a higher degree of surface passivation that would eliminate a significant number of non-radiative charge recombination centres due to unprotected surface atoms or dangling bonds. The 3D PL spectra in *Figure 5-4 (g)* shows a significant increase in the PL emission intensity of SnS/PVP 55 compared to the other three samples synthesised with shorter (*Figure 5-4 (a, d)*) and longer PVP chain lengths (*Figure 5-4 (j)*). This observation further supports the obtained results from the TEM analysis in *Figure* 5-2 and UV-Vis measurements (see *Figure 5-3*) confirming my initial hypothesis that

quenching of the PL emission is a result of compromised size-distribution due to partial surface passivation of the QDs leading to the formation of aggregates.

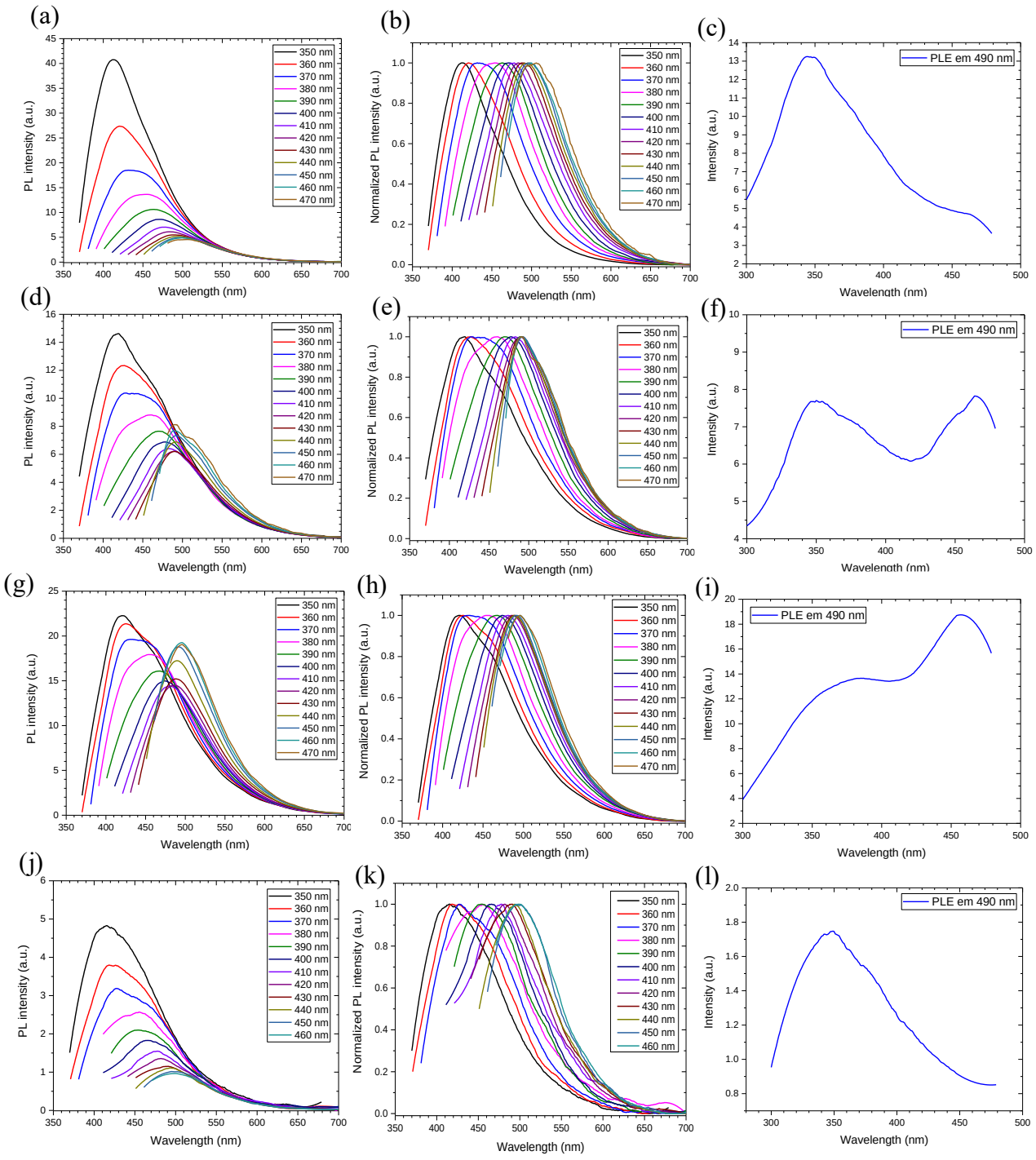

Figure 5- 4. Room temperature 3D PL, normalised 3D PL and PLE spectra of SnS CQDs passivated with (a-c) PVP 10, (d-f) PVP 40, (g-i) PVP 55 and (j-l) PVP 360 acquired. The 3D PL measurements were performed with excitation wavelengths in the range of 350 nm to 470 nm (in 10 nm increments) for all samples. PLE spectra were measured at a PL emission peak of 490 nm.

5.3.1.5 Discussion

Furthermore, the summary graphs in *Figure 5-5* show a comparison of the PL emission properties between the four samples in the study obtained from the performed 3D PL measurements. A significant reduction in the FWHM of the maximum PL emission peaks in sample SnS/PVP 55 (refer to *Figure 5-5 (c)*) at excitation wavelengths ranging from 400 nm to 460 nm is observed compared to the other three SnS/PVP CQDs samples. These results suggest improved sample uniformity and size-distribution of the quantum dots with reduced inter-particle distances, factors that all contribute to the narrowing of the PL emission peaks. Also, an enormous increase in the PL emission intensity (~ 20 times) of SnS/PVP 55 is evident. This observation suggests an optimised surface functionalization passivating unprotected surface atoms and thus quantising the electrons within the SnS core material rather than recombining or quenching at the surface trap centres. Improved surface passivation results in reduced non-radiative recombination processes, increasing PL emission and PL decay lifetimes of the excitons. In conclusion, PVP 55 was found to be more efficient at minimising surface inhomogeneities when compared to PVP 10, PVP 40 and PVP 360 due to the excellent surface packing of PVP 55 resulting in fewer voids, dangling bonds or aggregation of quantum dots.

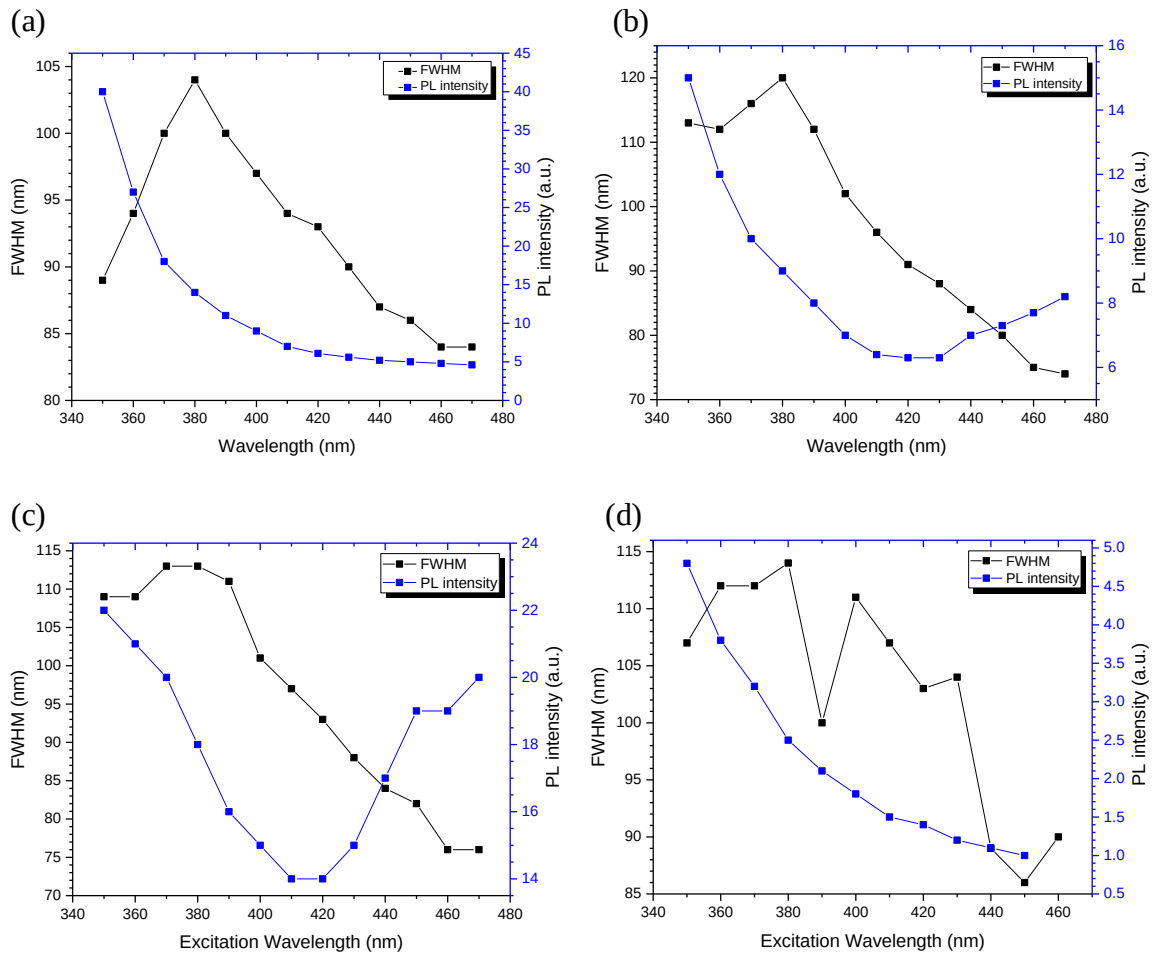

Figure 5- 5. Summary graphs of the PL emission properties of SnS/PVP CQDs with (a) PVP 10, (b) PVP 40, (c) PVP 55 and (d) PVP 360 comparing the FWHM versus PL emission intensity of the maximum PL emission peaks at excitation wavelengths ranging from 350 nm to 470 nm (with 10 nm increments).

5.3.2 Polymer concentration and reaction time studies

To determine the optimal surface passivation of the quantum dots, PVP 55 was chosen in the new study over the shorter PVP 10, PVP 40 and more extended chain PVP 360 polymers due to significantly improved optical, PL emission and size-distribution features of SnS QDs as shown in the previous section (refer to *Figure 5-3, 5-4 and 5-5*, respectively). Many scientific manuscripts, which have applied PVP 55 as a stabilising agent in the synthesis of colloidal quantum dots reported that when the concentration of PVP 55 was below a critical level (< 5 % (w/v)), then the resulting quantum dots had an insufficient absorption of PVP on certain

crystallographic facets.(175) The partial surface passivation increased the surface free energy due to a lower coordination number of the surface atoms affecting the final morphology of the quantum dots and their optoelectronic properties.(176)

On the other hand, increasing PVP 55 concentration above a critical level (> 10 % (w/v)) will increase the viscosity of the solution and thus deteriorate the inter-particle distances and final monodispersity of the quantum dots similar to PVP 360. In this section, I will compare the surface passivation of SnS CQDs by means of two different PVP 55 concentrations in the fabrication method as a starting point (as intermediates between low and high concentrations) and depending on the achieved results further changes in the PVP concentration might be attempted to improve the final surface optimisation of the quantum dots. The study aims to address the degree of surface passivation over time intervals during the growth of the quantum dots.

5.3.2.1 XRD analysis

XRD analysis was performed to determine the effect of PVP concentration on the crystal structure of PVP-capped SnS CQDs. The quantum dots were deposited onto a glass substrate by drop-casting followed by drying under ambient temperature and pressure. *Figure 5-6* represents the obtained XRD diffractograms of SnS CQDs thin film samples with PVP 55 used at 5 % (w/v) (see *Figure 5-6 (a)*) and 10 % (w/v) (refer to *Figure 5-6 (b)*). The diffraction peaks in both samples appear to be significantly broadened with relative peak heights having low intensities. Broadening of the XRD peaks is observed in nanomaterials with sizes less than 100 nm and more pronounced with sizes less than 50 nm.(179) As a general concept, the origin of the diffraction peak broadening can be assigned to different factors such as the small size of the crystallite, low crystallinity (amorphous nature of the material), lattice distortions and dislocations, random quantum dot orientations with respect to one another (due to sample

polycrystallinity) and crystal strains on the surface of the material. In the case of SnS/PVP CQDs, the explanation for the observed broadening in the diffraction patterns can be related to the small sizes of the quantum dots, which was previously observed from HRTEM (see *Figure 5-2*). The XRD data do not provide precise and conclusive results regarding the crystal structure and phase, morphology or related changes in SnS/PVP CQDs as a function of PVP concentration. Therefore, high-resolution TEM (HRTEM) analysis was performed to precisely assign the corresponding chemical form and morphology of the resulting SnS quantum dots.

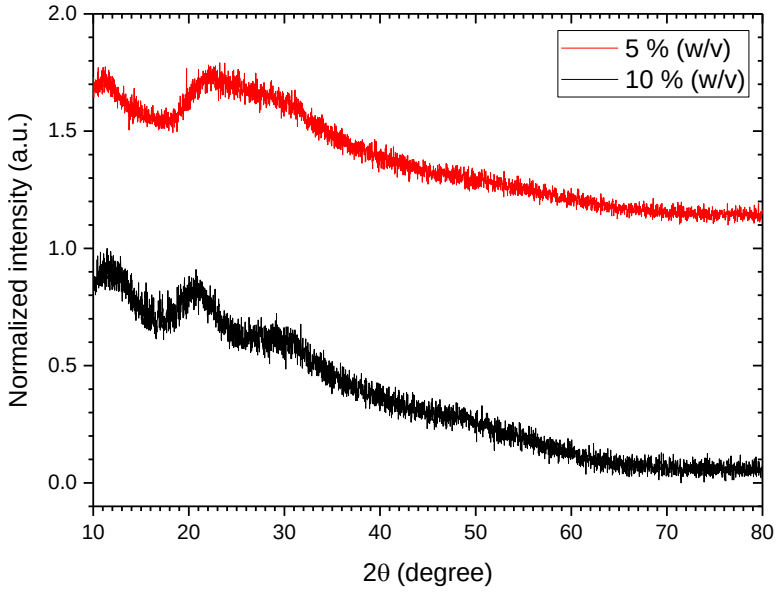

Figure 5- 6. XRD diffractograms of PVP-capped SnS CQDs fabricated with 5 % (w/v) PVP 55 and 10 % (w/v) PVP 55. The XRD samples were deposited on silicon substrates by drop casting.

5.3.2.2 TEM analysis

Figure 5-7 shows low and high-resolution TEM (HRTEM) micrographs of SnS CQDs achieved by varying the PVP 55 concentration. The highly versatile capping and size directing role of PVP 55 results in the formation of monodisperse samples with some minor aggregations of the quantum dots as seen in *Figure 5-7 (a)* and *(e)*. The inter-particle distances between the quantum dots are well separated. Furthermore, the concentration of PVP 55 does not affect the

shape and average size of the quantum dots. The resulting quantum dots have a semi-spherical shape with an average size of 5 nm. Moreover, the HRTEM images in *Figure 5-7 (b)* and *(f)* together with their corresponding reconstruction images (refer to *Figure 5-7 (d)* and *(h)*, respectively) confirm the high crystallinity nature of the quantum dots with clearly seen lattice fringes. The measured interplanar distances of SnS QDs are d= 0.29 nm (5 % (w/v) PVP 55) and d= 0.34 (10 % (w/v) PVP 55), which are close to the standard d-spacing values of d= 0.2931 nm and d= 0.3423 nm consistent with their respective lattice planes (101) and (120) of SnS orthorhombic phase (Pbnm, card no. 39-0354). The performed TEM analysis on individual quantum dots confirmed that the PVP-capped SnS CQDs are composed of a single crystal phase with similar morphologies regardless of PVP 55 concentration.

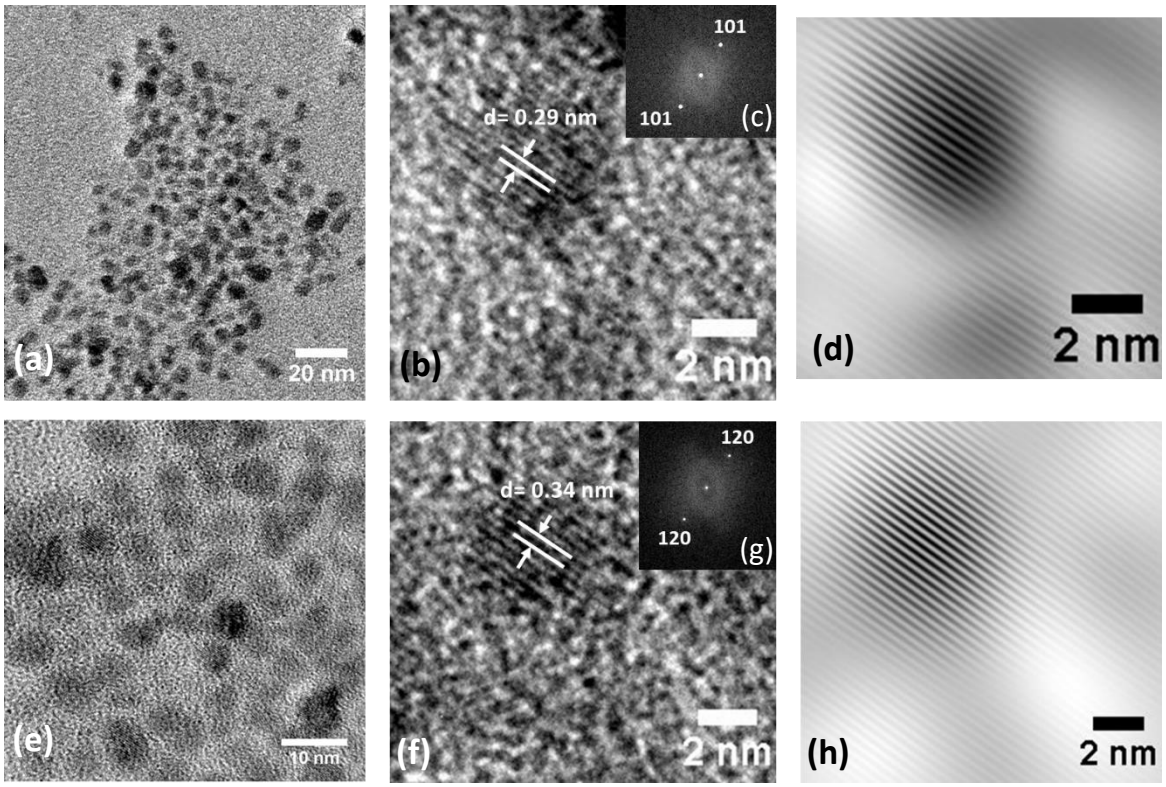

Figure 5- 7. TEM micrographs of PVP-capped SnS CQDs with a polymer concentration of (a-d) 5 % (w/v) PVP 55 and (d-g) 10 % w/v PVP 55. (a, e) Low and (b, f) HRTEM images of PVP/SnS CQDs and (c, g) generated FFT patterns obtained from the HRTEM images from the two sample. (d, h) HRTEM reconstruction micrographs generated from the FFT patterns of the two samples.

5.3.2.3 Effect on optical properties

The graphs in *Figure 5-8* illustrate the optical absorption spectra of five SnS/PVP solution aliquots together with their calculated band-gap energy values taken at different growing stages and compares the results to the absorption spectrum of pure PVP 55 at the same concentration used for the synthesis of the QDs. There is an increasing trend in the absorption spectrum of the quantum dots with time in both samples. This observation could be related to the higher number of SnS/PVP QDs synthesised at longer reaction times giving rise to increased optical absorption. Also, the appearance of an exciton peak at ~ 450 nm in the visible region of the spectrum compared to pure PVP 55 is a clear indication of quantum confinement. The intensity of the exciton peak progressively increases over time becoming more prominent at longer reaction times. This observation suggests a monodisperse sample composed of high-quality QDs with well-passivated surface atoms reducing non-radiative charge recombination processes. The large blue-shift in the exciton peak position (band gap of 2.8 eV) of the PVP-capped SnS QDs (see *Figure 5-8 (c)*) compared to the bulk band-gap energy value of SnS NCs (1.3 eV) indicates that the QDs have entered a strong quantum confinement regime. However, the absence of the exciton peak from the absorption spectra of the quantum dots stabilised with the lower PVP 55 concentration (see *Figure 5-8 (a)*) indicates the poor surface passivation and aggregation of the resulting QDs. The small exciton peak observed at 120 min of reaction time suggests that the atom rearrangements and surface reconstruction processes take longer when the amount of PVP 55 is reduced slowing down the reaction kinetics (both nucleation and growth rates) and increasing the reaction thermodynamics. Furthermore, the amount of PVP 55 might not be enough to cover the whole quantum dot surface resulting in non-passivated traps states and aggregations of QDs.

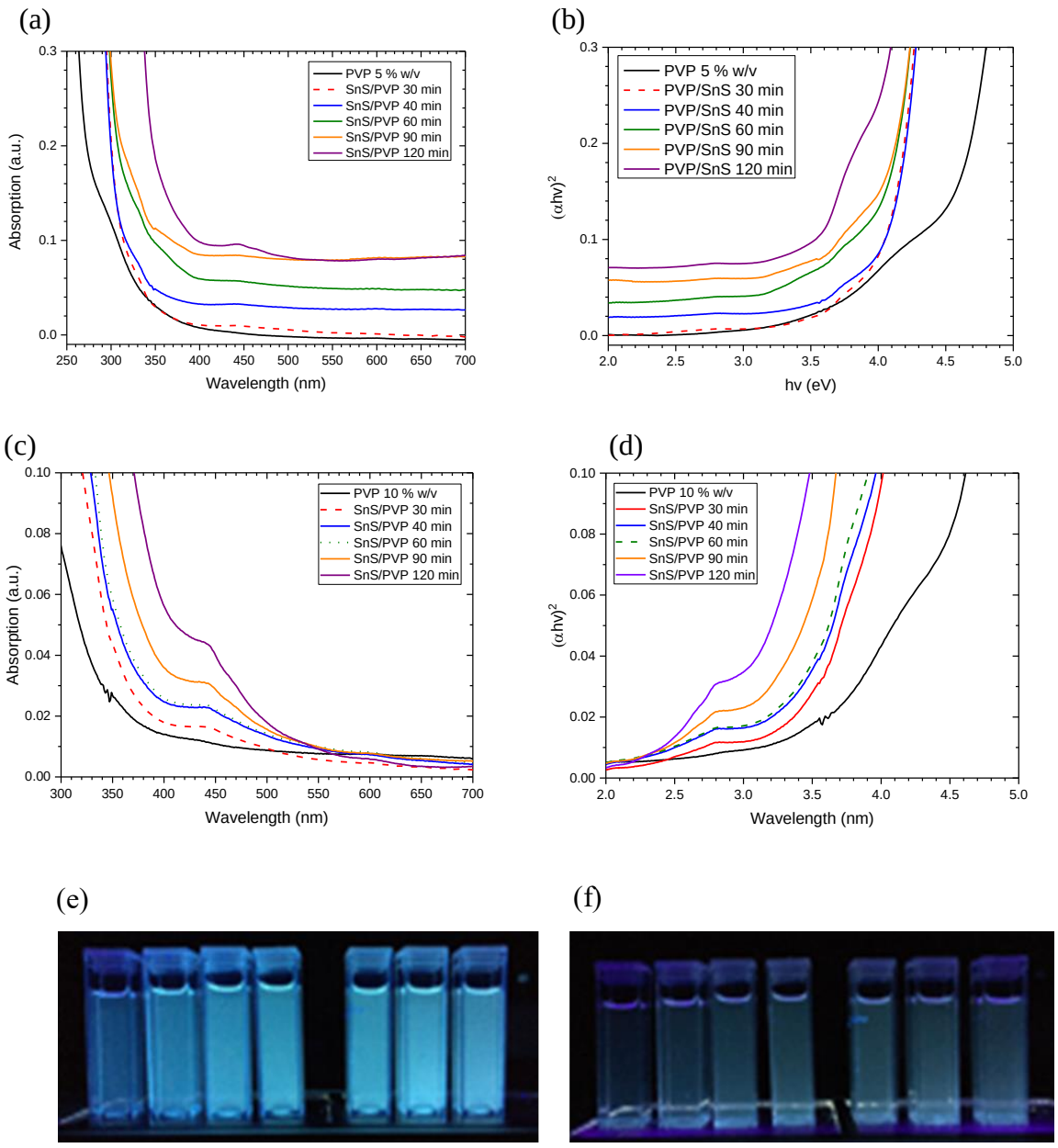

Figure 5- 8. UV-Vis absorption spectra and (b, d) calculated optical band-gap energy values of SnS CQDs passivated with PVP 55 used at (a, b) 5 % (w/v) and (c, d) 10 % (w/v). CQD aliquots were collected at reaction times between 30 and 120 min and washed before the analysis. Images of (e) 10 % (w/v) and (f) 5 % (w/v) aliquots excited at 365 nm.

5.3.2.4 Effect on emission properties

5.3.2.4.1 5 % (w/v) PVP 55

Figure 5-9 illustrates the PL emission properties of SnS CQDs stabilised with 5 % (w/v) PVP 55 measured by 3D PL and PLE analysis. Interestingly, SnS/PVP aliquots all show PL emission

features even at early reaction stages (reaction time of > 30 min). The intensity of the PL emission peak progressively increases by more than ten times with increasing reaction time reaching maximum intensity at 120 min. Also, a significant narrowing of the highest intensity PL peak is observed in the first 40 min of reaction time followed by a further narrowing over time as seen in the summary graph in *Figure 5-10*. This phenomenon could be related to optimum surface rearrangements and size-focusing processes during the growth of the quantum dots. The results of the 3D PL measurements support the data from the UV-Vis analysis as shown in *Figure 5-8 (a)*, which indicate an increase in the absorption spectrum at prolonged reaction times resulting in the formation of more quantum dots with identical optical and emission profiles and improved surface functionalisation giving rise to an excitonic absorption peak.

In addition, there are two main PL peaks observed in the emission spectra of each sample corresponding to two distinct species with different absorption profiles as seen in the PLE graphs in *Figure 5-9*. However, comparing the 3D PL and PLE spectra of pure PVP and SnS/PVP CQDs samples it can be clearly seen that the PL emission peaks excited at wavelengths ranging from 350 nm to 410-420 nm all have identical absorption profiles (refer to *Figure 5-9 (b)*) and thus belong to the PL emission coming from PVP itself.(180) However, the excitation-dependent PL emission in the pure PVP sample might be attributed to excitation of specific functional groups of PVP with a variety of electronic states giving rise to PL emission at a range of wavelengths, which is a commonly observed phenomenon in organic molecules.(181) PL peaks at excitation wavelengths > 420 nm correspond to the PL emission of SnS QDs as supported by the PLE measurements showing a secondary absorption peak at 470 nm (see *Figure 5-9 (e), (h, (k), (n), (q))*), which is missing in the PLE spectra of pure PVP (refer to *Figure 5-9 (b)*). In addition, it could be suggested that the intensities of the PLE peaks increase over time with changes in the concentration of formed quantum dots.

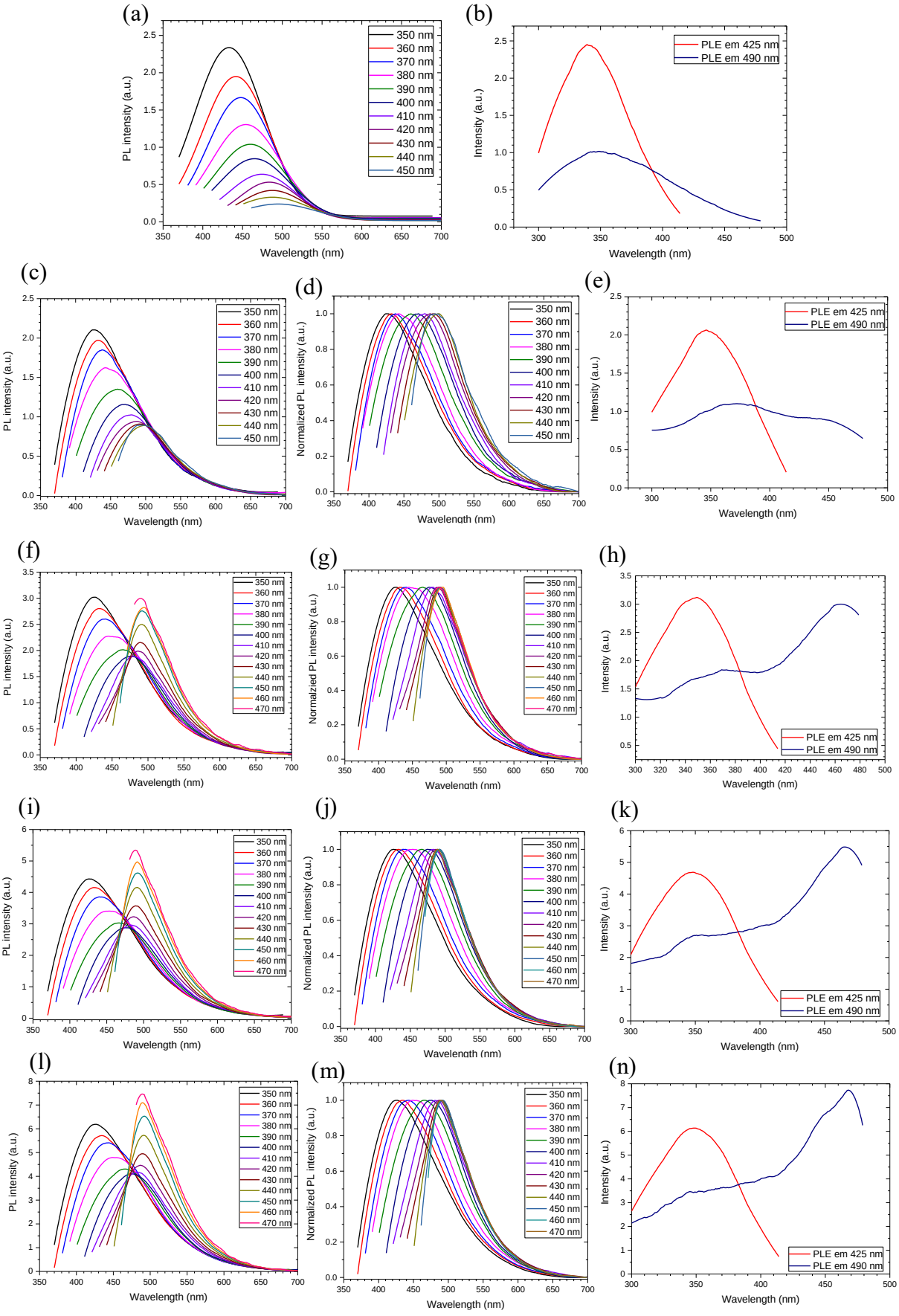
(a)
PL intensity (a.u.)
Wavelength (nm)
350 nm
360 nm
370 nm
380 nm
390 nm
400 nm
410 nm
420 nm
430 nm
440 nm
450 nm
(b)
Intensity (a.u.)
Wavelength (nm)
PLE em 425 nm
PLE em 490 nm
(c)
PL intensity (a.u.)
Wavelength (nm)
(d)
Normalized PL intensity (a.u.)
Wavelength (nm)
(e)
Intensity (a.u.)
Wavelength (nm)
(f)
PL intensity (a.u.)
Wavelength (nm)
(g)
Normalized PL intensity (a.u.)
Wavelength (nm)
(h)
Intensity (a.u.)
Wavelength (nm)
(i)
PL intensity (a.u.)
Wavelength (nm)
(j)
Normalized PL intensity (a.u.)
Wavelength (nm)
(k)
Intensity (a.u.)
Wavelength (nm)
(l)
PL intensity (a.u.)
Wavelength (nm)
(m)
Normalized PL intensity (a.u.)
Wavelength (nm)
(n)
Intensity (a.u.)
Wavelength (nm)

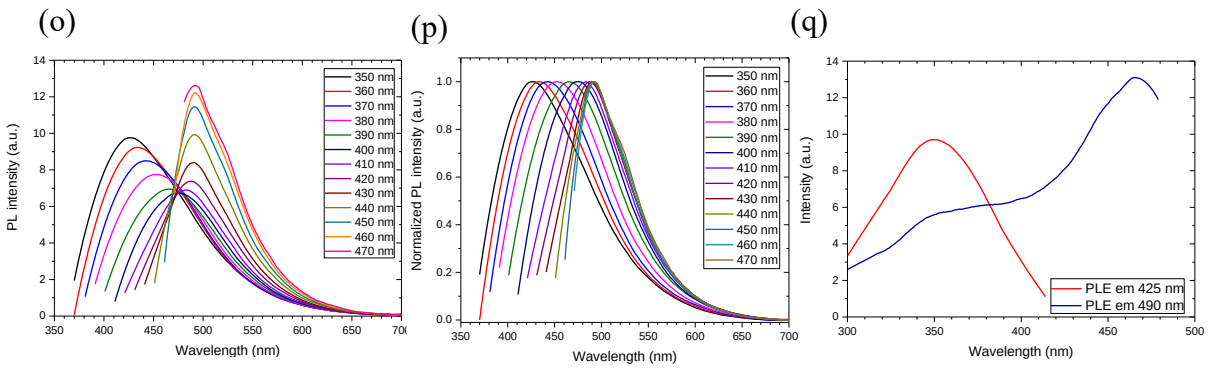

Figure 5- 9. 3D PL, normalised 3D PL and PLE measurements of SnS/PVP CQDs aliquots in methanol passivated with PVP 55 used at 5 % (w/v) at reaction time of (c-e) 30 min, (f-h) 40 min, (i-k) 60 min, (l-n) 90 min and (o-q) 120 min and compared to the (a) 3D PL and (b) PLE spectra of pure 5 % (w/v) PVP 55 re-dispersed in methanol as a reference sample. 3D PL spectra were obtained at excitation wavelengths from 350 to 470 nm. PLE spectra were measured at PL emission peaks of 425 nm and 490 nm in all samples.

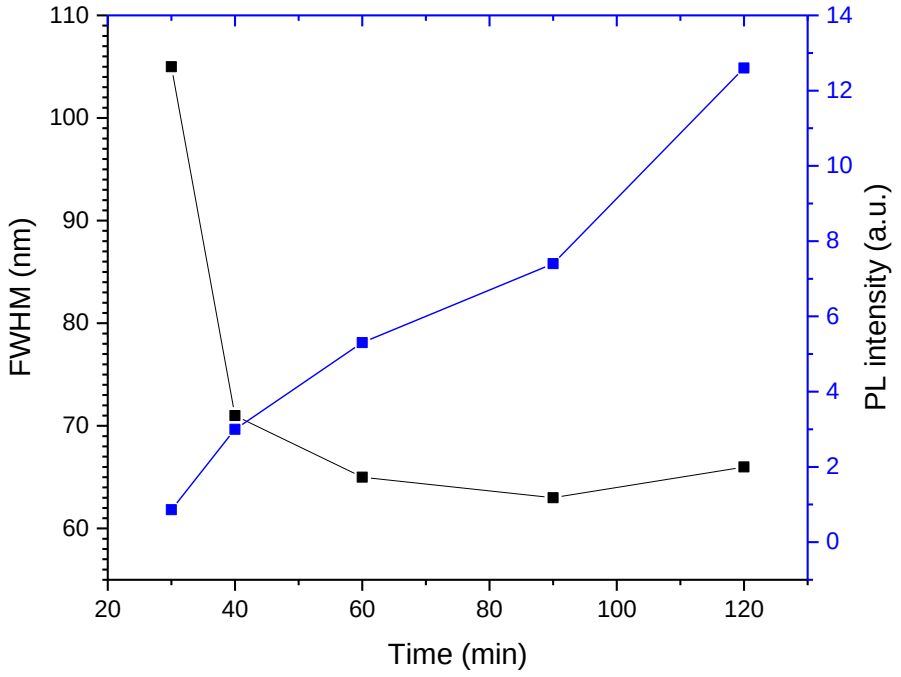

Figure 5- 10. A summary graph illustrating the PL emission intensity at 490 nm vs. size-distribution changes observed in SnS/PVP CQDs stabilised with 5 % (w/v) PVP 55 as a function of growing time.

5.3.2.4.2 10 % (w/v) PVP 55

The obtained 3D PL and PLE results (refer to *Figure 5-11*) of the samples synthesised with PVP 55 used at 10 % (w/v) show similar emission and absorption properties to the ones passivated with 5 % (w/v) PVP 55. Doubling the concentration of PVP 55 improved the passivation of trap states and dangling bonds on the surface of the quantum dots by significantly increasing the intensity of their PL emission. *Figure 5-11 (a-c)* shows 3D PL emission and PLE spectra of a pure 10 % (w/v) PVP 55 solution, which appear to be identical to the results obtained for the 5 % (w/v) PVP 55 solution in *Figure 5-9* except for a minor increase in the PL emission intensity due to a higher concentration but with no changes to the absorption wavelength. The PL emission intensity is improved by more than 20 times as seen in *Figure 5-11 (m)*, which indicates the improved surface optimisation of the resulting PVP-capped SnS CQDs. This is consistent with the observed increase in the absorption of the QDs measured by UV-Vis analysis as seen in *Figure 5-8 (c)* and PLE spectra (refer to *Figure 5-11 (o)*). Also, an overall PL peak narrowing of 22 nm is indicative of improved size-distribution with reduced inter-particle distances resulting in less aggregations and an overall improvement in sample monodispersity.

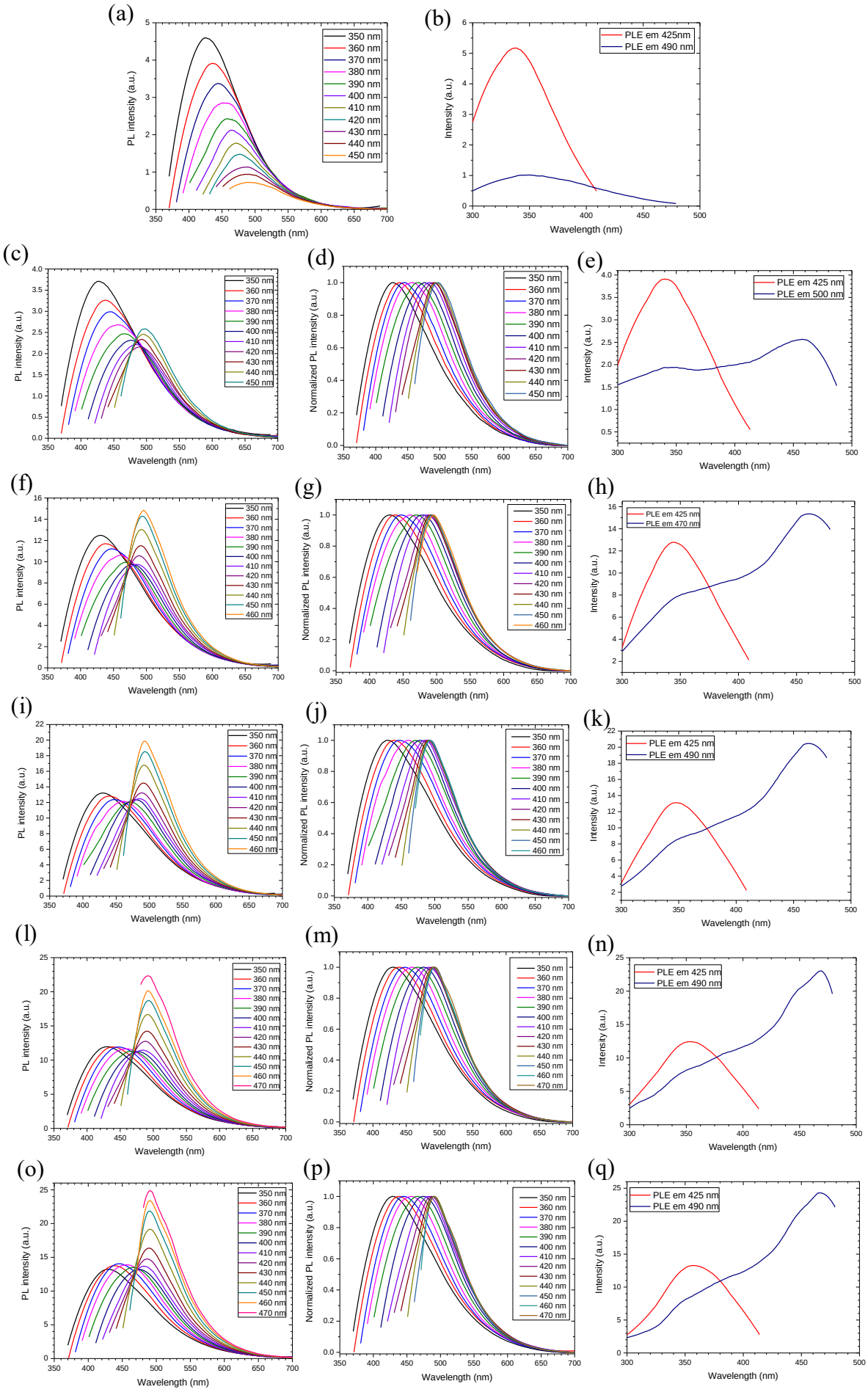
(a)
PL intensity (a.u.)
Wavelength (nm)
350 nm
360 nm
370 nm
380 nm
390 nm
400 nm
410 nm
420 nm
430 nm
440 nm
450 nm
(b)
Intensity (a.u.)
Wavelength (nm)
PLE em 425nm
PLE em 490 nm
(c)
PL intensity (a.u.)
Wavelength (nm)
(d)
Normalized PL intensity (a.u.)
Wavelength (nm)
(e)
Intensity (a.u.)
Wavelength (nm)
PLE em 425 nm
PLE em 500 nm
(f)
PL intensity (a.u.)
Wavelength (nm)
460 nm
(g)
Normalized PL intensity (a.u.)
Wavelength (nm)
460 nm
(h)
Intensity (a.u.)
Wavelength (nm)
PLE em 425 nm
PLE em 470 nm
(i)
PL intensity (a.u.)
Wavelength (nm)
460 nm
(j)
Normalized PL intensity (a.u.)
Wavelength (nm)
460 nm
(k)
Intensity (a.u.)
Wavelength (nm)
PLE em 425 nm
PLE em 490 nm
(l)
PL intensity (a.u.)
Wavelength (nm)
460 nm
470 nm
(m)
Normalized PL intensity (a.u.)
Wavelength (nm)
460 nm
470 nm
(n)
Intensity (a.u.)
Wavelength (nm)
PLE em 425 nm
PLE em 490 nm
(o)
PL intensity (a.u.)
Wavelength (nm)
460 nm
470 nm
(p)
Normalized PL intensity (a.u.)
Wavelength (nm)
460 nm
470 nm
(q)
Intensity (a.u.)
Wavelength (nm)
PLE em 425 nm
PLE em 490 nm

Figure 5- 11. 3D PL, normalised 3D PL and PLE measurements of SnS/PVP CQDs aliquots in methanol passivated with PVP 55 used at 10 % (w/v) at reaction time of (c-e) 30 min, (f-h) 40 min, (i-k) 60 min, (l-n) 90 min and (o-q) 120 min compared to the (a) 3D PL and (b) PLE spectra of pure 10 % (w/v) PVP 55 re-dispersed in methanol as a reference sample. A range of excitation wavelengths between 350 and 470 nm was used in the PL measurements. PLE spectra were recorded at PL emission wavelengths of 425 and 490 nm in all samples.

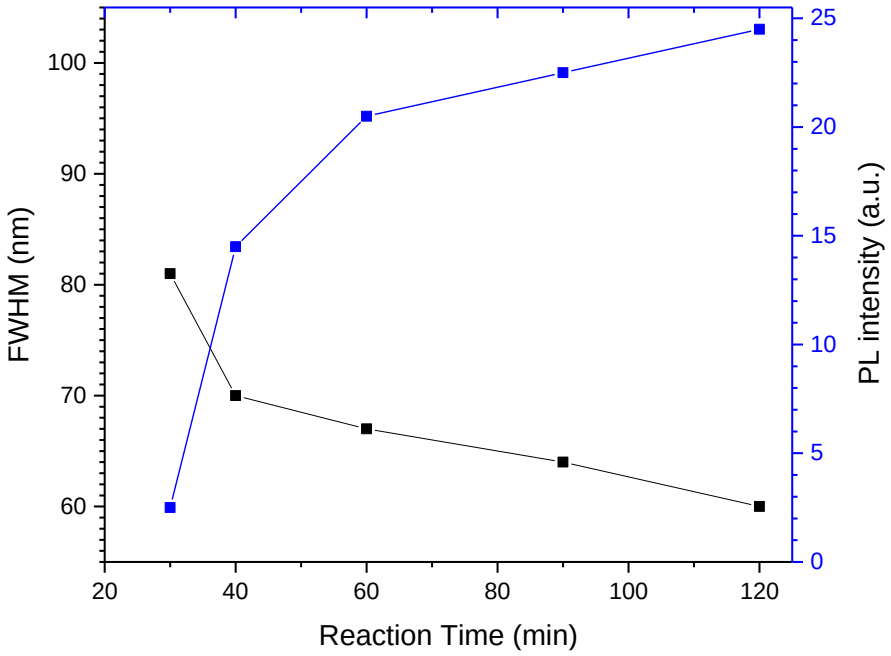

Figure 5- 12. A summary graph of the PL emission intensity at 490 nm vs. size-distribution changes observed in SnS/PVP CQDs stabilised with at 10 % (w/v) PVP 55 as a function of growing time.

5.3.2.5 FT-IR analysis

To determine the binding sites and the degree of surface coverage of PVP 55 on SnS CQDs, FTIR spectra of pure PVP 55 and PVP-capped SnS QDs were measured (refer to *Figure 5-13*). The 500-4000 cm^{-1} region of the IR spectra is shown in *Figure 5-13* where the most significant absorption bands are present. The observed similarities in the absorption modes of pure PVP and PVP-capped SnS CQDs corresponding to O-H stretching vibration at 3434 cm^{-1}, C=O stretching vibration at 1661 cm^{-1}, CH_2 bending vibration at 1424 cm^{-1} and C-H vibrations modes at 1291 cm^{-1} and 1018 cm^{-1} all confirm the PVP surface absorption on the quantum dots.(182) The increased absorption mode at 1661 cm^{-1} observed in both samples suggests that

the binding site for the surface passivation of PVP is through the interaction of the C=O stretching vibration with the metal ion on the surface of the quantum dots. However, there are some differences in the FTIR spectra of the PVP-passivated samples that could be assigned to the covering density of PVP on the surface of the quantum dots. *Figure 5-13 (b)* illustrates that the C=O stretching vibration mode at 1661 cm^{-1} in the sample synthesised with the higher PVP concentration is more pronounced compared to the sample stabilised with less PVP (refer to *Figure 5-13 (a)*). The FTIR data together with the PL spectra (see *Figure 5-9*) are in a good agreement implying that the surface of the quantum dots passivated with 5 % (w/v) PVP 55 is less protected and likely to form more non-radiative recombination pathways and thus decreasing the overall intensity of the PL emission.

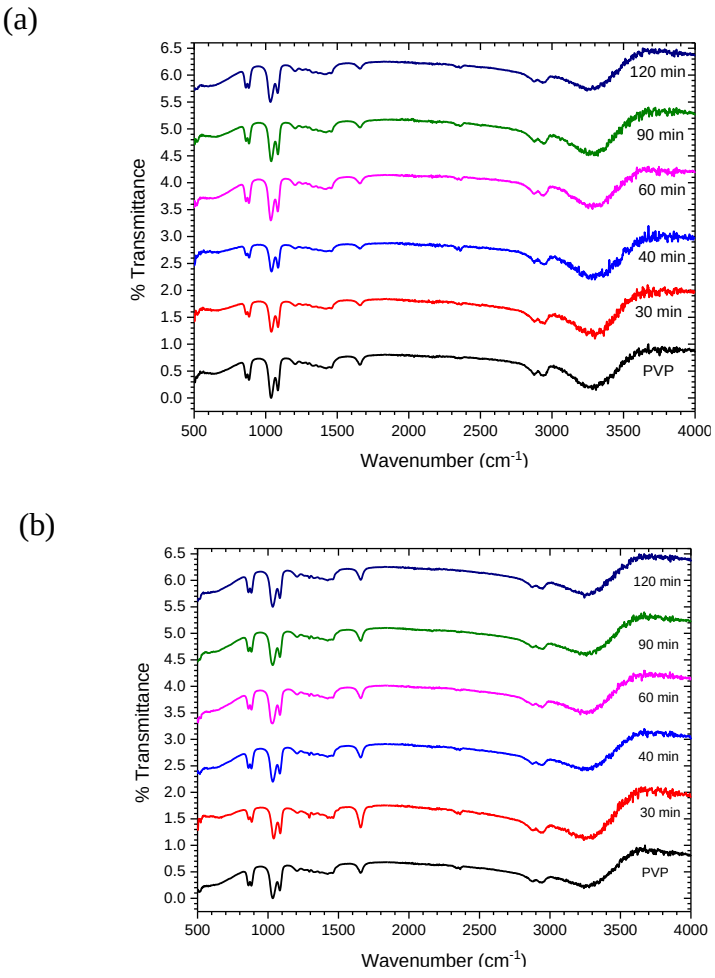

Figure 5- 13. FT-IR spectra plots of SnS CQDs passivated with PVP 55 at (a) 5 % (w/v) and (b) 10 % (w/v) recorded at various reaction times ranging from 30 to 120 minutes.

Table 5- 2. Representative FTIR modes and peak intensities of PVP-capped SnS CQDs visible in Figure 5-13.

Peak intensity (cm^{-1})	***Group band***
1290-1018	C-H vib
1424	CH_2 bend
1661	C=O stretch
2955	C-H asym stretch
3434	O-H stretch

5.3.2.6 Discussion

The 10 % (w/v) PVP 55 stabiliser provided the most effective long-lasting surface passivation of the resulting SnS CQDs. The PL emission properties of SnS/PVP QDs are improved more than two times using 10 % (w/v) PVP 55. This result could suggest a significant elimination of non-radiative charge recombination centres due to an improved surface optimisation of the QDs. However, the FWHM values in both samples appear to be close to one another with small difference regardless of their PL emission intensities.

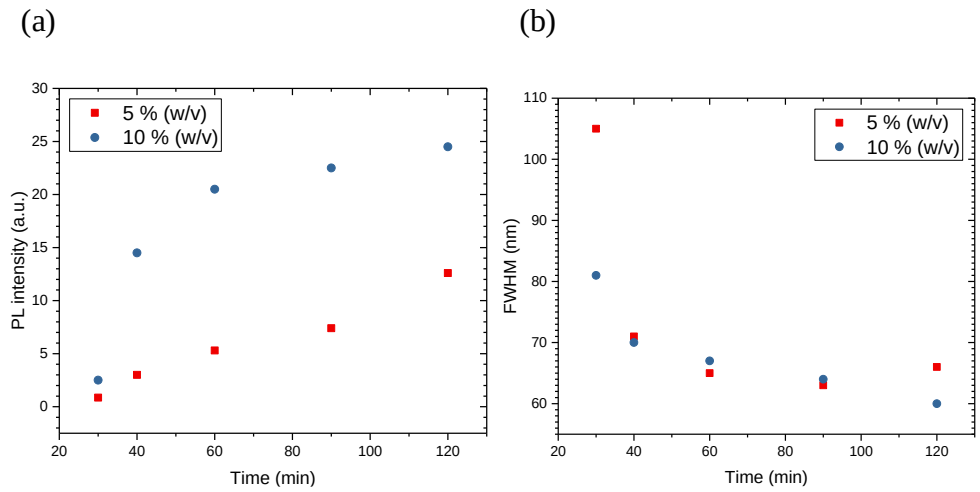

Figure 5- 14. Comparison of the (a) PL emission features and consequent (b) size-distribution changes in SnS/PVP CQDs measured by the FWHM of the highest intensity PL peak at reaction growing times between 30 and 120 minutes as a function of PVP molecular weight.

5.3.3 Reaction temperature studies

In the previous two sections, I have shown that a precise consideration of reaction conditions such as the type and amount of surfactant used in the synthesis is of a significant importance for the degree of surface passivation of the quantum dots improving their optical and emission features due to elimination of non-radiative charge recombination centres present in the QDs. In addition, I have performed a systematic study of the growing mechanism and surface reconstruction processes of the quantum dots recorded at various reaction times by using PL, PLE and UV-Vis analysis. The obtained results improved my understanding of the growing reaction kinetics and helped me consider the new reaction conditions for the further optimisation of the quantum dots. In this section, I will tune the reaction temperature with the aim of finding the best growing conditions for better surface passivation resulting in fewer trap sites.

5.3.3.1 Effect on optical properties

Figure 5-15 represents the performed UV-Vis measurements on SnS/PVP CQDs synthesised at different growing temperatures and a fixed reaction time of 120 minutes. The results reveal that the excitonic peak is retained in all three samples, which implies that the quantum dots belong to the quantum confinement regime irrespective of reaction temperature. However, changes in the absorption spectra with respect to temperature are evident. It appears that when the reaction temperature is lowered below 140^0 C, both the absorption and excitonic peak intensities are reduced compared to the other two samples synthesised at higher temperatures. This observation suggests that the nucleation and growth rates of the reaction are directly related to temperature by slowing down the formation of small nuclei and the growth of the quantum dots due to a lower concentration of reactant species with sufficient energies to react (energies greater than the activation energy).(173)

Also, the lower intensity of the excitonic peak observed at 120^0 C could be related to the smaller number of photoluminescent QDs present in the sample due to the slow growth rate or sample inhomogeneity (aggregation of QDs or un-passivated surface trap states). However, increasing the reaction temperature to 160^0 C shows a small intensity loss of the excitonic peak compared to the absorption spectrum of the quantum dots at 140^0 C, which is a clear indication of a partial loss of quantum confinement due to clustering of the quantum dots. Opposite to the reaction kinetics proposed in the growing process of the QDs synthesised at 120^0 C, it appears that 160^0 C is too high affecting the growth rate by creating higher chances of undesired interactions between the reactant species or molecules forming clusters of QDs. This hypothesis will be confirmed with any changes observed in the PL emission properties of the resulting quantum dots.

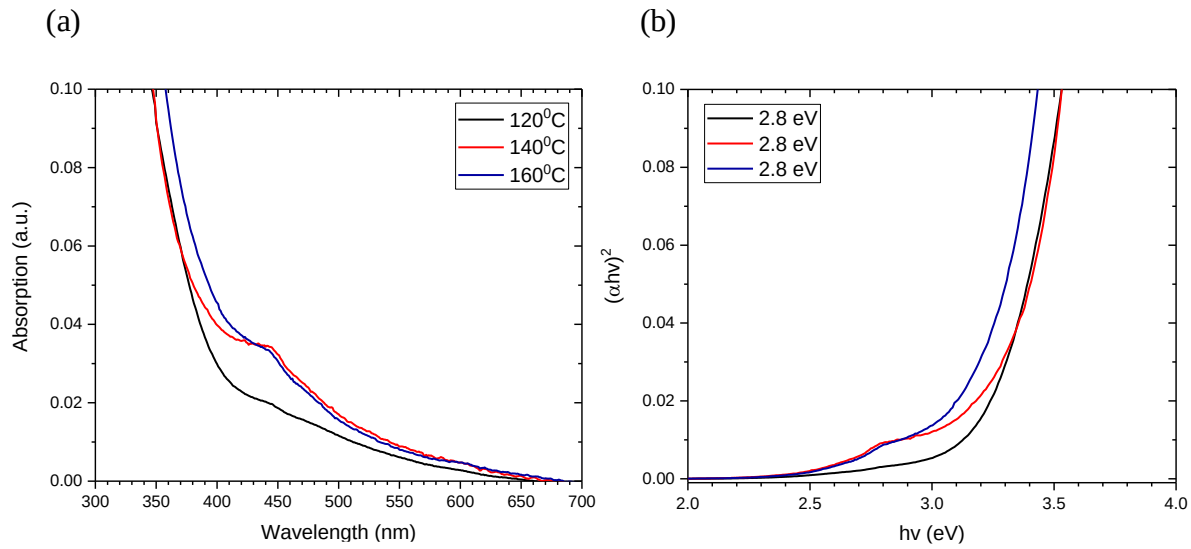

Figure 5- 15. (a) UV-Vis absorption and (b) band-gap energy changes of the optical spectra of PVP 55-encapsulated SnS CQDs at 120^0 C, 140^0 C, and 160^0 C.

5.3.3.2 Effect on emission properties

Figure 5-16 illustrates the PL spectra of the three samples synthesised at various temperatures, which is in a good agreement with the data from the UV-Vis measurements as seen in *Figure*

5-15 indicating a reduction in the PL emission intensity and an increase in dispersity of the quantum dots within the samples as a function of reaction temperature. The PL emission intensity appears to be the highest at 140^0C, which was also confirmed by the intensity of the excitonic peak observed from the absorption spectrum of SnS compared to the other two samples. However, the PL emission intensities at 140^0 C and 160^0 C are found to be relatively close to one another following the observed same changes from the absorption spectra (refer to *Figure 5-11*). *Figure 5-16* summarises the trend in the PL emission features and size-distribution changes observed during the growing stage of the quantum dots at each reaction temperature. It appears that the highest PL emission intensity belongs to the sample synthesised at the intermediate temperature with significant narrowing of the FWHM of the PL peaks throughout the different growth stages of the reaction. There is a progressive increase in the PL emission intensity of the sample at 160^0 C up to 60 min of reaction time followed by a drop when the growing time is further increased. The decrease in the PL intensity could be directly related to the increase in sample's polydispersity due to the formation of aggregates or surface defects as seen from the widening of the PL peaks at reaction times longer than 60 min.

This result supports my hypothesis based on the UV-Vis data that a high reaction temperature might result in unwanted collisions of reactant species due to their significantly higher thermal energies. Furthermore, a significant difference in the FWHM of the PL peaks at 120^0 C at early reaction times compared to the line width in the other two samples at 140^0 C and 160^0 C is observed. This observation could be related to the greater size-distribution of quantum dots in the sample at a lower temperature due to a slower growth rate and therefore, to slower size-focusing events. The UV-Vis measurements (refer to *Figure 5-15*) together with the PL data confirm that 140^0 C could serve as an optimum reaction temperature in future synthesis studies in the next sections.

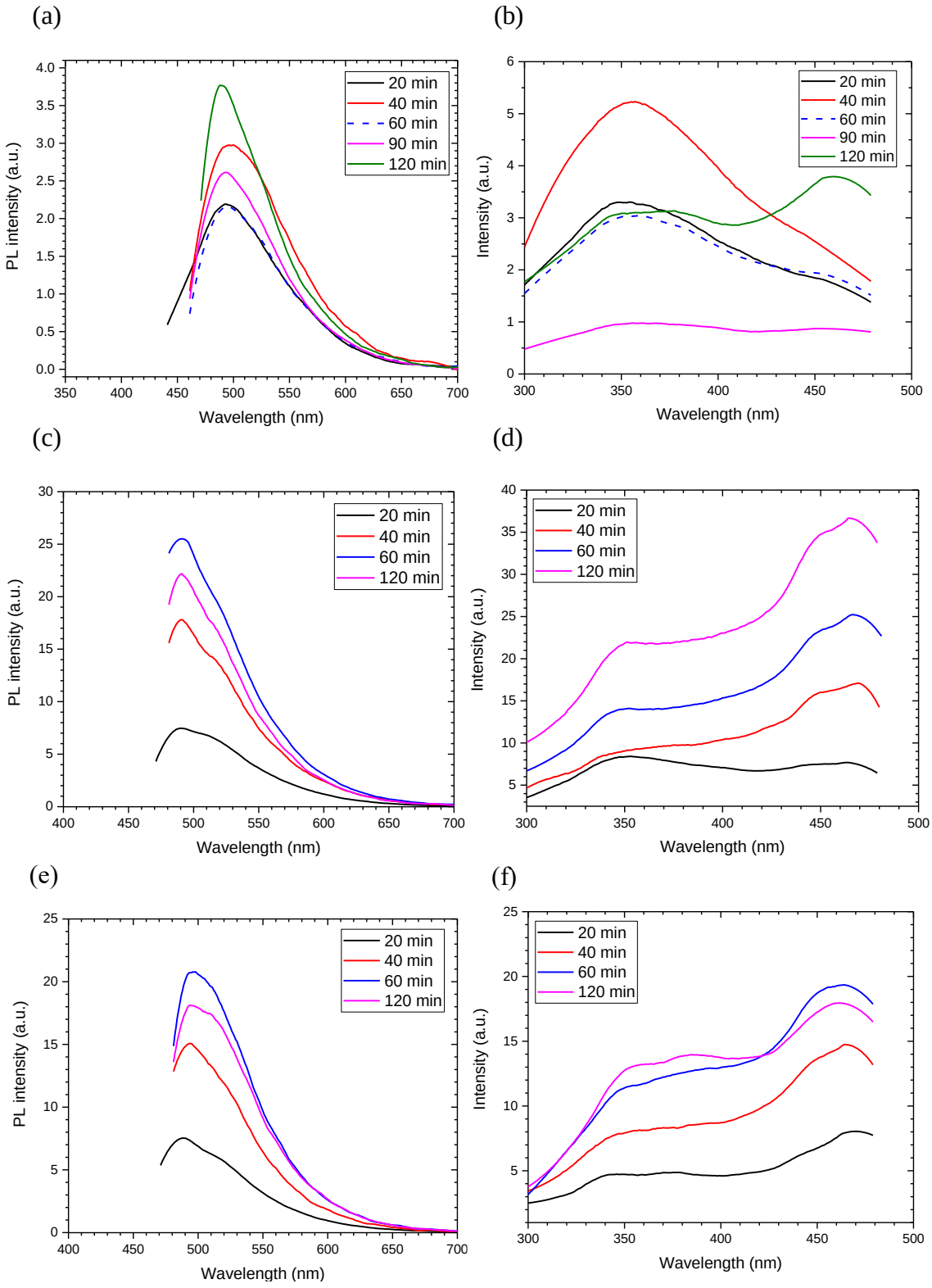

Figure 5- 16. PL and PLE spectra of the highest intensity PL emission peaks recorded at reaction times between 20 and 120 minutes at (a, b) 120^0 C, (c, d) 140^0 C and (e, f) 160^0 C. A progressive increase in the PL emission intensity and absorption with prolonged reaction times was observed. Samples were illuminated with an excitation wavelength of 470 nm.

Figure 5-17 summarises the results from the 3D PL measurements (as seen in *Figure 5-16*) and the corresponding changes in the PL emission intensity and narrowing of the size-distribution of the quantum dots at various reaction times as a function of temperature. Regardless of the drop in the PL emission intensity at reaction times longer than 60 min at 140^0 C, a progressive narrowing of the size distribution of the quantum dots is observed at longer reaction times reaching a line width of 63 nm at a growing time of 120 min. This observation suggests that the optimal surface structure of the quantum dots is reached at 60 min resulting in the formation of quantum dots with bright PL emission followed by a minor surface degradation at prolonged growing times (> 60 min). It could be clearly seen from the plots that the increase in reaction temperature resulted in a faster growth rate and surface rearrangement of atoms by enhancing the PL emission intensity of the QDs. Although the surface stabilisation of the quantum dots was found to be compromised at 120 min, I will continue working with prolonged reaction times due to improved size-distribution. I will attempt to improve the PL emission intensity by fine tuning of the precursors' molar ratios (Sn:S). I hypothesise that increasing the Sn ions with respect to S ions will result in even more successful surface passivation of non-radiative charge recombination sites increasing the overall PL emission intensity of the quantum dots.

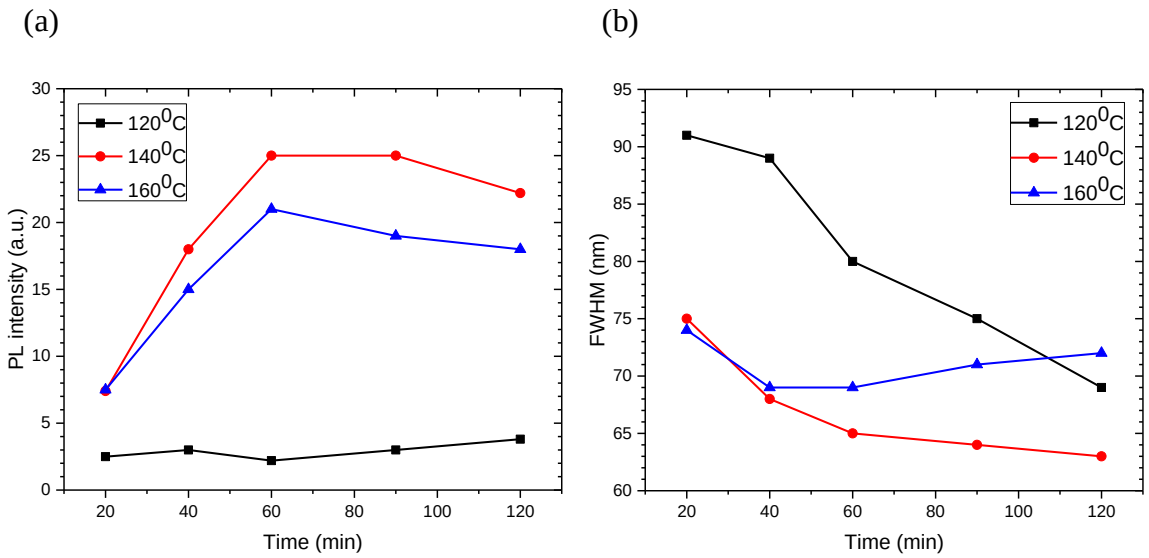

Figure 5- 17. Summary graphs of the PL emission characteristics of SnS/PVP CQDs synthesised at 120⁰ C, 140⁰ C, and 160⁰ C comparing the (a) PL emission intensity and (b) FWHM of the maximum PL peaks measured at growing intervals between 20 and 120 minutes. Samples were excited at 470 nm reaching a maximum PL emission intensity.

5.3.4 Precursor concentration studies

In this section, I will further investigate the surface stabilisation of PVP-capped SnS CQDs by means of determining the optimum molar ratios between Sn and S precursors by monitoring changes in the PL emission properties of the quantum dots. Then, I will further explore my studies by performing a fine tuning of the concentration of the Sn-based precursor keeping S constant with the aim of proving that precursors molar ratios are an important parameter when optimising the synthesis.

5.3.4.1 Sn:S molar ratios

5.3.4.2 Effect on emission properties

The graph in *Figure 5-18* shows a summary plot of the PL emission spectra of PVP-capped SnS CQDs fabricated by varying the Sn:S molar ratios. It is seen from the PL spectra that the amount of Sn ions has a detrimental effect on the PL emission properties of the resulting

quantum dots. As the molar ratio of Sn is reduced compared to the S molar ratio, the PL emission intensity decreases. This result can be explained by the formation of Sn vacancies (V_{Sn}) on the surface of the quantum dots creating non-radiative charge recombination centres thermalizing excitons. On the other hand, when the overall molar ratio of Sn:S is increased resulting in Sn-rich quantum dots, the PL emission intensity is considerably improved by more than three times. The higher the Sn content, the higher the degree of passivation of surface atoms and dangling bonds quenching non-radiative charge recombination sites and thus increasing the PL emission of the quantum dots. Also, in the sample composed of Sn-rich quantum dots, the FWHM of the PL peaks is significantly narrower compared to the Sn-poor samples as seen in *Figure 5-18 (b)*. This result can be attributed to the narrower sizer-distribution of the quantum dots in the sample. These observations suggest that not only the amount of PVP stabiliser is vital for achieving optimum surface passivation of the quantum dots but so is the careful consideration of the molar ratios of the reactant species.

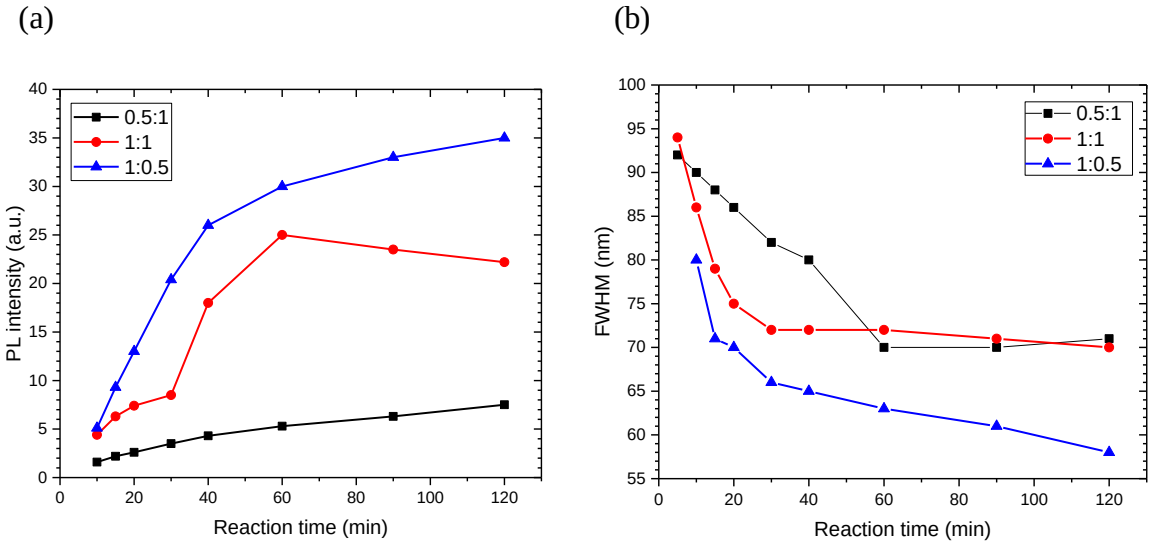

Figure 5- 18. Summary plots of the progression of the PL emission properties in PVP-capped SnS CQDs at different precursor concentrations (Sn:S) comparing the (a) PL emission intensity versus (b) FWHM of the PL peaks. The data points are acquired from the highest intensity PL peaks at each reaction time with an excitation wavelength of 470 nm.

5.3.4.3 Fine tuning of Sn:S molar ratios

Figure 5-18 shows that Sn-rich reaction conditions with Sn: S= 1:0.5 molar ratios result in quantum dots with enhanced PL emission features and a narrower size-distribution. In addition to the previous precursor concentration findings, further investigation of the precursors' molar ratios at 140^0C at different reaction times will be examined. In this study, I will perform fine tuning of the Sn-based precursor with respect to S (xSn: 1S) concentration keeping overall Sn-rich reaction conditions.

5.3.4.3.1 Effect on emission properties

The summary graph in *Figure 5-19 (a)* shows a systematic increase in the PL emission intensity of the quantum dots with increasing Sn concentration, which is in good accordance with the PL data recorded from the initial precursor concentration studies (refer to *Figure 5-18 (a)*). The results imply that the high Sn content within the crystal structure of the quantum dots improves the surface stabilisation as a source of Sn passivation ions. The higher the Sn concentration, the greater the degree of surface passivation in SnS boosting the PL emission. However, increasing the molar ratio of the Sn precursor more than two times with respect to the S precursor shows a decrease in the PL emission properties of the quantum dots (Sn: S= 4). Therefore, the obtained PL results indicate that there is an optimum precursor molar ratio of Sn: S= 2 required in the synthesis of PVP-capped SnS CQDs in order to obtain a full surface coverage of the quantum dots resulting in high-intensity PL emission and a narrowed size-distribution (FWHM= 57 nm).

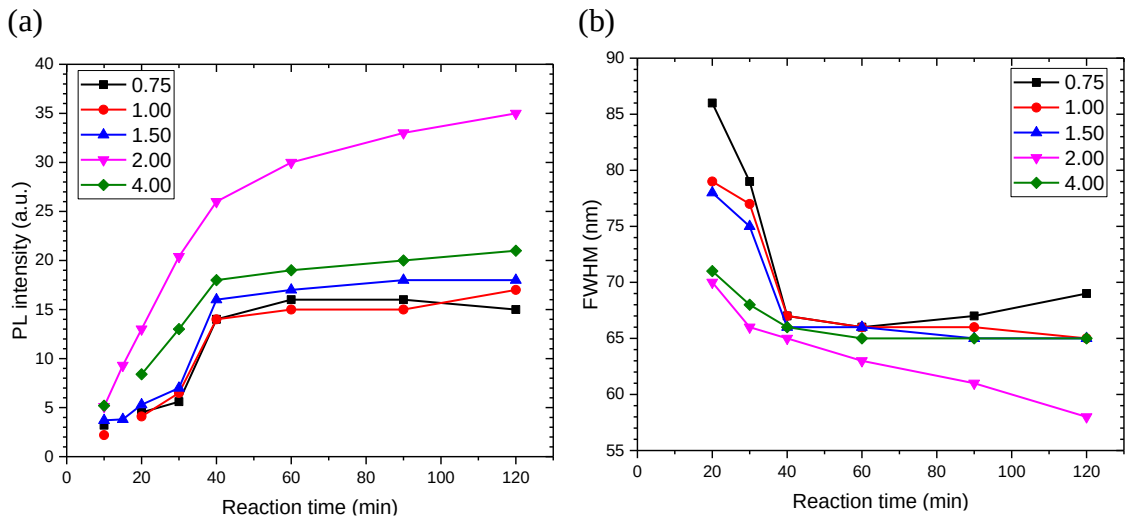

Figure 5- 19. Summary plots of the PL emission changes in PVP-capped SnS CQDs synthesised by tuning the molar ratios of the reacting precursors (Sn:S) synthesised at 140^{0}C with reactions times between 10 and 120 minutes. The (a) PL emission intensity and (b) FWHM of the highest intensity PL peaks at each concentration and reaction time were compared.

5.3.4.3.2 TEM analysis

Figure 5-20 represents HRTEM micrographs of individual SnS/PVP CQDs with distinctive interplanar distances. Regardless of their small average sizes (< 5 nm), the quantum dots are highly crystalline. *Figure 5-20 (c, f, i)* show HRTEM reconstruction images, which provide greater precision for measuring the interplanar distances (d-spacing) in each quantum dot. The d-spacing values of d= 0.40 nm measured in all three quantum dots closely match the standard d= 0.4035 nm for lattice plane (110) of the orthorhombic (Pbnm) phase of SnS. Also, a close examination of the individual quantum dots reveals their highly-ordered crystal atoms and absence of defects due to dislocations or twinning effects.

Furthermore, the performed EDX analysis on a larger area containing multiple quantum dots revealed the stoichiometric balance between the constituent elements (Sn: S= 1:1) summarised in *Table 5-3*. This observation suggests that the surface of the quantum dots is well-passivated resulting in less non-radiative recombination sites at the surface vacancies (trap states). TEM and EDX data as seen in *Figure 5-21* further support the PL results from the summary plots in

Figure 5-19 indicating an optimised surface coverage resulting in improved PL emission properties and narrowed size-distribution features of SnS/PVP CQDs.

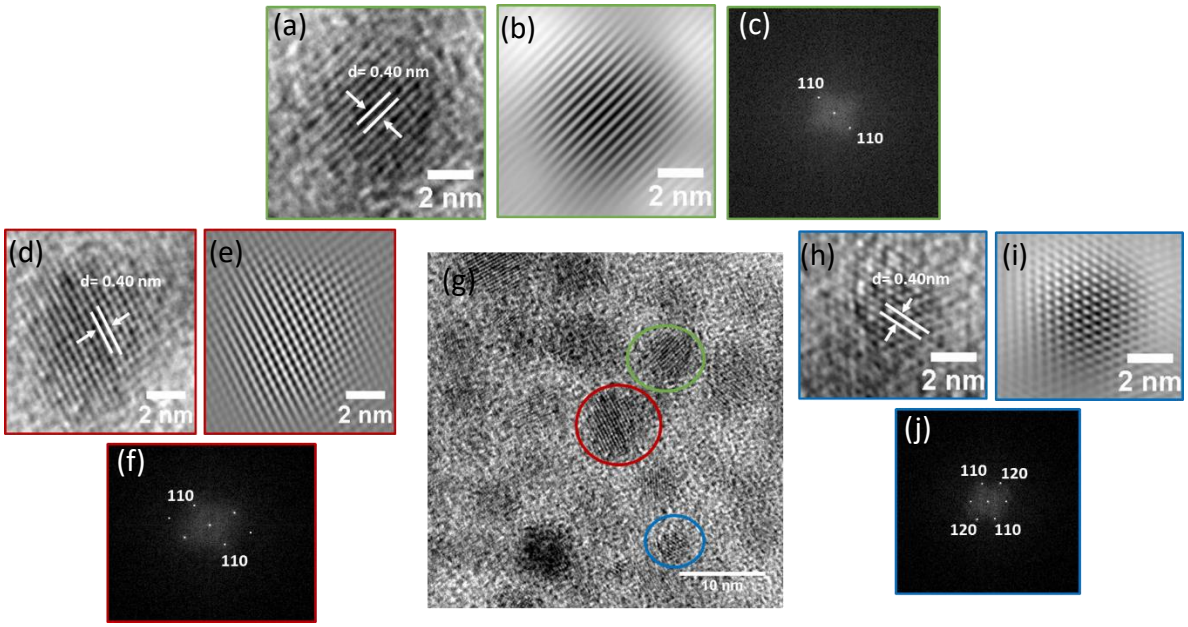

Figure 5- 20. TEM micrographs of SnS CQDs encapsulated with PVP 55 used at 10 % w/v and precursors' molar ratio of Sn: S= 2 synthesised at 140⁰ C. (g) Low (a, d, h) and HRTEM micrographs of single CQDs with clear lattice fringes. (c, f, j) FFT patterns and (b, e, i) HRTEM reconstruction images generated from the FFT patterns.

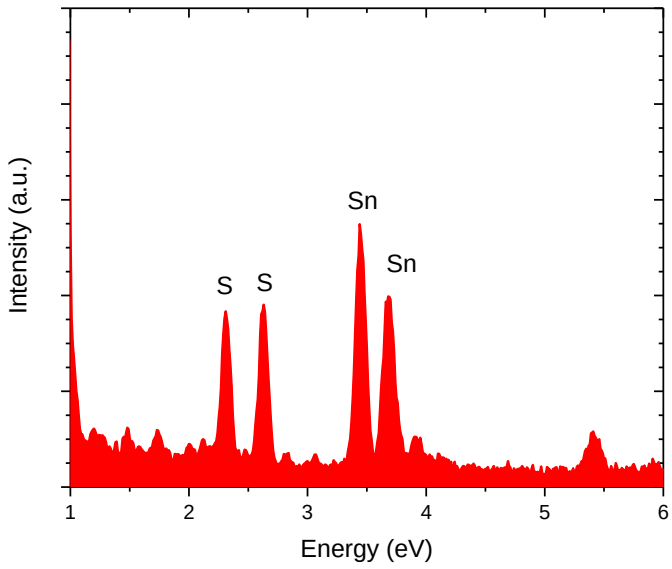

Figure 5- 21. An EDS map of PVP/SnS CQDs synthesised at 140⁰ C.

Table 5- 3. The average elemental composition of PVP-capped SnS CQDs, as shown in Figure 5-20.

Element	Weight %	Atomic %
S K	18.63	47.89
Sn L	81.37	52.18
		Atomic Ratio
Totals	100.00	Sn : S= 1 : 1

5.3.4.3.3 XPS analysis

Analogous to the TEM analysis in *Figure 5-20*, XPS measurements of the quantum dots were further carried out to prove the formation of SnS. The $3d_{5/2}$ and $3d_{3/2}$ peaks for Sn-$3d_5$ have binding energies of 486.7 eV and 494.9 eV, respectively as seen in *Figure 5-22 (a)*, which confirm the presence of Sn^{2+} oxidation state in the quantum dots.(183) In addition, the S 2p absorption peak at 161.5 eV is consistent with the literature values of S^{2-} (divalent S ion) as seen in *Figure 5-22 (b)*.(184) The obtained binding energies of the electronic states (3d) of Sn and S together with the crystal lattice measurements from TEM (see *Figure 5-20*) and the elemental composition analysis (refer to *Figure 5-21*) all confirm the formation of SnS.

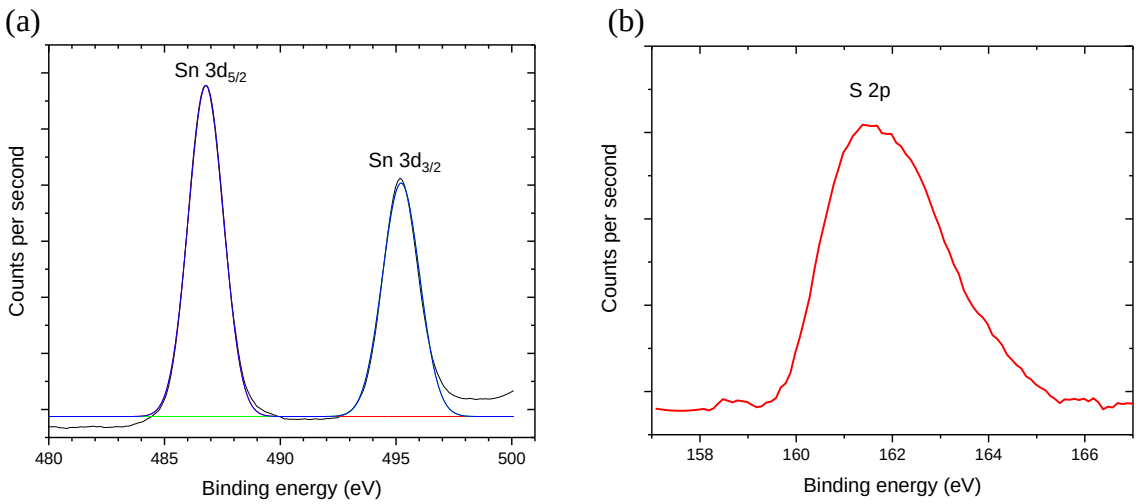

Figure 5- 22. XPS spectra of PVP-capped SnS CQDs. Samples were stored in air for a month before measurement.

5.3.4.3.4 Time-resolved µPL analysis (TRPL) as a function of reaction time

Time-resolved photoluminescence (TRPL) measurements of PVP-capped SnS CQDs synthesised with Sn: S= 2 and growing times ranging from 30 min to 120 min as a result of improved emission properties (as seen in *Figure 5-19*) at PL emission wavelength of 490 nm were carried. *Figure 5-23 (b)* shows a gradual increase in the PL lifetime from 2.8 ns (40 min aliquot) to 3.0 ns (90-120 min aliquots). The small changes in the PL lifetimes at early reaction stages could be related to surface rearrangements and size-focusing processes of the quantum dots as a function of growing time. This observation can be supported by the greater size-distribution of quantum dots measured from the FWHM of the PL emission peaks between 30 and 60 minutes of reaction time. A constant PL lifetime of 3.0 ns is reached as the reaction proceeds to completion (refer to *Figure 5-19 (b)*). Also, the fast exciton recombination suggests a well-passivated surface with a small number of defect sites for non-radiative charge recombination processes.

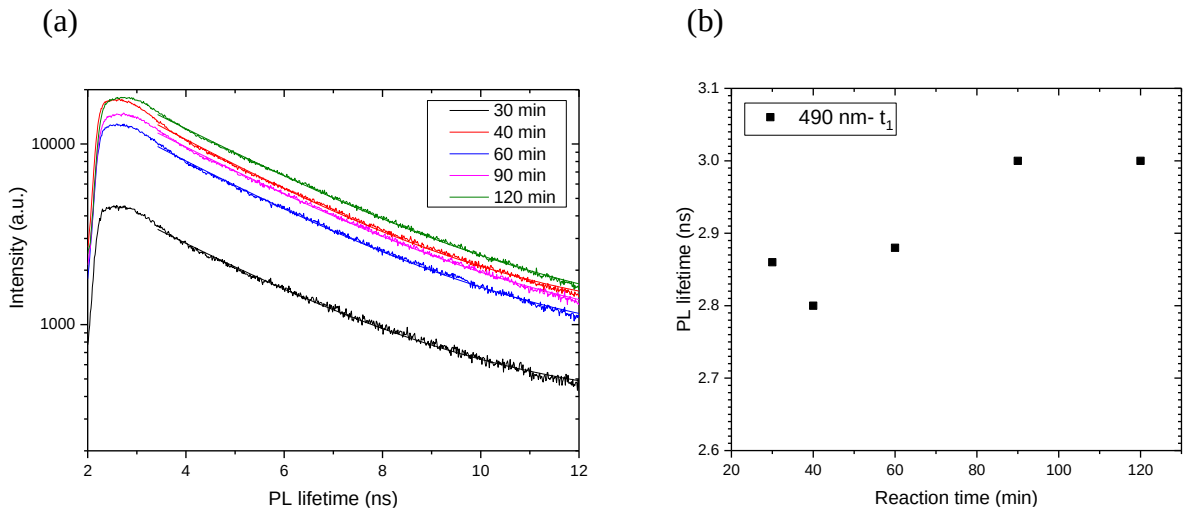

Figure 5- 23. (a) TRPL lifetime spectra of PVP-capped SnS CQDs with a precursor molar ratio of Sn: S= 2 using. The sample was illuminated with an excitation wavelength of 430 nm measuring the PL lifetime at 490 nm PL emission at reaction times ranging from 30 to 120 minutes. (b) Changes in the PL lifetimes of CQDs as a function of growing time obtained from the fitted PL decay curves in (a).

5.3.4.4 Wavelength-dependent photoluminescence measurements

5.3.4.4.1 Time-resolved micro-photoluminescence (TRPL) analysis

In addition to the time-resolved μPL measurements performed at an emission wavelength of 490 nm as seen in *Figure 5-23 (a)*, wavelength-dependent TRPL analysis was carried on SnS/PVP CQDs synthesised at 120 minutes (140^0 C) to study related size-dependent characteristics of the quantum dots at emission wavelengths ranging from 430 nm to 570 nm (in 20 nm increments) as seen in *Figure 5-24 (a)*. The PL lifetime of the quantum dots appears constant (~ 3.0 ns) regardless of the red-shift in the PL emission wavelength (from 490 nm to 570 nm), which suggests that the PL emission in that range does not possess size-dependent characteristics and belongs to a single population of quantum dots with similar or identical absorption/emission profiles. However, the faster PL lifetimes acquired at 450 nm and 470 nm could be related to the PL emission of PVP with a PL bright point at 430 nm (λ_{ex}= 350 nm) and lower intensity PL emission peak at 450 nm (λ_{ex}= 400 nm) as seen from the 3D PL spectra in *Figure 5-9 (a)* (refer to section 5.3.2.4.1). The precise tuning of Sn:S molar ratios resulted in

the fabrication of well-passivated quantum dots with good control over their morphology and size-distribution, factors that all contribute to their bright PL emission and fast radiative charge recombination lifetimes.

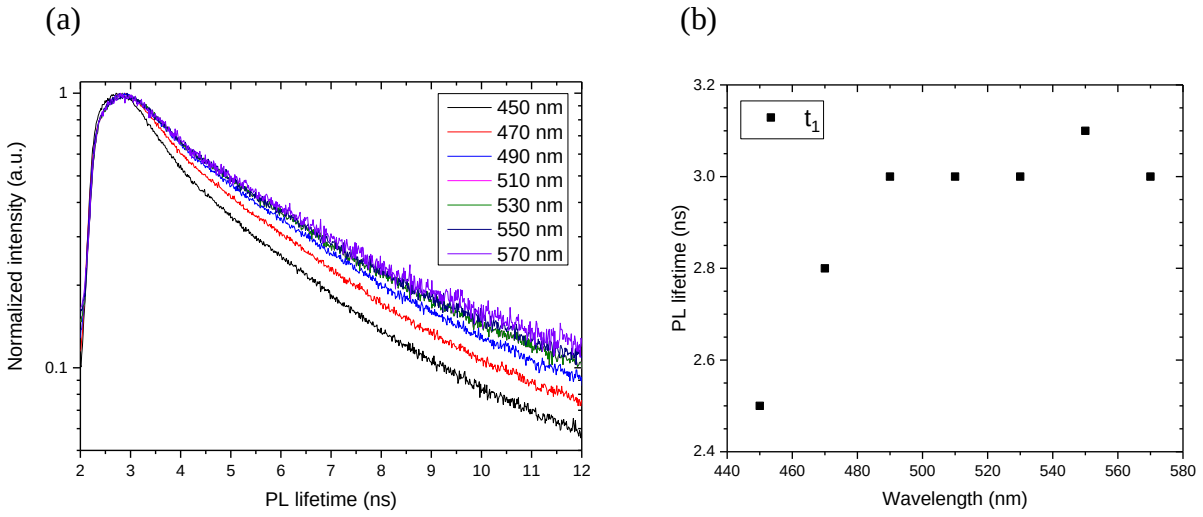

Figure 5- 24. (a) Wavelength-dependent TRPL decay curves of SnS/PVP CQDs (Sn: S= 2) synthesised at a reaction time of 120 minutes. An excitation wavelength of 430 nm was used to record the PL lifetime at various PL emission wavelengths ranging from 450 nm to 570 nm (with 20 nm increments). (b) Corresponding PL lifetimes from the fitted PL decay curves in (a).

5.4 Conclusions

In conclusion, a surface passivation method for the stabilisation of SnS CQDs applying PVP as an alternative capping agent has been developed. With the fine control of tuning the precursor molar ratios, reaction temperature and reaction times, high-quality PVP-encapsulated SnS CQDs with optimised surface stability were synthesised. TEM results reveal the crystalline nature of the quantum dots composed of a single crystal phase. The effectiveness of the surface passivation of SnS by the organic PVP shell was revealed by the high intensity of the PL emission as well as the narrowed line width of the PL peaks. Also, PL decay lifetime measurements further confirmed the good surface stability of the quantum dots showing fast

radiative PL lifetimes of ~ 3 ns, which indicates a reduction in the concentration of non-radiative charge recombination sites.

Chapter 6 SnS CQDs for Biofilm and Bioimaging applications

6.1 Introduction

Bioimaging labeling and sensing is a conventional and fast developing methodology used for bioanalysis.(185) These techniques are of great interest to the science community due to their high sensitivity,(186) fast acquisition times and responses as a result of the fluorescence lifetimes of the materials and versatility.(187) The most substantial requirements for a fluorescence material with optimum features are brightness and stability.

Many different materials such as complex organic dyes,(188) fluorescent proteins (189) and fluorescent nanoparticles have been explored and developed for various bioimaging applications in the past years due to their high photoluminescence quantum yields (PLQYs), relative stability and tunable sizes. The most prominent and established bioimaging label materials nowadays are the organic dyes and fluorescent proteins considering their commercial availability, water solubility, and small sizes. However, serious concerns in the use of these materials have been addressed due to their potential toxicity and carcinogenetic effects they might have on live organisms. Together with the poor photochemical stability and photobleaching characteristics of these materials, their relatively short lifetimes and narrow excitation range significantly hinder their optimum performance for life science applications.(190)(191) The requirement for more sensitive instrumentation and highly biocompatible materials has led researchers to the development of significantly improved imaging species and analytical instrumentations.

In response to the addressed drawbacks found in the current labeling agents, a new class of fluorescent nanomaterials has been highly researched. Interest in semiconductor nanomaterials

such as semiconductor quantum dots (QDs) as a new generation of bioimaging agents has been studied. This class of semiconductor nanomaterials is highly promising and capable of overcoming the present limitations found in the established bioimaging systems.(192)(193) The most recent advances in the bioimaging research using ultra-small inorganic nanomaterials (194) are summarised in *Table 6-1*.

When studying the biocompatibility of QDs two main requirements have to be considered such as the solubility and limited toxicity to living systems and cells. For example, the component elements of metal NCs are more earth-abundant compared to QD materials described in the table below. However, the lack of easy functionalization and fluorescence tunability makes those materials less attractive as bioimaging agents. Also, the development of complex synthetic procedures for the fabrication of Si NPs hinders the control over the reaction conditions and thus resulting in low QYs and lack of fluorescence tunability.

Table 6- 1. Fluorescent inorganic quantum dots for bioimaging applications. (Reprinted from reference 181).

Types	Representatives	Preparation Method	Size (nm)	Advantages	Disadvantages	Applications
QDs	CdSe, CdTe, InP, CuInS2 , CuInSe2 , and their core/shell	Solvothermal and hydrothermal methods	< 10	Tuneable size and fluorescence, high QY and relatively stable	Toxicity	Fluorescent labels and sensors
Metal NPs	Au, Ag, Cu, Pt, Pd	Reduction of metal salts or etching of large metal nanoparticles	< 2	Ultra-small size, easily taken up and excreted	Sensitive fluorescence, difficult for modification and functionalization	Imaging of cells and tissues Sensors
Carbon materials	C-dots, GQDs	Solvothermal and hydrothermal methods	< 10	Tunable fluorescence, excellent biocompatibility	Instability and unclearness of the fluorescence mechanism	Fluorescent biomarkers and sensors
UCNs	Yb3+/Ln3+-doped NaYF4, GdYF4 and their core/shell	Solvothermal and hydrothermal methods	> 10	Low background, large anti-Stokes shifts, sharp emission, high stability, deep penetration	Low QY, potential toxicity	Multimodal imaging agents and drug carriers
Si NP	Si	Etching annealed SiO_x, reduction of $SiCl_4$, and reaction of Na_4Si_4 with NH_4Br	< 5	Small size, ultrahigh stability	Laborious synthesis, low QY, difficult to tune fluorescence	Long-term imaging and labelling

6.2 Current materials

Despite the promising achievements in the synthesis and surface optimisation of QD materials, the toxicity of cadmium and lead (in CdTe, CdSe, CdS and PbSe, respectively) and the rareness of indium and tellurium (in CIGS, InAs and CdTe, respectively) lead to serious concerns about the production and bioimaging application of these materials.(195) The toxicity nature of Cd-based QDs is related to the degree of surface oxidation in those materials, leading to the free delivery of cadmium into the biological system. Surface passivation and types of surfactants used in the synthesis of QDs all play a cricial role in determining the cytotoxicity of the bioanalytical agents.

Derfus *et al*. investigated the effect of QDs on hepatic cells found in the liver as being the primary site for cells damage and QD accumulation.(196) Their observations revealed the increased oxidation of the Cd-based QDs as a function of either prolonged exposure to air before solubilization and cell incubation or UV light irradiation causing surface degradation of the QDs. In both cases, the QDs have been found to be inefficient in contact with the cells due to poor surface passivation and low photostability. Kirchner *et al.* reported the degradation of both CdSe core and CdSe/ZnS core/shell NPs when exposed to mercaptoacetic acid solutions during solubilization regardless of shell passivation. The release of Cd^{+} ions caused cell death.(197) The cytotoxicity drawback of the current CdSe and CdS QDs could be further improved and eliminated by overcoating the original core material with additional surface coatings.

6.3 Passivation strategies

6.3.1 Core/shell

The most common protection for semiconductor nanomaterials involves surface modification of the core material. In the coating procedure, a thin layer of a second semiconductor material is grown on the surface of the QD.(198) Depending on the precursor's concentrations and the rate at which the reagents are added to the crude core solution, the number of shell monolayers and overall shell thickness could be controlled and consequently tuned promoting homogeneous shell growth. Growing a ZnS semiconductor shell around CdSe QDs could significantly reduce the surface oxidation of the CdSe core QDs and potential toxicity effects on living organisms due to cadmium release. However, shell materials are also prone to oxidation and degradation similar to core QDs.(199)

6.3.2 Silica shells

Silica surface coatings offer an alternative approach to QD functionalization for live cell imaging applications. The extensive siloxane polymer network of silica shells adds additional protection and stability to the QDs. This passivation strategy protects the core material from oxidation effects of the surrounding environment and reducing the release of toxic core ions and decreasing the overall toxicity of the material to living cells. Silica shell coatings tend to form by replacing the hydrophobic groups or ligands on the QD surface.(200) An important point to be added in support of silica-coated QDs is that the optical properties of the core material can be preserved regardless of the overall size increase of the bare core quantum dot.

6.3.3 Amphiphilic polymers

Amphiphilic polymers can be successfully utilized as favorable functional coatings in the surface passivation of quantum dots. The main difference between the two organic polymers arises from the encapsulation procedure used to passivate the quantum dots. Amphiphilic polymers utilize the hydrophobic ligands on the QD surface as binding sites facilitating an organic shell coating.(201) Polymer materials are utilized not only as good surface passivation but also in solubilization techniques due to their various compositions and charges. Depending on the composition and variety of functional groups present in the polymer, controlled interactions between quantum dots and cells could be achieved. Ryman-Rasmussen *et al.* presented skin penetration of polymer coated QDs during an overnight exposure. They found that both PEG-coated (neutral) and PEG-amine-coated (cationic) QDs both penetrated the surface of the skin and localized within the dermal and epidermal layers after 8 h of exposure.(202) However, just adding more layers to quantum dots to eliminate cytotoxicity and improve stability is not an optimum strategy for biological applications.

6.4 New materials

Carbon QDs (CQDs) have been reported to be the current most promising candidate for bioimaging labeling and sensing applications due to low toxicity.(203) *Table 6-2* summarises various synthetic methods and features of CQDs from the literature and highlights essential advantages and disadvantages in those systems. The advantages of CQDs compared to the conventional QD materials such as small sizes, distinctive photoluminescence (PL) properties, cost-effectiveness, and low-toxicity, are a combination of significantly essential requirements from the ideal bioanalytical agent. The promising biocompatibility of CQDs could redirect current research and gradually replace the established bioimaging materials. However, the

relatively low brightness and photostability of CQDs are currently limiting their direct utilization in bioimaging applications.(204) Further work on the instability limitation is required to meet the required features.

Table 6- 2. Current achievements in synthesis, properties, and applications of CQDs. (Reprinted from reference 189).

Preparation Method	Size (nm)	Advantages	Disadvantages
Chemical ablation	< 10	Most accessible, various sources	Harsh conditions, drastic processes, multiple-steps, poor control over sizes
Electrochemical carbonization	< 2	Size and nanostructure are controllable, stable, one-step	Few small molecule precursors
Laser ablation	< 10	Rapid, effective, surface states tunable	Low QY, poor control over sizes, modification is needed
Microwave irradiation Hydrothermal/ solvothermal treatment	> 10	Rapid, scalable, cost effective, eco-friendly Cost effective, eco-friendly, non-toxic	Poor control over sizes Poor control over sizes

6.5 Objectives

The primary objective of this study is to incorporate SnS CQDs and investigate their potential biofilm and bioimaging applications on bacterial cells.

In the first part of this chapter, I will investigate two main hypotheses regarding the initiated biofilm formation as a result of the physicochemical interactions between two types of SnS CQDs with different surface fictionalizations and a medium containing *Pseudomonas fluorescens* ATCC 13525 *(P. fluorescence)* bacterial strain:

1) Effect of quantum dots' surface chemistry
2) Effect of quantum dot's toxicity

The two samples are abbreviated as SnS/L and PVP/SnS CQDs corresponding to ligand and polymer SnS surface passivation, respectively.

In the second part, I will demonstrate the efficiency of SnS/L CQDs as a potential fluorescent bioimaging material based on their excitation-dependent photoluminescence (PL) properties discussed in chapter 4.

6.6 Characterisation of biofilms

There are several hypotheses based on similar bacterial-QD interactions discussed in the literature explaining the origin of biofilm formation. The first hypothesis reveals that the biofilm formation could be a surface-induced process dependent on the surface chemistry or surface charge of the quantum dots concerning bacteria.(205) The second hypothesis suggests that the biofilm formation could be a toxicity induced process causing an interrupted growth of the bacterial cells altering their phenotype and thus resulting in the release of a polymeric substance (EPS) to protect the microbial community.(206) Cell to cell signaling known as quorum sensing is a process in which products or molecules are diffused from one cell and entering another cell.(207) Since the intracellular distances are quite small, minor disruptions to the regular cell growth by an external material could result in the transfer of bacterial products altering the state of the neighboring cells.

6.6.1 Effect of surface chemistry on biofilm formation

In the first study, the as-synthesised hydrophobic SnS/L and hydrophilic SnS/PVP CQDs were mixed with *P. fluorescence* culture medium. A small volume of the CQDs was added to the

bacterial cells forming a 0.8 % (v/v) solution concentration in each sample. Following overnight incubation (> 20 h) at 30^0 C, the changes to the cells were examined. *Figure 6-1* illustrates an evident biofilm-like growth for the culture containing SnS/L CQDs (refer to *Figure 6-1 (c)*) compared to the culture containing SnS/PVP CQDs in *Figure 6-1 (b)*, which shows no biofilm formation. These observations could be related to changes of the degree of bacterial attachment to and growth on the surface of the quantum dots as a result of the type of organic capping agent used for SnS surface passivation forming a biofilm. It appears that *P. fluorescence* show a preferential attachment to hydrophobic surfaces resulting in a biofilm formation as seen in *Figure 6-1 (c)*.

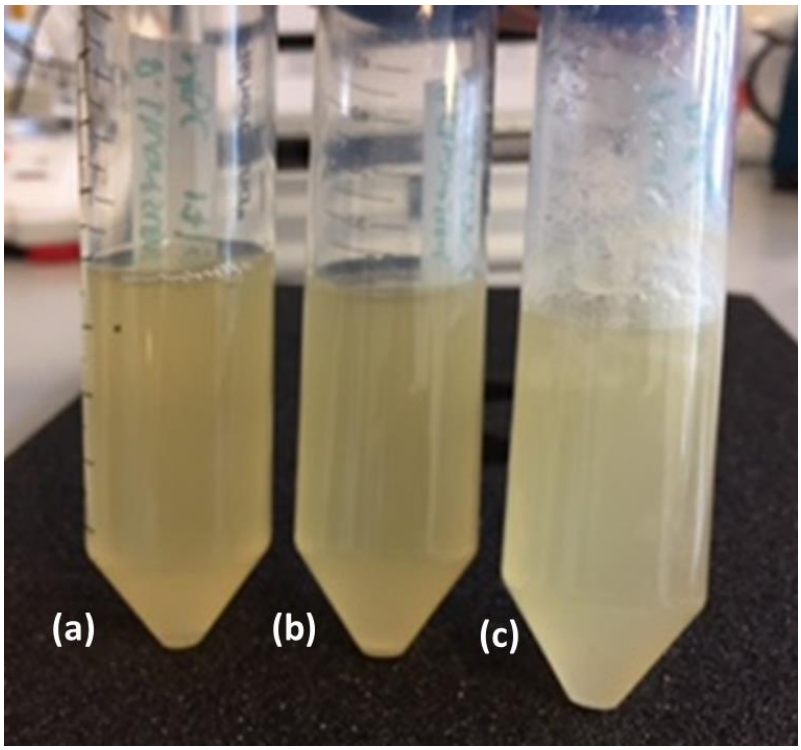

Figure 6- 1. Bacterial suspensions of P. fluorescence incubated with (a) no CQDs (reference sample), (b) 0.8 % (v/v) SnS/PVP and (c) 0.8 % (v/v) SnS/L CQDs for 20 hours.

Figure 6-2 provides a closer examination of the biofilm. The biofilm is observed to form on the walls of the centrifuge tube and more specifically at the surface interface between the air

and liquid medium. A uniform biofilm formation is observed in some parts of the walls, which could be explained by the angle at which the centrifuge tube was swirled at a certain speed as a mechanical agitation process during the overnight incubation. To gain a better understanding of the morphology of the biofilm, the sample was further examined under a fluorescent microscope and the results are presented in section 6.6.2.

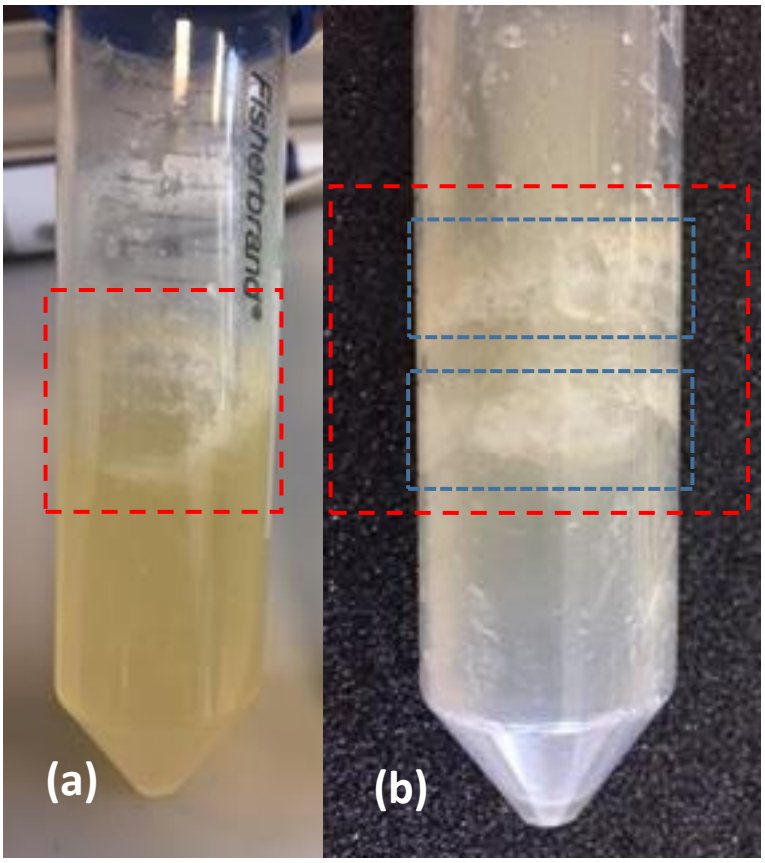

Figure 6- 2. (a) Image of P. fluorescence bacterial cells incubated with 0.8 % (v/v) SnS/L CQDs resulting in the initiation of biofilm formation. (b) The zoomed-in image is showing a closer view of the biofilm region on the walls of the centrifuge tube.

6.6.2 Morphological studies of the biofilm

In this section, the biofilm sample is further studied using an optical and spinning disc confocal microscope with a laser excitation wavelength of 488 nm. *Figure 6-3 (a)* presents a

fluorescence microscope image clearly showing the high surface roughness of the biofilm forming layers of bacteria and QDs. One interesting feature observed in the biofilm is the rearrangement and assembly of the QDs within the biofilm. There are two main ways they assemble: in the area where the resulting thickness of the biofilm is the highest (estimated by eye), bubble-like spheres are seen from the fluorescence image in *Figure 6-3 (b)*. The QDs tend to assemble at the surface edge of the bubbles as well as around the bacteria showing high-intensity green emission. An interesting point to be addressed here is that the bacteria were still alive and moving within the biofilm voids and throughout the entire biofilm regardless of its thickness, which could support my hypothesis of the lower to no toxicity of SnS/L CQDs. Furthermore, in the area where the surface of the biofilm appears to be thinner and smoother, composed of a thin biofilm layer, the QDs are well-dispersed and surrounding the bacteria. These findings could improve my understanding of the interaction between the bacterial cells and SnS/L CQDs and the consequent biofilm formation. Since the bacteria is still alive after an overnight incubation with the NPs, this might suggest that the formation of the biofilm is not due to the toxicity of the QDs changing their surface properties. In order to further explore the toxicity hypothesis, multiple concentration studies of SnS/L CQDs will be studied in the next section in order to understand and assign the origin of the biofilm formation.

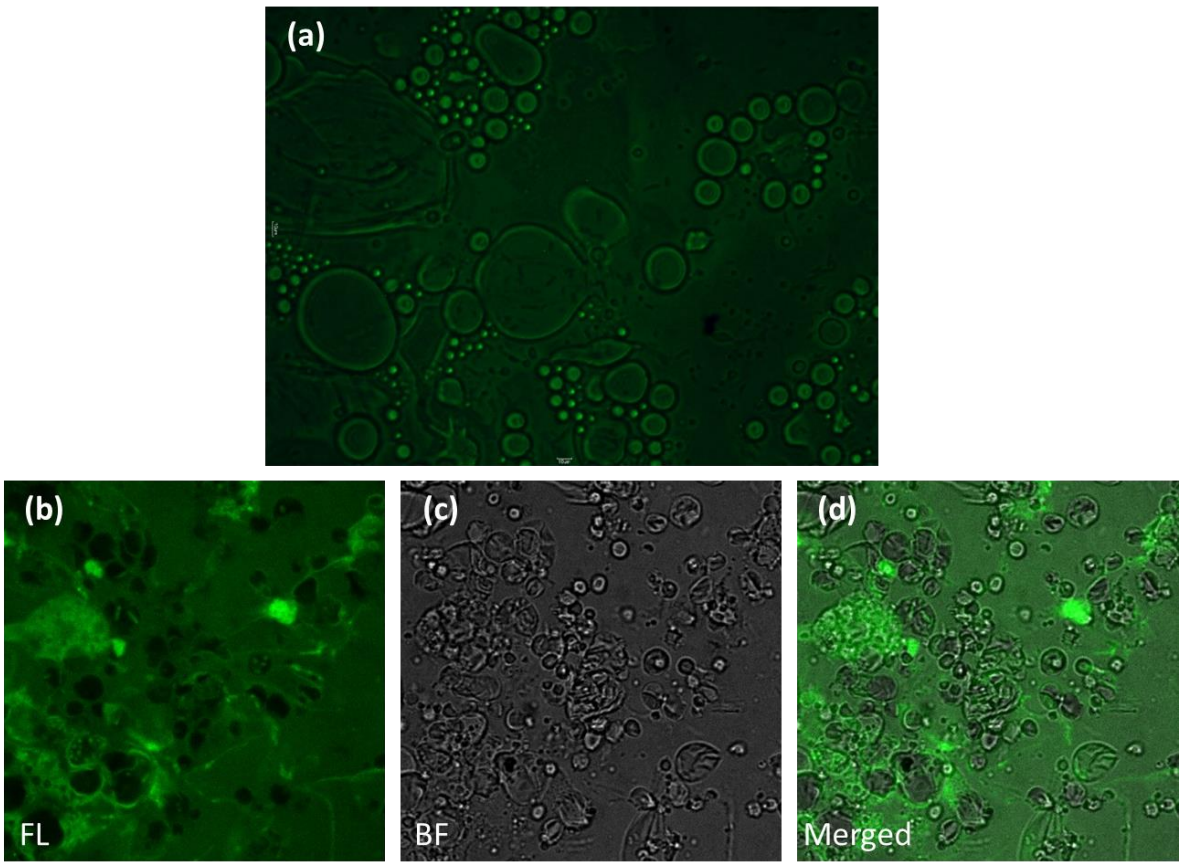

Figure 6- 3. (a) High-resolution fluorescence images of P. fluorescence cells incubated with 0.8 % (v/v) SnS/L CQDs for 20 hours imaged under (b) fluorescence (FL), (c) bright field and (d) merged mode with an optical or confocal microscope.

6.6.3 Toxicity test

6.6.3.1 Growth assay

To reveal whether the biofilm formation was induced by the toxicity of the quantum dots, the effect of different concentrations was studied by adding 0.3-20 % (v/v) of SnS/L CQDs to bacterial cultures of *P. fluorescens* prepared in a 96-well plate and growth was monitored over 24 h. *Figure 6-4* illustrates the growth curve of *P. fluorescens* bacterial strain, showing optical density changes as a function of the bacterial population over time. No significant impact on the bacterial growth is observed with different dosages of SnS/L CQDs comparing to the control, which was not exposed to the quantum dots. However, the overall trend shows a

relatively high consistency throughout the growing stages of the bacteria regardless of the QDs' concentration compared to the control growing curve of *P. fluorescens*. The observed findings confirm that the QDs are of no observable toxicity on the reproduction of *P. fluorescens* bacterial cells even at high loadings. The identified phenomenon in *Figure 6-4* together with the obtained results from the surface chemistry study of SnS/L and SnS/PVP CQDs as seen in *Figure 6-1* suggest that the biofilm formation is a non-toxicity induced process. However, it is initiated by the hydrophobic nature of the quantum dots acting as a preferential surface for bacterial cell adherence causing no apparent changes to the cell surface.

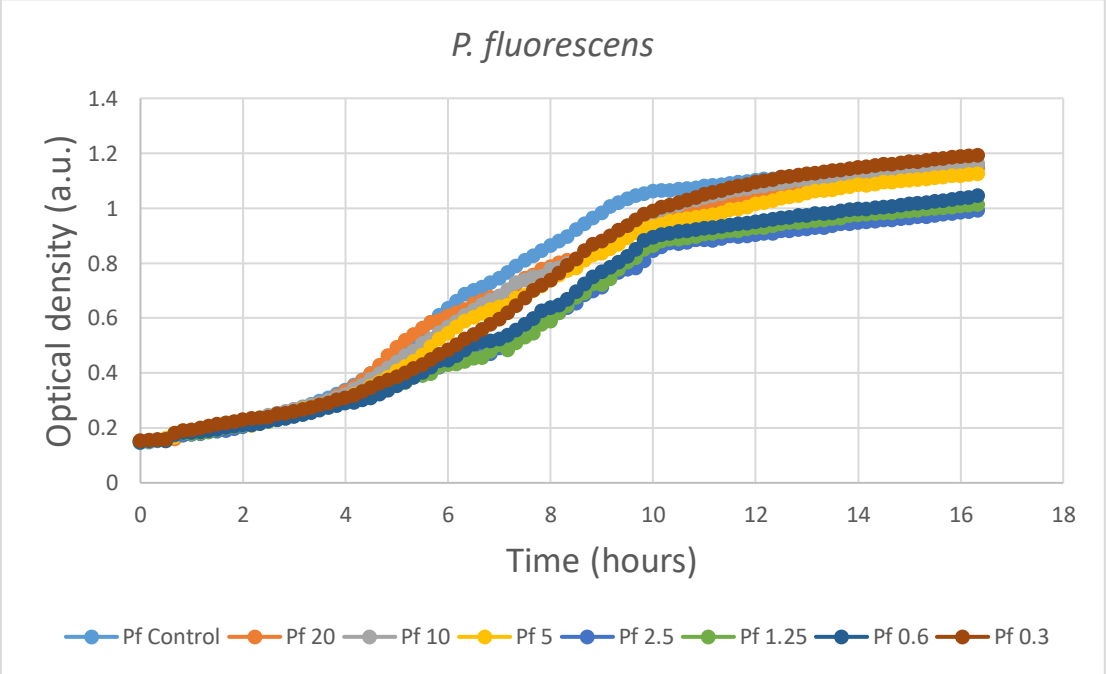

Figure 6- 4. Growth curve of P. fluorescence bacterial cells incubated with different dosages of SnS/L CQDs for 5 hours showing smooth growing conditions regardless of the quantum dots concentration.

6.7 Lambda scans of SnS CQDs

Lambda scan spectra were collected as a series of individual images within a wavelength range from 420 nm to 760 nm by collecting light every 10 nm in order to characterise the fluorescence emission features of SnS/L CQDs in the presence of bacteria when excited at 405 nm, 488 nm, and 561 nm. Data analysis was processed by measuring the fluorescence intensity of the QDs at each 10 nm collection band. *Figure 6-5* displays changes in the intensity of the emission characteristics of SnS/L CQDs excited at 405 nm (blue laser), 488 nm (green laser) and 561 nm (red laser). The lambda scan spectra reveal four emission peaks in the visible region of the spectrum with bright point emission wavelengths at 470 nm, 530 nm, 610 nm, and 660 nm. The obtained lambda scan results support that data from the 3D PL measurement in *Figure 4-8 (g, h)* (refer to section 4.3.1.1.2 in chapter 4) confirming the same peak emission wavelengths from SnS/L CQDs. It is important to be noted that the fluorescence properties of *P. fluorescens,* which emit light in the near-visible region of the electromagnetic spectrum, do not influence the interpretation of the emission properties of the QDs.(208) These observations suggest that the presence of the bacteria did not alter the emission wavelengths of the QDs confirming their stability with prolonged exposure to live cells and thus making SnS/L a suitable candidate for bioimaging applications.

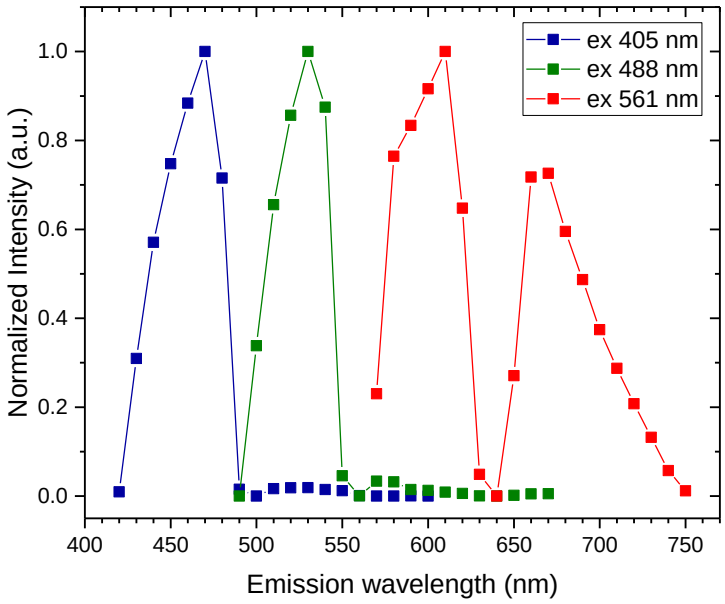

Figure 6- 5. Lambda scan spectra of the fluorescence intensity of SnS/L CQDs measured by collecting light in 10 nm bands from 420 nm-600 nm, 490 nm-690 nm and 570 nm-760 nm at 405 nm, 488 nm and 561 nm excitation wavelengths, respectively.

6.8 Bioimaging of bacterial cells

Figure 6-6 presents confocal fluorescence images of SnS/L CQDs (0.8 % (v/v)) incubated with *P. fluorescens* recorded at regions with different biofilm thickness. The intense blue, green and red fluorescence were obtained at excitation wavelengths at 405 nm, 488 nm, and 561 nm, respectively revealing the size-dependent emission characteristics of the quantum dots together with their imaging potential. The images illustrate that SnS/L CQDs are well-distributed within the biofilm showing higher emission intensities at regions of thicker biofilm formation. An important point to be addressed is that the QDs show no photobleaching properties even at prolonged excitation times, which is a common phenomenon observed in fluorescence dyes due to photochemical alterations of the organic molecules and their limited number of excitation cycles.

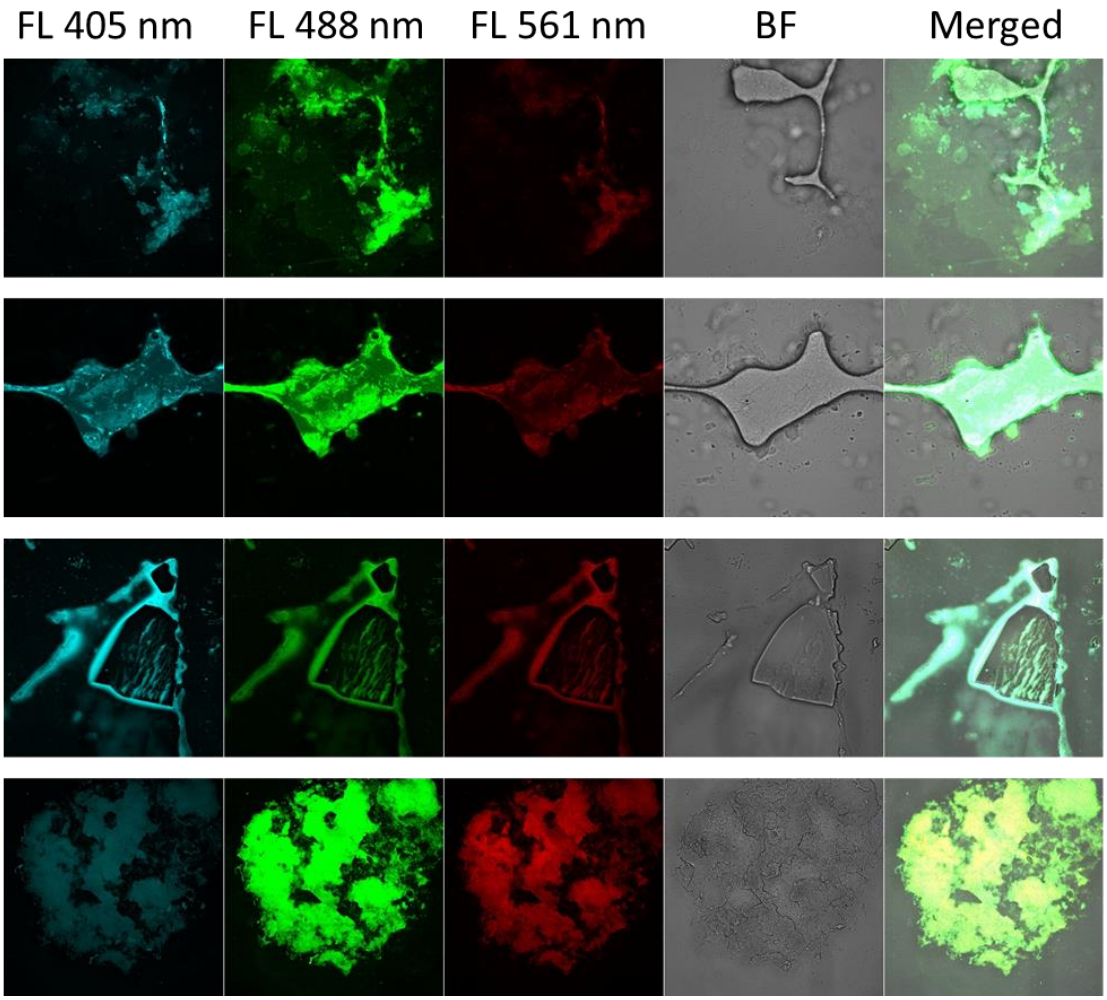

Figure 6- 6. High-resolution fluorescence images of P. fluorescence biofilms formed in the presence of SnS/L CQDs after 20 hours of incubation imaged under (a, b, c) fluorescence (FL) and (d) bright field mode with a confocal microscope excited at 405 nm (blue), 488 nm (green) and 561 nm (red) laser wavelengths. Images were acquired at biofilm regions of different thickness and adjusted for display purposes.

6.9 Conclusions

In conclusion, the exposure of bacterial suspensions of *P. fluorescens* to SnS/L CQDs induced biofilm formation with quantum dots surrounding the bacterial cells. By comparing the effect of quantum dots' surface passivation from samples containing SnS/L and SnS/PVP it was revealed that *P. fluorescens* possess a preferential adherence towards hydrophobic surfaces compared to hydrophilic surfaces, which was found to be in the origin of the biofilm formation.

Furthermore, the data analysis of the growth-based assay in *Figure 6-4* and the excitation-dependent emission properties of the quantum dots reveal that SnS/L CQDs can be successfully applied in bioimaging analysis of prokaryotes (bacterial cells) due to their excellent biocompatibility resulting in no toxicity-related division alterations in the bacterial cell community.

Chapter 7 Conclusions and future work

7.1 Conclusions

SnS CQDs is a promising candidate capable of overcoming the present toxicity limitations found in some of the highly researched semiconductor nanocrystals for biological labeling and imaging applications. The present work in this thesis describes optimised synthetic methods for tuning the optoelectronic properties of SnS resulting in highly fluorescent CQDs with novel size-dependent, multi-colour visible emission properties that have not been reported in the literature before. The observed drawback of SnS CQDs due to their excitation-dependent PL emission features is shown to be turned into their advantage. The key contributions and advances in this thesis are:

1) The use of a low-reactivity S precursor can tune the reaction mechanism by slowing down the rate of nucleation and growth of the quantum dots due to the slower formation of small nuclei used as templates in the crystal growth resulting in quantum dots with excitation-dependent PL emission characteristics covering the whole visible region of the electromagnetic spectrum.

2) The origin of the excitation-dependent PL emission of SnS CQDs is both size- and composition-related phenomenon. Small changes in the composition (Sn:S) result in different sizes of quantum dots with close absorption and emission profiles. For example, decrease in the atomic ratio of Sn to S ions results in the formation of quantum dots with bigger sizes as revealed by STEM/EDS analysis performed on multiple single CQDs as a statistical study. Mean particle sizes with aspect ratios between 2 nm and 3 nm and atomic ratios of Sn to S between 9:1 and 0.7:1 are attained.

3) In addition, time-resolved μPL measurements reveal size-dependent PL lifetime properties as a function of emission wavelength with a gradual increase from 2.2 ns (λ_{ex}= 400 nm, λ_{em}= 410 nm) to 4.7 ns (λ_{ex} = 400 nm, λ_{em} = 550 nm) with 20 nm increments. PL lifetimes reveal fast charge recombination rates suggesting good surface passivation with less non-radiative charge trap centres.

4) For the first time, SnS CQDs are shown to exhibit size-dependent PL emission properties as a function of size and composition tuning (stoichiometry changes in the atomic ratio of Sn:S).

5) An alternative surface passivation method by replacing the long chain organic ligands with an organic PVP polymer is exploited. With the fine control of tuning the precursor molar ratios (Sn:S), reaction temperature and reaction times, high-quality PVP-encapsulated SnS CQDs with bright PL emission and narrowed size-distribution features (FWHM= 57 nm) are achieved. Furthermore, fast PL decay lifetimes of ~ 3 ns indicate a reduction in the number of non-radiative charge trap states implying good surface stability of the quantum dots.

6) The multi-colour emission properties of SnS CQDs can provide a simultaneous bioimaging analysis with different emission colours in the visible spectrum as promising cell imaging nanoprobes. Lambda scan measurements reveal bright point emission in SnS CQDs at λ_{em}= 470 nm, 530 nm, and 660 nm. Also, the quantum dots show no photobleaching characteristics during the cell imaging, which is a common phenomenon in conventional organic dye probes.

7) Furthermore, bacterial cell incubation with SnS CQDs reveal no changes to the bacterial growth curve showing no alterations to the bacterial cell community of *P. fluorescens* over time revealing their non-toxic nature.

It has been shown that the high polydispersity nature of SnS CQDs containing various distributions of quantum dot sizes with size-dependent emission properties has been successfully utilised in bioimaging. Potential optoelectronic and photovoltaic applications can be considered.

7.2 Future work

1) Study the effect of different halide precursors on the rate of nucleation and growth kinetics and the overall surface passivation of the quantum dots.

2) Further improvements on the PL emission properties of ligand-stabilised SnS CQDs can be attempted by forming a core/shell structure.

3) Perform a biofilm quantification assessment performing a 96-well plate experiment using crystal violet as commonly used for staining grown biofilms on the walls of the wells.

4) Additional work can be performed in order to study the dynamics of the biofilm formation overtime by performing an in-situ live cell imaging under culturing conditions, which can provide precise information for determining the optimum growing parameters of the biofilm.

5) Consider the incorporation of SnS CQDs at different concentrations into human cells with the aim of studying their cytotoxicity.

6) Transform SnS into functionalized CQDs and apply them in various biomedical applications.

References

(1) BRUS L. A Simple-Model for the Ionization-Potential, Electron-Affinity, and Aqueous Redox Potentials of Small Semiconductor Crystallites. J Chem Phys 1983;79(11):5566-5571.

(2) Alivisatos A. Perspectives on the physical chemistry of semiconductor nanocrystals. J Phys Chem 1996 August 01;100(31):13226-13239.

(3) Chang J, Waclawik ER. Colloidal semiconductor nanocrystals: controlled synthesis and surface chemistry in organic media. Rsc Advances 2014;4(45):23505-23527.

(4) BRUS L. Electronic Wave-Functions in Semiconductor Clusters - Experiment and Theory. J Phys Chem 1986 June 05;90(12):2555-2560.

(5) Norris D, Bawendi M. Measurement and assignment of the size-dependent optical spectrum in CdSe quantum dots. Physical Review B 1996 June 15;53(24):16338-16346.

(6) BAWENDI M, STEIGERWALD M, BRUS L. The Quantum-Mechanics of Larger Semiconductor Clusters (Quantum Dots). Annu Rev Phys Chem 1990;41:477-496.

(7) Norris D, Bawendi M. Measurement and assignment of the size-dependent optical spectrum in CdSe quantum dots. Physical Review B 1996 June 15;53(24):16338-16346.

(8) Kim JY, Voznyy O, Zhitomirsky D, Sargent EH. 25th Anniversary Article: Colloidal Quantum Dot Materials and Devices: A Quarter-Century of Advances. Adv Mater 2013 September 01;25(36):4986-5010.

(9) Xia Y, Yang P, Sun Y, Wu Y, Mayers B, Gates B, et al. One-dimensional nanostructures: Synthesis, characterization, and applications. Adv Mater 2003 March 04;15(5):353-389.

(10) Moreels I, Lambert K, Smeets D, De Muynck D, Nollet T, Martins JC, et al. Size-Dependent Optical Properties of Colloidal PbS Quantum Dots. Acs Nano 2009 October 01;3(10):3023-3030.

(11) Sobhana SSL, Devi MV, Sastry TP, Mandal AB. CdS quantum dots for measurement of the size-dependent optical properties of thiol capping. Journal of Nanoparticle Research 2011 April 01;13(4):1747-1757.

(12) Azizian-Kalandaragh Y, Khodayari A, Zeng Z, Garoufalis CS, Baskoutas S, Cervera Gontard L. Strong quantum confinement effects in SnS nanocrystals produced by ultrasound-assisted method. Journal of Nanoparticle Research 2013 January 01;15(1):1388.

(13) Onyia AI, Ikeri HI, Nwobodo AN. Theoretical Study of the Quantum Confinement Effects on Quantum Dots using Particle in a Box Model. Journal of Ovonic Research 2018 February 01;14(1):49-54.

(14) Gao M, Xu Y, Jiang J, Yu S. Nanostructured metal chalcogenides: synthesis, modification, and applications in energy conversion and storage devices. Chem Soc Rev 2013;42(7):2986-3017.

(15) Li J, Wang Y, Guo W, Keay J, Mishima T, Johnson M, et al. Large-scale synthesis of nearly monodisperse CdSe/CdS core/shell nanocrystals using air-stable reagents via

successive ion layer adsorption and reaction. J Am Chem Soc 2003 October 15;125(41):12567-12575.

(16) Yang J, Ling T, Wu W, Liu H, Gao M, Ling C, et al. A top-down strategy towards monodisperse colloidal lead sulphide quantum dots. Nature Communications 2013 April 01;4:1695.

(17) Li Y, Tu JP, Huang XH, Wu HM, Yuan YF. Net-like SnS/carbon nanocomposite film anode material for lithium ion batteries. Electrochemistry Communications 2007 January 01;9(1):49-53.

(18) Rath JK, Prastani C, Nanu DE, Nanu M, Schropp REI, Vetushka A, et al. Fabrication of SnS quantum dots for solar-cell applications: Issues of capping and doping. Physica Status Solidi B-Basic Solid State Physics 2014 July 01;251(7):1309-1321.

(19) Alivisatos A. Semiconductor clusters, nanocrystals, and quantum dots. Science 1996 February 16;271(5251):933-937.

(20) Nozik AJ. Multiple exciton generation in semiconductor quantum dots. Chemical Physics Letters 2008 May 20;457(1-3):3-11.

(21) Moreau E, Robert I, Manin L, Thierry-Mieg V, Gerard J, Abram I. Quantum cascade of photons in semiconductor quantum dots. Phys Rev Lett 2001 October 29;87(18):183601.

(22) Volovichev I, Gurevich Y. Generation-recombination processes in semiconductors. Semiconductors 2001;35(3):306-315.

(23) Klimov V, Mikhailovsky A, McBranch D, Leatherdale C, Bawendi M. Quantization of multiparticle Auger rates in semiconductor quantum dots. Science 2000 February 11;287(5455):1011-1013.

(24) YABLONOVITCH E. Inhibited Spontaneous Emission in Solid-State Physics and Electronics. Phys Rev Lett 1987 May 18;58(20):2059-2062.

(25) SHOCKLEY W, READ W. Statistics of the Recombinations of Holes and Electrons. Physical Review 1952;87(5):835-842.

(26) HALL R. Electron-Hole Recombination in Germanium. Physical Review 1952;87(2):387.

(27) Mocatta D, Cohen G, Schattner J, Millo O, Rabani E, Banin U. Heavily Doped Semiconductor Nanocrystal Quantum Dots. Science 2011 April 01;332(6025):77-81.

(28) Kurzmann A, Ludwig A, Wieck AD, Lorke A, Gellert M. Auger Recombination in Self-Assembled Quantum Dots: Quenching and Broadening of the Charged Exciton Transition. Nano Letters 2016 May 01;16(5):3367-3372.

(29) Jha PP, Guyot-Sionnest P. Trion Decay in Colloidal Quantum Dots. Acs Nano 2009 April 01;3(4):1011-1015.

(30) Park Y, Bae WK, Pietryga JM, Klimov VI. Auger Recombination of Biexcitons and Negative and Positive Trions in Individual Quantum Dots. Acs Nano 2014 July 01;8(7):7288-7296.

(31) Wirths S, Geiger R, von den Driesch N, Mussler G, Stoica T, Mantl S, et al. Lasing in direct-bandgap GeSn alloy grown on Si. Nature Photonics 2015 February 01;9(2):88-92.

(32) Da Y, Xuan Y. Role of surface recombination in affecting the efficiency of nanostructured thin-film solar cells. Optics Express 2013 November 04;21(22):A1065-A1077.

(33) Zwijnenburg MA. Photoluminescence in semiconductor nanoparticles: an atomistic view of excited state relaxation in nanosized ZnS. Nanoscale 2012;4(12):3711-3717.

(34) Mir SH, Nagahara LA, Thundat T, Mokarian-Tabari P, Furukawa H, Khosla A. Review-Organic-Inorganic Hybrid Functional Materials: An Integrated Platform for Applied Technologies. J Electrochem Soc 2018;165(8):B3137-B3156.

(35) BRUS L. Electron Electron and Electron-Hole Interactions in Small Semiconductor Crystallites - the Size Dependence of the Lowest Excited Electronic State. J Chem Phys 1984;80(9):4403-4409.

(36) Alivisatos A. Perspectives on the physical chemistry of semiconductor nanocrystals. J Phys Chem 1996 August 01;100(31):13226-13239.

(37) Nirmal M, Brus L. Luminescence photophysics in semiconductor nanocrystals. Acc Chem Res 1999 May 01;32(5):407-414.

(38) McBride J, Treadway J, Feldman LC, Pennycook SJ, Rosenthal SJ. Structural basis for near unity quantum yield core/shell nanostructures. Nano Letters 2006 July 12;6(7):1496-1501.

(39) Bera D, Qian L, Tseng T, Holloway PH. Quantum Dots and Their Multimodal Applications: A Review. Materials 2010 April 01;3(4):2260-2345.

(40) COLVIN V, GOLDSTEIN A, ALIVISATOS A. Semiconductor Nanocrystals Covalently Bound to Metal-Surfaces with Self-Assembled Monolayers. J Am Chem Soc 1992 June 17;114(13):5221-5230.

(41) Peng X, Schlamp M, Kadavanich A, Alivisatos A. Epitaxial growth of highly luminescent CdSe/CdS core/shell nanocrystals with photostability and electronic accessibility. J Am Chem Soc 1997 July 30;119(30):7019-7029.

(42) Dabbousi B, RodriguezViejo J, Mikulec F, Heine J, Mattoussi H, Ober R, et al. (CdSe)ZnS core-shell quantum dots: Synthesis and characterization of a size series of highly luminescent nanocrystallites. J Phys Chem B 1997 November 13;101(46):9463-9475.

(43) Li L, Protiere M, Reiss P. Economic synthesis of high quality InP nanocrystals using calcium phosphide as the phosphorus precursor. Chemistry of Materials 2008 April 22;20(8):2621-2623.

(44) Dabbousi B, RodriguezViejo J, Mikulec F, Heine J, Mattoussi H, Ober R, et al. (CdSe)ZnS core-shell quantum dots: Synthesis and characterization of a size series of highly luminescent nanocrystallites. J Phys Chem B 1997 November 13;101(46):9463-9475.

(45) Kim S, Fisher B, Eisler H, Bawendi M. Type-II quantum dots: CdTe/CdSe(core/shell) and CdSe/ZinTe(core/shell) heterostructures. J Am Chem Soc 2003 September 24;125(38):11466-11467.

(46) Chaudhuri RG, Paria S. Core/Shell Nanoparticles: Classes, Properties, Synthesis Mechanisms, Characterization, and Applications. Chem Rev 2012 April 01;112(4):2373-2433.

(47) Reiss P, Protiere M, Li L. Core/Shell Semiconductor Nanocrystals. Small 2009 January 19;5(2):154-168.

(48) Park J, Kim S. CuInS2/ZnS core/shell quantum dots by cation exchange and their blue-shifted photoluminescence. Journal of Materials Chemistry 2011;21(11):3745-3750.

(49) Beberwyck BJ, Surendranath Y, Alivisatos AP. Cation Exchange: A Versatile Tool for Nanomaterials Synthesis. Journal of Physical Chemistry C 2013 October 03;117(39):19759-19770.

(50) Dloczik L, Engelhardt R, Ernst K, Fiechter S, Sieber I, Konenkamp R. Hexagonal nanotubes of ZnS by chemical conversion of monocrystalline ZnO columns. Appl Phys Lett 2001 June 04;78(23):3687-3689.

(51) Dloczik L, Konenkamp R. Nanostructure transfer in semiconductors by ion exchange. Nano Letters 2003 May 01;3(5):651-653.

(52) Park J, Zheng H, Jun Y, Alivisatos AP. Hetero-Epitaxial Anion Exchange Yields Single-Crystalline Hollow Nanoparticles. J Am Chem Soc 2009 October 07;131(39):13943-+.

(53) Yin Y, Rioux R, Erdonmez C, Hughes S, Somorjai G, Alivisatos A. Formation of hollow nanocrystals through the nanoscale Kirkendall Effect. Science 2004 April 30;304(5671):711-714.

(54) Lacroix L, Delpech F, Nayral C, Lachaize S, Chaudret B. New generation of magnetic and luminescent nanoparticles for in vivo real-time imaging. Interface Focus 2013 June 06;3(3):20120103.

(55) Erwin S, Zu L, Haftel M, Efros A, Kennedy T, Norris D. Doping semiconductor nanocrystals. Nature 2005 July 07;436(7047):91-94.

(56) Bryan JD, Gamelin DR. Doped Semiconductor Nanocrystals: Synthesis, Characterization, Physical Properties, and Applications. Progress in Inorganic Chemistry, Vol 54 2005;54:47-126.

(57) Fujii M, Yamaguchi Y, Takase Y, Ninomiya K, Hayashi S. Photoluminescence from impurity codoped and compensated Si nanocrystals. Appl Phys Lett 2005 November 21;87(21):211919.

(58) Yang H, Santra S, Holloway P. Syntheses and applications of Mn-doped II-VI semiconductor nanocrystals. Journal of Nanoscience and Nanotechnology 2005 September 01;5(9):1364-1375.

(59) Chen B, Zhong H, Zhang W, Tan Z, Li Y, Yu C, et al. Highly Emissive and Color-Tunable CuInS2-Based Colloidal Semiconductor Nanocrystals: Off-Stoichiometry Effects

and Improved Electroluminescence Performance. Advanced Functional Materials 2012 May 23;22(10):2081-2088.

(60) McDonald S, Konstantatos G, Zhang S, Cyr P, Klem E, Levina L, et al. Solution-processed PbS quantum dot infrared photodetectors and photovoltaics. Nature Materials 2005 February 01;4(2):138-142.

(61) Sargent EH. Infrared photovoltaics made by solution processing. Nature Photonics 2009 June 01;3(6):325-331.

(62) Gur I, Fromer N, Geier M, Alivisatos A. Air-stable all-inorganic nanocrystal solar cells processed from solution. Science 2005 October 21;310(5747):462-465.

(63) Wu Y, Wadia C, Ma W, Sadtler B, Alivisatos AP. Synthesis and photovoltaic application of copper(I) sulfide nanocrystals. Nano Letters 2008 August 01;8(8):2551-2555.

(64) Akhavan VA, Goodfellow BW, Panthani MG, Reid DK, Hellebusch DJ, Adachi T, et al. Spray-deposited CuInSe2 nanocrystal photovoltaics. Energy & Environmental Science 2010;3(10):1600-1606.

(65) Rath AK, Bhaumik S, Pal AJ. Mn-doped nanocrystals in light-emitting diodes: Energy-transfer to obtain electroluminescence from quantum dots. Appl Phys Lett 2010 September 13;97(11):113502.

(66) Singh M, Haverinen HM, Dhagat P, Jabbour GE. Inkjet Printing-Process and Its Applications. Adv Mater 2010 February 09;22(6):673-685.

(67) Thanh NTK, Maclean N, Mahiddine S. Mechanisms of Nucleation and Growth of Nanoparticles in Solution. Chem Rev 2014 August 13;114(15):7610-7630.

(68) LAMER V, DINEGAR R. Theory, Production and Mechanism of Formation of Monodispersed Hydrosols. J Am Chem Soc 1950;72(11):4847-4854.

(69) LEVINE J, MARK P. Theory and Observation of Intrinsic Surface States on Ionic Crystals. Physical Review 1966;144(2):751-&.

(70) Vengrenovich R, Gudyma Y, Yarema S. Ostwald ripening of quantum-dot nanostructures. Semiconductors 2001;35(12):1378-1382.

(71) Carey GH, Abdelhady AL, Ning Z, Thon SM, Bakr OM, Sargent EH. Colloidal Quantum Dot Solar Cells. Chem Rev 2015 December 09;115(23):12732-12763.

(72) de Kergommeaux A, Lopez-Haro M, Pouget S, Zuo J, Lebrun C, Chandezon F, et al. Synthesis, Internal Structure, and Formation Mechanism of Monodisperse Tin Sulfide Nanoplatelets. J Am Chem Soc 2015 August 12;137(31):9943-9952.

(73) Rempel JY, Bawendi MG, Jensen KF. Insights into the Kinetics of Semiconductor Nanocrystal Nucleation and Growth. J Am Chem Soc 2009 April 01;131(12):4479-4489.

(74) Hickey SG, Waurisch C, Rellinghaus B, Eychmueller A. Size and Shape Control of Colloidally Synthesized IV-VI Nanoparticulate Tin(II) Sulfide. J Am Chem Soc 2008 November 12;130(45):14978-+.

(75) Liu L., Tu H., Cremers C. and Stimming U. Solid-State Electrochemistry. 2006; 177, 2417-2419.

(76) LAMER V, DINEGAR R. Theory, Production and Mechanism of Formation of Monodispersed Hydrosols. J Am Chem Soc 1950;72(11):4847-4854.

(77) Tan F, Qu S, Wu J, Liu K, Zhou S, Wang Z. Preparation of SnS2 colloidal quantum dots and their application in organic/inorganic hybrid solar cells. Nanoscale Research Letters 2011 April 05;6:1-8.

(78) Ip AH, Thon SM, Hoogland S, Voznyy O, Zhitomirsky D, Debnath R, et al. Hybrid passivated colloidal quantum dot solids. Nature Nanotechnology 2012 September 01;7(9):577-582.

(79) Prastani C, Nanu M, Nanu D, Schropp REI, Rath JK. Synthesis of SnS/In2S3 core-shell nanoparticles. Chemical Physics Letters 2014 September 18;612:306-308.

(80) Antunez PD, Buckley JJ, Brutchey RL. Tin and germanium monochalcogenide IV-VI semiconductor nanocrystals for use in solar cells. Nanoscale 2011;3(6):2399-2411.

(81) Polking MJ, Urban JJ, Milliron DJ, Zheng H, Chan E, Caldwell MA, et al. Size-Dependent Polar Ordering in Colloidal GeTe Nanocrystals. Nano Letters 2011 March 01;11(3):1147-1152.

(82) Luther JM, Zheng H, Sadtler B, Alivisatos AP. Synthesis of PbS Nanorods and Other Ionic Nanocrystals of Complex Morphology by Sequential Cation Exchange Reactions. J Am Chem Soc 2009 November 25;131(46):16851-16857.

(83) Ba J, Polleux J, Antonietti M, Niederberger M. Non-aqueous synthesis of tin oxide nanocrystals and their assembly into ordered porous mesostructures. Adv Mater 2005 October 17;17(20):2509-+.

(84) Jayalakshmi M, Rao M, Choudary B. Identifying nano SnS as a new electrode material for electrochemical capacitors in aqueous solutions. Electrochemistry Communications 2004 November 01;6(11):1119-1122.

(85) Reddy NK, Hahn YB, Devika M, Sumana HR, Gunasekhar KR. Temperature-dependent structural and optical properties of SnS films. J Appl Phys 2007 May 01;101(9):093522.

(86) ALBERS W, HAAS C, VANDERMAESEN F. The Preparation and the Electrical and Optical Properties of Sns Crystals. Journal of Physics and Chemistry of Solids 1960;15(3-4):306-310.

(87) Burton LA, Walsh A. Phase Stability of the Earth-Abundant Tin Sulfides SnS, SnS2, and Sn2S3. Journal of Physical Chemistry C 2012 November 15;116(45):24262-24267.

(88) Shaposhnikov VL, Krivosheeva AV, Borisenko VE, Lazzari J-, d'Avitaya FA. Ab initio modeling of the structural, electronic, and optical properties of A(II)B(IV)C(2)(V) semiconductors. Physical Review B 2012 May 01;85(20):205201.

(89) MARIANO A, CHOPRA K. Polymorphism in some 4-6 Compounds Induced by High Pressure and Thin-Film Epitaxial Growth. Appl Phys Lett 1967;10(10):282-&.

(90) ETTEMA A, DEGROOT R, HAAS C, TURNER T. Electronic-Structure of Sns Deduced from Photoelectron-Spectra and Band-Structure Calculations. Physical Review B 1992 September 15;46(12):7363-7373.

(91) Ning J, Men K, Xiao G, Wang L, Dai Q, Zou B, et al. Facile synthesis of IV-VI SnS nanocrystals with shape and size control: Nanoparticles, nanoflowers and amorphous nanosheets. Nanoscale 2010;2(9):1699-1703.

(92) PARENTEAU M, CARLONE C. Influence of Temperature and Pressure on the Electronic-Transitions in Sns and Snse Semiconductors. Physical Review B 1990 March 15;41(8):5227-5234.

(93) Tanusevski A, Poelman D. Optical and photoconductive properties of SnS thin films prepared by electron beam evaporation. Solar Energy Mater Solar Cells 2003 November 01;80(3):297-303.

(94) Johnson J, Jones H, Latham B, Parker J, Engelken R, Barber C. Optimization of photoconductivity in vacuum-evaporated tin sulfide thin films. Semiconductor Science and Technology 1999 June 01;14(6):501-507.

(95) El-Nahass M, Zeyada H, Aziz M, El-Ghamaz N. Optical properties of thermally evaporated SnS thin films. Optical Materials 2002 October 01;20(3):159-170.

(96) Reddy TS, Kumar MCS, Shaji S. Deposition rate dependant formation and properties of Sn2S3 and SnS thin films by co-evaporation. Materials Research Express 2017 April 01;4(4):046404.

(97) Schneikart A, Schimper H, Klein A, Jaegermann W. Efficiency limitations of thermally evaporated thin-film SnS solar cells. Journal of Physics D-Applied Physics 2013 July 31;46(30):305109.

(98) RISTOV M, SINADINOVSKI G, GROZDANOV I, MITRESKI M. Chemical-Deposition of Tin(ii) Sulfide Thin-Films. Thin Solid Films 1989 June 01;173(1):53-58.

(99) Guo Y, Shi W, Wei G. Electrical properties of doped SnS thin films prepared by vacuum evaporation. ; 2007.

(100) Reddy KTR, Reddy NK, Miles RW. Photovoltaic properties of SnS based solar cells. Solar Energy Mater Solar Cells 2006 November 23;90(18-19):3041-3046.

(101) Konstantatos G, Howard I, Fischer A, Hoogland S, Clifford J, Klem E, et al. Ultrasensitive solution-cast quantum dot photodetectors. Nature 2006 July 13;442(7099):180-183.

(102) Tu C, Tang L, Huang J, Voutsas A, Lin LY. Visible electroluminescence from hybrid colloidal silicon quantum dot-organic light-emitting diodes. Appl Phys Lett 2011 May 23;98(21):213102.

(103) Keuleyan S, Lhuillier E, Brajuskovic V, Guyot-Sionnest P. Mid-infrared HgTe colloidal quantum dot photodetectors. Nature Photonics 2011 August 01;5(8):489-493.

(104) Li L, Pandey A, Werder DJ, Khanal BP, Pietryga JM, Klimov VI. Efficient Synthesis of Highly Luminescent Copper Indium Sulfide-Based Core/Shell Nanocrystals with Surprisingly Long-Lived Emission. J Am Chem Soc 2011 February 09;133(5):1176-1179.

(105) Steckel J, Coe-Sullivan S, Bulovic V, Bawendi M. 1.3 mu m to 1.55 mu m tunable electroluminescence from PbSe quantum dots embedded within an organic device. Adv Mater 2003 November 04;15(21):1862-1866.

(106) Qian L, Zheng Y, Xue J, Holloway PH. Stable and efficient quantum-dot light-emitting diodes based on solution-processed multilayer structures. Nature Photonics 2011 September 01;5(9):543-548.

(107) Barik S, Tan H, Jagadish C, Vukmirovic N, Harrison P. Selective wavelength tuning of self-assembled InAs quantum dots grown on InP. Appl Phys Lett 2006 May 08;88(19):193112.

(108) Vaughn DD, Hentz OD, Chen S, Wang D, Schaak RE. Formation of SnS nanoflowers for lithium ion batteries. Chemical Communications 2012;48(45):5608-5610.

(109) Zhou T, Pang WK, Zhang C, Yang J, Chen Z, Liu HK, et al. Enhanced Sodium-Ion Battery Performance by Structural Phase Transition from Two-Dimensional Hexagonal-SnS2 to Orthorhombic-SnS. Acs Nano 2014 August 01;8(8):8323-8333.

(110) Banai RE, Horn MW, Brownson JRS. A review of tin (II) monosulfide and its potential as a photovoltaic absorber. Solar Energy Mater Solar Cells 2016 June 01;150:112-129.

(111) Cai J, Li Z, Shen PK. Porous SnS Nanorods/Carbon Hybrid Materials as Highly Stable and High Capacity Anode for Li-Ion Batteries. Acs Applied Materials & Interfaces 2012 August 01;4(8):4093-4098.

(112) Ying H, Zhang S, Meng Z, Sun Z, Han W. Ultrasmall Sn nanodots embedded inside N-doped carbon microcages as high-performance lithium and sodium ion battery anodes. Journal of Materials Chemistry a 2017 May 14;5(18):8334-8342.

(113) Zheng P, Dai Z, Zhang Y, Khang Ngoc Dinh, Zheng Y, Fan H, et al. Scalable synthesis of SnS2/S-doped graphene composites for superior Li/Na-ion batteries. Nanoscale 2017 October 21;9(39):14820-14825.

(114) Qin K, Wang L, Wang N, Li J, Zhao N, Shi C, et al. Nitrogen and oxygen co-doped 3D nanoporous duct-like graphene@carbon nano-cage hybrid films for high-performance multi-style supercapacitors. Journal of Materials Chemistry a 2017 September 21;5(35):18535-18541.

(115) Wang Y, Zhang Y, Shi J, Kong X, Cao X, Liang S, et al. Tin sulfide nanoparticles embedded in sulfur and nitrogen dual-doped mesoporous carbon fibers as high-performance anodes with battery-capacitive sodium storage. Energy Storage Materials 2018 August 18.

(116) Kim JY, George SM. Tin Monosulfide Thin Films Grown by Atomic Layer Deposition Using Tin 2,4-Pentanedionate and Hydrogen Sulfide. Journal of Physical Chemistry C 2010 October 21;114(41):17597-17603.

(117) Muller M, Zentel R, Maka T, Romanov S, Torres C. Photonic crystal films with high refractive index contrast. Adv Mater 2000 October 16;12(20):1499-1503.

(118) Stavrinadis A, Smith JM, Cattley CA, Cook AG, Grant PS, Watt AAR. SnS/PbS nanocrystal heterojunction photovoltaics. Nanotechnology 2010 May 07;21(18):185202.

(119) Sinsermsuksakul P, Sun L, Lee SW, Park HH, Kim SB, Yang C, et al. Overcoming Efficiency Limitations of SnS-Based Solar Cells. Advanced Energy Materials 2014 October 28;4(15):1400496.

(120) Steinmann V, Brandt RE, Chakraborty R, Jaramillo R, Young M, Ofori-Okai BK, et al. The impact of sodium contamination in tin sulfide thin-film solar cells. Apl Materials 2016 February 01;4(2):026103.

(121) LOFERSKI J. Theoretical Considerations Governing the Choice of the Optimum Semiconductor for Photovoltaic Solar Energy Conversion. J Appl Phys 1956;27(7):777-784.

(122) Schaller RD, Sykora M, Jeong S, Klimov VI. High-efficiency carrier multiplication and ultrafast charge separation in semiconductor nanocrystals studied via time-resolved photoluminescence. J Phys Chem B 2006 December 21;110(50):25332-25338.

(123) Rath T, Gury L, Sanchez-Molina I, Martinez L, Haque SA. Formation of porous SnS nanoplate networks from solution and their application in hybrid solar cells. Chemical Communications 2015;51(50):10198-10201.

(124) Stevanovic V, Hartman K, Jaramillo R, Ramanathan S, Buonassisi T, Graf P. Variations of ionization potential and electron affinity as a function of surface orientation: The case of orthorhombic SnS. Appl Phys Lett 2014 May 26;104(21):211603.

(125) Sinsermsuksakul P, Hartman K, Kim SB, Heo J, Sun L, Park HH, et al. Enhancing the efficiency of SnS solar cells via band-offset engineering with a zinc oxysulfide buffer layer. Appl Phys Lett 2013 February 04;102(5):053901.

(126) Steinmann V, Jaramillo R, Hartman K, Chakraborty R, Brandt RE, Poindexter JR, et al. 3.88% Efficient Tin Sulfide Solar Cells using Congruent Thermal Evaporation. Adv Mater 2014 November 26;26(44):7488-7492.

(127) Yue GH, Wang LS, Wang X, Chen YZ, Peng DL. Characterization and Optical Properties of the Single Crystalline SnS Nanowire Arrays. Nanoscale Research Letters 2009 April 01;4(4):359-363.

(128) Shin H, Jang D, Hwang J, Jang Y, Cho M, Park K. Structural characterization of CdSe/ZnS core-shell quantum dots (QDs) using TEM/STEM observation. Journal of Materials Science-Materials in Electronics 2014 May 01;25(5):2047-2052.

(129) Greyson E, Barton J, Odom T. Tetrahedral zinc blende tin sulfide nanoand microcrystals. Small 2006 March 01;2(3):368-371.

(130) Hickey SG, Waurisch C, Rellinghaus B, Eychmueller A. Size and Shape Control of Colloidally Synthesized IV-VI Nanoparticulate Tin(II) Sulfide. J Am Chem Soc 2008 November 12;130(45):14978-+.

(131) Xu Y, Al-Salim N, Bumby CW, Tilley RD. Synthesis of SnS Quantum Dots. J Am Chem Soc 2009 November 11;131(44):15990-+.

(132) Salavati-Niasari M, Ghanbari D, Davar F. Shape selective hydrothermal synthesis of tin sulfide nanoflowers based on nanosheets in the presence of thioglycolic acid. J Alloys Compounds 2010 March 04;492(1-2):570-575.

(133) Liu H, Liu Y, Wang Z, He P. Facile synthesis of monodisperse, size-tunable SnS nanoparticles potentially for solar cell energy conversion. Nanotechnology 2010 March 12;21(10):105707.

(134) Deng Z, Han D, Liu Y. Colloidal synthesis of metastable zinc-blende IV-VI SnS nanocrystals with tunable sizes. Nanoscale 2011;3(10):4346-4351.

(135) de Kergommeaux A, Faure-Vincent J, Pron A, de Bettignies R, Malaman B, Reiss P. Surface Oxidation of Tin Chalcogenide Nanocrystals Revealed by Sn-119-Mossbauer Spectroscopy. J Am Chem Soc 2012 July 18;134(28):11659-11666.

(136) Prastani C, Nanu M, Nanu DE, Rath JK, Schropp REI. Synthesis and conductivity mapping of SnS quantum dots for photovoltaic applications. Materials Science and Engineering B-Advanced Functional Solid-State Materials 2013 May 15;178(9):656-659.

(137) Zhang J, Crisp RW, Gao J, Kroupa DM, Beard MC, Luther JM. Synthetic Conditions for High-Accuracy Size Control of PbS Quantum Dots. Journal of Physical Chemistry Letters 2015 May 21;6(10):1830-1833.

(138) Hendricks MP, Campos MP, Cleveland GT, Jen-La Plante I, Owen JS. A tunable library of substituted thiourea precursors to metal sulfide nanocrystals. Science 2015 June 12;348(6240):1226-1230.

(139) Garcia-Rodriguez R, Hendricks MP, Cossairt BM, Liu H, Owen JS. Conversion Reactions of Cadmium Chalcogenide Nanocrystal Precursors. Chemistry of Materials 2013 April 23;25(8):1233-1249.

(140) Alivisatos A. Perspectives on the physical chemistry of semiconductor nanocrystals. J Phys Chem 1996 August 01;100(31):13226-13239.

(141) Bai L, Ma X, Liu J, Sun X, Zhao D, Evans DG. Rapid Separation and Purification of Nanoparticles in Organic Density Gradients. J Am Chem Soc 2010 February 24;132(7):2333-2337.

(142) Wu X, Bittner A, Kern K. Synthesis, photoluminescence, and adsorption of CdS/dendrimer nanocomposites. J Phys Chem B 2005 January 13;109(1):230-239.

(143) Quan Z, Wang Y, Fang J. High-Index Faceted Noble Metal Nanocrystals (vol 46, pg 191, 2013). Acc Chem Res 2013 April 16;46(4):1050.

(144) Ferreira DL, Silva FO, Viol LCS, Schiavon MA, Licinio P, Valadares M, et al. Size Selective Precipitation of CdSe Colloidal Quantum Dots. Physics of Semiconductors 2009;1199:309-+.

(145) Park J, An K, Hwang Y, Park J, Noh H, Kim J, et al. Ultra-large-scale syntheses of monodisperse nanocrystals. Nature Materials 2004 December 01;3(12):891-895.

(146) Novak J, Nickerson C, Franzen S, Feldheim D. Purification of molecularly bridged metal nanoparticle arrays by centrifugation and size exclusion chromatography. Anal Chem 2001 December 01;73(23):5758-5761.

(147) Mori Y. Size-Selective Separation Techniques for Nanoparticles in Liquid. Kona Powder and Particle Journal 2015(32):102-114.

(148) Xu X, Caswell KK, Tucker E, Kabisatpathy S, Brodhacker KL, Scrivens WA. Size and shape separation of gold nanoparticles with preparative gel electrophoresis. Journal of Chromatography a 2007 October 05;1167(1):35-41.

(149) Kowalczyk B, Lagzi I, Grzybowski BA. Nanoseparations: Strategies for size and/or shape-selective purification of nanoparticles. Current Opinion in Colloid & Interface Science 2011 April 01;16(2):135-148.

(150) Peng X, Wickham J, Alivisatos A. Kinetics of II-VI and III-V colloidal semiconductor nanocrystal growth: "Focusing" of size distributions. J Am Chem Soc 1998 June 03;120(21):5343-5344.

(151) Qu L, Peng X. Control of photoluminescence properties of CdSe nanocrystals in growth. J Am Chem Soc 2002 March 06;124(9):2049-2055.

(152) Giansante C, Infante I. Surface Traps in Colloidal Quantum Dots: A Combined Experimental and Theoretical Perspective. Journal of Physical Chemistry Letters 2017 October 19;8(20):5209-5215.

(153) Wu N, Fu L, Su M, Aslam M, Wong K, Dravid V. Interaction of fatty acid monolayers with cobalt nanoparticles. Nano Letters 2004 February 01;4(2):383-386.

(154) Gerung H, Bunge S, Boyle T, Brinker C, Han S. Anhydrous solution synthesis of germanium nanocrystals from the germanium(II) precursor Ge[N(SiMe3)(2)](2). Chemical Communications 2005(14):1914-1916.

(155) WANG Y, HERRON N. Nanometer-Sized Semiconductor Clusters - Materials Synthesis, Quantum Size Effects, and Photophysical Properties. J Phys Chem 1991 January 24;95(2):525-532.

(156) Bang J, Yang H, Holloway P. Enhanced and stable green emission of ZnO nanoparticles by surface segregation of Mg. Nanotechnology 2006 February 28;17(4):973-978.

(157) Zheng J, Cao S, Wang L, Gao F, Weib G, Yang W. Temperature-dependent photoluminescence properties of Mn: ZnCdS quantum dots. Rsc Advances 2014;4(58):30948-30952.

(158) Ca NX, Bau NQ, Phan TL, Lien VTK, Lieu NTT, Nghia NX. Temperature-dependent photoluminescent and Raman studies on type-II CdS/ZnSe core/shell and CdS/CdZnS-ZnCdSe/ZnSe core/intermediate/shell nanoparticles. J Alloys Compounds 2017 March 15;697:401-408.

(159) Mork AJ, Weidman MC, Prins F, Tisdale WA. Magnitude of the Forster Radius in Colloidal Quantum Dot Solids. Journal of Physical Chemistry C 2014 June 26;118(25):13920-13928.

(160) Xia Y, Zhu C. Aqueous synthesis of type-II core/shell CdTe/CdSe quantum dots for near-infrared fluorescent sensing of copper(II). Analyst 2008;133(7):928-932.

(161) Zhang J, Zhang X, Zhang JY. Size-Dependent Time-Resolved Photoluminescence of Colloidal CdSe Nanocrystals. Journal of Physical Chemistry C 2009 June 04;113(22):9512-9515.

(162) BRUS L. Electronic Wave-Functions in Semiconductor Clusters - Experiment and Theory. J Phys Chem 1986 June 05;90(12):2555-2560.

(163) Xu F, Ma X, Haughn CR, Benavides J, Doty MF, Cloutier SG. Efficient Exciton Funneling in Cascaded PbS Quantum Dot Superstructures. Acs Nano 2011 December 01;5(12):9950-9957.

(164) Litvin AP, Parfenov PS, Ushakova EV, Fedorov AV, Artemyev MV, Prudnikau AV, et al. PbS Quantum Dots in a Porous Matrix: Optical Characterization. Journal of Physical Chemistry C 2013 June 13;117(23):12318-12324.

(165) Pokrant S, Whaley K. Tight-binding studies of surface effects on electronic structure of CdSe nanocrystals: the role of organic ligands, surface reconstruction, and inorganic capping shells. European Physical Journal D 1999 May 01;6(2):255-267.

(166) Underwood D, Kippeny T, Rosenthal S. Ultrafast carrier dynamics in CdSe nanocrystals determined by femtosecond fluorescence upconversion spectroscopy. J Phys Chem B 2001 January 18;105(2):436-443.

(167) Dabbousi B, RodriguezViejo J, Mikulec F, Heine J, Mattoussi H, Ober R, et al. (CdSe)ZnS core-shell quantum dots: Synthesis and characterization of a size series of highly luminescent nanocrystallites. J Phys Chem B 1997 November 13;101(46):9463-9475.

(168) Koczkur KM, Mourdikoudis S, Polavarapu L, Skrabalak SE. Polyvinylpyrrolidone (PVP) in nanoparticle synthesis. Dalton Transactions 2015;44(41):17883-17905.

(169) Saravanan L, Diwakar S, Mohankumar R, Pandurangan A, Jayavel R. Synthesis, Structural and Optical Properties of PVP Encapsulated CdS Nanoparticles. Nanomaterials and Nanotechnology 2011;1(2):42-48.

(170) Xia Y, Xiong Y, Lim B, Skrabalak SE. Shape-Controlled Synthesis of Metal Nanocrystals: Simple Chemistry Meets Complex Physics? Angewandte Chemie-International Edition 2009;48(1):60-103.

(171) Ataee-Esfahani H, Skrabalak SE. Attachment-based growth: building architecturally defined metal nanocolloids particle by particle. Rsc Advances 2015;5(59):47718-47727.

(172) Polavarapu L, Mourdikoudis S, Pastoriza-Santos I, Perez-Juste J. Nanocrystal engineering of noble metals and metal chalcogenides: controlling the morphology, composition and crystallinity. Crystengcomm 2015;17(20):3727-3762.

(173) Shchukin V, Schoell E, Kratzer P. Thermodynamics and Kinetics of Quantum Dot Growth. Semiconductor Nanostructures 2008:1-39.

(174) Kyrychenko A, Korsun OM, Gubin II, Kovalenko SM, Kalugin ON. Atomistic Simulations of Coating of Silver Nanoparticles with Poly(vinylpyrrolidone) Oligomers: Effect of Oligomer Chain Length. Journal of Physical Chemistry C 2015 April 09;119(14):7888-7899.

(175) Deivaraj T, Lala N, Lee J. Solvent-induced shape evolution of PVP protected spherical silver nanoparticles into triangular nanoplates and nanorods. J Colloid Interface Sci 2005 September 15;289(2):402-409.

(176) Xia X, Zeng J, Zhang Q, Moran CH, Xia Y. Recent Developments in Shape-Controlled Synthesis of Silver Nanocrystals. Journal of Physical Chemistry C 2012 October 18;116(41):21647-21656.

(177) Liu H, Liu Y, Wang Z, He P. Facile synthesis of monodisperse, size-tunable SnS nanoparticles potentially for solar cell energy conversion. Nanotechnology 2010 March 12;21(10):105707.

(178) Tsuji M, Nishizawa Y, Matsumoto K, Kubokawa M, Miyamae N, Tsuji T. Effects of chain length of polyvinylpyrrolidone for the synthesis of silver nanostructures by a microwave-polyol method. Mater Lett 2006 March 01;60(6):834-838.

(179) Liu I, Lo H, Chien C, Lin Y, Chen C, Chen Y, et al. Enhancing photoluminescence quenching and photoelectric properties of CdSe quantum dots with hole accepting ligands. Journal of Materials Chemistry 2008;18(6):675-682.

(180) Alias AN, Zabidi ZM, Harun MK, Yahya MZA, Ali AMM. Optical Transition, Excitation, and Emission Properties of Poly(N-Vinlycarbazole) Blended with Poly(Vinylidene Fluoride-co-Hexafluoropropene) and Polyvinylpyrrolidone. Acta Physica Polonica a 2015 April 01;127(4):1075-1078.

(181) Pan L, Sun S, Zhang A, Jiang K, Zhang L, Dong C, et al. Truly Fluorescent Excitation-Dependent Carbon Dots and Their Applications in Multicolor Cellular Imaging and Multidimensional Sensing. Adv Mater 2015 December 16;27(47):7782-7787.

(182) Liu H, Zhang B, Shi H, Tang Y, Jiao K, Fu X. Hydrothermal synthesis of monodisperse Ag(2)Se nanoparticles in the presence of PVP and KI and their application as oligonucleotide labels. Journal of Materials Chemistry 2008;18(22):2573-2580.

(183) Zhao Y, Zhang Z, Dang H, Liu W. Synthesis of tin sulfide nanoparticles by a modified solution dispersion method. Materials Science and Engineering B-Solid State Materials for Advanced Technology 2004 October 25;113(2):175-178.

(184) Salavati-Niasari M, Davar F, Mazaheri M. Synthesis and characterization of ZnS nanoclusters via hydrothermal processing from [bis(salicylidene)zinc(II)]. J Alloys Compounds 2009 February 20;470(1-2):502-506.

(185) Cassidy P, Radda G. Molecular imaging perspectives. Journal of the Royal Society Interface 2005 June 22;2(3):133-144.

(186) Hillman EMC. Optical brain imaging in vivo: techniques and applications from animal to man. J Biomed Opt 2007 October 01;12(5):051402.

(187) Luker GD, Luker KE. Optical imaging: Current applications and future directions. Journal of Nuclear Medicine 2008 January 01;49(1):1-4.

(188) Gong Y, Zhang X, Mao G, Su L, Meng H, Tan W, et al. A unique approach toward near-infrared fluorescent probes for bioimaging with remarkably enhanced contrast. Chemical Science 2016;7(3):2275-2285.

(189) Miyawaki A, Niino Y. Molecular Spies for Bioimaging-Fluorescent Protein-Based Probes. Mol Cell 2015 May 21;58(4):632-643.

(190) Resch-Genger U, Grabolle M, Cavaliere-Jaricot S, Nitschke R, Nann T. Quantum dots versus organic dyes as fluorescent labels. Nature Methods 2008 September 01;5(9):763-775.

(191) Jensen EC. Use of Fluorescent Probes: Their Effect on Cell Biology and Limitations. Anatomical Record-Advances in Integrative Anatomy and Evolutionary Biology 2012 December 01;295(12):2031-2036.

(192) Sapsford KE, Pons T, Medintz IL, Mattoussi H. Biosensing with luminescent semiconductor quantum dots. Sensors 2006 August 01;6(8):925-953.

(193) Sukhanova A, Devy M, Venteo L, Kaplan H, Artemyev M, Oleinikov V, et al. Biocompatible fluorescent nanocrystals for immunolabeling of membrane proteins and cells. Anal Biochem 2004 January 01;324(1):60-67.

(194) Li Z, Sun Q, Zhu Y, Tan B, Xu ZP, Dou SX. Ultra-small fluorescent inorganic nanoparticles for bioimaging. Journal of Materials Chemistry B 2014;2(19):2793-2818.

(195) Hardman R. A toxicologic review of quantum dots: Toxicity depends on physicochemical and environmental factors. Environ Health Perspect 2006 February 01;114(2):165-172.

(196) Derfus A, Chan W, Bhatia S. Probing the cytotoxicity of semiconductor quantum dots. Nano Letters 2004 January 01;4(1):11-18.

(197) Kirchner C, Liedl T, Kudera S, Pellegrino T, Javier A, Gaub H, et al. Cytotoxicity of colloidal CdSe and CdSe/ZnS nanoparticles. Nano Letters 2005 February 01;5(2):331-338.

(198) Reiss P, Bleuse J, Pron A. Highly luminescent CdSe/ZnSe core/shell nanocrystals of low size dispersion. Nano Letters 2002 July 01;2(7):781-784.

(199) Derfus A, Chan W, Bhatia S. Probing the cytotoxicity of semiconductor quantum dots. Nano Letters 2004 January 01;4(1):11-18.

(200) Ma Y, Li Y, Ma S, Zhong X. Highly bright water-soluble silica coated quantum dots with excellent stability. Journal of Materials Chemistry B 2014 August 21;2(31):5043-5051.

(201) Yu WW, Chang E, Falkner JC, Zhang J, Al-Somali AM, Sayes CM, et al. Forming biocompatible and nonaggregated nanocrystals in water using amphiphilic polymers. J Am Chem Soc 2007 March 14;129(10):2871-2879.

(202) Ryman-Rasmussen J, Riviere J, Monteiro-Riviere N. Penetration of intact skin by quantum dots with diverse physicochemical properties. Toxicological Sciences 2006 May 01;91(1):159-165.

(203) Zhang J, Yu S. Carbon dots: large-scale synthesis, sensing and bioimaging. Materials Today 2016 September 01;19(7):382-393.

(204) Wang Y, Hu A. Carbon quantum dots: synthesis, properties and applications. Journal of Materials Chemistry C 2014;2(34):6921-6939.

(205) Renner LD, Weibel DB. Physicochemical regulation of biofilm formation. MRS Bull 2011 May 01;36(5):347-355.

(206) Flemming H, Wingender J. The biofilm matrix. Nature Reviews Microbiology 2010 September 01;8(9):623-633.

(207) Carnes EC, Lopez DM, Donegan NP, Cheung A, Gresham H, Timmins GS, et al. Confinement-induced quorum sensing of individual Staphylococcus aureus bacteria. Nature Chemical Biology 2010 January 01;6(1):41-45.

(208) MEYER, J. M. ABDALLAH, M. A.The Fluorescent Pigment of Pseudomonas fluorescens: Biosynthesis, Purification and Physicochemical Properties. Microbiology 1978 August 01; 107: 319-328